Acta Physica Hungarica

VOLUME 71 · NUMBERS 1–2, 1992

Akadémiai Kiadó, Budapest

ACTA PHYS. HUNG. APAHAQ 71 (1–2) 1-142 (1992) HUS ISSN 0231–4428

ACTA PHYSICA HUNGARICA

A JOURNAL OF THE HUNGARIAN ACADEMY OF SCIENCES

EDITED BY
I. KOVÁCS

Acta Physica publishes original papers on subjects in physics. Papers are accepted in English, French, German and Russian.

Acta Physica is published in two yearly volumes (4 issues each) by

AKADÉMIAI KIADÓ
Publishing House of the Hungarian Academy of Sciences
H–1117 Budapest, Prielle Kornélia u. 19–35.

Subscription information

Orders should be addressed to

AKADÉMIAI KIADÓ
H-1519 Budapest, P. O. Box 245

Acta Physica Hungarica is abstracted/indexed in Chemical Abstracts, Mathematical Reviews, Science Abstracts, Physics Briefs, Risk Abstracts

CONTENTS

Acta Physica Hungarica 71 (1–2), pp. 3–7 (1992)

AGE–HARDENING CHARACTERISTICS OF AN AlMgSi ALLOY

Z. H. ISMAIL and B. BOUCHRA

Department of Metallurgy, NRC, Atomic Energy Commission
Cairo, Egypt

(Received 20 June 1990)

Age-hardening behaviour of an AlMgSi alloy was followed by hardness measurements during isochronal and isothermal ageing. The alloy is found to age-harden during natural ageing at room temperature after quenching from the solid solution temperature. The alloy exhibits peak hardness by artificial ageing at 200 °C for 2 hours. Isothermal ageing curves indicated that the rate of hardness increase at early stages of ageing, is dependent upon the ageing temperature in a manner which obeys an Arrhenius-type equation. An activation energy of 0.95 ± 0.05 eV was calculated from the Arrhenius plot of the results. This activation energy shows that the process responsible for hardness increase in the early stages of ageing may be controlled by the migration of solute-vacancy complexes.

1. Introduction

The AlMgSi system is the basis for a major class of heat-treable alloys used for both wrought and cast products. These alloys are of great technological interest since they combine many favourable characteristics including moderately high strength, relatively low quench sensitivity and good corrosion resistance. In a previous work [1] the precipitation behaviour during ageing of the supersaturated solid solution of an AlMgSi alloy was investigated using transmission electron microscope. The aim of the present work was to follow the precipitation from solid solution during ageing at various temperatures, by hardness measurements.

2. Materials and experimental

The material under investigation is cold-rolled sheets of AlMgSi alloy containing 0.98 wt % Si, 0.78 wt % Mg as major alloying elements and 0.31 wt % Mn and 0.06 wt % Fe as minor additions. Specimens of about 1 cm^2 area were cut from the as-received sheet, and solid solution annealed at 570 °C for one hour in air muffle furnace whose temperature is controlled to ±5 °C. The specimens were then quenched in water and were given 5 minutes standard delay at room temperature before artificial ageing. Artificial ageing was conducted in an air chamber furnace at temperatures from 100 up to 300 °C for various periods of time ranging from 5 minutes to 24 hours. The temperature of the furnace was controlled to ±5 °C.

Natural ageing was simply performed by leaving the specimens at room temperature in air for different time periods after quenching.

Vickers hardness was then measured using a hardness testing machine type W. P. M. Werkstoffprüfmaschinen, Leipzig, Germany. The relationship between hardness values and ageing temperature and/or time are plotted. Each data point on the hardness curves is the average of at least ten measurements.

3. Results

Isochronal ageing curves are presented in Fig. 1, from which it is shown that hardness increases with ageing temperature to a maximum, then decreases by further temperature increase. It can also be noticed that increasing duration of ageing resulted in a shift of the peak hardness towards lower temperatures. From Fig. 1 one can observe that maximum hardening of the alloy is achieved by ageing at 200 °C for 2 hours after quenching from the solid solution temperature.

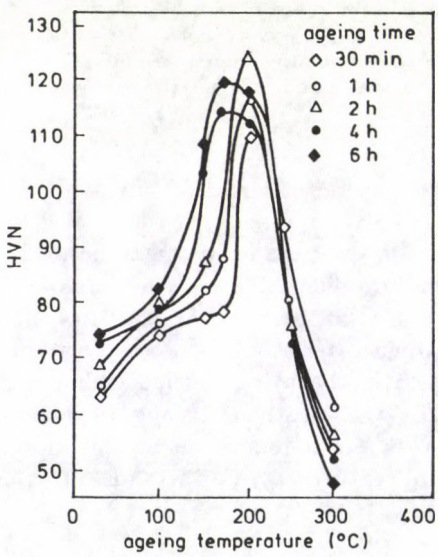

Fig. 1. Isochronal ageing curves for AlMgSi alloy solid solution annealed for 1 h at 570 °C and water-quenched

The isothermal ageing curves are illustrated in Fig. 2. It is clear that the supersatured solid solution exhibits hardening by natural ageing at room temperature as well as during artificial ageing at elevated temperatures. The hardness increases at a fast rate in the early stages of ageing at temperatures from room up to 200 °C. By prolonged ageing the hardness continues to increase but at a slower rate, except for ageing at 200 °C where the hardness achieves a maximum value

after 2 hours and then decreases with time. Ageing at 250 °C produced maximum hardness after 10 minutes; the shortest ageing time employed, then the hardness decreases continuously with time.

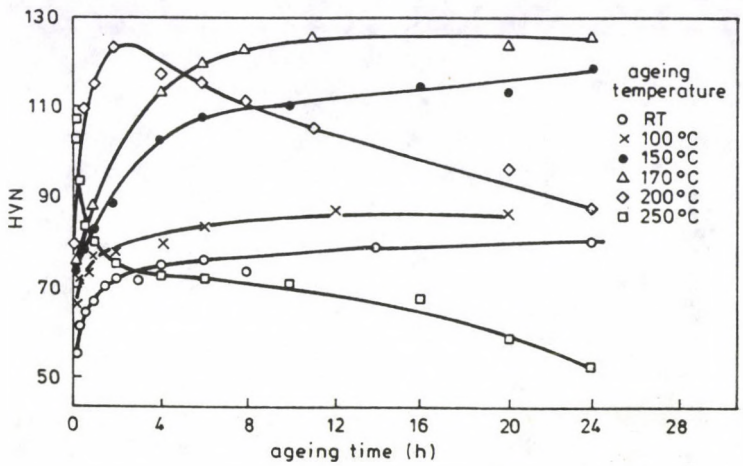

Fig. 2. Isothermal ageing curves for AlMgSi alloy solid solution annealed at 570 °C for 1 h and water-quenched

From Fig. 2 it is observed that the rate of hardness increase at early stages of ageing is enhanced by ageing temperature increase. The natural logarithm of hardening rate exhibited at different ageing temperatures (taken at constant hardness value) was plotted against the reciprocal of the absolute ageing temperature as shown in Fig. 3. The fact that the points lie on a straight line leads to the conclusion that the hardening rate during early stages of artifical ageing obeys an Arrhenius-type equation of the form:

$$H^{\bullet} = H_0^{\bullet} e^{-Q/RT},$$

where $H^{\bullet}$ is the hardening rate, $H_0^{\bullet}$ is a structure constant, Q is the activation energy, R is the gas constant and T is the absolute ageing temperature.

An activation energy of 0.95 ± 0.05 eV is calculated from the slope of the straight line in Fig. 3. This represents the activation energy for the process responsible for hardness increase.

4. Discussion

The precipitation sequence which takes place during ageing of AlMgSi type alloys known from X-ray diffraction and electron microscopy studies [1–5] is as follows:

Supersatured—	Coherent G. P. zones—	Semicoherent—	Incoherent
solid solution	of needle shape	B' rods	B(Mg_2Si) platelets

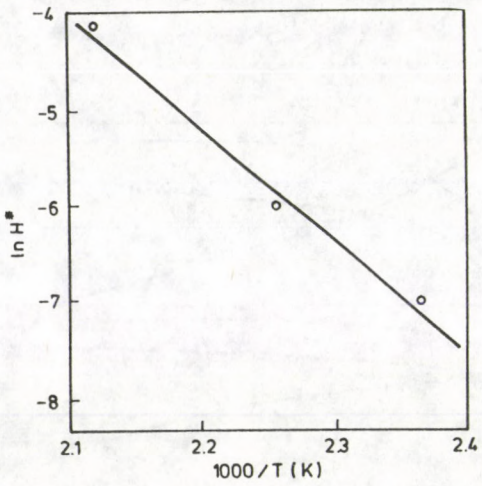

Fig. 3. Arrhenius plot of ln hardening rate H as a function of $1/T$ for Al–Mg–Si alloy solution annealed at 570°C for 1 h and water-quenched

The change in hardness with varying ageing temperature and/or time shown in Figs 1 and 2 could be attributed to the various precipitate structures formed as found previously [1]. During early stages of ageing (low temperature and/or short time), the increase in hardness takes place due to the formation of clusters or fine scale precipitates. These clusters or pre-precipitates as classified before [3] could not be revealed during bright field microscopy examination. However, their presence was only detected [1,6] by selected area diffraction pattern technique. By progressive ageing these clusters grow up in size to form the needle-like G. P. zones which are coherent with the matrix along $< 100 >$ cube direction. These needle-like precipitates are known [7] to be responsible for age-hardening of AlMgSi alloys. The peak hardness (Figs 1, 2) would thus correspond to the optimum size and density of such precipitates. The needle-like precipitates grow up by prolonged ageing and transform to larger widely spaced rod-like precipitates and then to the equilibrium Mg_2Si platelets with a corresponding drop in hardness, i.e. overageing.

The isothermal ageing curves in Fig. 2 indicate that the process responsible for hardness increase during early stages of ageing is diffusion controlled with an activation energy of 0.95 ± 0.05 eV. It was suggested [8,9] that during early stages of ageing precipitation is controlled by silicon diffusion. The activation energy of 0.95 eV determined in the present work is lower than the activation energies of 1.43 and 1.13 eV reported [10] for the diffusion of Si and Mg in Al, respectively. This low activation energy determined in the present results might be due to the formation of complexes between quenched-in vacancies and solute atoms [11], namely silicon. The activation energy for the migration of these complexes is expected to be less

than that for normal solute atoms [12]. The initial fast rate of hardness increase (Fig. 2) is thus thought to be due to the high rate of clustering or precipitation, enhanced by the large concentration of quenched-in vacancies. Due to the high binding energy between the vacancies and the clusters [4], the former will rapidly become incorporated in the latter and will be virtually eliminated from the matrix. Consequently, one would expect a change from a high to low rate of clustering or hardness increase (as shown in Fig. 2), as the concentration of vacancies in the matrix diminishes.

References

1. Z. H. Ismail, Ph. D. Thesis, Cranfield Inst. Techn., England, 1977.
2. G. Thomas, JIM, *90*, 57, 1961–62.
3. A. Lutts, Acta Met., *9*, 577, 1961.
4. G. Panseri and T. Federighi, JIM, *94*, 99, 1966.
5. M. H. Jacobs, Phil. Mag., *26*, 1, 1972.
6. D. W. Pashley, J. W. Rhodes and A. Sendorek, JIM, *94*, 41, 1966.
7. A. Kelly and R. B. Nicholson, Prog. Mat. Sci., *10*, 149, 1963.
8. I. Kovács, J. Lendvai and E. Nagy, Acta Met., *20*, 975, 1972.
9. J. P. Lynch, L. M. Brown and M. H. Jacobs, Acta Met., *30*, 1389, 1982.
10. H. Y. Hunsicker, Aluminium, ASM, *1*, 187, 1967.
11. E. W. Hart, Acta Met., *6*, 553, 1958.
12. R. C. Dorward, Met. Trans., *4A*, 507, 1973.

Acta Physica Hungarica 71 (1-2), pp. 9-13 (1992)

ROTATIONAL ENERGY TRANSFER WITHIN THE $A^1\Sigma_u^+$–STATE OF Na_2 INDUCED BY COLLISIONS WITH ($^2S_{1/2}$) Na

K. HUSSEIN

Lebanon University, Faculty of Science
Tripoli, Lebanon

and

O. BABAKY*

Sana'a University, Faculty of Science, Department of Physics
Sana'a, Yemen Republic

(Received in revised form 11 October 1990)

The ($v' = 34$, $J' = 14$) level in the $A^1\Sigma_u^+$ electronic state of Na_2 has been selectively populated by excitation with the 578.1 nm line of a ring dye-laser with rhodamine 6G. Through collisions with ($^2S_{1/2}$) Na atoms energy is transferred to neighbouring rotational levels in Na_2 and the density of these levels is determined by observing fluorescence to the electronic ground state. From previous measurements of the lifetime of the $A^1\Sigma_u^+$ state and new measurements of the intensities of collision induced spectral lines, absolute collision cross sections for all rotational transitions up to $\Delta J = \pm 6$ have been obtained; the total cross section for all rotational transitions observed is:

$$_{\text{rot}}\sigma^{\text{total}} = 0.41 \pm 0.11\,\text{nm}^2.$$

1. Introduction

In the last few years, there has been renewed interest in the spectroscopy of alkali dimer molecules. These systems offer attractive possibilities for the study of many fundamental phenomena such as dissociation, perturbations, and curve crossings [1–3]. Besides, collision processes of these molecules can be conveniently and precisely studied using spectroscopic techniques. In favourable cases laser induced fluorescence may be used to gain information about collisional processes.

Previously, we have reported the results of the analysis of the fluorescence excited by a dye-laser at 17297.387 cm^{-1} which populates $v' = 34$, $J' = 14$ in $A^1\Sigma_u^+$ of sodium molecules (see [1]). We now present results of the absolute cross section for rotational transitions to neighbouring rotational levels $v' = 34$, $J' = 14 \pm \Delta J$ with $\Delta J = \pm 2, \pm 4, \pm 6$).

*Author to whom correspondence should be addressed

2. Experimental

Fluorescence was excited by a ring dye-laser with rhodamine 6G (Spectra-Physics 380) delivering about 560 mW at 578.1 nm. Sodium vapour was contained in a heat-pipe at 760°K in the presence of argon at about 1.3×10^4 Pa. Spectra were recorded by high resolution Fourier transform spectroscopy and the dye-laser frequency was measured by a wave meter and found to be 17297.387 cm^{-1}. The vapour pressure could be controlled by the temperature of the side arm which was normally 527°C, corresponding to vapour pressure $P_{Na} = 0.8 \times 10^4$ Pa and $P_{Na_2} = 0.4 \times 10^3$ Pa [4].

The argon pressure was measured with a capacitance membrane manometer. The temperature was measured with thermocouples. The sodium density n and mean velocity $\overline{v}$ were calculated using the relation

$$P = nkT \text{ and } \overline{v} = \sqrt{\frac{8}{\pi} \cdot \frac{KT}{\mu}},$$

where μ is the reduced mass of the colliding system. The dye-laser radiation overlaps with the transition R(13) in the 34–6 band of $A^1\Sigma_u^+ - X^1\Sigma_g^+$ and the collisison induced fluorescence lines (satellite lines) from neighbouring rotational levels $(J' + \Delta J)$ are rather well resorved (Fig. 1). The identification of lines was made by calculating the satellite line wavelengths from the Na_2 molecular constants [1].

3. Method of cross-section determination and results

The method of obtaining cross-section for collision-induced rotational transitions from the fluorescence spectrum has been described in the literature [5]. The excited state $A^1\Sigma_u^+$ has a spontaneous lifetime $\tau \simeq 13$ ns [6] and some of the excited molecules may undergo inelastic collisions with atoms $(^2S_{1/2})$ Na, resulting in transitions to neighbouring rotational levels $(J' + \Delta J)$ in the $v' = 34$ level or to adjacent vibrational levels $v' + \Delta v$. Transitions to other electronics states (e.g. the $X^1\Sigma_g^+$ state of Na_2) are also posible, but with much smaller transition probabilities. The steady population $N(\Delta J)$ of a rotational level $J' + \Delta J$, in the excited $A^1\Sigma_u^+$ state, is determined by the following excitation and de-excitation processes:

a) Collisional excitation: this can result either directly from the laser excited level J (cross section ${}_{rot}\sigma(\Delta J)$) in a single collision or by a second collision from neighbouring collisional populated levels $\Delta J'({}_{rot}\sigma(\Delta J - \Delta J'))$ if these levels collide again with $(^2S_{1/2})$ Na atoms before they radiate spontaneously.

b) De-excitation: this may occur by spontaneous decay from level $(J' + \Delta J)$ to the electronic ground state with probability $1/\tau$, or by collisional energy transfer to all neighbouring rotational or vibrational levels or by electronic quenching with cross sections ${}_{rot}\sigma^{total}$, ${}_{vib}\sigma^{total}$ and ${}_{el}\sigma^{total}$, respectively.

In general, the probability for two successive collision induced transitions is small but detectable, and the possibility of more than two inelastic collisions of

an excited molecule can be neglected completely. With this assumption the rate equation for the population of level $(J' + \Delta J)$ can be written a follows:

$$\frac{dN(\Delta J)}{dt} = \left[N(\Theta)_{\text{rot}}\sigma(\Delta J) + \sum_{\Delta J'}^{II} N(\Delta J')_{\text{rot}}\sigma(\Delta J - \Delta J')\right] n_{\text{Na}} \cdot \overline{v} \qquad (1)$$
$$-N(\Delta J)\left(1/\tau + \left[{}_{\text{rot}}\sigma^{\text{total}} + {}_{\text{vib}}\,\sigma^{\text{total}} + {}_{\text{el}}\,\sigma^{\text{total}}\right] n_{\text{Na}} \cdot \overline{v}\right),$$

where $\overline{v}$ is the mean relative velocity of the collision partners. The term $\sum''_{\Delta J'} N(\Delta J')_{\text{rot}}\sigma(\Delta J - \Delta J')n_{\text{Na}} \cdot \overline{v}$ accounts for the increase of $N(\Delta J')$ by a second collisional transition from all neighbouring rotational levels $(\Delta J')$. The summation therefore, goes over all rotational levels excited level (for which $\Delta J = \Theta$) and the level ΔJ itself.

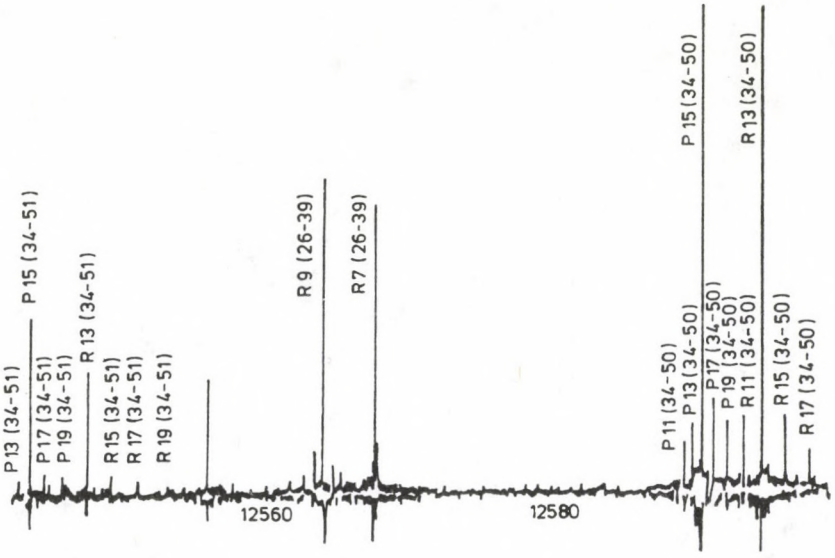

Fig. 1. The corresponding rotational satellite spectrum with 1.3×10^4 Pa. The assignments $P(\Delta J)$ and $R(\Delta J)$ indicate the fluorescence lines $(J' - J'' = \pm 1)$ from collisional population level $(J' + \Delta J)$

Eq. (1) holds for each collisional populated level. Under steady state conditions $\frac{dN(\Delta J)}{dt} = 0$ and Eq. (1) present a system of algebraic equations which are coupled by the Σ''-term with the abbreviation

$$\alpha = \left(\frac{-\sigma'' N(\Delta J')_{\text{rot}}\sigma(\Delta J - \Delta J')}{N(\Delta J)} + {}_{\text{rot}}\,\sigma^{\text{total}} + {}_{\text{vib}}\,\sigma^{\text{total}} + {}_{\text{el}}\,\sigma^{\text{total}}\right) n_{\text{Na}} \cdot \overline{v}\tau.$$

Table I
Experimental absolute cross-section for collision-induced rotational transitions

ΔJ	σ $_{rot}\sigma^{exp}(\Delta J)$ nm^2
6	0.05±0.01
4	0.08±0.02
2	0.11±0.03
-2	0.09±0.02
-4	0.05±0.02
-6	0.03±0.01

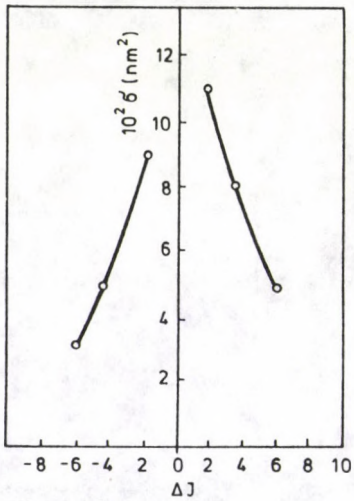

Fig. 2. Absolute cross-sections for all observed collision induced rotational transitions ΔJ in Na_2 with $(^2S_{1/2})$Na atoms

Eq. (1) can be rearranged for steady state conditions with $\frac{dN}{dt} = 0$

$$Q'(\Delta J) = \frac{N(\Delta J)}{N(0)}(1+\alpha) =_{rot} \sigma(\Delta J) n_{Na} \cdot \bar{v}\tau \qquad (2)$$

at low pressure

$$Q(\Delta J) = \frac{N(\Delta J)}{N(0)} =_{rot} \sigma(\Delta J) n_{Na} \bar{v}\tau.$$

The quantity $Q = \frac{N(\Delta J)}{N(0)}$ can be determined from the measured fluorescence intensities $I(\Delta J)$ and $I(0)$ corrected by the Hönl–London factors for the R (and p) satellites.

The resulting absolute cross section ${}_{\text{rot}}\sigma$ for collision-induced rotational transitions are presented in Fig. 2. Numerical values of absolute cross section are listed in Table I. The sum over all rotational transitions yields

$$ {}_{\text{rot}}\sigma^{\text{total}} = \sum_{\Delta J=-6}^{6} {}_{\text{rot}}\sigma(\Delta J) = 0.41 \pm 0.11 \text{ nm}^2. $$

The inelastic cross section ${}_{\text{rot}}\sigma(\Delta J)$ decreases rapidly with $|\Delta J|$ and $+\Delta J/-\Delta J$ asymmetry of cross sections can be observed.

4. Conclusion

The investigation has shown that the technique of laser-induced fluorescence is well suited for the study of inelastic collision processes between electronically excited molecules and other collision partners. In $Na_2^* - (^2S_{1/2})Na$ experimental cross section has been determined for individual collision-induced transitions between well defined initial and final states, with reasonable accuracy.

Acknowledgements

This work was supported by the Laboratoire de Spectrometrie Ionique et Moléculaire, Université de Lyon 1, France. We wish to thank professor J. D'Incan, Director of this Laboratory for his hospitality and his interest in this work. We are grateful to Dr. Madam Aubert-Frécon for many helpful discussions. Appreciation is extended to Dr. C. Effantin for her continued interest in this work.

References

1. R. F. Barrow, J. Verges, C. Effantin, K. Hussein and J. D'Incan, Chem. Phys. Lett., *104*, 3179, 1984.
2. K. Hussein and M. Aubert-Frécon, J. Mol. Spectr., *117*, 206, 1986.
3. C. Dufour et al., Chem. Phys., *98*, 315, 1985.
4. A. N. Nesmeyanov, Vapor Pressures of the Elements, London Infosearch Ltd., 1963.
5. K. Bergmann and W. Demtroder, Z. Physik, *243*, 1, 1971.
6. W. T. Zemke, K. K. Verma, T. Vu and W. C. Stwalley, J. Mol. Spectr., *85*, 150, 1981.

Acta Physica Hungarica 71 (1–2), pp. 15–23 (1992)

ENERGY LEVELS OF ^{237}Np

S. U. EL-KAMEESY

Physics Department, Faculty of Science
Ain-Shams University, Cairo, Egypt

(Received in revised form 28 December 1990)

The α decay of ^{241}Am to ^{237}Np has been studied using Si(Li) and H.P.Ge–NaI(Tl) spectrometers in the low energy range 5–45 keV. Twelve gamma transitions have been observed. Two of these transitions are found to be new and have energies 28.52 and 40.44 keV. Furthermore, it was possible to confirm the placement of the 27.1 keV transition in the level scheme of ^{237}Np. The levels from this and previous work are compared with those calculated by means of the unified model and the extracted parameters are given.

1. Introduction

The level structure of ^{237}Np has been studied previously by a variety of experimental techniques including the spectroscopic determination of γ rays and/or particles emitted during α decay, β decay and single nucleon transfer reactions [1–7]. Although the energy levels of ^{237}Np have received much attention, they continue to be a fruitful medium for testing theories of nuclear structure and the interrelated theories of nuclear decay processes.

The γ-ray intensities of ^{241}Am have been investigated in the low energy region (13–150 keV) using a high resolution Ge detector [8]. Energies and intensities of only two γ-lines were detected in the energy range 0–40 keV. The same result was obtained by Ovechkin and Khokhlov [9] in the same energy region. Moreover, in the accumulated results reported in NDS [10] four γ-transitions in the energy range 0–40 keV having energies 13.81, 27.03, 31.4 and 38.54 keV are still placed as doubted in the decay scheme of ^{241}Am.

It is hoped by such work to settle the previously reported discrepancies through the study of singles and coincidence spectra using better techniques and pure ^{241}Am source (ORTEC, USA). Another goal is to extend the comparison of the experimentally observed energy levels to those predicted by unified model calculations.

2. Experimental procedure

The low energy γ-transitions in ^{237}Np (5–45 keV) have been investigated using a 12 mm^2 Si(Li) detector of about 150 eV resolution at 5.9 keV. An IBM–XT

computer equipped with a nucleus 8192 MCA plug-in-card was used to analyse the obtained spectra.

The gamma–gamma coincidence measurements have been carried out using a 3″ × 3″ NaI(T1)–H.P.Ge fast-slow spectrometer. The time resolution of the fast coincidence pulse was about 20 ns, while that of slow coincidence was about 0.5 μs. In order to determine the energy per channel an energy and efficiency calibration has been carried out using available standard sources.

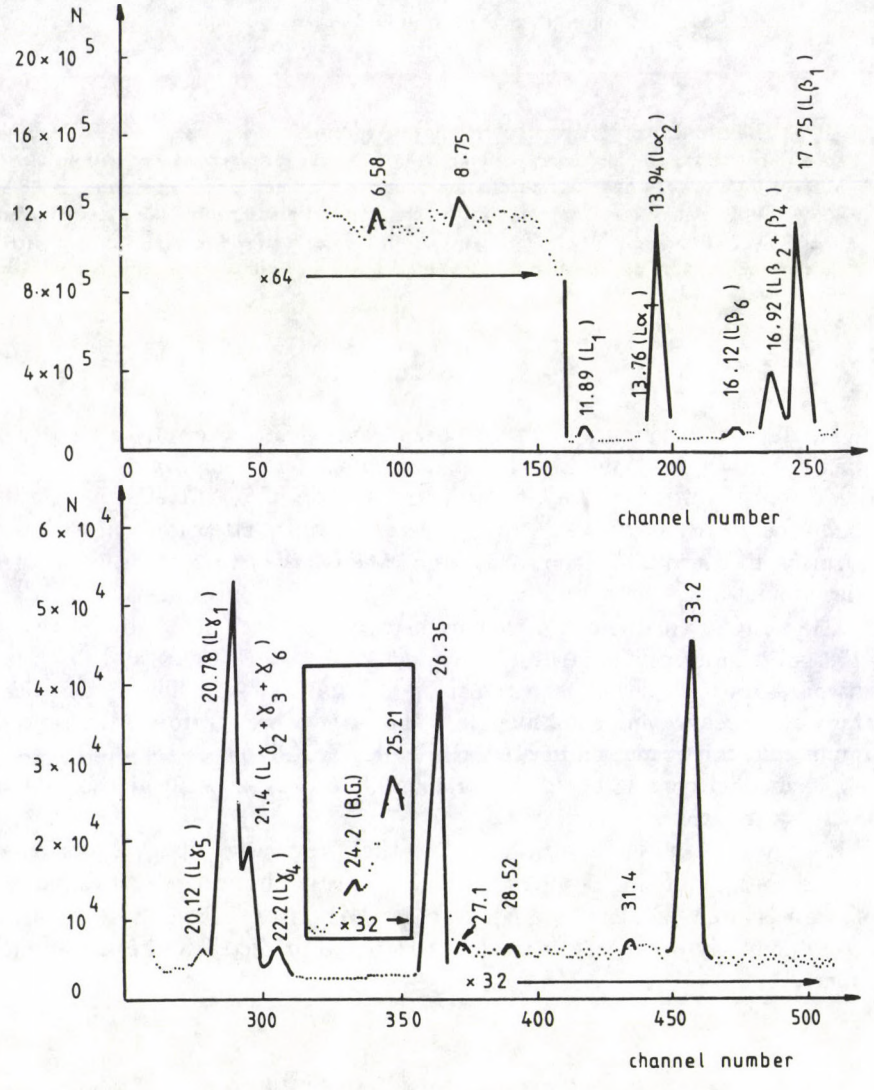

Fig. 1a

Figs 1a,b. Gamma singles of ^{241}Am using Si(Li) detector

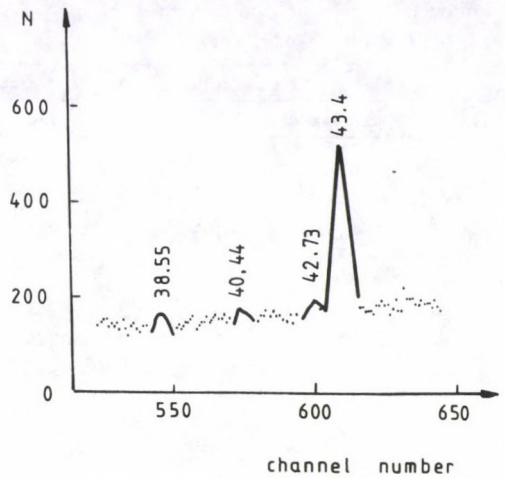

Fig. 1b

The background singles spectrum was undertaken and all the circumstances concerning the possible existence of escape and sumpeaks were taken in consideration.

3. Gamma rays singles and coincidence spectra

The gamma rays singles spectra in the low energy range 5–45 keV with good resolution is shown in Figs 1a,b. Twelve gamma transitions have been identified. Four of these transitions of energies 26.345, 33.195, 42.730 and 43.423 keV are well-established. The 27.1, 31.4 and 38.54 keV transitions are placed as doubted in the level scheme of ^{237}Np [10]. The remaining five transitions are observed for the first time in the present work. The 6.58, 8.75 and 25.21 keV transitions are considered to be probable because of their weak intensities but the 28.52 and 40.44 keV transitions are confirmed to be new by their presence in the coincidence spectrum as shown in Fig. 2.

The detected gamma transitions and their intensities compared with the previous work are given in Table I. The 13.81 keV proposed to depopulate the 281.36 keV level [10] was not observed in the γ-singles spectrum.

The X-ray lines attributed to ^{241}Am source are carefully selected as shown in Fig. 1a.

To confirm the placement of the 40.44 keV transition between the 800 and 840 keV levels, the 573.9 and 641.5 keV transitions depopulating the 800 keV level were selected as gating transitions. The obtained spectra confirm the presence of

Table I
Energy and intensity values for gamma transitions in ^{241}Am α-decay in the low energy range 5–45 keV

Present work				Ovechkin [9]			Genoux-Lubian [8]			
E_γ (keV)		I %		E_γ (keV)	I %		E_γ (keV)		I %	
6.58*	10	0.00046	12							
8.75*	20	0.00085	18							
25.21*	15	0.00888	25							
26.30	10	2.4	1	26.346	(2.27)		26.346	6	2.57	26
27.65	11	0.00117	15							
28.52	13	0.00332	26							
31.40	20	0.00066	19							
33.20	12	0.11	1	33.2	0.12	1	33.245	10	0.107	11
38.60	22	0.00745	30							
40.44	15	0.0032	8							
42.70	16	0.006	1				42.715	50	0.0056	11
43.44	20	0.07	1	43.42	0.066	5	43.413	10	0.0737	74

*Probable transitions observed in the present work.

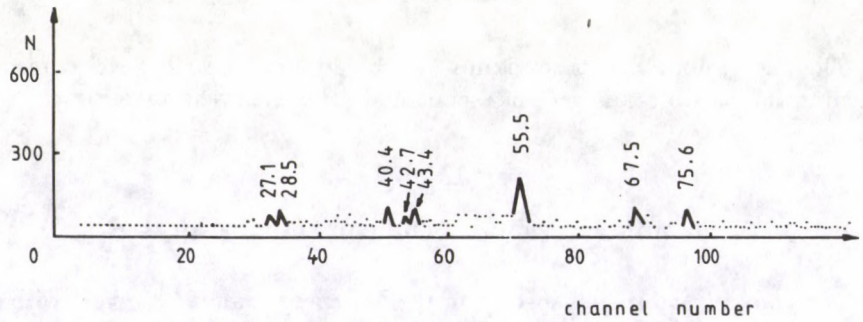

Fig. 2. Gamma–gamma coincidence spectrum using H.P.Ge-NaI(Tl) detectors

the 40.44 keV transition as shown in Fig. 2 (gate 550–650 keV). This result gives another support for the existence of the 840.0 keV level proposed previously for the first time by the authors [11].

The 28.52 keV transition was proposed to depopulate the 158.51 keV level. In this case the 597.5 and 641.5 keV transitions are suitable gating transitions included in the previous gate. However, the presence of the 28.52 keV transition in the coincidence spectrum shown in Fig. 2 supports our proposal for its placement.

To confirm the placement of the 27.1 keV doubted transition [10] between the 102.96 and 75.89 keV levels, the 619.01 keV transition, being the most intense line populating the 102.96 keV level was selected as a gating transition in the same

gate (550–650 keV). The obtained spectrum confirms the presence of the 27.1 keV transition as shown in Fig. 2.

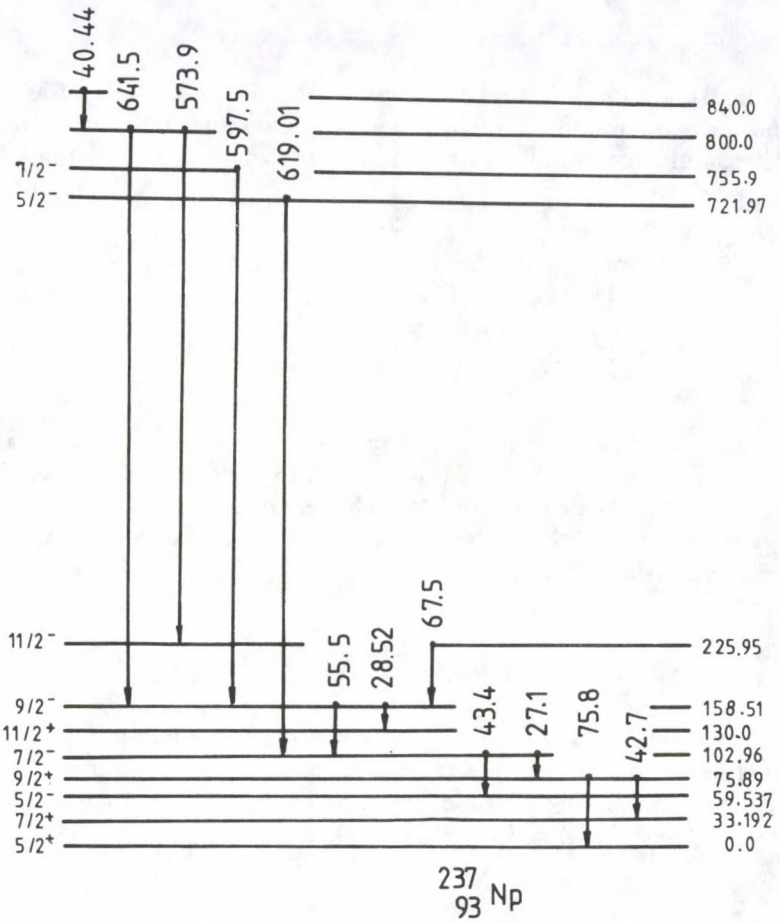

Fig. 3. Partial level scheme of ^{237}Np

The results of the present work have been used in constructing a partial level scheme of ^{237}Np (Fig.3).

4. Unified model calculations to ^{237}Np energy levels

Calculation of the energy spectrum was done making use of the well-known total Hamiltonian H for the system where

$$H = H_{\text{rot}} + H_p + V(r).$$

H_{rot} is the Hamiltonian for the rotor, H_p is the Hamiltonian for the odd-particle and $V(r)$ is the interaction potential between the particle and the rotor. The total Hamiltonian can be rewritten as

$$H = H_0 + H^0_{\text{rot}} + H_{\text{coupl}}.$$

The deviation from the rotational spectrum may be thought of as due to a coupling between the rotational mode of motion, and either vibrational or particle mode. This coupling contributes to a change in the energy given by the last terms in the energy relation

$$\begin{aligned} E_{I,k} = E_k &+ A_k I(I+1) + BI^2(I+1)^2 + \ldots \\ &+ (-1)^{I+1/2}(I+1/2)(A_1 + B_1 I(I+1) + \ldots) \quad k = 1/2 \\ &+ (-1)^{I+3/2}(I-1/2)(I+1/2)(I+3/2)(A_3 + B_3 I(I+1) + \ldots) \quad k = 3/2 \\ &+ \ldots\ldots . \end{aligned}$$

By means of this equation the energy spectra of seven bands are calculated and the set of parameters which yield the best fit to the data are adopted for every band. The energy bands are expanded to higher energies giving a correct prediction of the already adopted levels [10] and assigning the spin-parity character of some higher levels as shown in Fig. 4.

4.1 The ground state $5/2^+$ [642] band

In the previous study of ^{241}Am α decay and nuclear reactions [3] the members of this band have been established as rotational band members and given a $5/2^+[642]$ orbital. The regular spacing of these levels indicates a $k = 5/2$ band with fitting parameters $E_k = -39.77$, $A = 4.55$, $B = 0.0049$ and $A_5 = -0.0000258$.

4.2 The $5/2^-$ [523] band

The levels of this band were established previously [3] and were assigned to have $5/2^-$ [523] orbital. The comparison of theoretical and experimental energy levels for this band shows excellent agreement. The fitting parameters of our calculation to this band are $E_k = 4.994$, $A = 6.251$, $B = -0.00198$, $A_5 = 0.00001023$ and $B_5 = 0.000000221$.

4.3 The $1/2^-$ [530] band

The level spacing in this band can now be described by the parameters $E_k = 265.012$, $A = 6.603$, $B = 0.0350$ and $A_2 = 11.336$. All the levels assigned to this

band were observed in the (d,p) spectrum, only the one at 281.4 keV has not been observed. The decay pattern of this state is interesting in that competing modes involving E1, E2, M1 and M2 transitions are all observed. It is sufficient to say that the E1 and M1 transitions, in particular, are very slow and that accounts qualitatively for the failure to observe corresponding transitions from higher levels of the band.

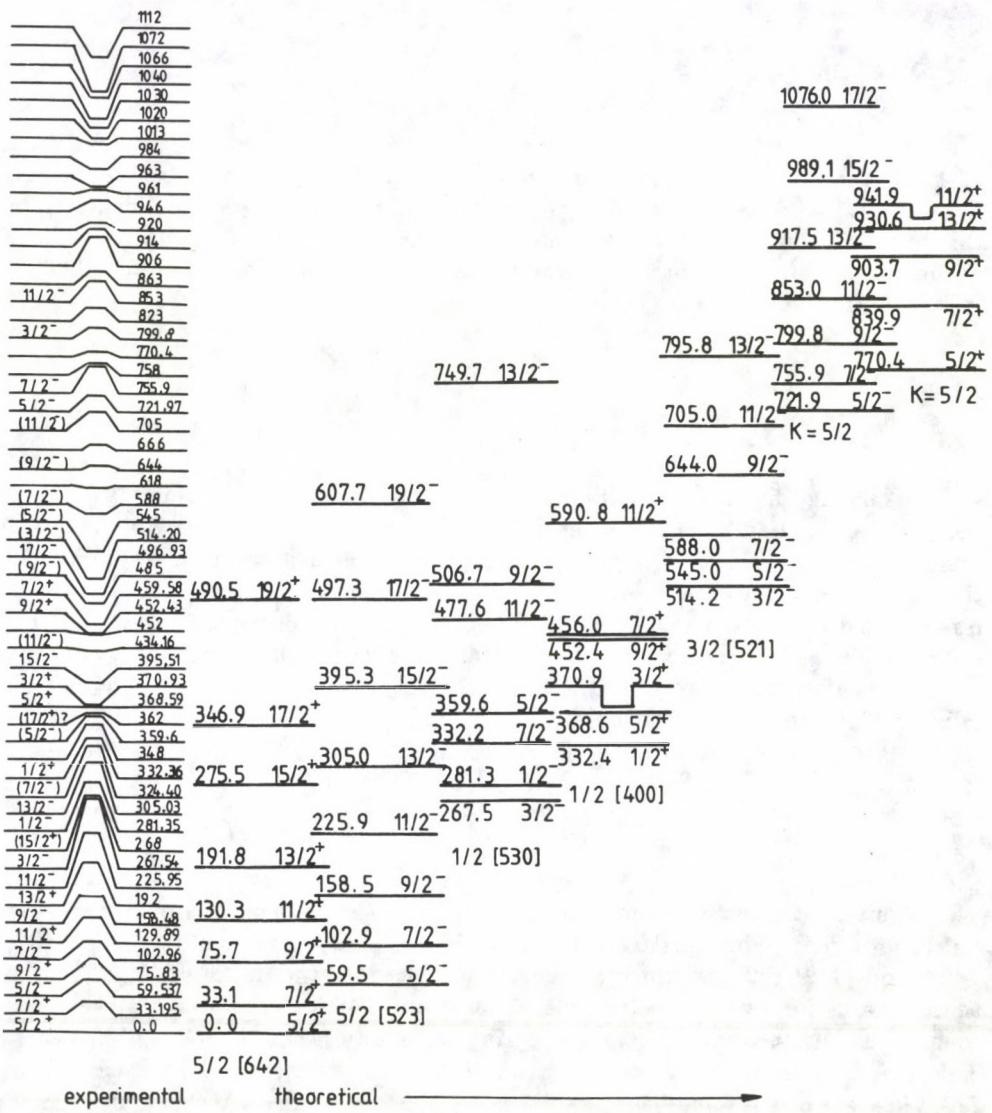

Fig. 4. Experimental energy levels of ^{237}Np compared with the unified model calculations

4.4 The $1/2^+$ [400] band

In previous studies [10] this band was proposed to consist of levels at 332.4, 368.6, 370.9, 452.4 and 459.6 keV with spin sequence $1/2 - 9/2$. From the energy spacing of this proposed levels the estimated parameters are $E_k = 334.328$, $A = 6.237$, $B = -0.00496$ and $A_2 = 6.6425$.

4.5 The $3/2^-$ [521] band

In the previous studies [10] this orbital has been assigned as $3/2^-$ [521]. Transitions that feed or depopulate the members of this band have been identified in this work. The observed level spacings indicate extreme agreement with our calculations where the fitting parameters are $E_k = 490.814$, $A = 6.237$, $B = -0.0038$, $A_3 = -0.0116$ and $B_3 = 0.0008496$.

4.6 The $k = 5/2$ band based on the 721.97 keV state

This band has a low hindrance factor for the α transition from ^{241}Am. The members of this band were also seen in the (d,d′) reaction where the B-vibrational band is not expected to be populated strongly, which led to an assumption that this band is not octupole vibrational band coupled with 5/2 [642] [3]. It is very difficult to describe this band through gamma ray transitions because its transitions are very weak. The level sequence of this band is very well reproduced by means of our calculations where the fitting parameters are $E_k = 679.586$, $A = 4.838$, $B = 0.000586$ and $A_5 = -0.0000443$.

4.7 The $k = 5/2$ band based on the 770.4 keV state

This orbital has not been identified in previous studies of ^{241}Am. Three weak transitions define this level at 770.4 keV [10]. These transitions feed the $5/2^+$, $7/2^+$ and $(7/2^-)$ states which are correctly placed in the decay scheme. In the same regard the levels at 840.0, 904.0, 930.0 and 946.0 keV which represent the main contribution of our previous experimental study [11] feed $5/2 - 11/2$ states. This led the authors to propose a band characterized by $k = 5/2$ based on the 770.4 keV state as a band head of spin-parity $5/2^+$. The levels at 840.0, 904, 830.0 and 946.0 keV are proposed the members of this band. Our calculations showed an excellent agreement with the experimental observed levels of this band both by us [11] and previous (d,d′) reaction [10]. The fitting parameters to this band are $E_k = 657.6172$, $A = 14.424$ and $B = -0.181$.

5. Conclusion

In this work an attempt has been made making use of good resolution detectors and pure ^{241}Am source to study the low energy spectra of ^{241}Am-α decay in the range 5–45 keV. Two new gamma transitions attributed to ^{237}Np are observed and placed in the decay scheme by means of γ-γ coincidence. The 27.1 keV doubted transition is confirmed and its placement in the decay scheme is assigned. In addition to that the energy spectra of seven bands are calculated by means of the unified model. The energy bands are expanded to higher energies giving a correct prediction for the already adopted levels and assigning the spin–parity character of some higher energy levels. This study indicates that the used model can give the correct ordering of the energy levels of ^{237}Np.

Acknowledgement

The author is grateful to Prof. Dr. H. Abou-Leila and Prof. Dr. L. Al-Houty for their useful help.

References

1. J. L. Wolfson and J. J. H. Pork, Canad. J. Phys., *42*, 1387, 1964.
2. W. Michaelis, Z. Phys., *186*, 42, 1965.
3. C. M. Lederer, J. K. Poggenburg, F. Asaro, J. O. Rasmussen and I. Perlman, Nucl. Phys., *84*, 481, 1966.
4. J. E. Cline, IN-1448 Rev., 1971.
5. A. Genoux-Lubian and G. Ardisson, C. R. Acad. Sc. Paris, *287B*, 13, 1978.
6. V. V. Ovechkin, Izv. Akad. Nauk. SSSR Ser. Fiz., *42*, 101, 1978.
7. J. Stanicek and P. Pouinec, Nucl. Inst. Meth., *B17*, 462, 1986.
8. A. Genoux-Lubian and G. Ardisson, Radiochem. Radioanal. Letts., *33*, 59, 1978.
9. V. V. Ovechkin and A. E. Khokhlov, Izv. Akad. Nauk. SSSR, Ser. Fiz., *48*, 1032, 1984.
10. Y. A. Ellis-Akovali, Nucl. Data, *49*, 181, 1986.
11. L. Al-Houty, S. U. El-Kameesy and H. Abou-Leila, Qatar Univ. Sci. Bull., *9*, 37, 1989.

Acta Physica Hungarica 71 (1–2), pp. 25–27 (1992)

DIRAC PARTICLE IN A SPATIALLY PERIODIC MAGNETIC FIELD

N. D. SEN GUPTA

Tata Institute of Fundamental Research
Colaba, Bombay, 400005 India

(Received 8 January 1991)

The exact general solution of the Dirac equation in the steady periodic magnetic field along a fixed direction is obtained.

1. Introduction

Recently, in this journal, there appeared a short paper on 'Dirac particle in a periodic field' by I. Lovas and Livia Molnár [1]. They have attempted to present some particular (exact) solution of the Dirac equation in a spatially periodic magnetic field. Unfortunately, some unjustifiable assumptions in the paper have impaired the validity of the solution.

They are:

i) The assumption about the nature of the solution, expressed by Eq. (10) of the reference, cannot be justified, as is manifested by the general solution obtained in the present paper.

ii) It is easy to check that there is no non-trivial spinor 'u', which simultaneously satisfies both Eqs (14) and (15) of the reference.

The object of the present short paper is to obtain the most general exact solution of the equation in a concise form. This is worked out in the following Section.

2. The equation and its solution

Let the spatial period magnetic field be along the x-axis, with space period $2\pi/k$, given by

$$H_x = H_0 \sin kz, \; H_y = 0 = H_z, \tag{1}$$

so that the corresponding vector potential a

$$a_y = \frac{H_0}{k} \cos kz, \; a_x = 0 = a_z. \tag{2}$$

The Dirac equation for the electron in this field is given by

$$\left[i\hbar\left\{\frac{1}{c}\frac{\partial}{\partial t}-\alpha_x\frac{\partial}{\partial x}-\alpha_y\left(\frac{\partial}{\partial y}+\frac{i\mu}{\hbar}\cos kz\right)-\alpha_z\frac{\partial}{\partial z}\right\}+\beta mc\right]\psi=0, \tag{3}$$

where

$$\mu=\frac{eH_0}{ck}. \tag{3'}$$

Since, only the z-coordinate appears in Eq. (2) explicitly one can write

$$\psi(\mathbf{r},t)=\psi(z)\cdot\exp-(i/\hbar)(Et-p_xx-p_yy) \tag{4}$$

and the equation for $\psi(z)$ is

$$\left[-i\hbar\alpha_z\frac{d}{dz}+\alpha_y(p_y+\mu\cos kz)+E+\alpha_xp_x+\beta mc\right]\psi(z)=0. \tag{5}$$

The matrices α_x and β may be eliminated from the above equation, by introducing the matrix Λ given by

$$\Lambda\sqrt{p_x^2+m^2c^2}=\alpha_xp_x+\beta mc,\ \Lambda^2=1. \tag{6}$$

Since Λ commutes with α_z and α_y, we can write Eq. (5), after multiplying it from left by $\exp-\Lambda\theta/2$,

$$\left\{-i\hbar\alpha_z\frac{\partial}{\partial z}+\alpha_y(\mu\cos kz+p_y)+Q\right\}\phi(z)-0, \tag{7}$$

where

$$\left.\begin{aligned}\phi(z)&=\exp\Lambda\theta/2\cdot\psi(z)\\ \tanh\theta&=\frac{E}{c\sqrt{p_x^2+m^2c^2}}\end{aligned}\right\} \tag{8}$$

and

$$Q^2=\frac{E^2}{c^2}-p_x^2-m^2c^2. \tag{9}$$

Eq. (7) contains only periodic coefficients hence, by Floquet's theorem, its solutions are of the form

$$\phi(z)=\sum A_n\exp i(p_z+nk\hbar)/\hbar, \tag{10}$$

where A_n (spinor) and p_z are constants. Substituting this expression in Eq. (7), the recurrence relation between A_n's are obtained as

$$\{\alpha_z(p_z+nk\hbar)+\alpha_yp_y+Q\}A_n+\alpha\frac{\mu}{2}(A_{n+1}+A_{n-1})=0. \tag{11}$$

The solution of this difference equation may be written as

$$A_n = J_n\left(\frac{i\mu}{k\hbar}\right)(au_+ + (-1)^n bu_-). \tag{12}$$

J_n's are the Bessel coefficients, so that

$$2nJ_n(u) = u\{J_{n+1}(u) + J_{n-1}(u)\} \tag{13}$$

and $u_\pm$ are eigen-spinors of $i\alpha_z\alpha_y$, such that

$$i\alpha_z\alpha_y u_\pm = \pm u_\pm \text{ and } \alpha_z u_\pm = u_\mp. \tag{14}$$

Each of $u_\pm$ consists of two linearly independent spinors. In order that the expression (12) for A_n is the solution of the difference Eq. (11), a and b must satisfy the equations

$$\begin{aligned}(p_z - ip_y)a \pm Qb &= 0,\\ Qa \pm (p_z + ip_y)b &= 0,\end{aligned} \tag{15}$$

$+$ or -1 according as n is even or odd. They lead to the relation (for compatibility),

$$Q^2 = p_z^2 + p_y^2. \tag{16}$$

Thus from Eq. (9)

$$\frac{E^2}{c^2} = p_x^2 + p_y^2 + p_z^2 + m^2c^2. \tag{16'}$$

So that A_n is given by

$$A_n(p_z, p_y, Q) = WJ_n\left(\frac{i\mu}{k\hbar}\right)\{Q + (-1)^n(ip_y - p_x)\alpha_z\}u_+, \tag{17}$$

W is an arbitrary constant. The most general solution is given by

$$\phi(z) = \int W(\mathbf{p})\sum A_n(\mathbf{p}, E)\exp\left\{-\frac{i}{\hbar}(Et - p\cdot r) + inkz\right\}d^3\mathbf{p}, \tag{18}$$

subject to the condition $p\cdot p + m^2c^2 = E^2/c^2$.

It is of interest to note that the non-localized part of the solution is like that of a free particle.

Reference

1. I. Lovas and Livia Molnár, Acta Phys. Hung., *65*, 331, 1989.

Acta Physica Hungarica 71 (1–2), pp. 29–33 (1992)

INFRARED BEHAVIOUR OF GREEN'S FUNCTION FOR FERMIONS IN SUPERSYMMETRIC YANG–MILLS THEORIES

HOANG NGOC LONG

Institute of Theoretical Physics, Academy of Sciences of Vietnam
Bo Ho, Hanoi 10000, Vietnam

(Received 14 January 1991)

Infrared behaviour of the Greens's function for fermions in supersymmetric Yang–Mills thebries is investigated. We show that only massless gauge vector fields give contributions to this behaviour.

The introduction of supersymmetry into quantum field theories has led to theories with improved quantum properties [1]. One of the most attractive features of supersymmetric theories is the reduction of the number of parameters containing ultraviolet divergences. It is known that in the simplest supersymmetric Wess–Zumino model only the wave function renormalization is sufficient to renormalize the theory [1–3]. The Yang–Mills gauge theory with the maximal supersymmetric extension ($N = 4$) [4,5] has been found to possess unique properties at the quantum level [6]. There are very strong indications that this theory is a finite quantum field theory. Originally this theory was found in two different ways, one of which was through the construction of supersymmetric Yang–Mills theories in space-times of higher dimension [4]. It was found that the 10-dimensional space is the largest space that carries a supersymmetric Yang–Mills theory and by dimensional reduction this can be taken into 4 dimensions where it emerges as an $N = 4$ extended theory. On the other hand, this theory was already known from the Neveu–Schwarz–Ramond dual model [7], a model which exists only in 10 dimensions. By letting the Regge slope α' to tend to zero, in the open-string sector of the model one gets the Born terms of a Yang–Mills field coupled to a spinor field, which in fact turn out to be the Born terms of the 10-dimensional supersymmetric Yang–Mills theory [1,5].

As it is well known, the vertex and the renormalized Green functions have a singularity at $p^2 = m^2$. In this paper we study the infrared behaviour of the Green's function for fermions in the theory describing the interaction of a $N = 1$ vector supermultiplet V with some chiral $N = 1$ supermultiplet S_i. The action can

be written [8] as

$$
\begin{aligned}
S =& \frac{1}{8g^2c}\mathrm{Tr}[\int dxd^2\theta W^\alpha W_\alpha] + \frac{2}{c}\mathrm{Tr}[\int dxd^2\theta d^2\overline{\theta}\exp(-2gV)S_i\exp(2gV)S_i] + \\
& \frac{4i\gamma}{3!c}\varepsilon_{ijk}\mathrm{Tr}\{\int dxd^2\theta S_i[S_j,S_k] + \int dxd^2\overline{\theta}\overline{S}_i[\overline{S}_j,\overline{S}_k]\} - \\
& \frac{1}{8\alpha c}\mathrm{Tr}[\int dxd^2\theta d^2\overline{\theta}(D^2V)(\overline{D}^2V)] + \\
& \frac{2}{c}\mathrm{Tr}\{\int dxd^2\theta d^2\overline{\theta}(\overline{a}'-\overline{a})L_{gV}[(a+\overline{a}) + C\mathrm{th}L_{gV}(a-\overline{a})]\} - \\
& \sum_{i=1}^{n}\frac{m_i}{c}\mathrm{Tr}[\int dxd^2\theta S_iS_i + \int dxd^2\overline{\theta}\overline{S}_i\overline{S}_i],
\end{aligned}
\tag{1}
$$

where $W^\alpha = (-\frac{\overline{D}^2}{4})(\exp(-2gV)D^\alpha\exp(2gV))$, a and a' are chiral ghost fields, α is the gauge parameter, $i,j,k = 1,2,\ldots,n$ and the Lie derivative is $L_xY = [X,Y]$. All fields are in the adjoint representation of the gauge group.

When $m_i = 0$, $\gamma = 0$ and $n = 1$ we have the $N = 2$ Yang–Mills theory in terms of $N = 1$ superfields. For $m_i = 0$, $\gamma = g$, $n = 3$ we get the $N = 4$ Yang–Mills theory in therms of $N = 1$ superfields [9]. When $m_i \neq 0$, we obtain a soft breaking of $N = 2,4$ supersymmetry.

Using the Wess–Zumino gauge [10] we have the following on-shell action in terms of ordinary fields

$$S = \int dxL,$$

$$
\begin{aligned}
L =& \frac{1}{c}\mathrm{Tr}\{-\frac{1}{4}F^{\mu\nu}F_{\mu\nu} + \frac{1}{2}D_\mu A_i)^2 + \frac{1}{2}(D_\mu B_i)^2 - \\
& \frac{i}{2}\overline{\Phi}_m\hat{D}\Phi_m + \frac{ig}{2}\overline{\Phi}_m[\alpha^i_{mn}A_i + \gamma^5\beta^i_{mn}B_i,\Phi_n] + \\
& \frac{g^2}{4}([A_i,A_j]^2 + [B_i,B_j]^2 + 2[A_i,B_j]) + \\
& \sum_{i=1}^{n}\frac{im_i\gamma\varepsilon_{ijk}}{2}(A_i[A_j,A_k] - A_i[B_j,B_k] + 2B_i[A_j,B_k])\} - \\
& \frac{1}{2c}\mathrm{Tr}\sum_{i=1}^{n}(m_i^2A_i^2 + m_i^2B_i^2 - m_i\overline{\Psi}_i\Psi_i),
\end{aligned}
\tag{2}
$$

where $\Phi = \begin{pmatrix}\psi_1\\ \vdots \\ \psi_n \\ \lambda\end{pmatrix}$, the α and β matrices obey the following relations:

$$[\alpha^i,\beta^j] = 0,\ \{\alpha^i,\alpha^j\} = \{\beta^i,\beta^i\} = -2\delta^{ij},$$

$$\mathrm{tr}(\alpha^r, \alpha^t) = \mathrm{tr}(\beta^r \beta^t) = -4\delta^{rt}.$$

Now, we study the singularity of the renormalized fermion mass operator at the one-loop level. For this purpose we have to calculate the one-loop diagrams of the self-energy operator for fermions. These diagrams are drawn in Fig. 1(a–c), where continuous, wave, dotted and dashed–dotted lines denote fermions, gauge vector, scalar and pseudoscalar particles, respectively.

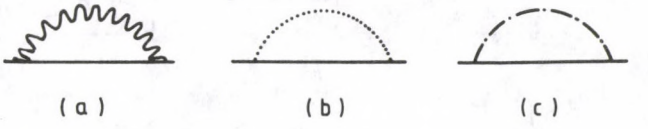

Fig. 1. One-loop diagrams contributing to the fermion self-energy operator in supersymmetric Yang–Mills model

To evaluate Feynman integrals corresponding to these diagrams, the algebraic manipulation program SCHOONSCHIP [11] was used.

Our one-loop expression for the self-energy Σ' reads:[1]

$$\begin{aligned}\Sigma'^{(2)}(p) = \frac{\alpha N}{4\pi}\{\hat{p}[-\frac{1}{\epsilon} - \gamma + 3 - \ln(-\pi m^2) + (2(1 - \frac{m^2}{p^2}) - \\ (1 - \frac{m^2}{p^2})^2)\ln(1 - \frac{p^2}{m^2}) - \frac{m^2}{p^2}] + m[\frac{4}{\epsilon} + 4(\gamma - \ln(-\pi m^2) + \frac{1}{2}) - \\ - 4(1 - \frac{m^2}{p^2})\ln(1 - \frac{p^2}{m^2})]\} - \frac{\hat{p}\alpha}{4\pi}\left[\frac{3}{\epsilon} + 3(\gamma - \ln(-\pi m^2)) + 7 - \right. \\ \left. 3\sqrt{1 - \frac{4m^2}{p^2}}\ln\frac{\sqrt{1 - \frac{4m^2}{p^2}} + 1}{\sqrt{1 - \frac{4m^2}{p^2}} - 1}\right],\end{aligned} \tag{3}$$

where $\alpha = \frac{g^2}{4\pi}$, $2\epsilon = (4 - D)$ and γ is the Euler constant. Here we remark that the first term in Eq. (3) proportional to N is the contribution from diagram a) and the last term comes from diagrams b) and c).

As in the quantum electrodynamics in order to get an expression independent of a regularization method the following polynomial is added to $\Sigma'^{(2)}(p)$, i.e., we define

$$\Sigma^{(2)}(p) = \Sigma'^{(2)}(p) + c_1(\hat{p} - m) + c_2 m.$$

The coefficients c_1 and c_2 are determined from the following conditions

$$\Sigma^{(2)}(m) = 0,$$

$$\frac{\partial}{\partial \hat{p}}\Sigma^{(2)}(p)_{|\hat{p}=m} = 0.$$

[1] In this paper the dimensional regularization [12] is used.

This yields

$$\Sigma^{(2)}(p) = \frac{\alpha}{4\pi}\hat{p}\left\{N\left[\frac{3}{2} - \frac{m^2}{p^2} - m^2 I_R + \frac{T}{2} + \right.\right.$$
$$2(1-\frac{m^2}{p^2})\ln(1-\frac{p^2}{m^2}) - (1-\frac{m^2}{p^2})^2\ln(1-\frac{p^2}{m^2})\Big] + 1 +$$
$$3\sqrt{1-\frac{4m^2}{p^2}}\ln\frac{\sqrt{1-\frac{4m^2}{p^2}}+1}{\sqrt{1-\frac{4m^2}{p^2}}-1} - i\sqrt{3}\ln\frac{(i\sqrt{3}+1)}{(i\sqrt{3}-1)}\Big\} + \qquad (4)$$
$$\frac{m\alpha}{4\pi}\left\{N\left[\frac{1}{2} - m^2 I_R + \frac{T}{2} - 4(1-\frac{m^2}{p^2})\ln(1-\frac{p^2}{m^2})\right] - \right.$$
$$\left. 3 - 2i\sqrt{3}\ln\frac{(i\sqrt{3}+1)}{(i\sqrt{3}-1)}\right\},$$

where $I_R \equiv \int \frac{d^4D_k}{k^2[(k+p)^2-m^2]^2}$ and $T \equiv (p^2-m^2)I_R$.

When $\hat{p} \to m$, I_R and $\ln(1-\frac{p^2}{m^2})$ are divergent and it is a manifestation of the infrared divergences.

Substituting (4) into the Green's function

$$G(p) = \frac{1}{\hat{p}-m}(1+\Sigma^{(2)}(p)\frac{1}{m-\hat{p}}) \equiv \frac{\hat{p}a + mb}{p^2-m^2},$$

we get

$$a = 1 - \frac{\alpha}{4\pi}\left\{-N\frac{(p^2-m^2)^2}{p^2m^2}A_1(p^2) - 8NA_1(p^2) + Nm^2I_R + \right.$$
$$\frac{N}{2} + N\frac{m^2}{p^2} - N\frac{T}{2} + 3\frac{p^2+m^2}{p^2-m^2}\sqrt{1-\frac{4m^2}{p^2}}\ln\frac{\sqrt{1-\frac{4m^2}{p^2}}+1}{\sqrt{1-\frac{4m^2}{p^2}}-1} - \qquad (5)$$
$$\left. i\sqrt{3}\frac{6m^2}{p^2-m^2}\ln\frac{(i\sqrt{3}+1)}{(i\sqrt{3}-1)} - i\sqrt{3}\ln\frac{(i\sqrt{3}+1)}{(i\sqrt{3}-1)}\right\},$$

$$b = 1 + \frac{\alpha}{4\pi}\left\{-2N(1-\frac{p^2}{m^2})A_1(p^2) + Nm^2I_R - 4A_1(p^2) + \frac{N}{2}(3-T) - \right.$$
$$3i\sqrt{3}\frac{p^2+m^2}{p^2-m^2}\ln\frac{(i\sqrt{3}+1)}{(i\sqrt{3}-1)} - 6\frac{m^2}{p^2-m^2}\sqrt{1-\frac{4m^2}{p^2}}\ln\frac{\sqrt{1-\frac{4m^2}{p^2}}+1}{\sqrt{1-\frac{4m^2}{p^2}}-1} - \qquad (6)$$
$$\left. i\sqrt{3}\ln\frac{(i\sqrt{3}+1)}{(i\sqrt{3}-1)} - 3\right\},$$

where

$$A_1(p^2) = \frac{m^2}{p^2} \ln(1 - \frac{p^2}{m^2}).$$

Using the renormalization group equation for $s = a, b$ (see, for example [13]), we find the behaviour of the full Green's function for fermions in the region $p \sim m^2$

$$G(p) \sim \frac{1}{(p^2 - m^2)^{1+\beta}}, \tag{7}$$

where

$$\beta = N\frac{\alpha}{\pi}. \tag{8}$$

Note, that in the QED, $\beta = \frac{\alpha}{\pi}$ with α is the fine structure constant.

From (8) we can conclude that only the gauge vector fields give contributions to the infrared behaviour of the Green's function for fermions.

Acknowledgements

The author would like to thank Dr. O. V. Tarasov for useful discussions, Prof. H. D. V. Shirkov for encouragement, Professor Abdus Salam, the International Atomic Energy Agency and UNESCO for hospitality at the International Centre for Theoretical Physics, Trieste, Italy.

References

1. See, for example S. Ferrara, Supersymmetry, 2 volumes, North-Holland and World Scientific, 1987, and references therein.
2. J. Iliopoulos and B. Zumino, Nucl. Phys., *B76*, 310, 1974.
3. H. H. Bang and H. N. Long, Czech. J. Phys., *40*, 605, 1990.
4. L. Brink, J. Schwarz and J. Scherk, Nucl. Phys., *B121*, 77, 1977.
5. F. Gliozzi, J. Scherk and D. Olive, Nucl. Phys., *B122*, 256, 1977.
6. L. V. Avdeev, O. V. Tarasov and A. A. Vladimirov, Phys. Lett., *96B*, 94, 1980.
   M. Grisaru, M. Rocek and W. Siegel, Phys. Rev. Lett., *45*, 1063, 1980.
   W. Caswell and D. Zanon, Phys. Lett., *B100*, 152, 1980.
7. P. Ramond, Phys. Rev. *D3*, 2415, 1971;
   A. Neveu and J. Schwarz, Nucl. Phys., *B131*, 86, 1971.
8. B. T. Sazdovic and O. V. Tarasov, JINR preprint E2–83–213 and JETP Lett., *37*, 602, 1983.
9. P. Fayet, Nucl. Phys., *B149*, 137, 1979.
10. J. Wess and B. Zumino, Nucl. Phys., *B201*, 292, 1982.
11. M. Weltman, SCHOONSCHIP, a CDC program for symbolic evaluation of algebraic expressions, CERN Report 1967 (unpublished);
    H. Strubbe, Comp. Phys. Comm., *8*, 1, 1974.
12. G. t'Hooft and M. Veltman, Nucl. Phys., *B44*, 189, 1972.
13. N. N. Boguliubov and D. V. Shirkov, Introduction to the Theory of Quantized Fields, 4th ed., Interscience, NY., 1987, Chap. 50.3.

Acta Physica Hungarica 71 (1-2), pp. 35-44 (1992)

THE EFFECT OF MAGNETIC FIELD ON THE SCINTILLATION EFFICIENCY OF ORGANIC SCINTILLATORS

FAIZAN-UL-HAQ, M. Z. BUTT, GHOUS ALI, S. Q. M. ZAIDI and R. SIDDIQUE

Nuclear Research Laboratory, Government College Lahore-54000, Pakistan

(Received in revised form 15 January 1991)

The fluorescence of different organic plastic and liquid scintillators has been measured as a function of magnetic field H up to 13 mT (milli tesla). In the case of NE213, NE230 and stilbene, the percentage change in scintillation efficiency $\Delta E(\%)$ increases with increasing H till it becomes maximum at an optimum value H_m, and then it decreases with further increase in H. However, in the case of pamolene crystal $\Delta E(\%)$ increases monotonically with H throughout the magnetic field range referred to.

Introduction

The main criteria for the selection of scintillators is their high relative light output and enhanced scintillation efficiency. Many methods of increasing the light output, e.g. (a) addition of wavelength shifter, (b) removal of dissolved oxygen and (c) reduction in temperature have been tried. But when the above three conditions are fulfilled, the fluorescence efficiency of the scintillator can be further increased by applying some optimum magnetic field.

Only few authors have worked on the influence of magnetic field [e.g. 1–4] and of temperature (e.g. [5]) on the scintillation efficiency of liquid and plastic scintillators. Jeenicke et al [1] studied the efficiency of NE235 organic mineral oil based scintillator as a function of magnetic field up to 10 mT and found that increase in efficiency reached 1.5 % at 4 mT and saturated at 10 mT to a value 1.8 %. Bodenstedt et al [2] found that fluorescent efficiency in their plastic scintillator is dependent upon magnetic field up to 10 mT. As work in this field is very scarce, it was considered appropriate to extend the investigation to other liquid and plastic scintillators by applying higher magnetic fields.

Experimental procedure

To produce a variable magnetic field, a parallel combination of two solenoids was fabricated in the laboratory. It was fitted inside a light-proof, wooden box of

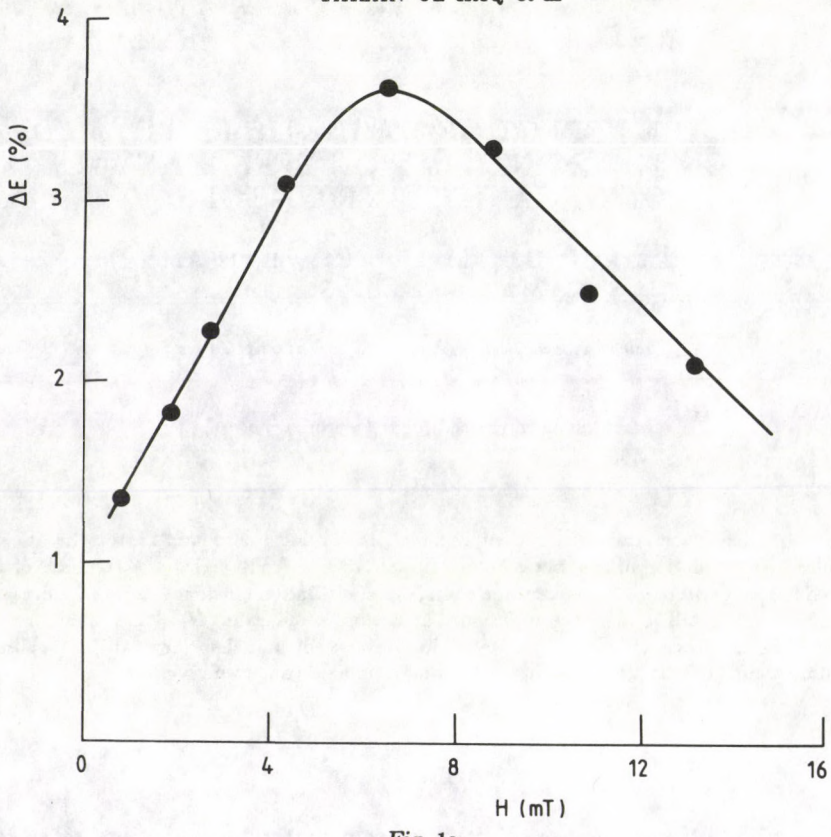

Fig. 1a

Figs 1a,b. Relation between change in scintillation efficiency $\Delta E(\%)$ and applied magnetic field H in the case of stilbene crystal. Data points denoted by open circles in (b) were obtained by reversing the direction of the field with respect to that used for the data points depicted by full circles in (a)

rectangular shape, covered with a wooden lid. The organic scintillator under observation was placed in such a way that it was completely surrounded by the solenoids. Liquid scintillator (NE213 or NE230) was contained in a sealed pyrex glass bottle, which was all covered, except its base, with aluminium foil. Similarly the cylindrical specimens of plastic scintillators (5 cm height × 5 cm diameter stilbene crystal or 4 cm height × 4 cm diameter pamolene crystal) were also covered, leaving one face open with aluminium foil. This was done to ensure that the fluorescent light emanating from the scintillator and falling on an EMI 6255 photomultiplier tube, fixed in the base of the wooden box, was maximum due to reflection from the aluminium shield. A long light guide pipe was interposed between the photocathode of the photomultiplier and the base of the scintillator to eliminate any direct effect of the magnetic field on the photomultiplier. Ra^{226} gamma source was placed on the centre of the lid of the box. The geometry was made constant by fixing the position

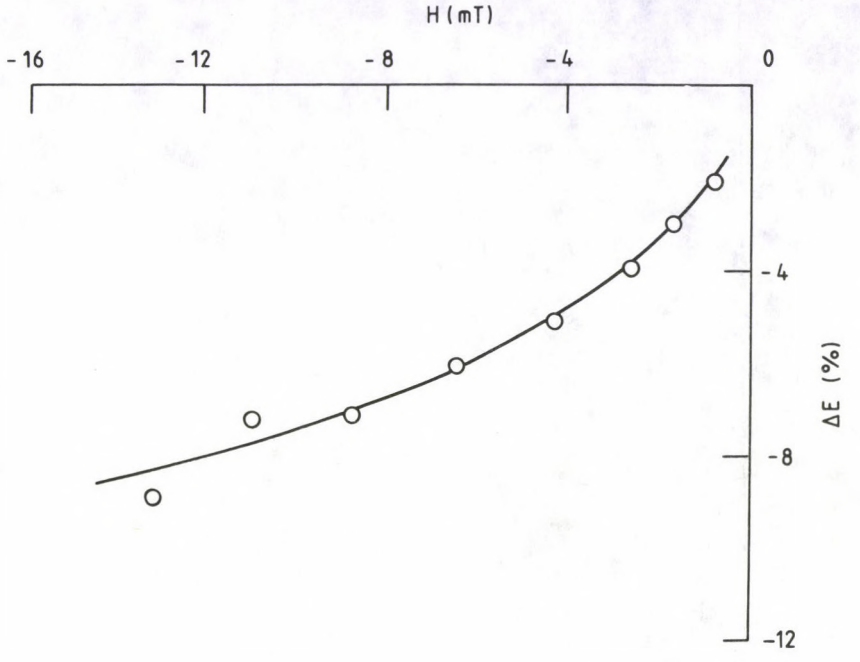

Fig. 1b

Table I
Change in efficiency for organic scintillators

Organic scintillator	Maximum change in efficiency ΔE_m(%)	Magnetic field for maximum change in efficiency H_m (mT)	Magnetic field for no change in efficiency H_0 (mT)
Pamolene crystal	13	at 13 mT in one direction	
	7	at 13 mT in reverse direction	
Stilbene crystal	3.6	6.5	–
NE213	8.3	4.5 (in one direction)	11.9
	3.4	4.5 (in reverse direction)	6.5
NE230	2.6	1.7	3.2

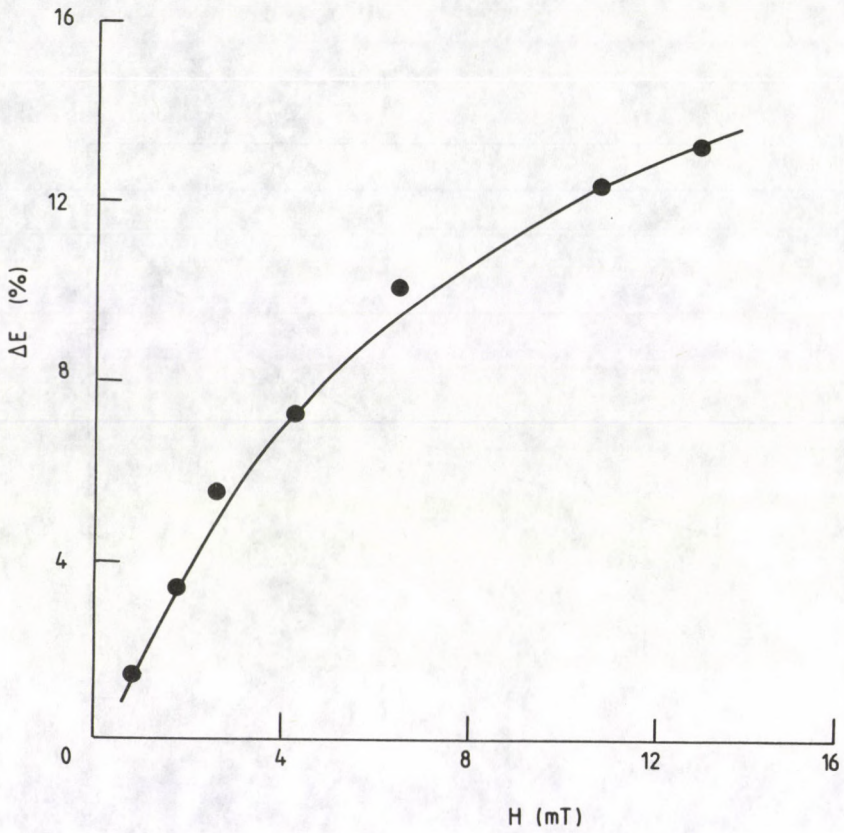

Fig. 2a. Same as Fig. 1 but for pamolene crystal

of the photomultiplier scintillator under observation and the gamma source.

The solenoid was connected to a DC current source for the production of the magnetic field, and the photomultiplier (EMI 6255) was connected to a preamplifier followed by a linear amplifier, a discriminator of single channel analyser and a digital scalar (all ORTEC origin). Regulated power supply was used to provide stable voltage to the photomultiplier base.

Since the dissolved oxygen in the scintillator NE213 or NE230 has a marked effect in quenching the light output of the scintillator, it was eliminated by passing argon gas for some time in the solution. Direct and reserved current was used for producing magnetic field in both directions in the case of plastic scintillators, i.e. stilbene and pamolene, as well as liquid scintillators, i.e. NE213 and NE230.

Counts/min were taken without magnetic field and then with magnetic field. The relationship between magnetic field H and percentage change in scintillation counting efficiency $\Delta E(\%)$ was determined as $\Delta E(\%) = \frac{N_2 - N_1}{N_1} \times 100$, where $N_1 =$ counts/min without magnetic field under gamma excitation, and $N_2 =$ counts/min

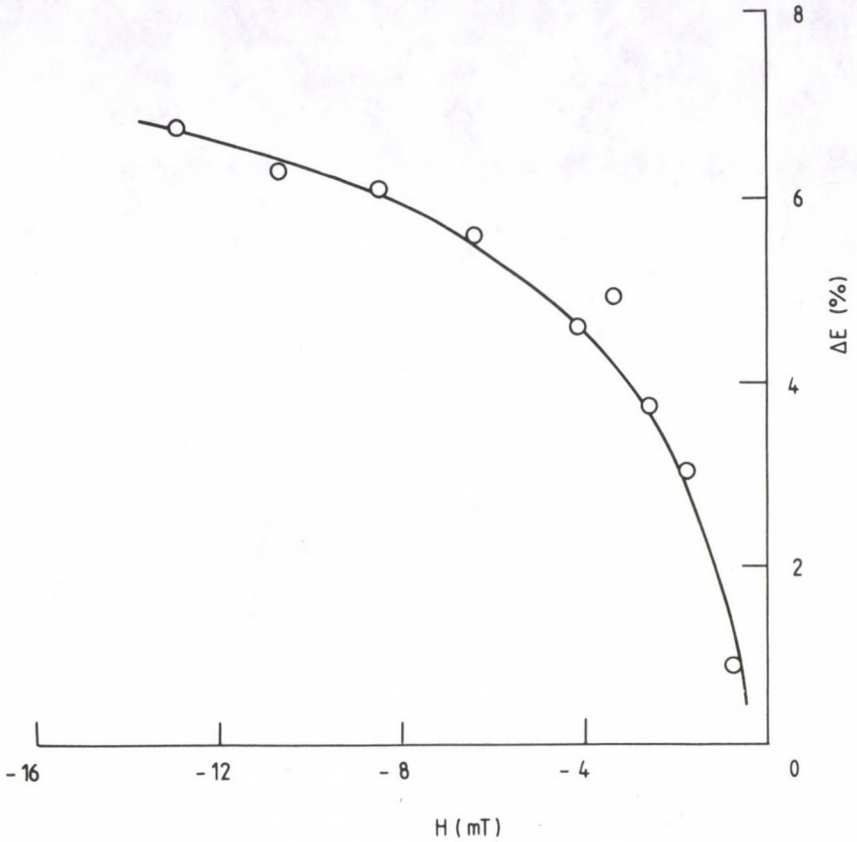

Fig. 2b. For caption see Fig. 2a

with magnetic field under gamma excitation. Because of low atomic number $Z(H)$ in organic scintillators, only Compton electrons would be produced due to impact of gamma rays from Ra^{226} source. Counts with and without magnetic field were taken by taking the mean of five independent readings at each magnetic field. The data concerning change in scintillation efficiency of different scintillators due to applied magnetic field have been denoted by points in Figs 1 to 4.

Results and discussion

It is evident from Figs 1(a), 3(a) and 4(a) that in the case of stilbene, NE213 and NE230, the change in scintillation efficiency, $\Delta E(\%)$, increases with increase in magnetic field, attains a maximum value ΔE_m at an optimum magnetic field H_m and then it decreases with further increase in magnetic field. Beyond a certain critical magnetic field H_0, the value of $\Delta E(\%)$ for NE213 and NE230 becomes negative (Table I). By reversing the direction of the applied magnetic field H, the

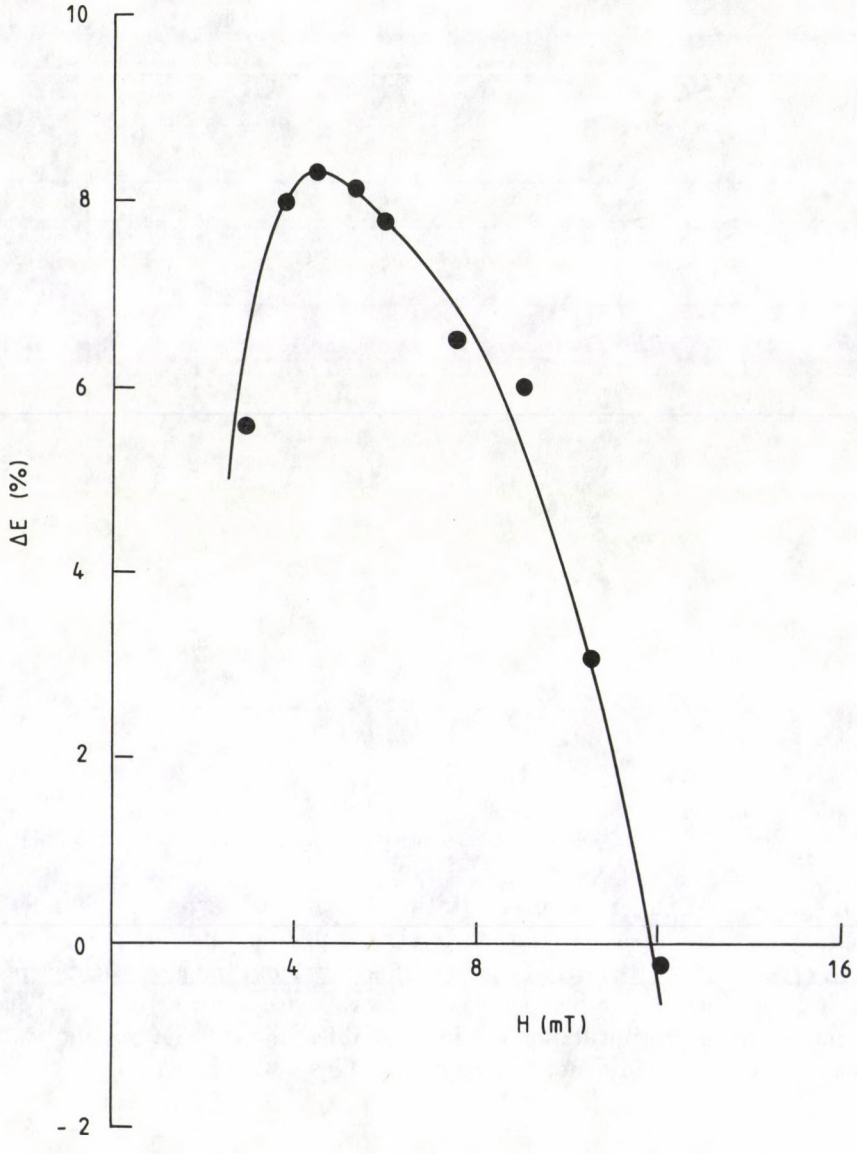

Fig. 3a. Same as Fig. 1 but for NE 213 liquid scintillator

change in scintillation efficiency, $\Delta E(\%)$, in stilbene crystal becomes negative and varies with H first rapidly and then slowly (Fig. 1b). However, in the case of NE213 and NE230, $\Delta E(\%)$ is positive at low values of H and then becomes negative at rather higher magnetic fields (Figs 3b and 4b).

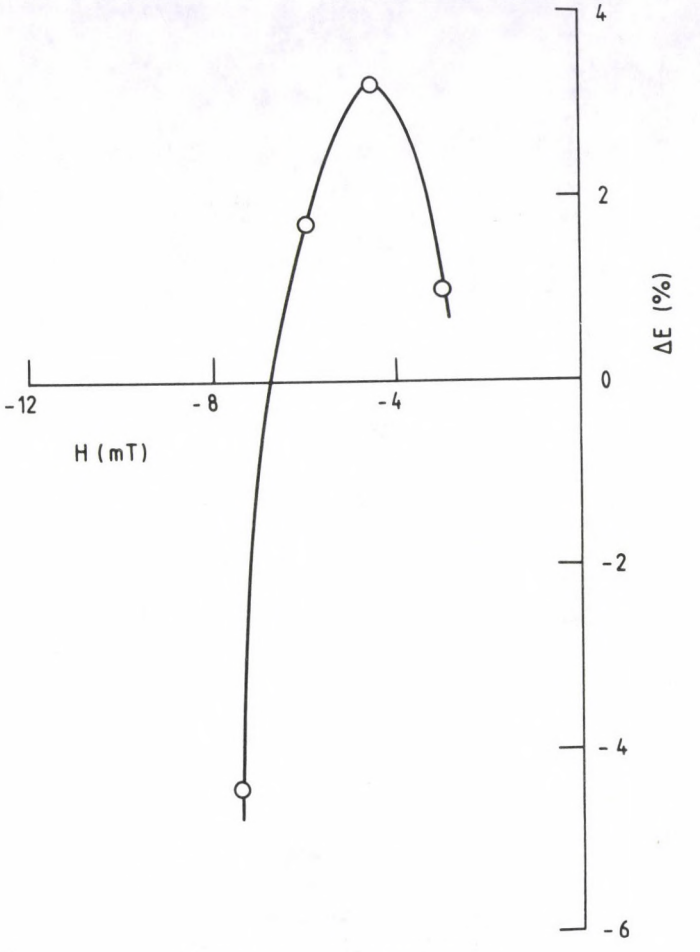

Fig. 3b. For caption see Fig. 3a

The scintillation response of pamolene crystal under gamma excitation (Fig. 2) is quite peculiar. The change in scintillation efficiency, $\Delta E(\%)$, increases with increase in the strength of magnetic field, irrespective of its direction. A peak is not observed in the ΔE versus H curve in the range of 0 to 13 mT investigated in the present work. The value of ΔE measured at the upper limit of 13 mT is 13 %, which reduces to 7 % on reversing the direction of the magnetic field. However, the change in scintillation efficiency $\Delta E(\%)$ in the case of pamolene is appreciably higher compared with that of stilbene, NE213 and NE230 (Table I).

The trend of the ΔE versus H curve obtained with pamolene crystal is almost the same as that of Jeenicke et al [1], who measured relative change in scintillation efficiency of NE235 oil based mineral scintillators up to 10 mT under beta excitation. However, our results cannot be directly compared with the data of other authors because we used different scintillators and different magnetic field range.

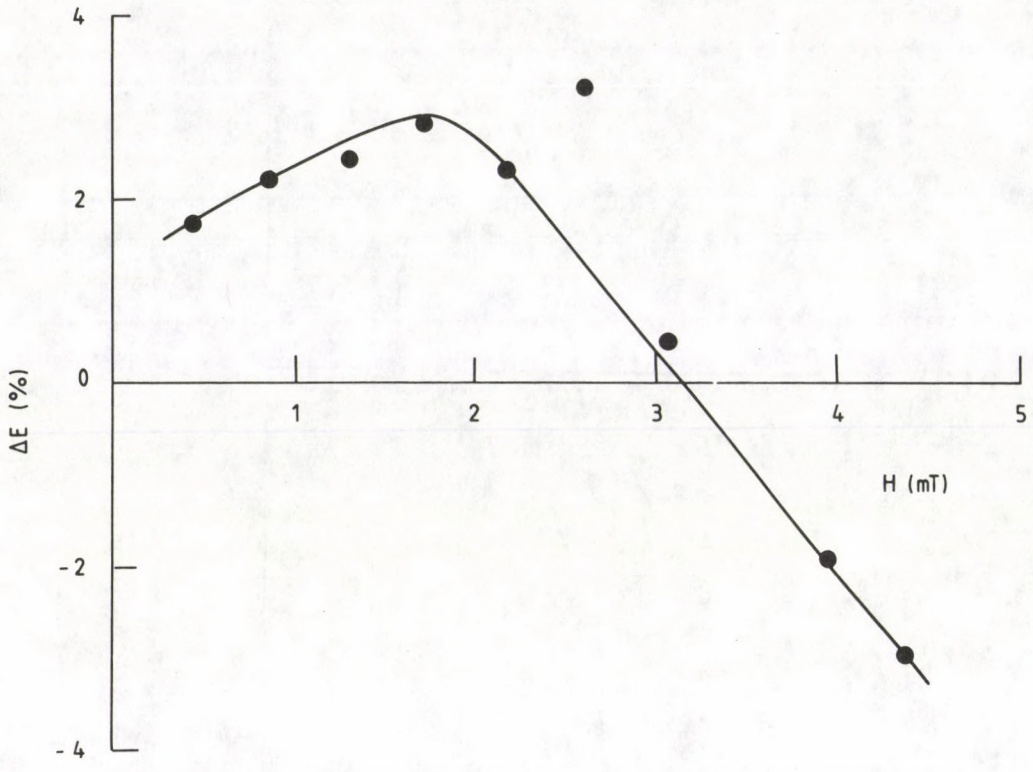

Fig. 4a. Same as Fig. 1 but for NE 230 liquid scintillator

There is no single generally accepted theoretical explanation available so far for the observations referred to above. However, there are many plausible explanations to account for the increase or decrease in the scintillation efficiency of organic scintillators due to the application of magnetic field. Some of these are as follows.

(a) The magnetic field dependence of the sensitivity of the organic scintillators is intrinsic and is due to their molecular structure. This was proposed by Jeenicke et al [1] and Swenberg and Geacintor [3].

(b) The enhancement of scintillation efficiency due to magnetic field can be ascribed to the change in the trajectories of Compton electrons leaving the surrounded scintillator by air, when the air–liquid or air–solid interface is situated in a region of rather high magnetic field. Jeenicke et al [1] tried to prove this hypothesis in their experiments carried out with NE235 applying magnetic field up to 10 mT, but they were not able to deflect the Compton electrons from the air back to the scintillator due to the rather 'low' magnetic field used by them. In the case of stilbene, NE213 and NE230 used in the present work, the applied magnetic field seems to be 'high' enough to deflect Compton electrons from the air back to the scintillators. This results in further excitation and ionisation in the scintillators giving rise

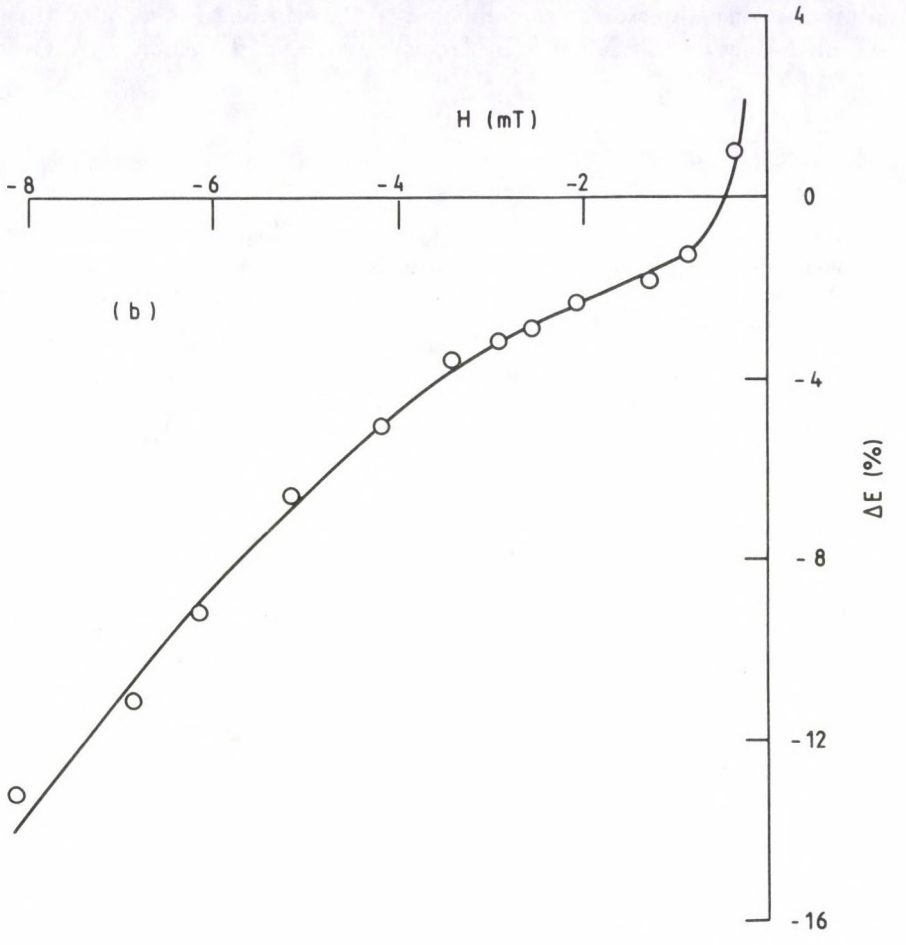

Fig. 4b. For caption see Fig. 4a

to the enhancement of light output and hence the counting rate. At optimum axial magnetic field, H_m, maximum Compton electrons will enter the scintillator resulting in maximum light output and hence maximum change in scintillation efficiency ΔE_m. For axial magnetic field less or greater than H_m, the value of ΔE would be less than ΔE_m. The cause of negative ΔE observed in the case of NE213, NE230 and stilbene is, however, not understood.

Conclusion

The fluorescence efficiency of the organic scintillators is dependent on magnetic field and can be appreciably enhanced. It is believed that enhancement in fluorescent efficiency due to magnetic field is most probably due to deflection of

Compton electrons trajectories from air back to the scintillator and/or to changes in molecular structure as referred to by Jeenicke et al [1] and Swenberg and Geacinitor [3].

References

1. E. Jeenicke, P. Liaud, B. Vignious and R. Wilson, NIM, *126*, 459, 1975.
2. E. Bodenstedt, L. Ley, H. O. Schlen, U. Wohman, Nucl. Phys., A, *137*, 33, 1969.
3. C. Schwenberg and N. E. Geacinitor, Organic Molecules Photo Physics, Vol. I. ed. John B. Birks, J. Wiley and Sons, New York, 1973.
4. R. Siddique, F. Haq, M. Z. Butt and F. A. Durrani, J. Nat. Sci. Maths., *27*, 131, 1987.
5. F. Haq, M. Z. Butt, W. Ali, S. Jammil and F. A. Durrani, Radiation Effects and Defects in Solids, *115*, 135, 1990.

Acta Physica Hungarica 71 (1–2), pp. 45–52 (1992)

INTERNAL BREMSSTRAHLUNG FROM ^{204}Tl

GÜNES TANIR, BAŞAR ŞARER

Gazi University, Faculty of Arts and Sciences
06500 Ankara, Turkey

and

HAKKI KÍZILTAN

Hacettepe University, Department of Physics
Ankara, Turkey

(Received in revised form 12 February 1991)

The continuous spectrum of internal bremsstrahlung from the unique first forbidden beta decay of ^{204}Tl was measured using the β stopper method with a multichannel analyzer and NaI (Tl) scintillation detector together with a standard geometrical arrangement. The raw spectrum was corrected for several factors using the step-by-step process of Liden and Starfeld and compared with theoretical results such as KUB (Knipp, Uhlenbeck and Bloch), LF (Lewis and Ford) and N (Nilsson) theories. The divergence between experiment and theory was found to increase with increasing energy.

Introduction

Internal bremsstrahlung (IB) is produced by the changing dipole moment of the electron–nucleus system due to the creation and emission β-particles. IB radiation accompanying β-decay has been explained in the literature [1,2,3] that in the case of forbidden β-decays transitions through virtual states may contribute to the continuous photon spectrum. In these so-called "detour transitions" the nucleus first emits a photon going to a virtual excited state then β decay follows or vice versa [4]. Several studies on IB were reported [3,4,5,6]. Despite various experimental and theoretical studies on IB there exist various disagreements not only between theory and experiment but even among the individual measurements especially at high photon energies.

In the studies by Ricci [3] on IB from ^{204}Tl, the measurements were confined to an energy region extending from 80 to 400 keV to compare with theory. The experimental results were found to disagree with KUB (Knipp, Uhlenbeck and Bloch) [8] theory throughout the energy region investigated and they tended to agree with the Nilsson [9] approximation. Below 150 keV there was complete disagreement between the experimental results and the KUB as well as Nilsson theories. Narasimhamurty and Jananda [4] studied the IB from ^{204}Tl in the region from 90 to 550 keV. They reported that there is reasonable agreement between experimental results and

Coulomb corrected theory of Nilsson above 300 keV while the experimental results are much greater than the theoretical ones below 300 keV.

Studies on IB are not only of theoretical interest but also of fundamental importance. IB explains a secondary means of understanding β-decay. There is, however, a lack of agreement among the studies. Since the β emitter ^{204}Tl is of the first forbidden type, an investigation of the IB of ^{204}Tl may also give an idea of the contribution to the IB from the detour transitions.

Furthermore ^{204}Tl has a relatively low beta end-point energy (0.76 MeV) and high atomic number IB from it would probably explain the importance of the Coulomb effect and also the degree of forbiddenness especially in the high energy region. In addition, IB is an important factor in nuclear physics for shielding calculations. Therefore, in the present work, the continuous IB spectrum from ^{204}Tl was measured and the results were compared with the corresponding theoretical and experimental predictions.

Experimental details

The decay scheme of ^{204}Tl and the experimental set-up are shown in Fig. 1.

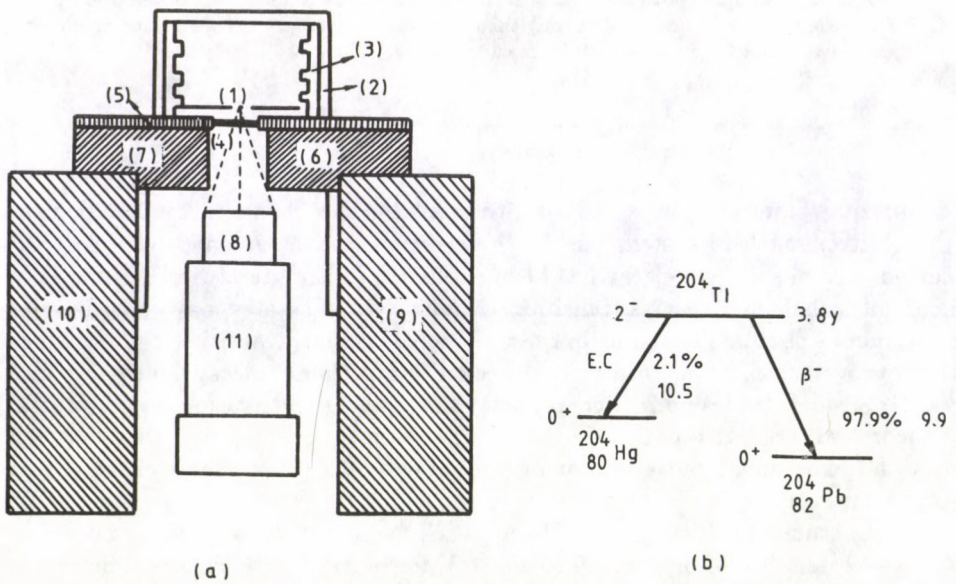

Fig. 1. (a) Cross-sectional view of the geometrical set-up for the study of IB. (1) source, (2) perspex ring, (3) perspex rod, (4) β-stopper, (5) perspex disk, (6) and (7) lead collimator inside surface lined with aluminium, (8) NaI(Tl) detector, (9) and (10) lead shielding, (11) photomultiplier. (b) Decay scheme of ^{204}Tl

The IB spectrum from ^{204}Tl was measured in the energy region from 298 to 760 keV with a NaI(Tl) crystal ($2'' \times 2''$) scintillation spectrometer. The source was obtained in the form of point source from Amersham (England). The source activity is 1μc. Owing to the low intensity of the IB, a strong source would have been preferable, so that the counting rate would far exceed the background counting rate. However, this was not possible because in thick sources external bremsstrahlung is created in the source itself. Counting time is tested until sufficient counts/s was determined. The background level was greatly minimized by housing the NaI(Tl) crystal-photomultiplier assembly in a lead shield of a wall thickness of ~ 5 cm.

Because of the low activity, a lead shielding material was not placed between source and detector, only perspex β-stopper of sufficient thickness was placed.

The linearity of analyzer was checked by using the following γ-ray lines: 285 keV (^{203}Hg), 662 keV (^{137}Cs), 835 keV (^{54}Mn), 511 keV, 1227 keV (^{22}Na).

The source was placed 1 cm above the surface of the detector and the perspex β-stopper was kept between the source and detector to absorb all the β-particles from the source. In order to reduce the EB (External Bremsstrahlung) interference and scattering effects from the air the source was covered with a perspex chamber. The full width at half maximum of the 662 keV γ line of ^{137}Cs was 11 %. During the experimental measurements of IB pulse height distributions, sufficient collection time was used. The raw IB spectrum from ^{204}Tl was shown in Fig. 2.

Some of the errors (back-scatter, crystal efficiency, external bremsstrahlung e.g) can be diminished by using a suitable geometry. The geometry used in the measurements was found experimentally.

Evaluation of the IB spectrum

In order to obtain the true photon distributions, the measured pulse height spectrum should be corrected for background, energy resolution, K–X ray escape, Compton electron distribution, geometrical and γ detection efficiency of the crystal, for backscattering from the photomultiplier window and also from the surrounding material used as shielding.

Because of the small resolving time ($\sim 2\ \mu$s) of the analyzer and small strength of the source used, corrections for dead-time counting loss was found to be negligible.

Of the various corrections mentioned above, the correction due to the Compton electron distribution becomes important when there are photons of high energy. A detailed account of it is given in what follows. If the fraction of photons detected with full energy is $K(E_\gamma)$ at energy E_γ, it is obvious that the fraction of photons detected with less than the full energy is $1 - K(E_\gamma)$. If the number of photons of energy E_γ absorbed in the crystal is $N_a(E_\gamma)$, then the number of Compton electrons, having energies ranging from zero to E_γ^*, where E_γ^* is the maximum Compton electron energy, is $N_a(E_\gamma)(1 - K(E_\gamma))$. The total number of Compton electrons at energy E due to all incoming photons from zero to $E_{\max}$ is

$$N_c = \int_0^{E_{\max}} C(E, E_\gamma) N_a(E_\gamma)(1 - K(E_\gamma)) dE_\gamma .$$

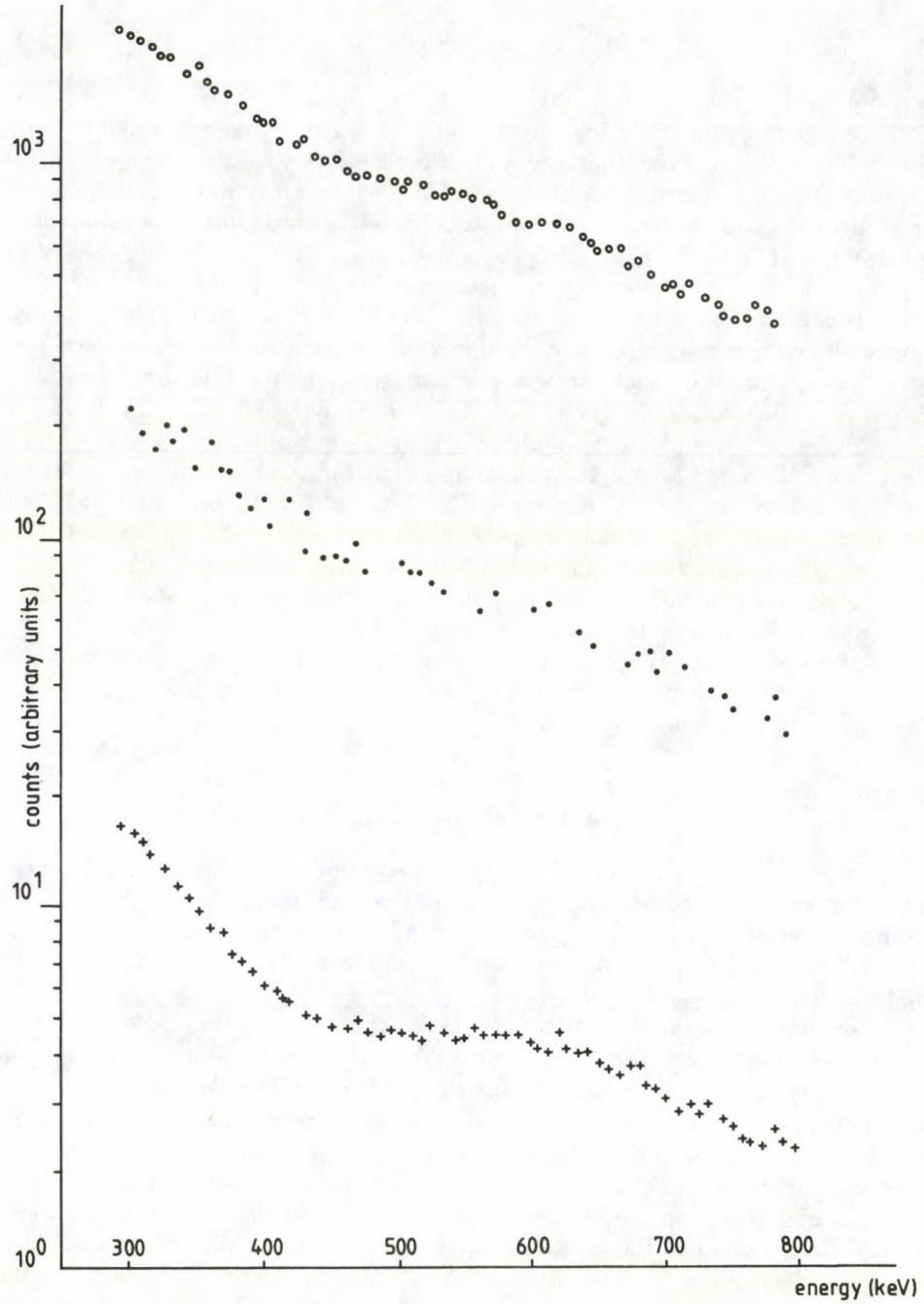

Fig. 2. o o oo - Measured distribution, ... - background, xxxxx - Compton electron distribution

In general, on the assumption that the Compton electron distribution for any gamma ray energy is approximately constant over the energy range from zero to E_γ^*, the following approximation is made:

$$C(E, E_\gamma) = C(E_\gamma) = \frac{1}{E_\gamma^*} \quad \text{for} \quad 0 < E < E_\gamma^*,$$

$$C(E, E_\gamma) = 0 \quad \text{for} \quad E > E_\gamma^*.$$

Actually, the observed pulse-height is first extrapolated to the end-point. Next the corresponding $1 - K(E_\gamma)$ is calculated and by choosing a suitable value of ΔE_γ, the smaller the better, the ordinate $(\Delta N_c)E_\gamma$ of the Compton distribution from zero to E_γ^* due to photons of energy between E_γ and $E_\gamma + \Delta E_\gamma$ is calculated by the relation

$$(\Delta N_c)_{E_\gamma} = \frac{1}{E_\gamma^*} N a(E_\gamma)(1 - K(E_\gamma))\Delta E_\gamma.$$

This process is repeated throughout the spectrum and the Compton electron distribution is obtained. This distribution has to be subtracted from the observed pulse-height distribution. In the present calculations an energy of 8 keV is used for ΔE_γ. The Compton electron distribution thus calculated is shown in Fig. 2.

The correction for the geometrical and gamma-detection efficiency of the detector is obtained as follows. The gamma-detection efficiency (photopeak efficiency) $E_p(E_\gamma)$ at energy E_γ is determined as the product of the peak-to-total ratio $K(E_\gamma)$ and the intrinsic efficiency $\epsilon_t(E_\gamma)$, that is $E_p(E_\gamma) = K(E_\gamma) \cdot \epsilon_t(E_\gamma)$. An experimental determination of the peak-to-total ratio is made by recording in the same geometrical arrangement the complete pulse–height spectra of the monoenergetic γ-ray lines. The values of $K(E_\gamma)$ thus determined are shown in Fig. 3. The values of intrinsic efficiency for the present geometry were determined by using the total absorption coefficient values of White [10] and the values of the geometrical factor for the present geometry are calculated according to the values of Özmutlu [11]

The values of both $K(E_\gamma)$ and $\epsilon_t(E_\gamma)$ thus used belong to a point source geometry.

Correction for iodine K–X-ray escape is important only in the energy region below 150 keV. Since our measurements were restricted to the region above $\sim$ 300 keV this correction was neglected.

The photons backscattered from the photomultiplier window, source backing, the crystal container and the lead shield make undesirable contributions to the spectrum in the range 100–300 keV. Since the energy region of present interest is above 300 keV this correction was also neglected.

Comparison with theory

Knipp and Uhlenbeck and independently Bloch were the first to make the theoretical calculation of the IB spectral distribution and this is known as KUB theory. Lewis and Ford and Nilsson accounted for the Coulomb effects on the IB

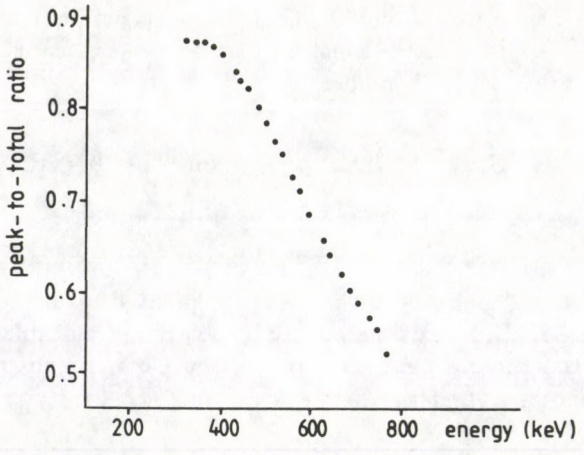

Fig. 3. Peak-to-total ratios for the gamma-ray detector employing a NaI(Tl) crystal of 2″ in diameter and 2″ in thickness.

spectrum. Ford and Martin theories included the detour transitions.

According to the KUB theory the number of IB photons per β disintegration per unit energy interval is given by

$$S(K) = \int_{1+K}^{W_{max}} dW_e P(W_e)\phi(W_e K),$$

where $P(W_e)dW_e$ is the distribution of the β spectrum with end-point energy W_{max} and $\phi(W_e, K)$ is the probability of an electron coming from the nucleus with energy W_e emitting a quantum of energy K.

The function $\phi(W_e, K)$ is given as

$$\phi(W_e, K) = \frac{\alpha P}{\pi P_e K}\left(\frac{W_e^2 + W^2}{W_e P}\ln(W + P) - 2\right),$$

where W_e and W and P_e and P are energies and momenta of the electron before and after the emission of the photon of energy K, respectively, and $\alpha = \frac{1}{137}$ is the fine-structure constant. All energies are in units of mc^2 and all momenta in units of mc.

The probability for bremsstrahlung production per 1 MeV energy interval per data disintegration is chosen for comparison with the experimental results. After effecting all the necessary corrections, the final experimental distributions are all normalized to 1 MeV energy interval per beta disintegration by dividing the corrected IB pulse height distributions by the channel width ΔK in units of mc^2 and then by multiplying by 1 MeV in units of mc^2. According to the theoretical results the number of IB photons is given as per β disintegration per unit energy interval.

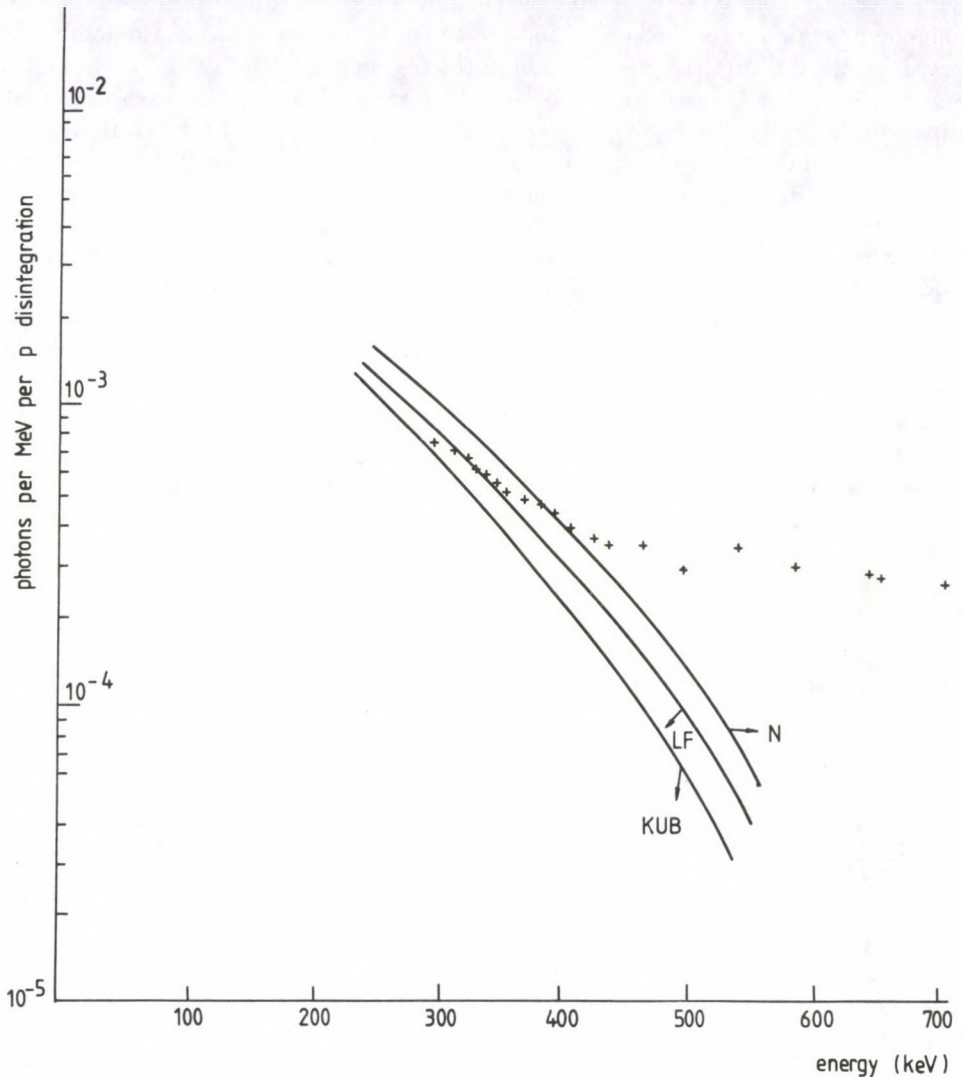

Fig. 4. ^{204}Tl internal bremsstrahlung intensity spectrum. xxxx - experimental data; theoretical curves: KUB, LF and N theories

Results and discussion

^{204}Tl is found to have a spectral shape of the unique first-forbidden type and it has an end-point energy of 760 keV and a half-life of the order of 3.9 years. There is also a weak electron capture branch ($\sim$ 1.5 %) in the decay of this isotope. The end-point energy for the internal bremsstrahlung associated with the electron capture has been variously reported to be 250 keV [12].

It can be seen from Fig. 4 that the portion of the experimental spectrum in the high-energy region form 300 keV to 350 keV corresponds closely to the Coulomb-corrected Lewis and Ford [13] distribution in the region above 400 keV. Experimental excess over all the three theories is more than about 100 %. This excess may be explained as partly due to the detour transitions taking place in ^{204}Tl, it being a forbidden β emitter [4]. The contribution to the IB from the so-called detour transitions is significant, although it is almost negligible for allowed β decay. In order to explain the generally observed behaviour of the disagreement between experiment and theory concerning IB, namely a positive deviation of experiment from theory which increases with increasing photon energy, it is necessary to carry out more theoretical and experimental studies.

It is concluded from the present results that the influence of the Coulomb field of the nucleus is very important, especially at high photon energies. To perform new theoretical calculations by taking into account the Coulomb effect of the nucleus, the forbiddenness of the β spectrum and also detour transitions in a more exact manner than in the already existing theories, more work should be done.

Acknowledgements

The authors thank Dr. F. Apaydin, Professor and Head of Department of Physics, University of Hacettepe, for his interest and encouragement.

References

1. B. I. Persson, Proc. Conf. on Higher Order Processes in Nuclear Decay. Vol. II. ed. D. Berényi, p. 142, 1968.
2. D. G. S. Narayana, K. Narasimhamurty and V. V. V. Subrahmanyam, Current Science, *46*, 1, 1977.
3. R. A. Ricci, Physica, *24*, 297, 1958.
4. K. Narasimhamurty and S. Jananandа, Proc. Phys. Soc., *90*, 109, 1967.
5. R. Prasad Babu, K. Narasimhamurty and V. A. Narasimhamurty, Phys. Rev. C, *13*, 1267, 1976.
6. H. Sanjeevaiah and B. Sanjeevaiah, Phys. Rev. C, *18*, 974, 1978.
7. B. R. S. Babu et al., J. Phys. G: Nucl. Phys., *11*, 1213, 1985.
8. J. K. Knipp and G. E. Uhlenbeck, Physica, *3*, 425, 1936.
9. S. B. Nilsson, Ark. Fys., *10*, 467, 1956.
10. G. White, NBS Circular NBS-1003, 1957.
11. C. Özmutlu and A. Z. Ortaovali, Nucl. Inst. and Meth., *133*, 149, 1976.
12. E. Der Matosian and A. Smith, Phys. Rev., *88*, 1186, 1952.
13. R. R. Lewis and G. N. Ford, Phys. Rev., *107*, 756, 1957.

Acta Physica Hungarica 71 (1–2), pp. 53–60 (1992)

EFFECT OF ALIPHATIC AND AROMATIC SUBSTITUENTS ON THE FLUORESCENCE OF SOME POLYMERS

K. P. DHAKE, S. N. PATIL

Applied Physics Department
Faculty of Technology of Engineering
M. S. University of Baroda
Baroda – 390 001, India

and

RITA RAJA

Physics Department, University Department of Chemical Technology
University of Bombay, Matunga, Bombay – 400 085, India

(Received 18 February 1991)

7–8 dihydroxy–4–methyl coumarin A and its copolyesters A_1 through A_5 have been investigated here to study the effect of aliphatic and aromatic substituents in the polymers, on the fluorescence of these compounds. It has been observed that along with other emissions 480 nm emission present in all the polymer specimens has been missing in the monomer specimen. The fluorescence of these polymers is shown to depend on the aliphatic and aromatic substitutions at various positions.

Introduction

The fluorescence efficiency of coumarins depends on the nature and position of a substituent in the parent molecule [1] and also changes due to the change in the surrounding media. Though coumarin by itself does not exhibit fluorescence; many of the derivatives of coumarin are known to be fluorescent in nature [2]. Further, in view of the use of coumarin derivatives in the solar cells the present study aims at examining the fluorescence spectra of some of the coumarin derivatives.

The 7–8 dihydroxy–4–methyl coumarin monomer and five of its polyesters have been investigated here with the view to study the effect of the substituent group such as aliphatic or aromatic nuclei in the polymer chains.

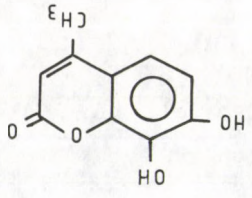

Fig. 1a. Monomer specimen A

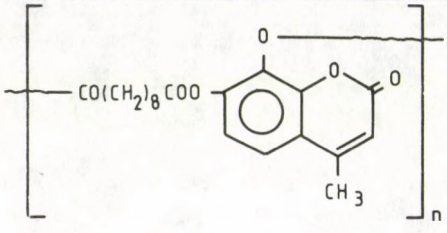

Fig. 1b. Monomer specimen A_1

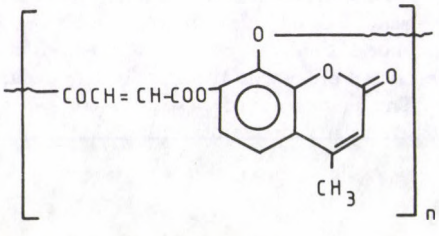

Fig. 1c. Monomer specimen A_2

Experimental

The fluorescence spectra, excitation and emission, have been recorded at room temperature (25 ± 2 °C) by using Aminco Bowmann Spectrophotofluorometer (SPF). The fluorescence spectra have been corrected for the non-linear response

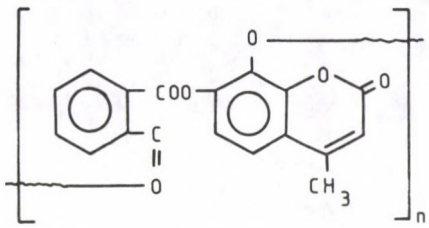

Fig. 1d. Monomer specimen A_3

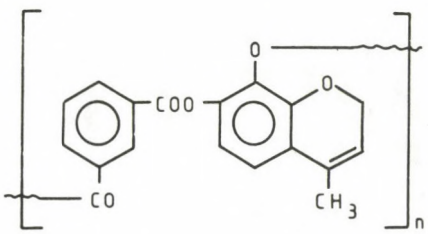

Fig. 1e. Monomer specimen A_4

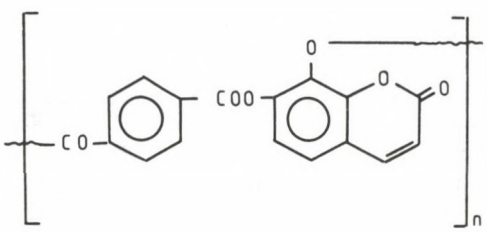

Fig. 1f. Monomer specimen A_5

of the detector photomultiplier tube (IP–21) and the non-uniform emission of the source, the Xenon lamp.

The coumarin derivatives investigated presently were synthesized according to the known method [3] and were checked for purity by melting point (M.P) and infra red (IR) spectra. The coumarin monomer 7–8 dihydroxy–4–methyl coumarin (A) was subjected to copolymerize [4] with dibasic acids namely sebacic acid (A_1),

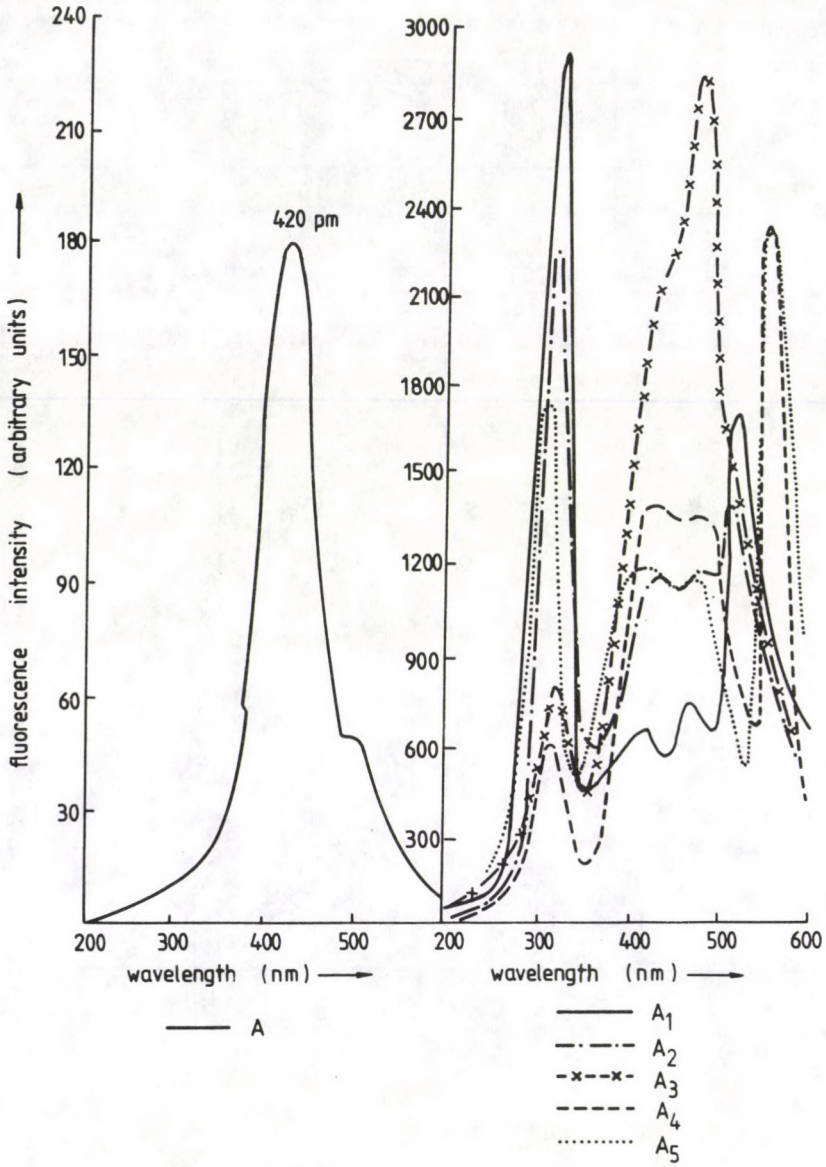

Fig. 2

maleic acid (A_2), phthalic acid (A_3), isophthalic acid (A_4) and terphthalic acid (A_5) in pyridine. All polymers were purified by solvent and non-solvent method. DMF was used as the solvent while ethyl alcohol was the non-solvent. The structures of specimens A, A_1, A_2, A_3, A_4 and A_5 are shown in Fig. 1.

A batch of the above specimens has been preheat-treated at 100 °C for 2 hours and suddenly cooled to room temperature for the study of the annaled and quenched specimens. Another batch of the above specimens is treated mechanically under high pressure to transform into pellets.

Results and discussion

The emission band at 480 nm is present in all polymer specimens A_1 to A_5, however, it is missing in the monomer specimen A (Fig. 2). The positions at 7–8 have been occupied by the hydroxyl group in the specimen A, however, for the specimens A_1 to A_5 the ester group has been substituted in these positions. The presence of ester groups in the repeating units of specimens A_1 through A_5 are considered to be responsible for the 480 nm emission. The absence of ester group automatically makes up for the missing 480 nm emission in the specimen A.

In the aliphatic compounds A_1 and A_2, the intensity of 480 nm emission for specimen A_2 is larger than for specimen A_1. This has to be expected as the presence of double bonds –C=CH– in the repeating units of specimen A_2 enhances intensity. The intensity of emission in the specimens A_3, A_4 and A_5 should diminish due to the aromatic substitution [5] in place of the aliphatic nuclei. However, contrary to this the observations show a sharp enhancement in the intensity for specimen A_3. The intensity of the emission drops successively for the specimens A_4 and A_5. In these compounds the ester group has been substituted at -ortho, -meta and -para positions in the specimens A_3, A_4 and A_5, respectively. The closeness of the ester group in the specimen A_3 improves the intensity of the emission. Further, 520 nm emission is also completely wiped off for the specimen A_3. It is possible that 480 nm emission might have built up at the cost of 520 nm. The intensity for the specimens A_3, A_4 and A_5 depends on the steric factors of the polymer systems. Higher steric interaction due to 1,3 and 1,2 substitution on the benzene ring of the di-acid repeat units for A_4 and A_3 should make up for the decrease [6] in the intensity for specimens in the order A_3 to A_4 to A_5. The -ortho substitution of ester group in polymer chain results in the closer packing of molecules of specimen A_3. This closer packing gives rise to the increased rigidity to the specimen A_3, compared to A_4 and A_5. Since intense fluorescence is characterized by rigid [7,8] structured molecules, the fluorescence intensity for specimen A_3 is the largest.

The intensity pattern observed for 480 nm emission in the specimens A_1 to A_5 agrees with the explanations provided for 420 nm emission [9] on the basis of the structural changes taking place from specimen to specimen. The agreement is expected to be observed as 420 and 480 nm emissions are portrayed as doublets.

It is observed that the 480 nm band gets shifted to 460 nm after the specimens have been mechanically deformed into pellets. Because 420 and 480 nm emissions are doublets, it is observed in Fig. 3 that whenever 420 nm becomes more pronounced, it is at the cost of the intensity of the 480 nm emission. Further, it can be seen in Fig. 3 that 480 nm emission appears as a shoulder to the main emission band at 420 nm.

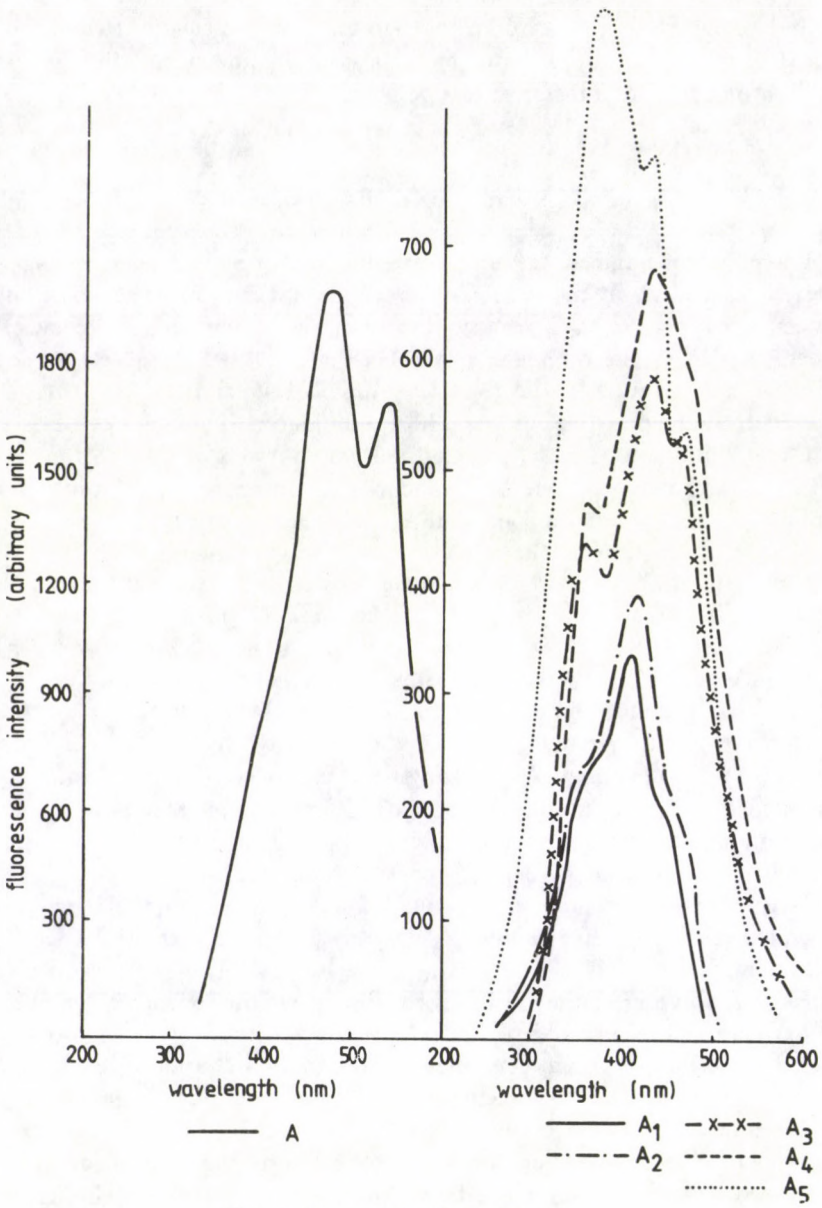

Fig. 3. After mechanical treatment

The intensities for 480 nm emission after plastic deformation in the specimens A_1 to A_5 are more or less similar to those in the powered specimens. This emission has been absent in the specimen A as expected due to the absence of the ester group.

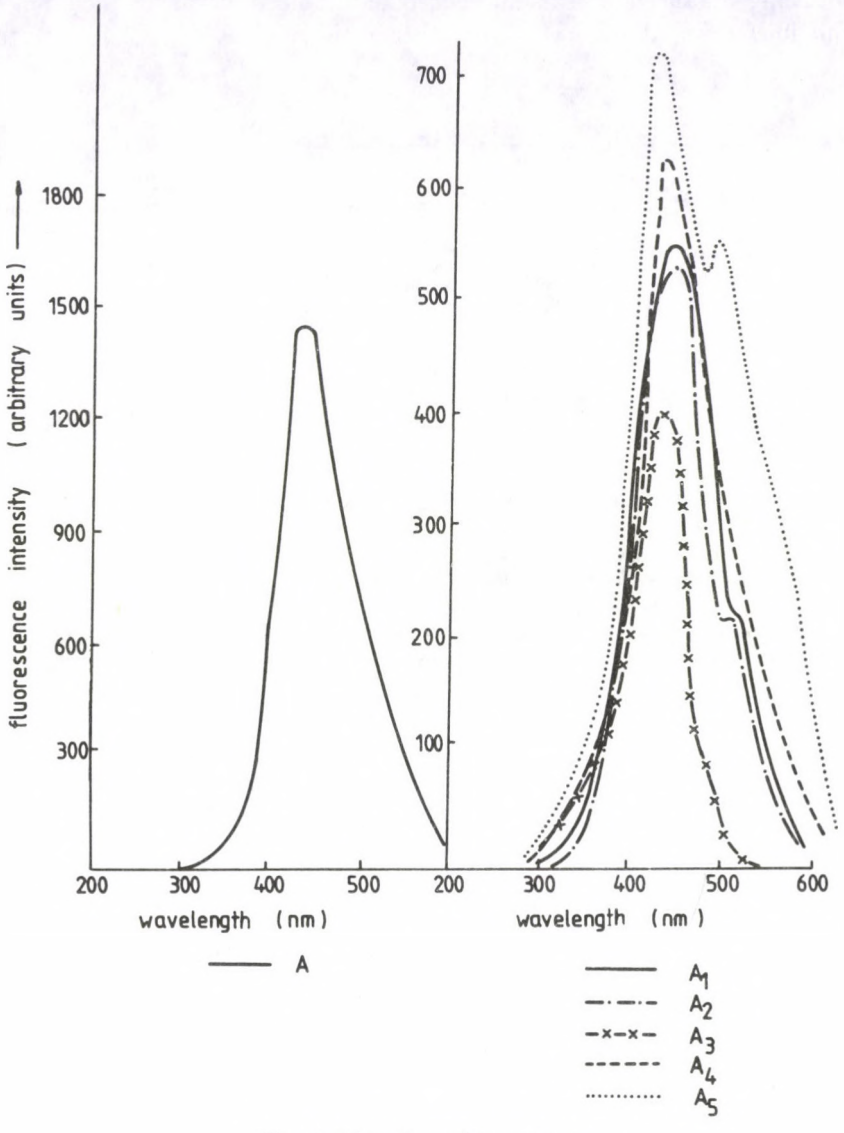

Fig. 4. After thermal treatment

The thermal treatment to the specimens shifts the 480 nm emission to 500 nm. This is due to the configurational changes in the polymer specimens and the long chains will be broken into smaller chains of larger numbers. This is responsible for the shift of 480 nm. However, the 420 nm emission is dominant in all thermally treated specimens, and it is obvious that the other emission, namely 480 nm from the doublet is observable in the form of a weak peak. In the specimen A_4, the emission band at 480 nm is conspicuous by its absence, the intensity of emission at

420 nm being enhanced. This is an additional fact in favour of the idea that one of the emissions grows at the cost of the other in the doublet.

Acknowledgements

One of the authors (S. N. Patil) is thankful to the Council of Scientific and Industrial Research (CSIR) for the award of a Senior Research Fellowship.

References

1. S. S. Rathi et al, Current Science, *50*, 802, 1987.
2. C. N. R. Rao, UV and Visible Spectroscopy and Chemical Applications, Butterworth and Co. Publishers Ltd., London, 1975.
3. S. Sethana et al, Chemical Review, *36*, 30, 1945.
4. P. W. Morgan, Interfacial and Condensation Polymerizations, John Wiley and Sons, N. Y. 1970.
5. W. West, Chemical Applications of Spectroscopy, N. Y. 1956.
6. Kasha, Radiation Res. Suppl., *2*, 243, 1960.
7. W. Rhodes et al, J. Mol. Spectr., *9*, 42, 1962.
8. R. M. Hochstrasser, Can. J. Chem., *39*, 459, 1961.
9. J. Jayashree, Ph. D. Thesis, M. S. University of Baroda, 1989.

Acta Physica Hungarica 71 (1–2), pp. 61–65 (1992)

RELATIVISTIC SCHRÖDINGER EQUATION INCLUDING SPIN–ORBIT INTERACTION

H. A. MOURAD

Department of Physics, Faculty of Science
University of Zagazig, Zagazig, Egypt

and

I. SH. VASHAKIDZE

Tbilisi State University, 380028 Tbilisi, Georgia

(Received 25 February 1991)

A relativistic Schrödinger equation including spin–orbit interaction has been derived. The equation contains two types of potentials. It is shown that when one of the potentials is a potential well, the exact solution of the equation with and without spin–orbit interaction can be obtained using the boundary condition method. The influence of the spin–orbit interaction is investigated.

1. Introduction

As we know, the relativistic free electron can be described by the Dirac equation (in units $\hbar = c = 1$)

$$\{E - (\overrightarrow{\alpha}, \mathbf{p}) - \beta m\}\psi(r) = 0. \tag{1}$$

However, to solve a practical problem such as the motion of a relativistic particle in a definite potential field we must use the Dirac equation. But it is often not clear, to which term in (1) the potential must be added. Also, it is not obvious which form of the potential must be taken in spin space.

Recently, the above variants are studied by considering the potential form $\frac{1}{2}(1+\beta)V$ in the Dirac equation, i.e. the potential is added, with equal weight, to both the energy and mass [1,2,3].

In the present work, a relativistic Schrödinger equation including spin–orbit interaction has been derived. We show that when the potential is a potential well the relativistic Schrödinger equation can be solved with and without spin–orbit interaction using the boundary condition method.

2. Relativistic Schrödinger equation including spin–orbit interaction

Considering the potential form

$$\frac{1+\beta}{2}V = \begin{pmatrix} V & 0 \\ 0 & V \end{pmatrix}, \tag{2}$$

then, the Dirac equation can be simplified as [1]

$$(E - m - V)\phi - (\vec{\sigma} \cdot \mathbf{p})\chi = 0, \tag{3a}$$

$$(E + m)\chi - (\vec{\sigma} \cdot \mathbf{p})\phi = 0. \tag{3b}$$

Introducing the notation

$$E_s = \frac{(E-m)(E+m)}{2m}, \quad V_s = \frac{E+m}{2m}V \tag{4}$$

we have for the bispinor $\phi(r)$

$$[-\mathbf{p}^2 + 2m(E_s - V_s)]\phi = 0, \tag{5}$$

which is of the same form as the non-relativistic Schrödinger equation. Naturally, Eq. (5) is called the Schrödinger relativistic equation where the relativistic effects are taken into account only at a kinematic level.

In the non-relativistic limit when $E \to E' + m$, $E + m \to 2m$, Eq. (5) coincides with the Schrödinger equation. The radial equation which corresponds to (5) takes the form [2]

$$\frac{d^2G}{dr^2} + \frac{\kappa(\kappa+1)}{r^2}G + 2m(E_s - V_s)G(r) = 0, \tag{6}$$

where $\kappa = l(l+1) - j(j+1) - 1/4$. Eq. (6) turned out very fruitful for clearing up some special quark systems which, consequently, indicates that the addition of parts of the potential energy to the mass in the Dirac equation has a serious basis. Furthermore, such addition in case of positive potential removes the Klein paradox which is not the least of the factors either.

But Eq. (5) has a large defect since $\kappa(\kappa+1) = l(l+1)$ then it does not include spin–orbit interaction. Therefore, it is important to choose the potential matrix in order that all the attractive sides of (6) are conserved and (6) will contain spin–orbit interaction.

Therefore, we believe that in the Dirac equation the potential must take the general matrix

$$\begin{pmatrix} V_{11} & V_{12} \\ V_{21} & V_{22} \end{pmatrix}, \tag{7}$$

where the central interaction $V_{ik}(r)$ is the diagonal matrix of the second rank. The matrix (7) is constituted by means of a linear combination of three matrices: 1, ρ_2

and ρ_3. For the conservation of space parity it is necessary that the coefficient of ρ_2 be equal to zero. Therefore, the interaction matrix must take the form

$$\begin{pmatrix} V & 0 \\ 0 & U \end{pmatrix} = \frac{1+\beta}{2}V + \frac{1-\beta}{2}U. \tag{8}$$

For the potential (8) the Dirac equation takes the form

$$\begin{aligned} (E - m - V)\phi - (\vec{\sigma} \cdot \mathbf{p})\chi = 0, \\ (E + m - U)\chi - (\vec{\sigma} \cdot \mathbf{p})\phi = 0. \end{aligned} \tag{9}$$

Assuming V an arbitrary potential and U satisfies the condition

$$U \ll E + m, \tag{10}$$

then, the function χ may be given by

$$\chi(r) = \frac{1}{E+m}[1 + \frac{U}{E+m} + \cdots +](\alpha \cdot \mathbf{p})\phi, \tag{11}$$

thus, the first equation in (9) gives

$$[-\mathbf{p}^2 + (E+m)(E-m-V) - \frac{(\vec{\sigma} \cdot \mathbf{p})U(\vec{\sigma} \cdot \mathbf{p}}{E+m}]\phi(r) = 0, \tag{12}$$

which is the "relativistic Schrödinger equation" including spin–orbit interaction and other relativistic corrections of the same order.

If we retain only the spin–orbit term in Eq. (12) and go on to the equation for the radial function, we have

$$\left\{\frac{d^2}{dr^2} - \frac{l(l+1)}{r^2} + 2m[E_s - V_s - \frac{1}{m(E+m)}\frac{1}{r}\frac{dU}{dr}(\mathbf{s} \cdot \mathbf{l})]\right\} G(r) = 0, \tag{13}$$

which, unlike (6), includes spin–orbit interaction and, on keeping the condition (9), it is free from the Klein paradox.

In case of an attractive well of depth U_0 and width r_c noting that $2(\mathbf{l} \cdot \mathbf{s}) = -(\kappa + 1)$ then, Eq. (13) takes the form

$$\left\{\frac{d^2}{dr^2} - \frac{\kappa(\kappa+1)}{r^2} + 2m[E_s - V_s - \frac{\kappa+1}{2m(E+m)}\left(\frac{U_0}{r_c}\right)\delta(r - r_c)]\right\} G(r) = 0, \tag{14}$$

where r_c is the radius of the sphere where the potential has infinite value. Eq. (14) can be used to solve a wide range of problems and, the attractive is that the inclusion of spin–orbit interaction is equivalent to the following boundary condition

$$\left(\frac{1}{G}\frac{dG}{dr}\right)_{r_c+0} - \left(\frac{1}{G}\frac{dG}{dr}\right)_{r_c-0} - \frac{\kappa+1}{E+m}\left(\frac{U_0}{r_c}\right) = 0, \tag{15}$$

where $G(r)$ is the solution of (15) without the last term and assuming that $V(r)$ has no singularity at $r = r_c$.

3. Solution without spin–orbit interaction

For an attractive potential well $V(r)$ of depth V_0 and width r_0 we introduce the notation:

$$\beta^2 = (E+m)(E-m+V_0), \quad w^2 = m^2 - E^2, \tag{16}$$

where $E - m + V_0 > 0$, i.e. $V_0 > (m - E) = \epsilon (V_0 > 2m)$; ϵ is the binding energy, then, the solution of Eq. (6) is given by

$$\begin{aligned} G(r) &= A_l r j_l(\beta r), \qquad r < r_0, \\ G(r) &= A_l \frac{j_l(\beta r_0)}{K_l(w r_0)} r K_l(w r), \quad r > r_0, \end{aligned} \tag{17}$$

where A_l is the normalization coefficient and, j_l and K_l are the spherical and modified spherical Bessel functions, respectively [4]. The energy eigenvalues in the Dirac theory are found from the condition [5]

$$\left[\frac{F(r)}{G(r)}\right]_{r_0+0} = \left[\frac{F(r)}{G(r)}\right]_{r_0-0}, \tag{18}$$

which for the potential well reduces to the identity

$$\frac{1}{E+m+V_0}\left(\frac{1}{G}\frac{dG}{dr} + \frac{\kappa}{r}\right)_{r_0+0} = \frac{1}{E+m}\left(\frac{1}{G}\frac{dG}{dr} + \frac{\kappa}{r}\right)_{r_0-0}, \tag{19}$$

while for the relativistic Schrödinger equation, also, as for the Schrödinger equation the condition (18) reduces to the continuity of the logarithmic derivatives, i.e.

$$\left(\frac{1}{G}\frac{dG}{dr}\right)_{r_0+0} = \left(\frac{1}{G}\frac{dG}{dr}\right)_{r_0-0}, \tag{20}$$

from which the energy eigenvalues are given by

$$\frac{\beta j_{l-1}(\beta r_0)}{j_l(\beta r_0)} = -\frac{w K_{l-1}(w r_0)}{K_l(w r_0)}, \tag{21}$$

which coincides, within a kinematic factor, with the eigenvalues equation of the potential well in the Schrödinger theory.

It is clear that Eq. (21) differs from the eigenvalues equation obtained in the Dirac theory. This difference is evidently in the special case $l = 0$. Really, equation (21) gives the expression

$$\beta r_0 \operatorname{ctg} \beta r_0 = -w r_0, \tag{22}$$

then, as in the Dirac theory, we obtain the equation

$$\beta r_0 \operatorname{ctg} \beta r_0 = -w r_0 \left(1 + \frac{V_0}{2m-\epsilon}\right) - \frac{V_0}{2m-\epsilon}. \tag{23}$$

4. Solution with spin–orbit interaction

Now in the potential well problem ($V = V_0$ for $r \leq r_0$ and $V = 0$ for $r > r_0$) the spin–orbit interaction is included. To solve this problem we shall use Eq. (14) in which, for definitely, we shall assume that $r_c \geq r_0$.

The corresponding radial wave functions take the form

$$\begin{aligned} G(r) &= A_l r j_l(\beta r); && r \leq r_0, \\ G(r) &= B_l r K_l(wr) + C_l r i_l(wr); && r_0 < r < r_c, \\ G(r) &= D_l r K_l(wr); && r < r_c, \end{aligned} \tag{24}$$

where A_l, B_l, C_l and D_l are constants and $i_l(wr)$ is the modified spherical Bessel function [4].

Applying the continuity condition of the wave functions at $r = r_0$ and the condition (15) at $r = r_c$, we have

$$\frac{\beta j_{l-1}(\beta r_0)}{j_l(\beta r_0)} = -\frac{wK_{l-1}(wr_0) + wi_{l-1}(wr_0)B_l}{K_l(wr_0) + i_l(wr_0)B_l}, \tag{25}$$

where B_l is given by

$$B_l = \frac{wK_{l-1}(wr_c) - \left[w\frac{K_{l-1}(wr_c)}{K_l(wr_c)} - b_\kappa\right] K_l(wr_c)}{wi_{l-1}(wr_c) + \left[w\frac{K_{l-1}(wr_c)}{K_l(wr_c)} + b_\kappa\right] i_l(wr_c)}, \tag{26}$$

where b_κ is defined by

$$b_\kappa = \frac{\kappa + 1}{2m - \epsilon}\left(\frac{U_0}{r_c}\right). \tag{27}$$

In the absence of spin–orbit interaction, $b_\kappa = 0$ and $b_l = 0$ and, as expected, expression (25) reduces to expression (21). When $r_0 = r_c$ the eigenvalues equation (25) may be simplified and reduced to the form

$$\frac{\beta j_{l-1}(\beta r_c)}{j_l(\beta r_c)} = -\frac{wK_{l-1}(wr_c)}{K_l(wr_c)} + \frac{\kappa + 1}{2m - \epsilon}\left(\frac{U_0}{r_c}\right). \tag{28}$$

In this case the correction due to spin–orbit interaction is given by the second term in the right hand side of equation (28). When $l = 0$, then $\kappa = -1$ and the correction due to spin–orbit interaction equals zero.

References

1. G. B. Smith and L. J. Tassie, Ann. of Phys., *65*, 352, 1971.
2. A. A. Khilashvili, Teor. i. Mat. Fiz., USSR, *51*, 201, 1982; L. D. Miller, Ann. of Phys., *91*, 40, 1975.
3. M. G. do Amaral and N. Zagury, Phys. Rev., *27D*, 2668, 1983.
4. M. Abramovitz and I. A. Stegun, Handbook of Mathematical Functions, Naúka, Moscow, 1979.
5. A. I. Akhiezer and V. B. Berestecky, Quantum Electrodynamics, John Wiley and Sons, New York, 1963.

Acta Physica Hungarica 71 (1–2), pp. 67–76 (1992)

LATTICE DYNAMICAL STUDY OF SOME fcc METALS

M. K. MISHRA

Department of Physics, D. A. V. College
Kanpur, India

A. K. BAJPAI

Department of Physics, R. B. S. College
Kanpur, India

and

R. P. S. RATHORE

Department of Physics, R. B. S. College
Agra, India

(Received in revised form 26 February 1991)

The Morse potential is modified to determine the two and three body forces in consistent manner. These forces are employed to build up the dynamical matrix, which predicts the qualitative features of phonon dispersion in some of the face centered cubic (fcc) metals.

1. Introduction

Incorporation of wave vector dependent dielectric screening in microscopic theories [1–2] for phonon dispersion in fcc metals appears to be inadequate in view of its dependence [3] on phonon frequency as well. The microscopic model given by Animalu [4] does not account for the three-body forces, which affect the phonon dispersion decisively. The three-body forces reported by Upadhyay and Prakash [5] do influence dominantly only transverse branches. Further, the determination of models of these forces is with a certain degree of ambiguity. The study due to Sarkar et al [6] makes use of energy dependent HA [7] potentials, which does not account for the repulsive forces, which contribute significantly to recent forms [8–10] of the model potential. These latter forms [8–10], however, lack miserably the inclusion of the three-body forces and combine the short range repulsive and attractive forces with the long-range Coulomb forces.

Most of the phenomenological models [11–12] add up the short range ion–ion and long range electron–ion forces. The latter forces are commonly given by the Krebs scheme [13] which suffers with the deficiency of crystal inequilibrium [14] and does not account for proper dielectric screening.

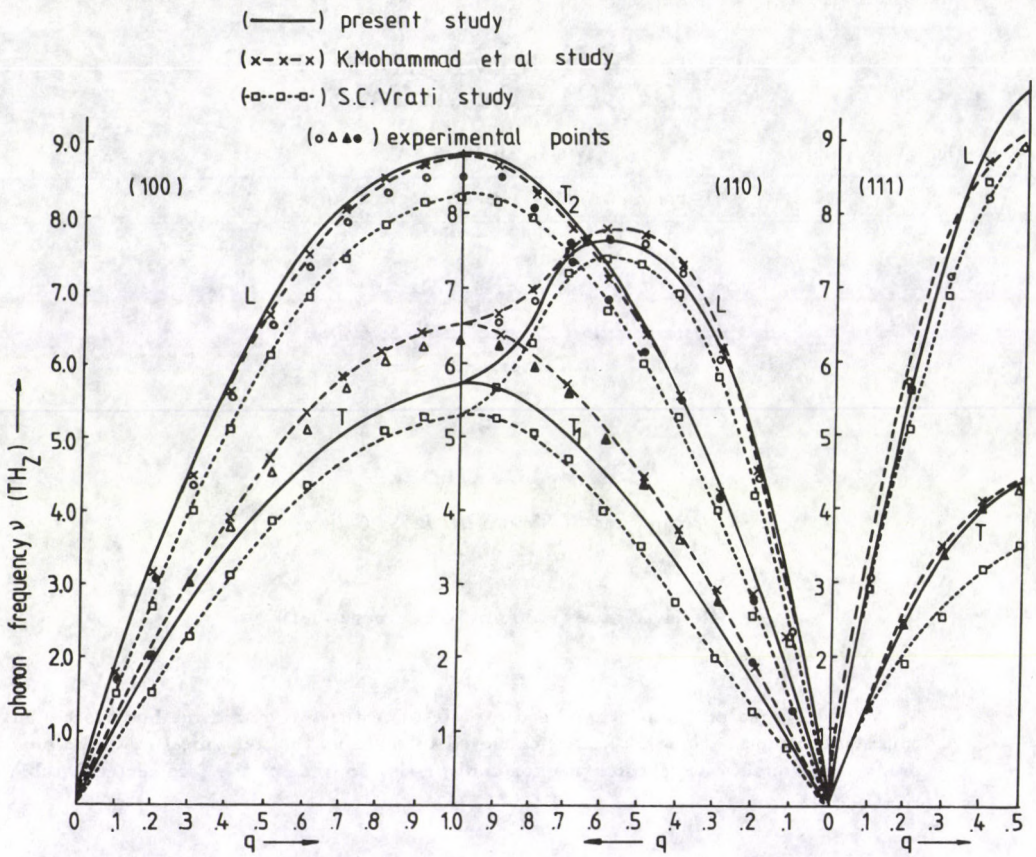

Fig. 1. Phonon dispersion curve for nickel

The lattice dynamical studies [15] prove emphatically the role of three-body forces in coupling the nearby neighbours. For bringing about a logical consistency in deriving the two- and three-body forces, we have chosen the Morse potential [16], which is modified for explaining the reasonable bindings of the fcc metals. The dynamical matrix so developed is employed to predict the phonon dispersion in some of the fcc metals.

2. Theory

2.1 Three-body potential

The response of the loosely coupled electrons towards the ionic displacement necessitates the inclusion of three-body forces into the system. For this purpose the

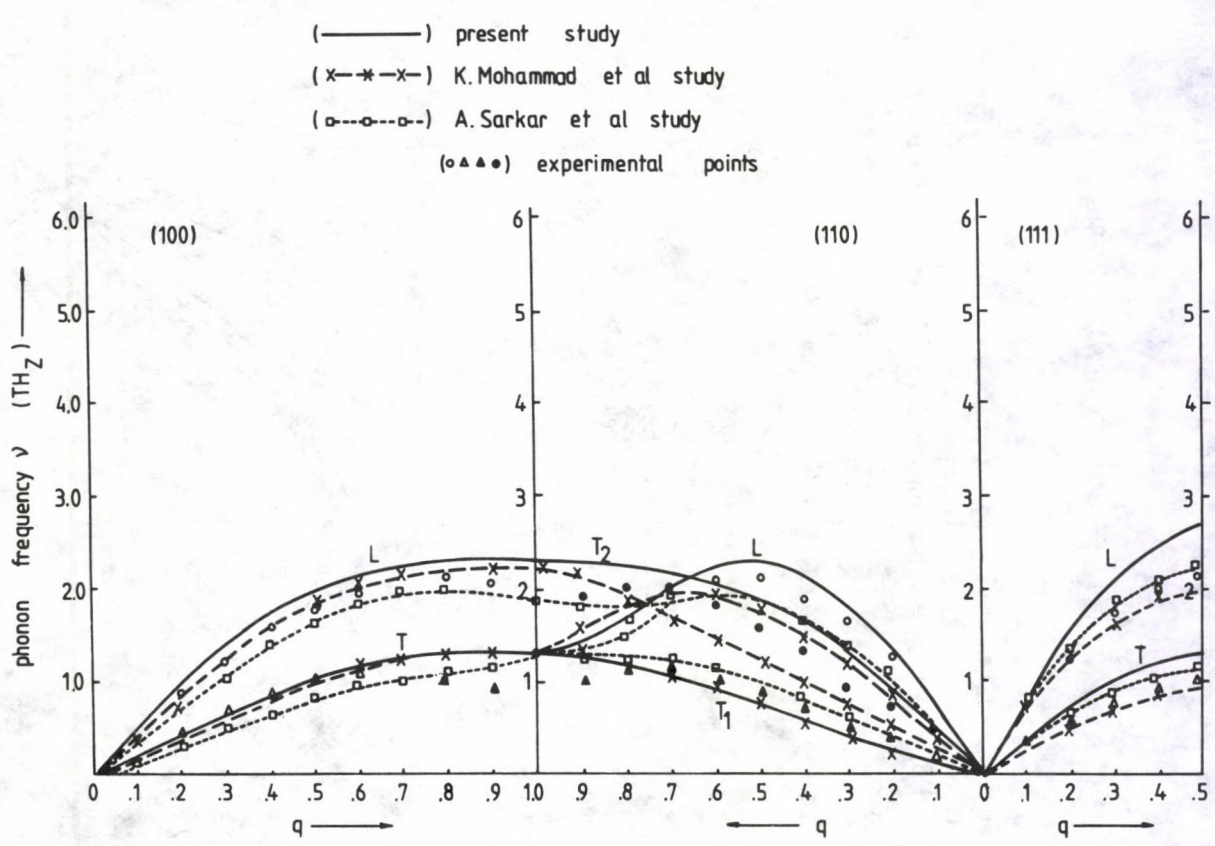

Fig. 2. Phonon dispersion curve for lead

effect of the third common nearest (l'', k'') neighbour into the coupling of the atom (l', k') with the atom (l, k) is considered. The trio considered here are located on the vertices of an equilateral triangle. The Morse [16] potential modified to represent the three-body interaction among the said atoms (l, k), (l', k') and (l'', k'') assumes the form

$$\phi^{(3)}(r_1, r_2) = \sum_{\substack{l',k' \\ l'',k''}}^{1} \sum_{l,k} \frac{A(k)}{2} [\beta^2 \exp\{-2\alpha(r_1 + r_2)\} - 2\beta \exp\{-\alpha(r_1 + r_2)\}], \quad (1)$$

where r_1 and r_2 are the respective separations of the atoms (l', k') and (l'', k'') from the atom (l, k), $A(k)$ the three-body parameter, α measures the hardness of the potential and β, a parameter depending on the equilibrium separation r_0, may be written as

$$\beta = \exp(\alpha r_0). \quad (2)$$

The prime on first summation in Eq. (1) means $(l', k') \neq l'', k''$.

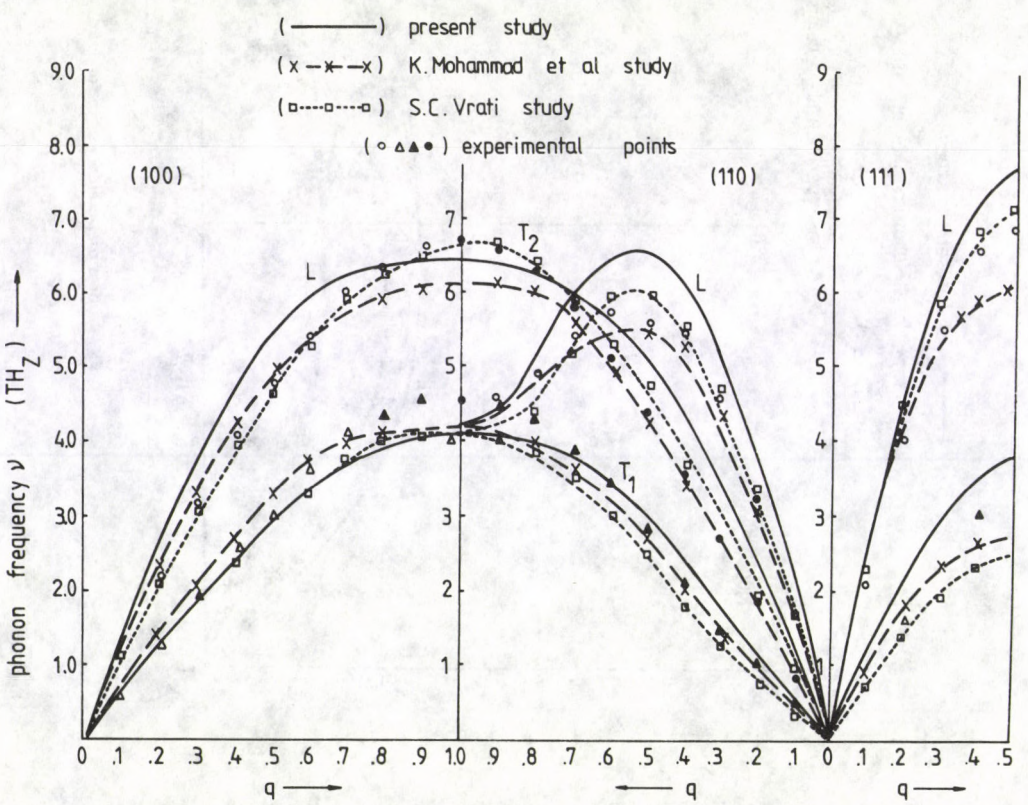

Fig. 3. Phonon dispersion curve for palladium

2.2 The two-body Morse potential

Morse has expressed the two-body potential energy $\phi_{r_J}^{(2)}$ per atom as

$$\phi_{r_J}^{(2)} = \frac{D}{2} \sum [\exp\{-2\alpha(r_J - r_0)\} - 2\exp\{-\alpha(r_J - r_0)\}], \tag{3}$$

where D is the dissociation energy of the pair and r_J the distance of Jth atom from the origin which may be given as

$$r_J = (m_J^2 + n_J^2 + l_J^2)^{1/2} a = M_J a, \tag{4}$$

where (m_J, n_J, l_J) are integers representing the co-ordinates of the Jth atom of the lattice and a the semi lattice constant.

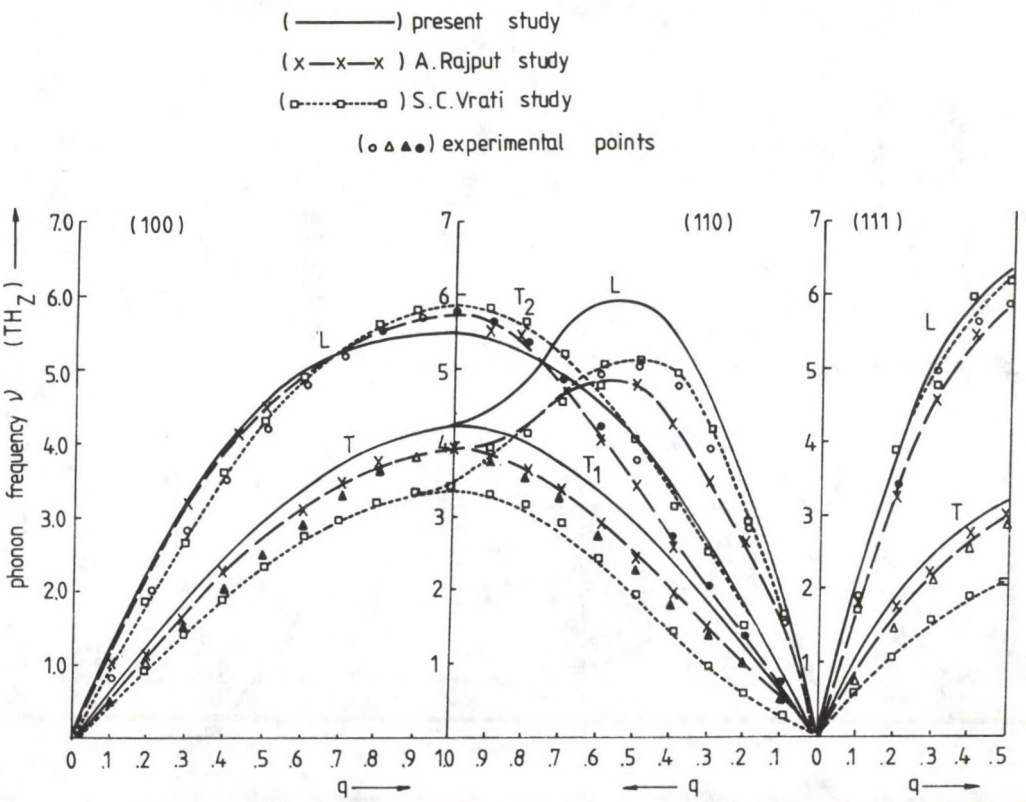

Fig. 4. Phonon dispersion curve for platinum

2.3 The dynamical matrix

The three-body potential $\phi^{(3)}(r_1, r_2)$ is first used to build up the dynamical matrix. The usual procedure leads to the following diagonal and off-diagonal elements of the matrix, i.e.

$$D^{(3)}_{\alpha'\alpha'}(\mathbf{q}) = 4\beta_3[4 - 2C_{2\alpha'} - C_{\alpha'}(C_{\beta'} + C_{\gamma'})],$$
$$D^{(3)}_{\alpha'\beta'}(\mathbf{q}) = 4\beta_3[C_{\alpha'}(C_{\beta'} + C_{\gamma'}) - 2], \tag{5}$$

where β_3 is the second derivative of $\phi^{(3)}(r_1, r_2)$, $C_{\alpha'} = \cos\frac{(aq\alpha')}{2}$ and $C_{2\alpha'} = \cos(aq\alpha')$.

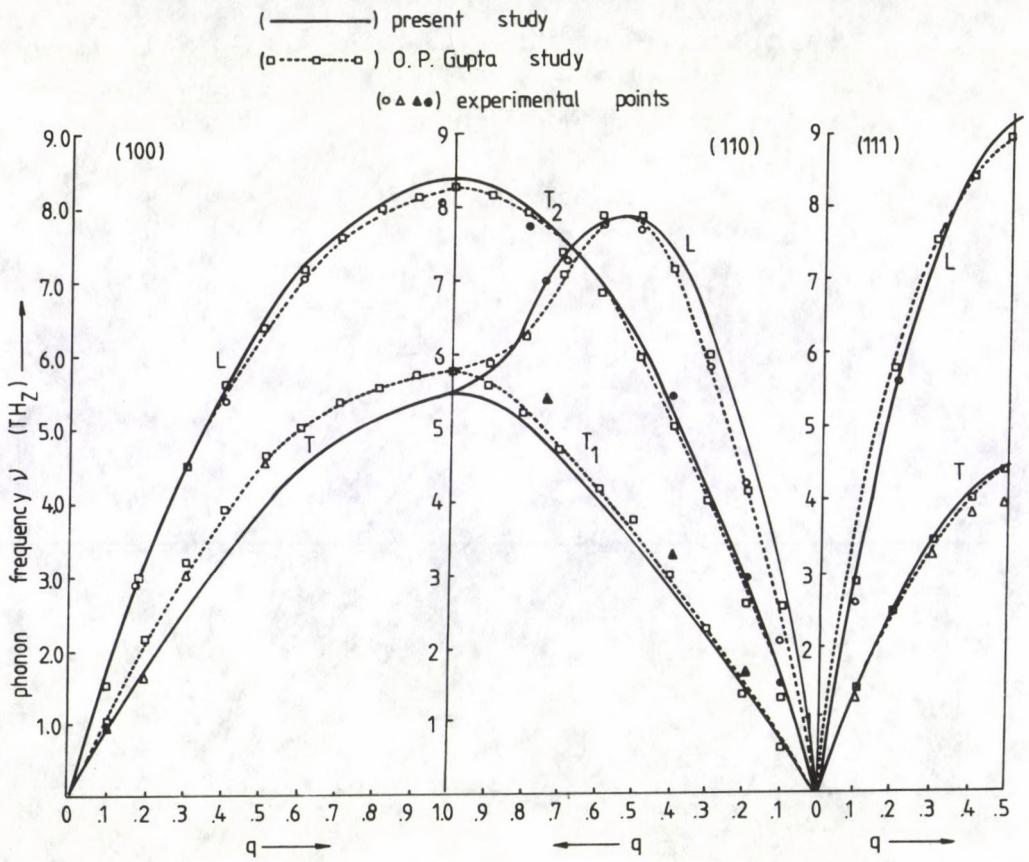

Fig. 5. Phonon dispersion curve for cobalt

The two-body potential accordingly describes the following contribution to the dynamical matrix

$$\begin{aligned} D^{(2)}_{\alpha'\alpha'}(\mathbf{q}) =& 4(\beta_1 + 2\alpha_1) - 2(\beta_1 + \alpha_1)C_{\alpha'}(C_{\beta'} + C_{\gamma'}) \\ & - 4\alpha_1 C_{\beta'} C_{\gamma'} + 4\beta_2 S^2_{\alpha'} + 4\alpha_2(S^2_{\beta'} + S^2_{\gamma'}), \qquad (6) \\ D^{(2)}_{\alpha'\beta'}(\mathbf{q}) =& 2(\beta_1 - \alpha_1)S_{\alpha'} S_{\beta'}, \end{aligned}$$

where $S_{\alpha'} = \sin(\frac{aq\alpha'}{2})$, α_1, α_2 are the first derivatives of the potential coupling the first and second neighbours and β_1, β_2 the second derivative.

The phonon frequencies (ν) are obtained by solving the usual secular equation, i.e.

$$D_{\alpha'\beta'}(\mathbf{q}) - 4\pi^2\nu^2 mI = 0, \qquad (7)$$

where m is the mass of the atom, I is the unit matrix of 3×3 order and $D_{\alpha'\beta'}$ is the total dynamical matrix.

3. Computations and results

We have considered the two-body coupling extending to the eigth neighbour of the fcc structure, i.e. 140 atoms. The three parameters defining the two-body potential $\phi^2(r_j)$ are evaluated by the knowledge of the equilibrium lattice constant, cohesive energy and bulk modulus ($k^{(2)}$) of the solid by the procedure laid down by Girifalco and Weizer [17]. The three-body parameter $A(k)$ is evaluated from the knowledge of measured Cauchy discrepancy in the second order elastic constants. Table I shows the input data needed for the four potential parameters ($D, \alpha, r_0, A(k)$) and force constants ($\alpha_1, \alpha_2, \beta_1, \beta_2, \beta_3$) which are enlisted in Table II for the metals under study, i.e. Ni, Pb, Pt, Co and Th.

4. Conclusion

We have drawn the dispersion curves for Ni, Pb, Pd, Pt, Co and Th (Figs 1–6). We have compared the phonon dispersion in Ni (Fig. 1) to those reported experimentally by Bergenau et al [24] and theoretically by Mohammad et al [12] and Vrati [25]. It may be seen that our results agree more closely to the experimental findings as compared to other mentioned above. The experimental data [26] on Pb have been compared with our results (Fig. 2) and also with theoretical findings of Mohammad et al [12] and Sarkar et al [6]. Our results deviate near the zone boundaries. These deviations are common in other theoretical studies [12]. The neutron scattering data [27] on Pd exhibit general agreement with our results (Fig. 3). The theoretical findings due to Mohammad et al [12] dip down while that of Vrati [25] rise up especially near the zone boundary in all the symmetry directions. Our results in Pt (Fig. 4) show slight deviations over the experimental data

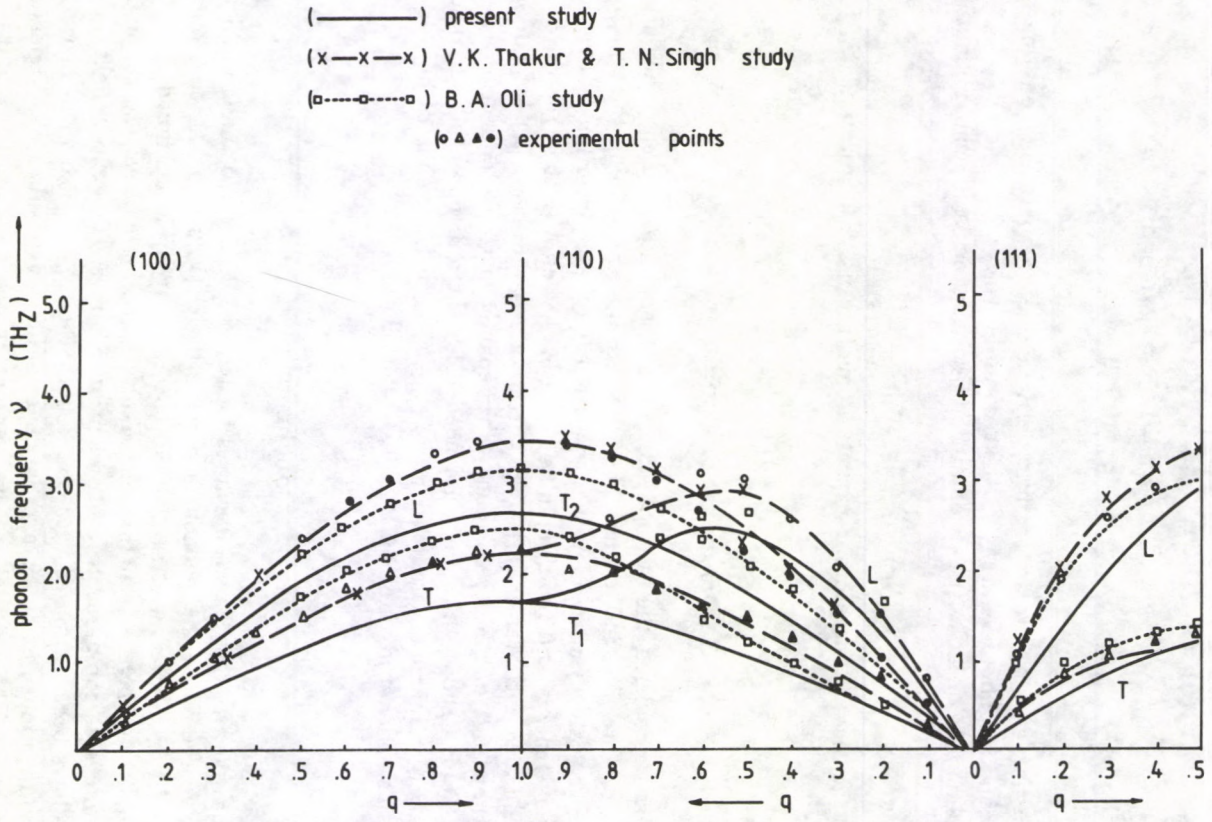

Fig. 6. Phonon dispersion curve for thorium

Table I
Input data for fcc metals

Metals	Bulk modulus (ionic) $\times 10^{11}$ N/m^{-2}	Cohesive energy (ϕ) $\times 10^{-19}$ J	Semi lattice constant $\times 10^{-10}$ m	Measured Cauchy discrepancy $\times 10^{11}$ N/m^{-2}	Reference to the measured Cauchy discrepancy
Ni	1.571	7.104	1.760	0.265	Rayne [18]
Pb	0.173	3.248	2.475	0.273	Kittel [19]
Pd	0.887	6.224	1.945	1.043	Allers et al [20]
Pt	1.085	9.344	1.960	1.742	Macfarlane [21]
Co	1.486	7.024	1.775	0.230	Sapiro and Moss [22]
Th	0.566	9.920	2.540	0.011	Aurad [23]

Table II
Computed potential parameters and force constants

Metals	D $\times 10^{-19}$J	α $\times 10^{10}$m	r_0 $\times 10^{-10}$m	$A(k)$ $\times 10^{-19}$J	α_1 $\times$N/m^{-1}	α_2 $\times$N/m^{-1}	β_1 $\times$N/m^{-1}	β_2 $\times$N/m^{-1}	β_3 $\times$N/m^{-1}
Ni	0.584	1.228	2.855	−0.436	−2.560	0.500	29.520	−0.450	0.410
Pb	0.182	0.671	4.387	−0.107	−0.510	0.050	03.910	−0.210	0.540
Pd	0.453	1.018	3.242	−2.115	−1.790	0.290	17.790	+0.080	1.750
Pt	0.569	0.895	3.405	−3.387	−2.470	0.300	20.320	+0.750	2.820
Co	0.566	1.201	2.892	−0.342	−2.490	0.470	27.840	−0.340	0.320
Th	0.647	0.722	4.346	−0.013	−1.610	0.220	14.170	+0.340	0.006

[28] at the zone boundary. The theoretical results of Rajput [29] deviate upwardly while those of Vrati [25] deviate downwardly with the experimental findings. Our predictions in Co (Fig. 5) follow closely the experimental data [22]. The theoretical findings of Gupta [32], however, exhibit deviations with the experimental findings. Our predictions in Th (Fig. 6) show downward deviations with respect to the experimental findings [30]. The theoretical findings of Thakur and Singh [31] and Oli [33], however, incorporate more explicitly the response of conduction electrons and therefore give rise to fair agreement with the experimental findings.

References

1. W. R. Hanke, Phys. Rev., *8*, 4591, 1973.
2. J. Singh, H. Singh and S. Prakash, Phys. Rev., *B-18*, 2954, 1978.
3. G. Mukhopadhyay, IC/148, International Centre for Theoretical Research, preprint, 1987.
4. A. O. E. Animalu, Phys. Rev., *B-8*, 3542 and 3555, 1973.
5. J. C. Upadhyay and D. Prakash, Phys. Rev., *B-33*, 1416, 1986.
6. A. Sarkar, D. Sen and S. Sen Gupta, Pramana, *26*, 231, 1986.
7. V. Heine and I. Abarenkov, Philos. Mag., *9*, 451, 1964.
8. S. Nand, H. C. Gupta and B. B. Tripathi, Phys. Lett., *70A*, 241, 1979.
9. O. P. Kulshretha, J. C. Upadhyay and H. C. Gupta, Solid Stat. Commun., *17*, 291, 1975.
10. S. C. Vrati, N. Rani, D. K. Gupta and H. C. Gupta, Phys. Lett. *64A*, 333, 1977; Phys. Lett. *74A*, 139, 1979.
11. H. Closs and M. M. Shukla, Nuovo Cimento, *42B*, 213, 1977.
12. K. Mohammad, M. M. Shukla, F. Milstein and J. L. Merz, Phys. Rev., *B-29*, 3117, 1987.
13. K. Krebs, Phys. Rev., *138*, 148, 1965.
14. W. Cochran, Acta Crystal, *A27*, 557, 1971.
    L. Cheveau, Phys. Rev., *169*, 495, 1968.
    C. S. Hentecler and M. N. de-Meveryneis, Proc. Inelast. Scattering of Neutrons in Solids and Liquids, IAEA, Vienna, Vol. I, p. 153, 1968.
15. C. M. Bertoni, V. Bartolani, C. Calandra and F. Nizzoli, J. Phys., *F-4*, 19, 1974.
16. P. A. M. Morse, Phys. Rev., *34*, 57, 1929.
17. L. A. Girifalco and V. G. Weizer, Phys. Rev., *114*, 687, 1959.
18. J. A. Rayne, Phys. Rev., *95*, 1428, 1954.
19. C. Kittel, Introduction to Solid State Physics, John Wiley and Sons, New York, p. 149.
20. G. A. Allers, J. H. Neighbours and H. Sato, Bull. Amer. Phys. Soc., *4*, 131, 1959.
21. R. F. Macfarlane, J. A. Rayne and C. K. Jones, Phys. Lett. (A), *18*, 91, 1965.
22. S. M. Sapiro and S. C. Moss, Phys. Rev., *B-15*, 2726, 1977.
23. S. Aurad, International Tables for Selected Constants, Pergamon Press, Oxford, 1969.
24. R. L. Bergeneau, J. Cordes, G. Dolling and A. D. B. Woods, Phys. Rev., *136*, 1359, 1965.
25. S. C. Vrati, Agra University, Thesis, 1980.
26. A. Furrer and W. Holg, Phys. Stat. Sol., *42*, 821, 1970.
27. A. P. Miller and B. N. Brochouse, Can. J. Phys., *49*, 704, 1971.
28. D. H. Dutton, B. N. Brochouse and A. P. Miller, Can. J. Phys., *50*, 2915, 1972.
29. A. Rajput, Phys. Stat. Sol., (b) *128*, 411, 1985.
30. R. A. Reese, S. K. Sinha and D. T. Peterson, Phys. Rev., *128*, B-8, 1332, 1973.
31. V. K. Thakur and T. N. Singh, Phys. Stat. Sol. (b), *138*, 1407, 1986.
32. O. P. Gupta, Sol. Stat. Commun., *42*, 31, 1982.
33. B. A. Oli, J. Phys. *F-8*, 2441, 1978.

Acta Physica Hungarica 71 (1-2), pp. 77-87 (1992)

LASER-ASSISTED NUCLEAR PROCESSES

P. KÁLMÁN

Department of Experimental Physics, Institute of Physics
Technical University of Budapest
1521 Budapest, Hungary

(Received 28 February 1991)

The theory of the problem of the direct effect of intense laser field on nuclear gamma and beta decays is briefly summarized. The laser-assisted internal conversion process and electronic-bridge mechanism, which seem to be candidate processes where the intense field can modify nuclear transitions, are treated in one model. As their characteristics near the threshold and near a resonance have special interest they are investigated in more detail. The recent results on laser-assisted alpha decay are also discussed.

1. Introduction and historical review

Shortly after the appearence of optical lasers efforts have been made to use them for modifying nuclear processes. Most of these early works are related to the gamma-ray laser (graser) problem and are well summarized in the review paper of Baldwin et al [1]. The application of the laser in other nuclear processes, such as laser-induced nuclear orientation, isotope and isomer separation etc. were also reviewed at the end of the 70's [2].

A decade ago the Albuquerque group suggested using the laser for the enhancement of nuclear beta decay of ^{3}H enlarging the phase space of the outcoming electron by an extremely intense laser [3]. The proposed experiment was criticized by Reiss [4]. Two years later Reiss predicted the enhancement of nuclear beta decay by intense low-(radio)-frequency radiation field [5]. The articles of Reiss were followed by a debate between the two groups on the possibility of enhancement of nuclear decays by means of intense radiation fields of optical or lower frequencies [6]. The problem is closely related to the question, how one has to discuss matter–radiation field interaction and in what manner one has to treat gauge transformations in a calculation without violating gauge invariance [7]. Finally both parts came to the same conclusion, namely that enhancement is generally not possible [8].

The main reason for this conclusion can be understood from the

$$H_1 = e \sum_{p=1}^{Z} \mathbf{x}_p \cdot \mathbf{E}_L(t) \tag{1}$$

form of the interaction Hamiltonian, which is given in the Göppert–Mayer gauge, where $\mathbf{x}_p$ denotes the proton coordinates and $\mathbf{E}_L(t)$ stands for the electric field

strength of the laser field. A simple, order of magnitude analysis shows that the coupling of two nuclear states by the interaction given by Eq. (1) is weak at the laser intensities available nowadays. The nuclear dimensions are in the order of $2 - 10 \times 10^{-13}$ cm and the electric field strength of the laser is $E_L \sim 40\, I^{1/2}$, where I is given in W/cm^2 units. Thus, the magnitude of matrix elements of H_1 is about $10^{-12} - 10^{-13} \times I^{1/2}$ eV. The energy differences generally encountered are larger than 1 keV, thus the coupling strength can be estimated as $10^{-15} - 10^{-16} \times I^{1/2}$ in an optimum case. Moreover, the shielding of the laser beam by the electron cloud at the nucleus is strong for a neutral atom because the centre of mass remains fixed causing large atomic response [9]. This fact further decreases the possibility of the direct modification of nuclear decays by intense laser beams.

However, a special case, the case of $O^+ \rightarrow O^+$ transitions, which is forbidden for direct gamma emission seemed to be appropriate for the demonstration of the effect of laser radiation on nuclear γ-transitions [10]. In a two step process the nucleus can emit a γ-photon and can emit or absorb a laser photon. The process takes place through an intermediate state. It was shown contrary to the earlier statement [11] that the intermediate state is not located very close to the initial one but it is a giant resonance built up the initial, isomeric state. However, even this two step process needs extremely high laser intensities. Spontaneously the laser-free decay also takes place partly by two photon emission. In the presence of the laser one can expect an enhancement in that channel of the two photonic decay, for which the energy of one of the outcoming photons equals that of a laser photon [12].

We want only to mention that enhancement of the low-energy neutron absorption cross section in intense radiation field was also predicted [13] but the magnitude of the calculated enhancement was quired [14].

However, modifications of nuclear processes can be expected if a characteristic energy of the process is comparable to the laser photon energy. As the laser–electron interaction is stronger than the laser–nucleon one it is more promising to find some effect of the laser radiation on combined electronic–nuclear processes, e.g. on internal conversion and on electronic bridge mechanism. Moreover, the condition mentioned above is easier to fulfil in the laser-assisted internal conversion near the threshold and in the laser-assisted electronic bridge mechanism near a resonance.

Before dealing with these processes in more detail, we mention that the inverse processes, i.e. the coupling of laser radiation to nuclei via collective electronic oscillations driven by the laser radiation [15] and the possibility of nuclear excitation by laser-driven electronic motion in strong laser field [16] have been investigated recently also in connection with the graser problem [17].

Nuclear γ-deexcitation with an energy a little less than the energy difference of two bound states in the electronic shell can be drastically modified in the presence of an intense laser field. In the process, which is called laser-assisted electronic-bridge mechanism, the nuclear excitation energy is transferred to an electronic excitation, which leads to the emission of an X-ray photon. The mechanism can be amplified in the laser field if the condition of N-photonic resonance fulfils.

The first experimental observation of the normal laser-free electronic-bridge mechanism has been reported recently [18]. This process is a third order one and

takes place in the following manner. In consequence of the nuclear deexcitation one electron of the atom becomes excited, leaves the atom, furthermore, an X-ray is emitted. Thus the energy of the nuclear transition is converted to the energy of the outcoming electron and X-ray. The process is similar to the internal conversion one but in the electronic bridge mechanism X-ray is also emitted.

Here we deal with a special type of laser-assisted electronic-bridge mechanism. We investigate those processes, where the energy of the γ-transition is nearly resonant to one of the bound–bound electronic transitions, but the energy defect is equal to a small integer times the photon energy of the applied intense laser beam. In our process the initial and final electronic states are the same. The three steps of the process are nuclear deexcitation, electron excitation into a dressed state and electron transition to the initial state by X-ray emission. The intermediate electronic state, which is also bound, is strongly modified by the intense laser [19] and therefore it is called a dressed state. We deal with resonant processes only, i.e. with those, in which the sum of the energies of the γ-photon and that of a few laser-photons is equal to one of the energies of the possible bound–bound electronic transitions.

2. Simple model of laser-assisted internal conversion and electronic-bridge processes

Now we treat the problem of laser-assisted internal conversion [20,21,22] and laser-assisted electronic bridge mechanism [23] in one model. We restrict our consideration to near the threshold in case of internal conversion and to near a bound–bound electronic resonance in case of electronic-bridge mechanism, as noticeable changes are expected in these cases only.

We use a very simple model for the description of electron–nucleus interaction. The total Hamiltonian of the system can be written as

$$H = H_0 + H_1 + H_2 + H_3, \tag{2}$$

where

$$H_0 = -\frac{\hbar^2}{2\mu}\nabla^2 - \frac{Ze^2}{r} + H_N, \tag{3}$$

$$H_1 = e\mathbf{r} \cdot \mathbf{E}_L(t), \tag{4}$$

$$H_2 = \frac{Ze^2}{r} - \sum_{p=1}^{Z} \frac{e^2}{|\mathbf{r} - \mathbf{x}_p|} \tag{5}$$

and

$$H_3 = e\mathbf{r} \cdot \mathbf{E}_x(t). \tag{6}$$

Here the following notation is used: μ is the rest mass of the electron, Z is the proton number of the nucleus, $\mathbf{r}$ stands for the electron coordinate, $\mathbf{E}_L(t)$ is the

electric field strength of the laser radiation, which is treated classically and has the form

$$\mathbf{E}_L(t) = E_0 \hat{\mathbf{e}}_3 \sin(\omega t) \tag{7}$$

in the case of linear polarization and

$$\mathbf{E}_L(t) = E_0[\hat{\mathbf{e}}_1 \sin(\omega t) + \hat{\mathbf{e}}_2 \cos(\omega t)] \tag{8}$$

in the case of circular polarization. E_0 and ω are the amplitude and the angular frequency of the laser radiation, $\hat{\mathbf{e}}_1$, $\hat{\mathbf{e}}_2$ and $\hat{\mathbf{e}}_3$ are unit vectors perpendicular to each other and define the frame of reference. H_N is the nuclear Hamiltonian,

$$\mathbf{E}_x(t) = i \sum_{\omega_X, \mathbf{E}} \left(\frac{2\pi\hbar\omega_X}{V} \right)^{1/2} \vec{\varepsilon}(a e^{-i\omega_X t} - a^+ e^{i\omega_X t}) \tag{9}$$

describes the quantized X-ray field. $\hbar\omega_X$ is the X-ray photon energy, $\vec{\varepsilon}$ determines the state of linear polarization, a and a^+ are the photon annihilation and creation operators and V is the volume of normalization. H_1 describes the laser–electron interaction, H_2 is a very simple model Hamiltonian for the electron–nucleus interaction [24] and H_3 represents the interaction of the electron and the quantized electromagnetic field, and describes X-ray emission.

The evolution of the many electron system is approximated by the evolution of one electron, but the effect of other electrons is taken into account by using effective nuclear charges $Z_{\text{eff}}(n)$ in the one electron eigensolutions of H_0.

3. Nonresonant, laser-assisted internal conversion process

First we discuss the non resonant, laser-assisted internal conversion process. The initial electronic state has the form

$$\psi_i = \varphi_0(\mathbf{r}) e^{-i\varepsilon_0 t}, \tag{10}$$

where $\varphi_0(\mathbf{r})$ is a hydrogen-type solution of quantum numbers k, l_0, m_0 and of energy $E_0 = \hbar\varepsilon_0$, the final electronic state is a so called Coulomb–Volkov solution [25] of the form

$$\psi_f = u^{(-)}(\mathbf{r}, \mathbf{q}) e^{ie\mathbf{A}(t)\cdot\mathbf{r}/\hbar c} e^{[-i\int^t (\hbar\mathbf{q} - e\mathbf{A}(t')/c)^2 dt'/2\mu\hbar]}, \tag{11}$$

where $u^{(-)}(\mathbf{r}, \mathbf{q})$ is a Coulomb function [26], $\hbar\mathbf{q}$ is the momentum of the outcoming electron, the vector $\mathbf{A}(t)$ is defined

$$\mathbf{A}_{\text{lin}}(t) = -(cE_0/\omega)\hat{\mathbf{e}}_3 \cos(\omega t) \tag{12}$$

in the case of linear state of polarization and

$$\mathbf{A}_{\text{circ}}(t) = -(cE_0/\omega)[\hat{\mathbf{e}}_1 \sin(\omega t) - \hat{\mathbf{e}}_2 \cos(\omega t)] \tag{13}$$

in the case of circular state of polarization of the laser. The final state is valid only if the

$$\hbar q \gg eE_0/\omega \tag{14}$$

condition holds [25a]. We work in the electric field gauge.

The S-matrix element of the nonresonant process can be written as [20]

$$S_{\mathrm{fi}} = (i\hbar)^{-1} \int dt \int d^3r \int d\tau < f(t)|H_2|i(t) >, \tag{15}$$

where $|i(t) >= \psi_1 |a(t) >$ is the initial state with

$$|a(t) >= |a > e^{-i\varepsilon_a t} \tag{16}$$

and $|f(t) >= \psi_f |b(t) >$ is the final state with

$$|b(t) >= |b > e^{-i\varepsilon_b t}, \tag{17}$$

$|a >$ and $|b >$ denote the space dependent parts of the nuclear initial and final states (a) and (b) whose energies $E_a = \hbar\varepsilon_a$ and $E_b = \hbar\varepsilon_b$, respectively, and $d\tau$ refers to the integration over the proton coordinates. $E_a - E_b = \hbar\omega_{ab}$ is the transition energy.

We investigate inner shells and the laser can have intermediately high intensity because of condition (14). The extension of the initial electronic state determines a characteristic volume, that has to be taken into account in the integration over $\mathbf{r}$ in Eq. (15) and which is generally small enough for the $e^{ie\mathbf{A}(t)\mathbf{r}/\hbar c} = 1$ approximation to be made in it. Thus the effect of the laser remains in the time-dependent factor of Eq. (11) and the space- and time-dependent parts of the S-matrix element can be separated. We can recognize that the space dependent part is the same as in the laser-free case, which fact provides the possibility of the simplified structure of the laser-assisted internal conversion coefficient given below.

Using the Jacobi–Anger formula [27] (circ case) and the definition and properties of the generalized Bessel functions [28] (lin case) after some algebra, and dividing the transition probability per unit time of the process by the gamma transition rate we obtain the following form for the laser-assisted internal conversion coefficient (LA-ICC) $\alpha^{L,\mathrm{las}}_{k,j,l_0}$ of a transition of multipolarity L and for an electronic state of quantum numbers k, j, l_0

$$\alpha^{L,\mathrm{las}}_{k,j,l_0} = \sum_{N>-r} \alpha^{\mathrm{free}}_{k,j,l_0}(q_N) T(b_N), \tag{18}$$

where $T(b_N) = \{T_{\mathrm{circ}}(b_N) \text{ or } T_{\mathrm{lin}}(b_N)\}$ with

$$T_{\mathrm{circ}}(b_N) = \frac{1}{2b_N} \int_0^{2b_N} J_{2|N|}(x)dx = \int_0^{\pi/2} J_N^2(b_N \sin\vartheta) \sin\vartheta d\vartheta \tag{19}$$

and

$$T_{\rm lin}(b_N) = \int_0^1 J_N^2(b_N x, -d/4)dx. \tag{20}$$

Here $\alpha^{\rm free}_{k,j,l_0}(q_N)$ is the laser-free ICC at $q = q_N$; k, j, l_0 are the principle, the total and the orbital angular momentum quantum numbers of the electronic state; L is the multipolarity of the gamma transition;

$$q_N = [(N + r_0)\hbar\omega/R_y]^{1/2}/a_B; \tag{21}$$

$R_y = e^2/2a_B$; a_B is the Bohr radius; $r = r_0 - d_{\rm pol}$; $r_0 = \Delta/\hbar\omega$; $\Delta = E_0 + \hbar\omega_{ab}$; $J_{2|N|}(x)$ is a Bessel function of the first kind; N is an integer; $d_{\rm pol} = \{d_{\rm circ}$ or $d_{\rm lin}\}$ with

$$d_{\rm circ} = d,\ d_{\rm lin} = d/2,\ d = e^2E_0^2/2\mu\hbar\omega^3, \tag{22}$$

$$b_N = eE_0q_N/\mu\omega^2 = b_0(N + r)^{1/2}, \tag{23}$$

with $b_0 = 1.07 \times 10^{-6} \times I^{1/2}(\hbar\omega)^{-3/2}$, I is the intensity of the laser in W/cm^2 and $\hbar\omega$ is in units of eV.

Near the threshold Eq. (18) can be approximated as

$$\alpha^{L,{\rm las}}_{k,j,l_0} = \alpha^{L,{\rm Th}}_{k,j,l_0}T, \tag{24}$$

where $\alpha^{L,{\rm Th}}_{k,j,l_0}$ is the threshold value of the laser-free ICC, $T = \{T_{\rm circ}$ or $T_{\rm lin}\}$,

$$T_{\rm circ} = \sum_{N>-r} T_{\rm circ}(b_N), \tag{25}$$

$$T_{\rm lin} = \sum_{N>-r} T_{\rm lin}(b_N), \tag{26}$$

$T_{\rm circ}$ and $T_{\rm lin}$ depend on r_0 and b_0 only. Their curves were computed and published for different values of parameters in papers dealing with laser-assisted X-ray absorption [29].

4. Laser-assisted, resonant electronic-bridge mechanism

Now we turn to the problem of laser-assisted electronic-bridge process. The motion of the bound electron under the joint action of the Coulomb and laser fields is described by the wave function Ψ, which can be approximately written in a given subshell of principal quantum number n as [19]

$$\Psi(nn_1n_2m) = \Phi_{n_1n_2m} \sum_{N=-\infty}^{\infty} J_N(\lambda_{n_1n_2})e^{-i(E_n+N\hbar\omega)t/\hbar}, \tag{27}$$

where $\Phi_{n_1 n_2 m}$ is a hydrogen-type solution in parabolic coordinates and J_N denotes a Bessel function of first kind, N is an integer, which corresponds to the absorbed or emitted number of laser photons, $E_n = \hbar\varepsilon_n - i\hbar\gamma_n/2$ is the complex energy of the intermediate electronic state and

$$\lambda_{n_1 n_2} = \frac{3/2n(n_1 - n_2)E_0 e a_B}{Z_{\text{eff}}\hbar\omega}. \tag{28}$$

Here n is the principal quantum number of the subshell, $n = n_1 + n_2 + |m| + 1$, m is the magnetic quantum number and n_1, n_2 are the parabolic quantum numbers [30]. We use the λ abbreviation further on.

The electronic Green function of the laser–Coulomb problem in this shell can be approximately written as [19]

$$G(t_2 - t_1) = -i\Theta(t_2 - t_1) \sum_{n_1 n_2 m} |\Psi(n n_1 n_2 m) >< \Psi(n n_1 n_2 m)|, \tag{29}$$

where Θ denotes the step function.

The S-matrix element governing the laser-assisted, resonant electronic-bridge process can be written as

$$S_{\text{fi}} = (i\hbar)^{-2} \int_{t_0}^{t} dt_2 \int_{t_0}^{t_2} dt_1 < f(t_2)|H_3(t_2)\times \tag{30}$$
$$\times\, |b(t_2) > |0\omega_X > G(t_2 - t_1) < 0\omega_X| < b(t_1)|H_2|i(t_1) >,$$

where

$$|f(t) >= \varphi_0(\mathbf{r})e^{-i\varepsilon_0 t}|b(t) > |1\omega_X >, \tag{31}$$

$$|i(t) >= \varphi_0(\mathbf{r})e^{-i\varepsilon_0 t}|a(t) > |0\omega_X > \tag{32}$$

are the final and initial states of the electron–nucleus–X-ray system, respectively, $|0\omega_X >$ and $|1\omega_X >$ are photon number states of angular frequency ω_X. The initial and final electronic states are the same. We suppose that φ_0 describes an inner state, thus the effect of the laser on this state can be neglected because of the shielding of the outer electrons, thus φ_0 is a hydrogenic type solution in the usual spherical coordinates. Furthermore, we introduce the following notations: $\omega_{\text{no}} = \varepsilon_n - \varepsilon_0$.

In Eq. (30) the cross term of the S-matrix element is neglected as we search for a resonance type process only. Furthermore, as in our simple model we use only H_2 for the description of electron–nucleus interaction the γ-photon exchange between the nucleus and the electron cloud does not appear in our formalism.

If we calculate the transition probability per unit time W_{fi}^{las} of the process [23] and introduce the quantity η, which is defined as $\eta = W_{fi}^{\text{las}}/W_{fi}^{\text{spont}}$, where W_{fi}^{spont} is the transition probability per unit time of the spontaneous γ-ray emission [24] and restrict ourselves to the $L = 1$ case discussed below we obtain

$$\eta = \frac{e^4}{27}\left(\frac{\omega_X}{\omega_{ab}}\right)^3 \frac{|J_{nk}|^2|I_{1,nk}|^2}{\Delta^2 + (\hbar\gamma_n/2)^2}\mathbf{F}_{(L=1)}, \tag{33}$$

where $\Delta = \hbar(\omega_{ab} - N\omega - \omega_{no})$ is the detuning,

$$J_{nk} = \int R_{ko}(Z_{\text{eff}}(k), r) R_{n1}(Z_{\text{eff}}(n), r) r^3 dr, \tag{34}$$

$$I_{L,nk} = \int R_{ko}(Z_{\text{eff}}(k), r) R_{nL}(Z_{\text{eff}}(n), r) r^{1-L} dr, \tag{35}$$

and

$$\mathbf{F} = \sum_K \left[\sum_{\mu_1,\mu_2,M} | < 1M|\mu_1\mu_2 > |^2 J_K(\lambda_{n_1,n_2}) J_N(\lambda_{n_1 n_2}) \right]^2 . \tag{36}$$

The energy of the X-ray photon is $\hbar\omega_X = \hbar(\omega_{ab} - N\omega + K\omega)$. For the sake of clarity we have denoted the different effective charges of the states of different principal quantum numbers in Eqs (34) and (35), where R_{k0} and R_{n1} are the radial parts of the hydrogen-type wave functions, furthermore $\mu_1 = (m + n_1 - n_2)/2$, $\mu_2 = (m - n_1 + n_2)/2$. The ratio η can characterize the yield of the laser-assisted, resonant electronic-bridge mechanism related to the spontaneous γ-decay.

Now we restrict ourselves to the isomeric state ^{183m}W, which has an E1 transition of energy 544 eV, and to the $4s^{1/2}(N_1)$ shell, which has binding energy of 592 eV, thus in this case the energy defect is -48 eV [31]. For this state and nuclear transition the $n = 6$ shell with binding energy of about 8 eV can be the intermediate state.

In the case of small laser intensity, i.e. $\lambda \ll 1$, the $K = 0$ order process will be dominant. If we use a laser of photon energy about 13.33 eV we have a third order ($N = 3$) process from the point of view of laser–atom interaction. The intensity of the laser is restricted to $I = 10^{15}$ W/cm^2. The other quantities we need are $J_{46} = 0.0175 a_B$, $I_{1,46} = 0.0122 a_B^{-2}$, which were obtained with hydrogen-type radial functions of $Z_{\text{eff}}/4 = 6.6$ and $Z_{\text{eff}}/6 = 0.766$, and $\hbar\gamma_n/2 = 3.9 \times 10^{-4}$ eV, which is estimated by the width of a $2p - 1s$ transition of the same energy [32]. So we obtain the estimation $\eta = 1.38$. Thus we can see that in the presence of an intense laser beam of appropriate angular frequency fulfilling the condition of resonance the transfer of the nuclear excitation energy through the electron bridge can become effective.

5. Laser-assisted α decay — a tool for determination of low-energy separation of near nuclear states

Finally we deal with the possibility of a special, laser-assisted α-decay process. In a recent article [33] for the energy separation Δ of two intrinsic states at the ground state of ^{229}Th nucleus 1 ± 4 eV but in any event almost less than 10 eV was reported. Here we propose a method, which seems to be capable of determining this difference more precisely with the aid of lasers. Earlier it was stated that the nowadays available intense lasers of optical and soft X-ray frequencies are not

appropriate to modify nuclear γ-transitions. While this statement is not questioned, but as the energy difference to be investigated is small enough we have the chance, as will be seen below, to modify the nuclear process in this special case.

A resonant-type process is discussed here. An experimentalist needs a better estimate of the energy difference given above for practical reasons in order to be able to tune the laser to the resonance as the resonance-type process has a very strong frequency requirement. But we have no idea now how to achieve this better approximation of the energy difference.

The levels investigated are connected with an $M1$ transition, thus we can use the interaction Hamiltonian

$$H_{\text{int}} = \mu \cdot \mathbf{B} = \mu_p B \hat{\mu} \hat{\mathbf{e}} \cos(\omega t) \tag{37}$$

describing the laser–nucleus interaction where μ_p is the Bohr magneton of the proton, B is the amplitude of the magnetic induction in the laser beam, ω and $\hat{\mathbf{e}}$ are the angular frequency and the unit vector parallel to the state of polarization of the laser, respectively and $\hat{\mu}$ is the magnetic dipole operator in μ_p units.

The transition probability W per unit time for a laser driven resonant process in one channel, i.e. the decay rate to one of the levels of the daughter nucleus, can be written as

$$W = W_0 + \nu W_{3/2}, \tag{38}$$

where W_0, $W_{3/2}$ are the transition probabilities per unit time of alpha decays without laser for the states in question of angular momentum $5/2^+$ and $3/2^+$ of ^{229}Th, respectively and

$$\nu = \frac{\pi^2 e^2 I}{M^2 c^3 \Delta\omega} \beta\tau, \tag{39}$$

where M is the nucleonic mass, I and $\Delta\omega$ are the intensity and the bandwidth of the laser, respectively and τ is the irradiation time. Here it is supposed that we are far from saturation and the ordinary time dependent perturbation calculation is valid [34]. β is the reduced $M1$ transition matrix element, measured in μ_p units

$$\beta = \frac{1}{(2J_i + 1)} \sum_{m_i, m_f, \mu} | < a | \sum_{\text{nucleon}} \hat{\mu}_{1\mu}(\text{nucleon}) | b > |^2. \tag{40}$$

In the case of $\beta \sim 10^{-6}$, which is two orders of magnitude less than the usual β values of $M1$ transitions [35], we can still expect a laser intensity and frequency dependent effect with the use of the nowadays available lasers.

If the applied laser is so intense that the resonance process reaches its saturation and we take into account the decays of the states in question then the results of the saturation probability of a damped Rabi flopping can be used [36]. Furthermore, for an irradiaton time, which is appropriately long compared to the inverse width of the state investigated the steady state excitation probability is valid [37]

$$\nu = \frac{2\pi e^2 I \beta}{M^2 c^3 [(\omega - \Delta/\hbar)^2 + \gamma^2/4]}, \tag{41}$$

where γ is the half width of the upper state that is supposed to have much shorter half life compared to that of the $5/2^+$ state.

The quantity, which is common in Eqs. (39) and (41), $K = \pi e^2/M^2c^3 = 9.6 \times 10^4$, meanwhile the intensity has to substitute in W/cm^2 units. The bandwidth $\Delta\omega$ of a glass laser is of the order 5.7×10^6 Hz [38], the intensity of the laser is expressed in W/cm^2 and $\beta \sim 10^{-6}$. With these conditions a laser of 1 kW/cm^2 intensity with an integrated irradiation time of one hour gives $\nu = 0.19$. This effect, which is thus proportional to the radiation time, can be described by Eq. (39).

6. Summary

On the basis of our results we can draw the following conclusions:

It is possible to modify a nuclear decay by intense radiation fields if the process has a characteristic energy, which is comparable with the laser photon energy. It is found that modification can be expressed in combined processes, which take place in consequence of the interaction between the nucleus and the electron cloud. The presence of the intense laser beam has an essential role in two types of such processes, in the near-below-threshold, laser-assisted internal conversion process and in a resonant, laser-assisted electronic-bridge mechanism. In both processes the intense beam provides the laser photons, the absorption of which is necessary in order to fulfil energy conservation and resonance conditions in the above processes, respectively. It was also shown that if the energy difference between nuclear states has a magnitude of a few eV, then a laser of resonant, optical frequency can mix the nuclear states modifying the α-decay in this manner.

Acknowledgements

This work was partly supported by the Hungarian National Science Research Fund (I/2-No. 194/88) and the MTA-Soros Foundation (Budapest–New York).

References

1. G. C. Baldwin, J. C. Solem and V. I. Gol'danskii, Rev. Mod. Phys., *53*, 687, 1981.
2. S. E. Murnick and M. S. Feld, Ann. Rev. Nucl. Part. Sci., *29*, 411, 1979.
3. W. Becker, W. H. Louisell, J. D. McCullen and M. O. Scully, Phys. Rev. Lett., *47*, 1262, 1981.
4. H. R. Reiss, Phys. Rev. Lett., *48*, 652, 1982.
5. H. R. Reiss, Phys. Rev. C, *27*, 1199, 1983, ibid. *27*, 1229, 1983.
6. W. Becker, R. R. Schlicher and M. O. Scully, Nucl. Phys., *A426*, 125, 1984 and the references therein.
7. R. R. Schlicher, W. Becker, J. Bergou and M. O. Scully, in: Quantum Electrodynamics and Quantum Optics, ed. by A. O. Barut, Plenum, New York, 1984, p. 405; W. E. Lamb, Jr., R. R. Schlicher and M. O. Scully, Phys. Rev., *A36*, 2763, 1987.
8. J. L. Friar and H. R. Reiss, Phys. Rev. C, *36*, 283, 1987.

9. J. I. Gersten and M. H. Mittleman, Phys. Rev. Lett., *48*, 651, 1982.
10. P. Kálmán and I. Lovas, J. Phys. G. Nucl. Phys., *13*, 495, 1987.
11. W. Becker, R. R. Schlicher and M. O. Scully, Phys. Lett., *A106*, 441, 1984.
12. V. M. Kolomijec, B. N. Kondratyev and A. I. Sandzsur, Izv. Akad. Nauk. SSSR, *53*, 69, 1989, in Russian.
13. D. F. Zaretskii and V. V. Lomonosov, JETP Lett. (Sov. Phys.) *30*, 508, 1979, JETP (Sov. Phys.) *54*, 229, 1981.
14. Y. K. Ho, F. C. Khanna and M. A. Lone, Nucl. Phys., *A440*, 189, 1985.
15. J. C. Solem and L. C. Biedenharn, J. Quant. Spect. Rad. Trans., *40*, 707, 1988.
16. J. F. Berger, D. Gogny and M. S. Weiss, J. Quant. Spect. Rad. Trans., *40*, 717, 1988.
17. See the special issue of J. Quant. Spect. Rad. Trans., *40*, Number 6 (1988), which is devoted to the gamma-ray lasers.
18. D. Kekez, A. Ljubčic, K. Pisk and B. A. Logan, Phys. Rev. Lett., *55*, 1366, 1985.
19. L. Pan, B. Sundaram and L. Armstrong, Jr., J. Opt. Soc. Am. *B4*, 754, 1987.
20. (a) P. Kálmán and J. Bergou, Phys. Rev. C, *34*, 1024, 1986;
(b) P. Kálmán, Phys. Rev. C, *37*, 2676, 1988.
21. P. Kálmán, Phys. Rev. C, *39*, 2452, 1989.
22. The resonant, laser-assisted internal conversion coefficient is treated elsewhere, P. Kálmán, unpublished.
23. P. Kálmán, Phys. Rev. *A43*, 2603, 1991.
24. J. M. Blatt and V. F. Weisskopf, Theoretical Nuclear Physics, Wiley, New York, 1952, Ch. XII.
25. (a) P. Cavaliere, G. Ferrante and C. Leone, J. Phys. B, *13*, 4495, 1980;
(b) M. Jain and N. Tzoar, Phys. Rev. A, *18*, 538, 1978; J. Banerji and M. H. Mittleman, J. Phys. B, *14*, 3717, 1981; L. Rosenberg, Phys. Rev. A, *34*, 4567, 1986.
26. K. Alder, A. Bohr, T. Huns, B. Mottelson and A. Winther, Rev. Mod. Phys., *28*, 432, 1956.
27. Higher Transcendental Functions, ed. by E. Erdélyi, McGraw-Hill, New York, 1953, Vol. 2.
28. H. R. Reiss, Phys. Rev. A, *22*, 1786, 1980.
29. P. Kálmán, Phys. Rev. A, *38*, 5458, 1988; ibid. *39*, 3200, 1989.
30. L. D. Landau and E. M. Lifsic, Quantummechanics, Tankönyvkiadó, Budapest, 1978.
31. C. M. Lederer and V. S. Shirley, Table of Isotopes, 7th ed. Wiley, New York, 1978.
32. H. W. Kugel and D. E. Murnick, Rep. Prog. Phys., *40*, 297, 1977.
33. C. W. Reich and R. G. Helmer, Phys. Rev. Lett., *64*, 271, 1990.
34. L. I. Schiff, Quantum Mechanics, McGraw-Hill, 1949.
35. J. M. Eisenberg and W. Greiner, Nuclear Theory, Vol. 2. Excitation Mechanism of the Nucleus, North-Holland, Amsterdam–London, 1970.
36. M. Sargent III, M. O. Scully and W. E. Lamb, Jr., Laser Physics, Addison-Wesley, 1974, Ch. 2. If we make the $\omega \to \Delta$, $pE_0 \to \mu_p B\sqrt{\beta}$ and $\nu \to \omega$ substitutions on pages 26–28 we obtain the wanted formulae.
37. P. L. Knight and L. Allen, Concepts of Quantum Optics, Pergamon, Oxford, 1983.
38. M. J. Weber, Editor, CRC Handbook of Laser Science and Technology, Vol. 1. Lasers and Masers, CRC, Boca Raton, Florida, 1982, Section 2.3.

Acta Physica Hungarica 71 (1–2), pp. 89–98 (1992)

A POSSIBLE PATH TOWARDS MASSIVE VECTOR FIELDS

R. M. DORIA

ICEN Universidade Católica de Petrópolis
Petrópolis, Rio de Janeiro, Brasil

and

J. A. HELAYËL-NETO

ICEN Universidade Católica de Petrópolis
Petrópolis, Rio de Janeiro, Brasil
and
DCP Centro Brasiliero de Pesquisas Físicas
Rio de Janeiro, RJ, Brasil

(Received 18 March 1991)

Considering the inclusion of more than a single potential field in the same local symmetry group, we study a sort of "dynamical transmutation mechanism" in which the freezing of matter degrees of freedom yields the appearance of massive vectors in the physical spectrum.

1. Introduction

It is a well-known fact that the imposition of a local symmetry on a Lagrangian implies the existence of massless particles in the spectrum of the theory it describes. The symmetry principle alone does not offer instructions to avoid the presence of massless vector fields. Thus, gauge theories could be seen as if they contain a razor principle for models that do not display massless spin-1 particles. In view of such a situation, a complement to the gauge principle is required in order that the experimental demand for massive particles can be considered. The observation that symmetries may be realized not only in a manifest form, but also in a spontaneously broken way, has developed a standard approach to investigate a spectrum containing massive gauge bosons [1]. However, although the conjecture that physical models possessing symmetries which are not shared by the vacuum of the system has been satisfactory for the description of the electroweak forces, Higgs scalars have not been detected so far. We do not know how many Higgs bosons exist and there are no general limits that can be set on their masses (constrains do exist, but they only become limits if supplemented by a number of assumptions). On the other hand, it is a fact the Higgs contribution to perturbative unitarity and renormalizability [2]. For instance, the $f\overline{f} \to WW$ scattering cross-section has a

bad high-energy behaviour that is cured by the inclusion of a Higgs boson exchange. The challenge brought by the latter has motivated the investigation of several different approaches: methods based on the replacement of the Higgses by composite objects or more complicated structures [3], gauge-fixing and non-local Lagrangians [4], anomalies [5] have been presented and are currently under investigation. A contribution to this polemic stems also from the importance of understanding the self-coupling $\lambda\phi^4$ [6].

It is then a very relevant matter to known to which extent gauge theories contain indications for the appearance of massive vector fields. The attempt here is to study a method based on the inclusion of more than one potential field in the same group, as given below:

$$A_\mu \to UA_\mu U^{-1} - \frac{i}{g_1} U\partial_\mu U^{-1}, \tag{1.1}$$

$$B_\mu \to UB_\mu U^{-1} - \frac{i}{g_2} U\partial_\mu U^{-1}. \tag{1.2}$$

There are different reasons for claiming that gauge theories intrinsically contain instructions for carrying more than one potential field as in (1.1) and (1.2), but with just one genuine gauge field [7]. The arguments are based on the existence of enough independent degrees of freedom, a Kaluza–Klein-type description and the local Noether theorem [7]. Incidentally, by studying the purely gravitational sector of higher-dimensional gravity coupled to fermions with non-vanishing pair condensation, the effective four-dimensional theory exhibits two potential fields that transform under the action of a single gauge group. By including torsion, one can prove that these fields are indeed independent [7].

Thus, considering the results from the spontaneous compactification of a $D > 4$-dimensional gravity-matter theory, one could use the rearrangement of the $\frac{D(D-3)}{2}$ physical degrees of freedom of the graviton to look for some alternative method to build up massive gauge theories. In Section 2, we briefly present the consequences from the inclusion of two potential fields. In Section 3, we combine the results of Section 2 with the canonical procedure for discussing the spontaneous breaking of a symmetry. Finally, a possible path for massive fields, by considering a kind of background potential and integrating out the involved scalar fields, is proposed and described in Section 4.

2. Physical masses for two potential fields in the same group

From (1.1) and (1.2), it is possible to build up the following gauge-invariant mass term:

$$\mathcal{L}_m = \frac{1}{2} m^2 tr(g_1 A_\mu - g_2 B_\mu)^2, \tag{2.1}$$

where m is a mass parameter, whereas g_1 and g_2 are dimensionless constants. At a first glance, one might suspect the presence of massive terms for both fields A_μ and B_μ. Nevertheless, in order to calculate the physical masses, we have to observe that in perturbation theory a physical particle is defined as the pole of the complete and renormalized two-point Green's function. This interpretation is not straightforward in the case of two fields: there appear mixed propagators originated from the non-diagonal terms in the kinetic Lagrangian. For instance, they can appear from the following field-strength tensor:

$$G_{\mu\nu} = g_1\partial_\mu A_\nu - g_2\partial_\nu B_\mu + g_1 g_2[B_\mu, A_\nu]. \tag{2.2}$$

Thus, the bilinear part of a Lagrangian containing two potential fields can generally be written as below:

$$\mathcal{L} = (A_\mu B_\mu)K^{\mu\nu}\begin{pmatrix} A_\nu \\ B_\nu \end{pmatrix} + \frac{1}{2}m^2 tr(g_1 A_\mu - g_2 B_\mu)^2, \tag{2.3}$$

where

$$K_{\mu\nu} = (A\Box + M^2)\eta_{\mu\nu} + B\partial_\mu\partial_\nu, \tag{2.4}$$

with

$$A = \begin{pmatrix} a_{11} & a_{12} \\ a_{21} & a_{22} \end{pmatrix}, \quad B = \begin{pmatrix} b_{11} & b_{12} \\ b_{21} & b_{22} \end{pmatrix}, \quad M = \begin{pmatrix} m_{11} & m_{12} \\ m_{21} & m_{22} \end{pmatrix}. \tag{2.5}$$

The tree-level physical masses, λ_1 and λ_2, are shown to be the eigenvalues of the matrix $A^{-1}M^2$:

$$\lambda_{1,2} = \frac{1}{(a_{11}a_{22} - a_{12}^2)}\left\{\frac{a_{11}}{2}m_{22} + \frac{a_{22}}{2}m_{11} - a_{12}m_{12} \pm \left[\left(\frac{a_{11}}{2}m_{22} - a_{22}m_{11}\right)^2 + a_{12}^2 m_{11}m_{22} + m_{12}(a_{11}a_{22}m_{12} - a_{11}a_{22}m_{11} - a_{12}a_{22}m_{11})\right]^{\frac{1}{2}}\right\}. \tag{2.6}$$

Apparently, (2.6) could lead us to think that both fields are massive. This would violate the razor principle. However, through a suitable reparametrisation of the fields,

$$\begin{aligned} D_\mu &= A_\mu + B_\mu \\ C_\mu &= g_1 A_\mu - g_2 B_\mu, \end{aligned} \tag{2.7}$$

one can observe the existence of just one massive field. This means that the introduction of more potential fields in the same group yields a gauge-invariant infrared regularisation for massless fields without, however, violating the gauge theory instruction that a local symmetry systematises the existence of a massless particle in the physical spectrum (at least in four-dimensional space-time).

3. Spontaneous symmetry breaking

Basic facts such as translational invariance and absence of ghosts, along with the hypothesis that a continuous symmetry may be broken by some order parameter, are enough to ensure the presence in the spectrum of a massless scalar boson via the Goldstone theorem. This result does not depend on the field content of the Lagrangian and is indeed model-independent. We shall in the present section reconsider the Goldstone theorem in its local version (actually, the Higgs mechanism) with a family of N potential fields associated to a single $U(1)$ gauge symmetry that is spontaneously broken by the vacuum expectation value of a scalar.

We start off with a set of k scalar fields transforming under the gauge group according to:

$$\underset{i=1,2,\ldots,k}{\Phi_i \longrightarrow \Phi_i' = e^{iq_i\alpha(X)}\Phi_i}, \tag{3.1}$$

where q_i is the charge of the i-th field. The $U(1)$-invariance and renormalisability fix the Lagrangian to be

$$\mathcal{L} = K_{ij}\partial_\mu\Phi^{i*}\partial^\mu\Phi^j - m_{ij}^2\Phi^{I*}\Phi^j - \frac{\lambda}{4}(\Phi_i^*\Phi^i)^2. \tag{3.2}$$

K and m^2 are taken to be real and symmetric matrices (K is also assumed to be positive-definite); the coupling parameter λ is such that $\lambda > 0$.

In order to be the closest to the usual case, we prefer to choose a framework in which the kinetic term is diagonalised. Consider an orthogonal transformation, R, such that

$$\tilde{\phi} = R^t\Phi, \tag{3.3a}$$

$$\tilde{K}_{ij} = (R^tKR)_{ij} = \omega_i\delta_{ij}. \tag{3.3b}$$

Also, performing a field rescaling according to

$$\phi_i = \sqrt{\omega_i}\tilde{\phi}_i, \tag{3.4}$$

one gets for ϕ_i the Lagrangian below:

$$\mathcal{L} = \partial_\mu\phi^{i*}\partial^\mu\phi^i - \mu_{ij}^2\phi^{i*}\phi^j - \frac{\lambda}{4}\left(\frac{\phi_i^*}{\sqrt{\omega_i}}\frac{\phi^i}{\sqrt{\omega_i}}\right)^2, \tag{3.5}$$

where μ^2 is a symmetric mass matrix given by

$$\mu_{ij}^2 = \frac{1}{\sqrt{\omega_i}}(R^tm^2R)_{ij}\frac{1}{\sqrt{\omega_j}}. \tag{3.6}$$

The ω_i's are the eigenvalues of the kinetic matrix K and, according to our initial assumptions on the latter, they are all positive. From (3.5), the Higgs potential can immediately be read off:

$$V(\phi) = \mu_{ij}^2 \phi^{i*} \phi^j + \frac{\lambda}{4} \left(\frac{1}{\omega_j} \phi^* \phi^i \right)^2 . \tag{3.7}$$

A possible way to bring N independent gauge potentials, $A_\mu^i(x)$, in association with the $U(1)$ symmetry given in (3.1), is to take $N = k$ and to couple them to the scalars as below:

$$\partial_\mu \phi_i \to D_\mu(A_i)\phi_i \equiv (\partial_\mu + igq_i A_{\mu i})\phi_i, \tag{3.8}$$

where g is a dimensionless coupling parameter.

The gauge transformed potentials read

$$A'_{\mu i} = A_{\mu i} - \frac{1}{g}\partial_\mu \alpha, \tag{3.9}$$

and the gauge-invariant Lagrangian for the ϕ_i's and $A'_{\mu i}$s can be written as:

$$\mathcal{L} = \mathcal{L}_{\text{gauge}}(A_{\mu i}) + \mathcal{L}_{\text{gauge-matter}} + V(\phi_i), \tag{3.10}$$

where $\mathcal{L}_{\text{gauge}}(A_{\mu i})$ is the extension of the Maxwell Lagrangian to include N gauge potentials (it is discussed in details in [9] and [10]),

$$\mathcal{L}_{\text{gauge-matter}} = \left[D_\mu(A_i)\phi_i\right]^* \left[D^\mu(A_i)\phi^i\right], \tag{3.11}$$

and $V(\phi_i)$ is the Higgs potential of Eq. (3.7). Based on general arguments [1], we can conclude that, though the N vector potentials are mixed up in $\mathcal{L}_{\text{gauge}}$, the genuine gauge field of the model (see [10]),

$$D_\mu \equiv \frac{1}{N} \sum_{i=1}^{N} A_{\mu i} \tag{3.12}$$

acquires mass whenever $V(\phi_i)$ allows for the spontaneous breaking of the gauge symmetry.

Another model that can be proposed, based on the introduction of N gauge potentials, couples just one scalar, $\Phi(x)$, to the $A_{\mu i}$'s according to the Lagrangian

$$\mathcal{L} = \mathcal{L}_{\text{gauge}}(A_{\mu i}) + \left[D_\mu^i(A_i)\Phi\right]^* N_{ij} \left[D^{\mu j}(A_j)\Phi\right] + V(\Phi), \tag{3.13}$$

with

$$D_{\mu i}(A_i)\Phi \equiv (\partial_\mu + ig_i A_{\mu i})\Phi, \tag{3.14}$$

where no summation over i is understood in (3.14) and N is a real symmetric matrix. Lagrangian (3.13) is invariant under the local transformations

$$\Phi(x) \to \Phi'(x) = e^{i\alpha(x)}\Phi(x) \tag{3.15a}$$

and

$$A_{\mu i}(x) \to A'_{\mu i}(x) = A_{\mu i}(x) - \frac{1}{g_i}\partial_\mu \alpha(x). \tag{3.15b}$$

Upon replacement of the covariant derivative (3.14) into (3.13), we get

$$\mathcal{L} = \mathcal{L}_{\text{gauge}}(A_i) + \sum_{i,j=1}^{N} N_{ij}\partial_\mu \Phi^* \partial^\mu \Phi + i\Phi^* \overleftrightarrow{\partial}_\mu \Phi \sum_{i,j=1}^{N} N_{ij} g_i A_i^\mu + \sum_{i,j=1}^{N} N_{ij} g_i g_j A_{\mu i} A_j^\mu \Phi^* \Phi + V(\Phi). \tag{3.16}$$

Taking now

$$V(\Phi) = \mu^2 \Phi^* \Phi + \frac{\lambda}{4}(\Phi^* \Phi)^2, \tag{3.17}$$

with $\mu^2 < 0$, the ground state is non-trivial and degenerate, giving rise to the spontaneous symmetry breaking. As usually done, we choose a real vacuum, ν, and parametrize Φ as below:

$$\Phi = v + \chi_1 + i\chi_2, \tag{3.18}$$

where χ_1 and χ_2 are the right field fluctuations. This yields:

$$\begin{aligned}\mathcal{L}(\chi_1, \chi_2; A_i) =& \mathcal{L}_{\text{gauge}}(A_i) + \sum_{i,j=1}^{N} N_{ij}(\partial_\mu \chi_1 \partial^\mu \chi_1 + \partial_\mu \chi_2 \partial^\mu \chi_2 + \\ &+ v^2 \sum_{i,j=1}^{N} N_{ij} g_i g_j A_{\mu i} A_j^\mu + 2m^2 \chi_1^2 - 2(\chi_1 \overleftrightarrow{\partial}_\mu \chi_2 + v\partial_\mu \chi_2) \cdot \\ &\cdot \sum_{i,j=1}^{N} N_{ij} g_i A_i^\mu + 2v \sum_{i,j=1}^{N} N_{ij} g_i g_j A_{\mu i} A_j^\mu \chi_1 + \\ &+ \sum_{i,j=1}^{N} N_{ij} g_i g_j A_{\mu i} A_j^\mu (\chi_1^2 + \chi_2^2) + \\ &- \frac{\lambda}{4}(4v\chi_1\chi_2^2 + 2\chi_1^2\chi_2^2 + 4v\chi_1^3 + \chi_1^4 + \chi_2^4).\end{aligned} \tag{3.19}$$

The scalar field χ_2 can be eliminated by choosing the so-called unitary gauge. Thus the spectrum will display N massive vector particles along with the Higgs scalar. Still, the Higgs particle is a physical dynamical field we have to live with. An advantage, however, of the introduction of the N potentials is that power-counting renormalisability can be achieved even in the unitary gauge [9,10].

4. Other paths towards massive vector fields

In this Section, we shall initially discuss the possibility of introducing and giving a role to non-dynamical fields. This means to propose a consistent and meaningful quantum field theory where some of the fields do not appear in the physical spectrum of the theory. The advantage of working with more potential fields in the same group is that such an approach yields naturally the enlargement of the symmetry considerations. Recalling that the razor principle judgment applies to gauge theories without massless fields, it is enough to work with only two potential fields in order that our proposals can be tested.

Parametrising the complex field Φ in terms of polar coordinates,

$$\Phi(x) = \eta(x)e^{i\xi(x)}, \tag{4.1}$$

and substituting in (3.16), we get

$$\begin{aligned}\mathcal{L} =& \mathcal{L}_{\text{gauge}}(A;B) + (x_1 + x_2 + 2x_3)\left[(\partial_\mu\eta)^2 + \eta^2(\partial_\mu\xi)^2\right] + \\ & - \mu^2\eta^2 - \frac{\lambda}{4}\eta^4 + \left[x_1 g_1^2 A_\mu A^\mu + x_2 g_2^2 B_\mu B^\mu + 2x_3 g_1 g_2 A_\mu B^\mu\right]\eta^2 + \\ & + (x_1 + x_3)A_\mu\eta^2\partial^\mu\xi + (x_2 + x_3)B_\mu\eta^2\partial^\mu\xi,\end{aligned} \tag{4.2}$$

where x_1, x_2 and x_3 are the free parameters that specify the matrix N. The attitude here is that, by imposing the relation

$$x_1 + x_2 + 2x_3 = 0, \tag{4.3}$$

there remain no scalar quanta to be identified as physical degrees of freedom in the theory. Therefore, it turns out necessary to understand which is the meaning of the interacting scalar fields in (4.2). Notice that condition (4.3) in the Lagrangian (4.2) still preserves the underlying gauge symmetry

$$\begin{aligned}\eta(x) &\to \eta(x) \\ \xi(x) &\to \xi(x) + \alpha(x)\end{aligned} \tag{4.4}$$

and the corresponding conserved current. The survival of gauge invariance upon imposition of (4.3) shows that η and ξ only work as a complement to symmetry. This means that they can be characterized as background fields of the theory. Rewriting (4.2) with condition (4.3) as

$$\mathcal{L} = \mathcal{L}_{\text{gauge}}(A;B) + V_{\text{background}}(A,B;\eta,\xi), \tag{4.5}$$

one can see that the fields η and ξ appear just as auxiliary to build up to quanta of the vector fields. For instance, applying the standard engineering of breaking down symmetries to (4.5), it yields massive vector fields. Thus in this case, the fields

η and ξ would work as background fields in order that the massless vector fields acquire mass without the need for physical propagating scalars.

A second point to be contemplated in this Section is the investigation of the possibilities for the dynamics of the theory to evolve its structure to a final picture where the fields η and ξ are absorbed into the potential fields. In this direction, let us first draw our attention to the possibilities for eliminating the field ξ. By virtue of the gauge invariance of the theory, we can suitably choose the arbitrary parameter $\alpha(x)$ so as to eliminate the mode ξ. However, we have to be careful about the nature of a mass when it is manifested through a gauge-fixing. So, it would be better if the ξ-field could be eliminated without requiring a gauge-fixing procedure: there would not be any danger of confusing this mass with a gauge artifact. Then, a possible relevance of this approach is that Lagrangian (4.2) contains an insight for eliminating the ξ-field without breaking gauge invariance. Considering the condition (4.3), the ξ-field acts as a multiplier that enforces the following gauge-invariant constraint:

$$\partial_\mu \left\{ [(x_1 + x_3)A^\mu + (x_2 + x_3)B^\mu]\eta^2 \right\} = 0. \tag{4.6}$$

Hence, as a consequence of the latter equation to be a gauge-invariant condition, the dimensionless field $\xi(x)$ does not contain any track of acting as a gauge parameter.

The constraint (4.6) can be put in a simpler form,

$$(x_1 - x_2)\partial_\mu(\eta^2 C_\mu) = 0, \tag{4.7}$$

where C_μ is the gauge-invariant combination of the potential A_μ and B_μ:

$$C_\mu \equiv A_\mu - B_\mu. \tag{4.8}$$

By simply choosing the parameters x_1 and x_2 to be equal,

$$x_1 = x_2, \tag{4.9}$$

and this is compatible with the symmetry of the matrix N, (4.7) is automatically satisfied and the η-field equation of motion reads

$$\eta(\eta^2 - \frac{2}{\lambda}F) = 0, \tag{4.10}$$

where

$$F \equiv -\mu^2 + x_1(g_1^2 A_\mu A^\mu + g_2^2 B_\mu B^\mu) + 2x_3 g_1 g_2 A_\mu B^\mu. \tag{4.11}$$

The equation of motion (4.10) shows that the theory displays two phases: one for which there is a massless gauge field along with a massive vector, and another phase for which there are two massive vector particles. This can be readily checked

if we eliminate η from Lagrangian (4.2) in terms of the solutions to equation (4.10). In the case of the non-trivial configuration

$$\eta^2 = \frac{2}{\lambda} F, \tag{4.12}$$

the theory is described by the effective Lagrangian, $\mathcal{L}_{\text{eff}}$, which reads:

$$\mathcal{L}_{\text{eff}} = \mathcal{L}_{\text{gauge}}(A; B) + \frac{1}{\lambda} F^2, \tag{4.13}$$

whose spectrum exhibits the presence of two massive gauge fields. So, just to conclude, we understand that the introduction of more than a single gauge potential enlarges the possibilities of writing down gauge-invariant Lagrangians. This, in turn, gives room to more free parameters that can be suitably arranged so as to freeze matter degrees of freedom without explicitly breaking the gauge invariance. The invariance of the non-propagating matter fields reveals the presence of massive vector bosons in the spectrum.

Acknowledgements

The authors wish to express their appreciation to the ICTP, through Prof. G. Furlan, for the oppurtunity of proposing a dialogue between North and South through science.

They would also like to express their gratitude to the Coca-Cola of Brazil, through Sônia Barreto and Johnson & Higgins (Corretores de Seguros), through Dr. Michael Wyles, for the invaluable financial help.

References

1. P. W. Higgs, Phys. Lett., *12*, *132*, 1964; Phys. Rev. Lett., *13*, 508, 1964; Phys. Rev., *145*, 1156, 1966;
   P. W. Anderson, Phys. Rev., *130*, 439, 1963;
   F. Englert and R. Brout, Phys. Rev. Lett., *13*, 321, 1964;
   G. S. Guralnik, C. R. Hagen and T. W. B. Kibble, Phys. Rev. Lett., *13*, 585, 1964;
   S. Coleman, Aspects of Symmetry, Cambridge University Press, 1985.
2. J. S. Bell, Nucl. Phys., *B60*, 427, 1973;
   C. H. Llewellyn Smith, Phys. Lett., *46B*, 233, 1973;
   J. M. Cornwall, O. N. Levin, G. Tiktopoulos, Phys. Rev. Lett., *30*, 1268, 1973 and Phys. Rev., *D10*, 1145, 1974.
3. E. Farhi and L. Susskind, Phys. Rep., *74*, 277, 1981;
   M. Dugan, H. George and D. B. Kaplan, Nucl. Phys., *B254*, 299, 1985.
4. R. Delbourgo and G. Thompson, Phys. Rev. Lett., *57*, 21, 1986;
   G. Thompson and R. Zhang, A Gauge Principle Consistent Chiral Theories, ICTP preprint, March, 1987;
   M. Carena, C. Wagner and L. Masperi, Phys. Rev., *D37*, 493, 1988.
5. R. Jackiw and R. Rajaraman, Phys. Lett., *54*, 12, 1985;
   L. D. Faddeev, S. L. Shatashivili, Phys. Lett., *167b*, 2, 1985;

Ashok Das, Phys. Rev. Lett., *55*, 20, 1985;
M. S. Chanowitz, Phys. Lett., *B171*, 2, 1986;
R. Barnerjee, Phys. Rev. Lett., *56*, 18, 1986;
S. G. Rajeev, Quantization of an Anomalous Gauge Theory, MIT preprint, October, 1986;
M. V. Manias, M. C. von Reichenbach, F. A. Schaposnick and M. Trabo, Current Algebra for Chiral Gauge Theories, Universidad de La Plata, preprint, 1986;
N. K. Falck, G. Kramer, Ann. Phys., *176*, 330, 1987.

6. K. G. Wilson, Rev. Mod. Phys., *55*, 583, 1983;
B. Freedman, P. Smolensky and D. Weingarten, Phys. Lett., *113B*, 481, 1982;
C. Aragão de Carvalho, C. S. Caraciolo and J. Fröhlich, Nucl. Phys., *B215*, 209, 1983.
7. R. M. Doria and C. Pombo, Il Nuovo Cim., *96*, 153, 1986;
C. M. Doria, R. M. Doria and J. A. Helayël-Neto, Rev. Bras. de Fis., *17*, 351, 1987;
L. P. Colatto, R. M. Doria and J. A. Helayël-Neto, Il Nouvo Cim., *98A*, 359, 1987.
8. A. M. Polyakov, Phys. Lett., *103B*, 207, 1981.
9. R. M. Doria, A. Z. Dubničkova and J. A. Helayël-Neto, Il Nuovo Cim., *94A*, 51, 1986;
R. M. Doria, J. A. Helayël-Neto and C. Pombo, Il Nuovo Cim., *98A*, 337, 1987.
10. R. M. Doria and F. A. B. Rabelo de Carvalho, Rev. Bras. de Fís., *18*, 453, 1988.

Acta Physica Hungarica 71 (1–2), pp. 99–115 (1992)

TRAJECTORY STUDIES FOR THE FUSION OF TWO HEAVY NUCLEI

AHMED OSMAN, S. S. ABDEL-AZIZ and M. M. GOGARY

Physics Department, Faculty of Science, Cairo University
Cairo, Egypt

(Received in revised form 28 May 1991)

The dynamical aspects of two heavy nuclei colliding with energies above the Coulomb barrier are considered. The macroscopic aspects of the asymmetric and symmetric collisions have been studied. The classical trajectories for the fusing systems are numerically calculated. Effects due to increasing the initial kinetic energy or the initial asymmetry on the calculated trajectories are investigated. The results lead to three typical trajectories which correspond to the deep-inelastic, the quasifission and the formation of compound system reactions. It is found that the effect of the asymmetry plays the same role as that of the initial kinetic energy.

1. Introduction

In the last few years, an enormous amount of data resulting from the collision between complex nuclei have been obtained leading to experimental investigations for the different mechanisms of the reactions between complex nuclei. These reactions are characterized by features which are intermediate between those of the simple quasielastic or few nucleon transfer and those of the highly complex compound nucleus reactions. These reactions are defined as the damped nuclear reactions characterized by the damping of the collective nuclear motion through interactions with intrinsic nucleonic modes. The experimental observation of two massive fragments produced with asymmetry and close to the initial interacting two nuclei, supports the concept of damped reactions as a peripheral contact of two macroscopic unstructured bodies. Theoretical investigations have been obtained [1], [2] from the application of the classical dynamical models to the damped reactions. Classical dynamical calculations have been carried out [2]–[7] for both of the damped reactions and the nuclear fusion using different models for the nuclear configuration of the interacting system.

The more realistic dynamical model is that which includes [5], [8] deformation degrees of freedom in the classical dynamical calculations to explain a wide variety of fusion data [9], [10] including those for heaviest systems. This model predicts three important configurations [11] from the dynamical evolution of the nucleus–nucleus collisions known as the contact, the conditional saddle and the unconditional saddle configurations. These mentioned configurations are associated with the three threshold contact, extra push and extra–extra push energies, respectively. This

model has been modified [12] by including the asymmetry friction term to the dissipation function for shapes with a small neck. The previous dynamical model predictions have been re-examined [13] to investigate the effect of including the asymmetry friction term. Calculations using realistic geometrical shapes and a weighted superposition between the two limiting cases of the one-body dissipation have been carried out and compared with the experimental data [6], [7]. Another variety of experimental data have been observed [14] for damped nuclear reactions below the Coulomb barrier. The neck formation cross sections have been calculated [15] using the liquid drop model where a strong relation has been evaluated between the calculated cross-sections and the sum of the experimental values of the fusion and deep-inelastic cross-sections. With the help of the obtained relations, these processes may be understood classically.

In the present work, the classical dynamical theory is reconsidered. This theory is introduced as to consist of the liquid drop model together with a generalized one-body dissipation formula. The nuclear configuration is parametrized by considering the two heavy nuclei of the interacting system as two spheres connected together with a conical neck. Then, numerical calculations are carried out for the classical trajectories describing the fusion of different fusing systems. The effects of changing the initial conditions concerning the injection kinetic energy and the asymmetry on the dynamical trajectories are investigated.

In Section 2, the mathematical and theoretical expressions of the dynamics of two fusing nuclei are introduced as functions of the different collective degrees of freedom. Numerical calculations and results are given in Section 3. Section 4 is left for discussion and conclusions.

2. Mathematical and theoretical expressions of the dynamics of two fusing nuclei

In the present Section, we consider the dynamical equations of motion describing the dynamical trajectories showing the shape evolutions with respect to time for the two fusing nuclei. There are two interesting cases considering the two fusing nuclei, namely, the asymmetric and the symmetric cases.

The dynamical trajectories of two asymmetric fusing nuclei are considered. In this case, the trajectories are governed by the chaotic regime dynamical theory by considering the liquid drop model and one-body dissipation. For this purpose, three basic dynamical ingredients will be introduced to obtain the Lagrangian equations of motion. To obtain the shape parametrization and potential energy of the two asymmetric fusing nuclei, the nuclear surface is parametrized by the axially symmetric shape which consists of two asymmetric spheres connected together by a conical neck as shown in Fig. 1. The set of the three dimensionless degrees of freedom [13] describing the shape parametrization completely are known as the radial distance S, the neck size N and the mass asymmetry D. The liquid drop potential energy formula as a function of the above three degrees of freedom is given explicitly

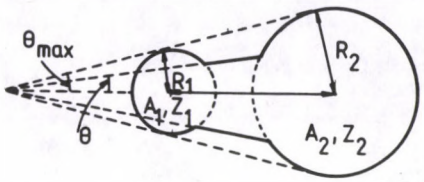

Fig. 1. Schematic diagram representing the two heavy nuclei moving towards fusion

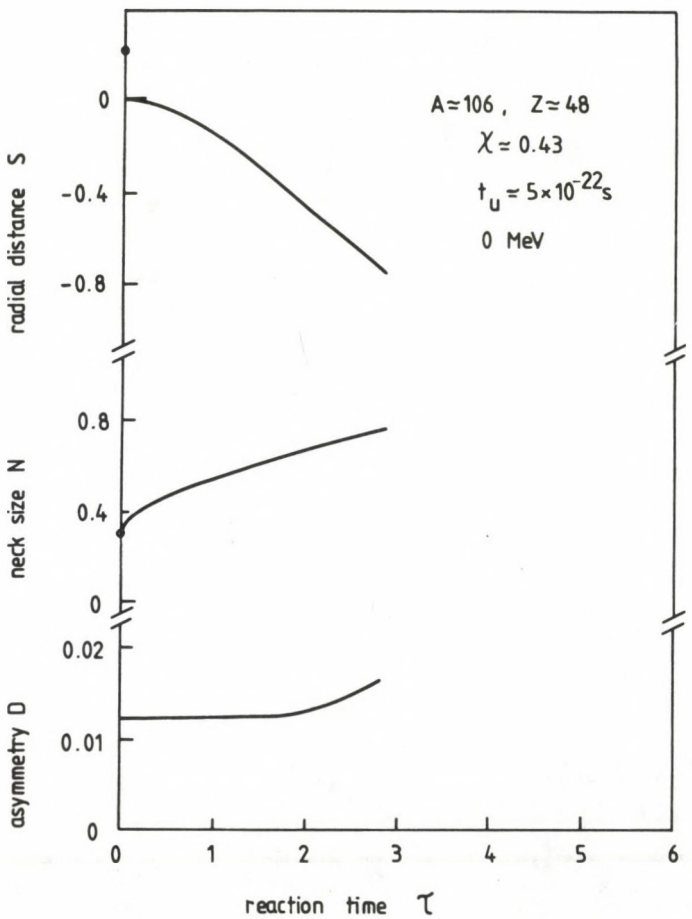

Fig. 2. Radial distance S, neck size N and asymmetry D of the system $^{106}X_{48}$ as a function of the dimensionless time τ for zero initial kinetic energy

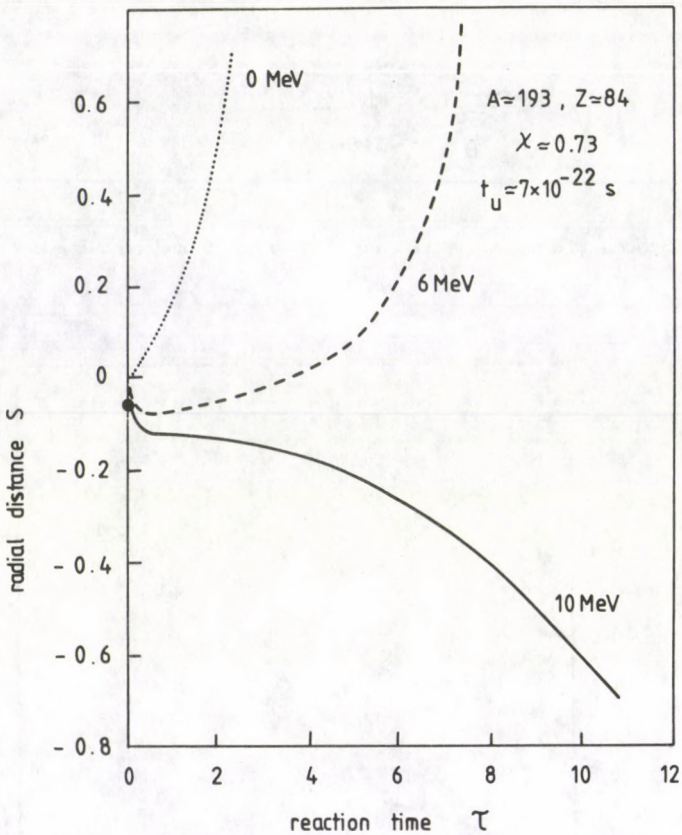

Fig. 3. The calculated trajectories of the radial distance S of the system $^{193}X_{84}$ as a function of the dimensionless time τ for different values of the initial kinetic energy

in reference [13] by an expression as

$$\text{P.E.}(S,N,D) = 4\pi\gamma R^2 \left[\left\{ \frac{2(1+D)}{(2+6D)^{2/3}} + \frac{1}{2}NS - \frac{1}{2}N^2 + \frac{(2+6D)^{1/3}}{2(1-D)}N^3 - 1 \right\} + \frac{12}{5}\chi \left\{ \frac{17+105D+75D^2-5D^3}{6(2+6D)^{5/3}} - \frac{5}{12}\frac{(1-D)^3}{(2+6D)^{4/3}}S - 1 \right\} \right]. \quad (1)$$

In Eq. (1), γ is the surface tension, R is the radius of the spherical compound nucleus and χ is the fissibility parameter.

For calculating the kinetic energy, we shall consider only the central collision as a matter of simplicity. Therefore, in this case we employ the assumption of considering that the motions in the neck and asymmetry degrees of freedom are

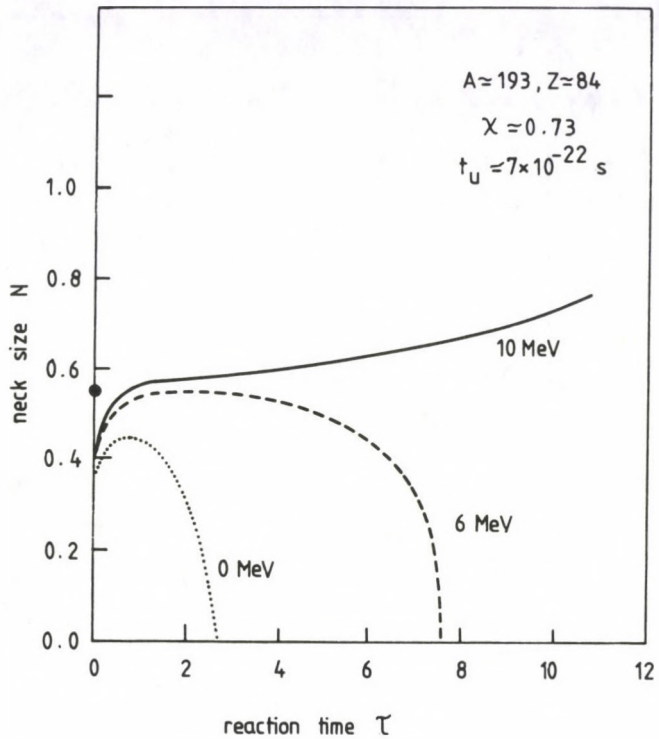

Fig. 4. The calculated trajectories of the neck size N of the system $^{193}X_{84}$ as a function of the dimensionless time τ for different values of the initial kinetic energy

strongly overdamped. Hence the only effective degree of freedom in the kinetic energy is the radial distance. Also, we assumed that when the shapes of the neck between the two colliding nuclei are very thin, the inertia is taken to be the reduced mass of the non-communicating nuclei, while for shapes without neck, the inertial forces are neglected entirely. Making use of these assumptions the kinetic energy can be given by an expression as

$$\text{K.E.} \simeq \frac{1}{2}\mu R^2 \dot{S}^2. \tag{2}$$

R is the radius of the spherical compound nucleus. μ is the reduced mass of the separated fragments and is given by

$$\mu = m(A_1A_2/A).$$

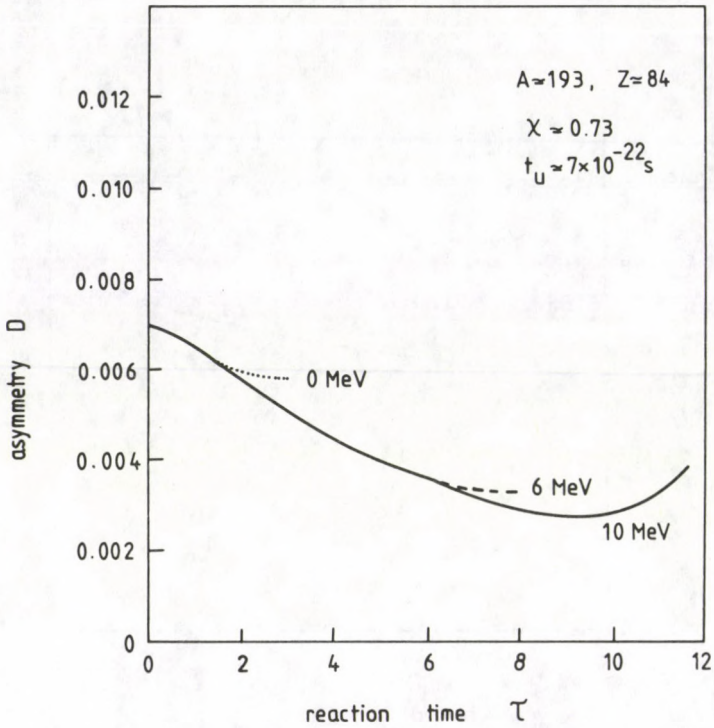

Fig. 5. The calculated trajectories of the asymmetry D of the system $^{193}X_{84}$ as a function of the dimensionless time τ for different values of the initial kinetic energy

A_1 and A_2 are the mass number of the separated fragments, $A = A_1 + A_2$, and $m = 931$ MeV/c^2.

In terms of the radial distance S and the mass asymmetry D, Eq. (2) can be expressed as

$$\text{K.E.} \simeq \frac{1}{8} MR^2 \frac{(1-D)^3}{(1+3D)^2} \dot{S}^2, \tag{3}$$

where $M = mA$.

For the dissipation energy [17], it has been shown that the one-body dissipation theory [12] is the most successful one applied to the nuclear dynamics. The rate of energy $\dot{Q}$ which is dissipated during the fusion of the two heavy nuclei is derived as a function of our shapes for the degrees of freedom and their derivatives. Two limiting cases are considered leading to two different formulas. The first one is $\dot{Q}_\omega$ referring to the wall formula which describes the compact shapes. The second one is $\dot{Q}_{\omega\omega}$ which stands for the wall-plus-window formula describing the necked-in shapes [13]. A generalized formula considered as a weighted superposition of $\dot{Q}_\omega$ and $\dot{Q}_{\omega\omega}$ has been assumed [6], [7], [13] for any arbitrary shape. This generalized

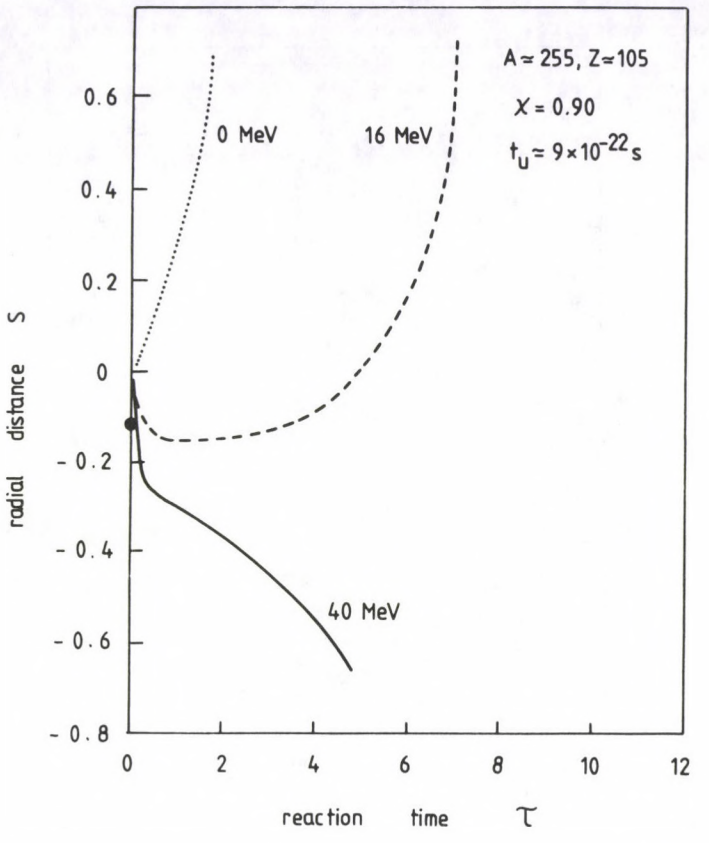

Fig. 6. The calculated trajectories of the radial distance S of the system $^{255}X_{105}$ as a function of the dimensionless time τ for different values of the initial kinetic energy

formula is given by the expression

$$\dot{Q} = \dot{Q}_\omega(1-f) + f\dot{Q}_{\omega\omega}. \tag{4}$$

f is a smooth weighting factor defined by the expression

$$f = \cos^2\left[\frac{\pi}{2}\frac{(2+6D)^{2/3}N^2}{(1-D)^2}\right]. \tag{5}$$

In terms of the present three shape degrees of freedom, Eq. (4) can be expressed as

$$\begin{aligned}\dot{Q} =& \rho\bar{v}\pi R^4\left\{\left[\frac{1}{2}N^2\dot{S}^2 + \frac{16}{9}\frac{(1-D)^4\dot{D}^2}{D(1+3D)^4N^2} - \frac{2(1-D)^2\dot{S}^2}{3(2+6D)^{2/3}(1+D)}\right]\right.\\ &\cdot\cos^2\left[\frac{\pi}{2}\frac{(2+6D)^{2/3}N^2}{(1-D)^2}\right] + \frac{(1-D)^2(1+D)\dot{D}^2}{D(2+6D)^{1/3}(1+3D)^3} + \frac{2(1-D)^2\dot{S}^2}{3(1+D)(2+6D)^{2/3}}\\ &\left.+2N\left[S + \frac{(2+6D)^{1/3}N^2}{(1-D)}\right]\dot{N}^2\right\},\end{aligned} \tag{6}$$

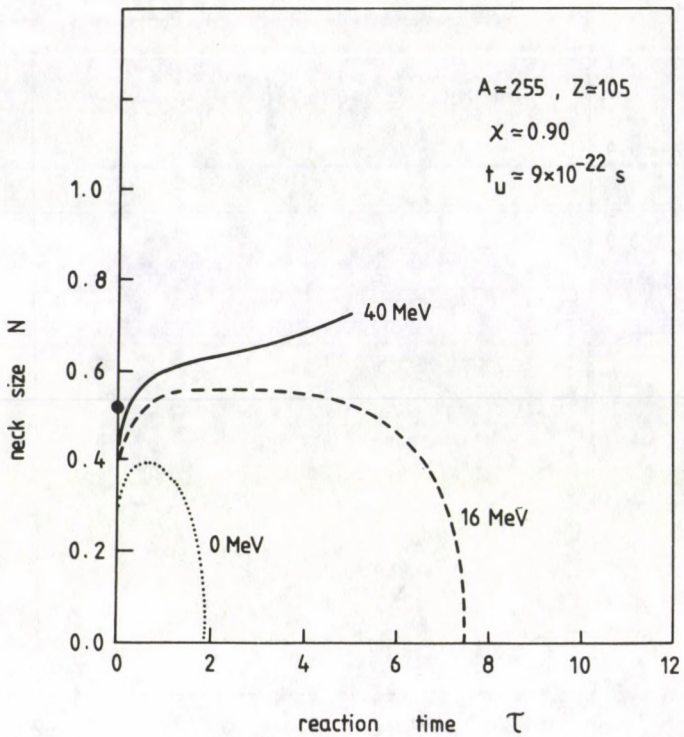

Fig. 7. The calculated trajectories of the neck size N of the system $^{255}X_{105}$ as a function of the dimensionless time τ for different values of the initial kinetic energy

where ρ is the nuclear matter density and $\overline{v}$ is the mean nucleonic velocity.

The dynamical ingredients introduced by the preceding equations are used to obtain the Lagrange and Rayleigh dissipation functions given as

$$\mathcal{L} = \text{K.E.} - \text{P.E.} \tag{7}$$

and

$$\text{DF} = \frac{1}{2}\dot{Q}. \tag{8}$$

Then the equations of motion can be obtained from an expression given by

$$\frac{d}{dt}\left(\frac{\partial \mathcal{L}}{\partial \dot{q}_i}\right) = \frac{\partial \mathcal{L}}{\partial q_i} - \frac{\partial \text{DF}}{\partial \dot{q}_i}, \tag{9}$$

where

$$q_i = \{S, N, D\}.$$

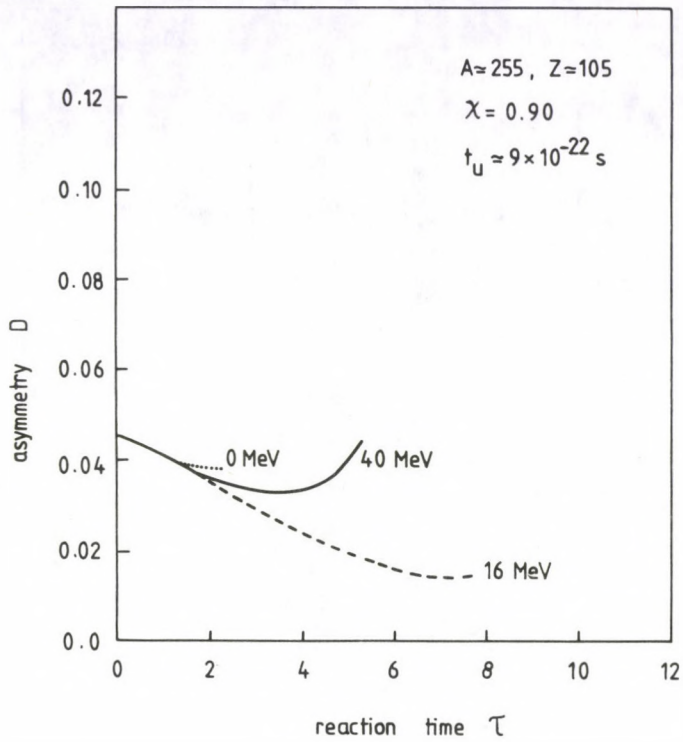

Fig. 8. The calculated trajectories of the asymmetry D of the system $^{255}X_{105}$ as a function of the dimensionless time τ for different values of the initial kinetic energy

The different equations of motion given by Eq. (9) are reduced to three dimensionless coupled nonlinear differential equations. These equations are given by the expressions

$$\left(\frac{d^2S}{d\tau^2}\right) = \left[\frac{3(3+D)}{(1+3D)(1-D)}\right]\cdot\left(\frac{dS}{d\tau}\right)\cdot\left(\frac{dD}{d\tau}\right) - \left[\frac{2\pi(\rho\bar{\nu}R^2)^2}{9M\gamma}\right]\left[\frac{(1+3D)^2N}{(1-D)^3}\right]$$
$$- \left[\frac{\pi(\rho\bar{\nu}R^2)^2}{3M\gamma}\right]\left(\frac{(1+3D)^2}{(1-D)^3}\right)\left(\frac{dS}{d\tau}\right)\left\{N^2 - \frac{4(1-D)^2}{3(2+6D)^{2/3}(1+D)}\right\}$$
$$\cos^2\left(\frac{\pi}{2}\frac{(2+6D)^{2/3}N^2}{(1-D)^2}\right) + \left[\frac{4\pi(\rho\bar{\nu}R^2)^2\chi}{9M\gamma}\right]\left(\frac{(1+3D)^2}{(2+6D)^{4/3}}\right), \qquad (10)$$

$$\left(\frac{dN}{d\tau}\right) = \frac{2(1-D)N - (1-D)S - 3(2+6D)^{1/3}N^2}{6[NS(1-D) + (2+6D)^{1/3}N^3]} \qquad (11)$$

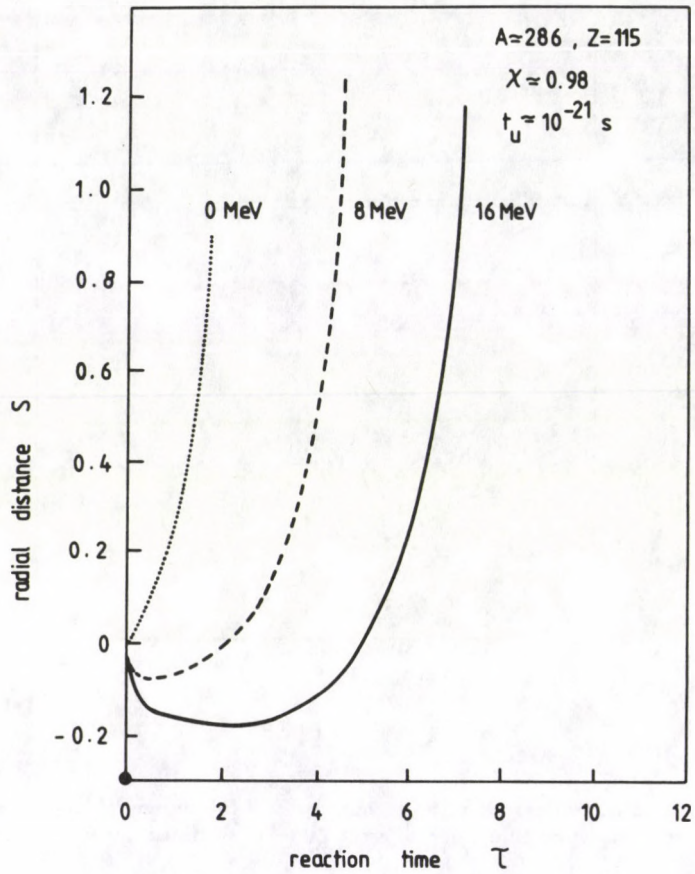

Fig. 9. The calculated trajectories of the radial distance S of the system $^{286}X_{115}$ as a function of the dimensionless time τ for different values of the initial kinetic energy

and

$$\left(\frac{dD}{d\tau}\right) = -\left[\frac{9M\gamma}{4(\rho\bar{\nu}R^2)^2}\right]\left(\frac{dS}{d\tau}\right)^2\left[\frac{(3+D)}{\frac{(1+D)}{D(2+6D)^{1/3}}+\frac{16}{9}\frac{(1-D)^2 f}{D(1-3D)N^2}}\right]$$
$$-\left(\frac{\chi}{3}\right)\left[\frac{(7+5D)S}{\frac{(1+D)}{D(1+3D)}+\frac{16}{9}\frac{(2+6D)^{1/3}(1-D)^2 f}{D(1+3D)^2N^2}}\right] \qquad (12)$$
$$-\left[\frac{4}{3(2+6D)^{1/3}}\right]\left[\frac{\frac{(D-1)}{(1+3D)}+\frac{(D+1)N^3}{(1-D)^2}+\frac{2\chi(1-D)^3}{(1+3D)^2}}{\frac{(1-D)^2(1+D)}{D(1+3D)^3}+\frac{16}{9}\frac{(1-D)^4(2+6D)^{1/3}f}{D(1+3D)^4N^2}}\right].$$

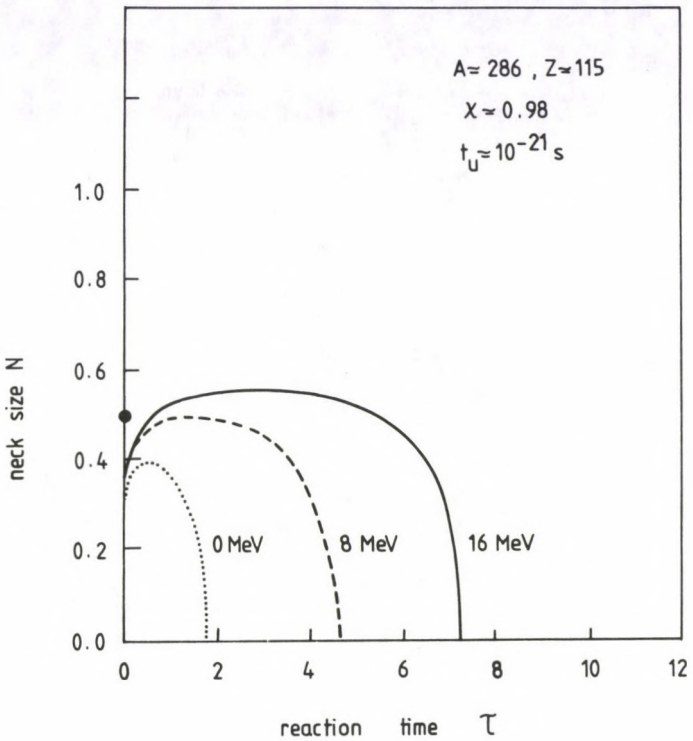

Fig. 10. The calculated trajectories of the neck size N of the system $^{286}X_{115}$ as a function of the dimensionless time τ for different values of the initial kinetic energy

τ is the dimensionless time given by

$$\tau = t/t_u, \tag{13}$$

where t_u is the unit time defined as

$$t_u = \rho\bar{\nu}R^2/6\gamma. \tag{14}$$

Eq. (10)–(12) are coupled differential equations which can be solved together numerically by using the Runge-Kutta method subjected to the initial conditions for the collision process. The dynamical equations of motion for the case of symmetric collision can be obtained from Eqs (1), (3) and (6) by taking the value of $D = 0$ since the mass asymmetric D vanishes.

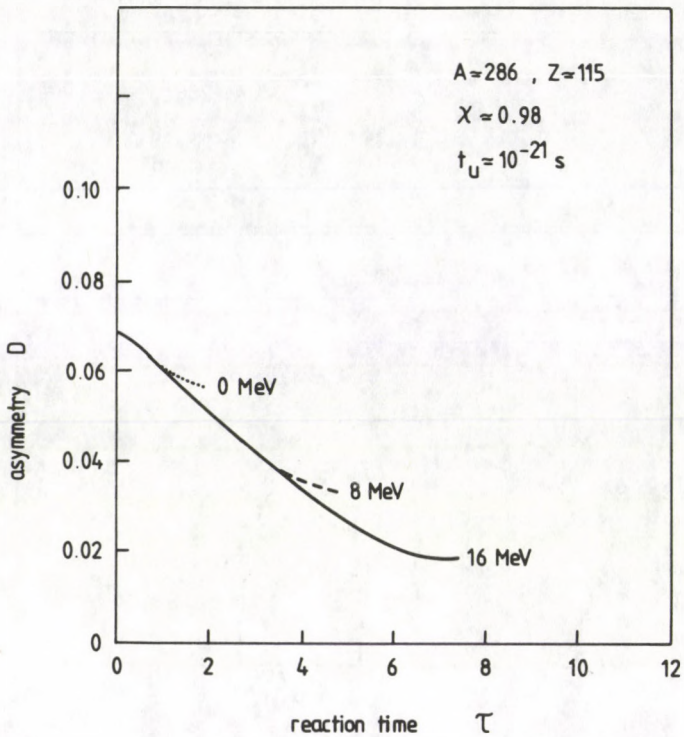

Fig. 11. The calculated trajectories of the asymmetry D of the system $^{286}X_{115}$ as a function of the dimensionless time τ for different values of the initial kinetic energy

3. Numerical calculations and results

In the present work, we introduced a theoretical study for the dynamics of the fusion of two heavy nuclei. The time evolution of our collective degrees of freedom has been studied. These trajectories are obtained by solving the equations of motion numerically with the fourth-order Runge–Kutta method. The time evolution in the vicinity of the touching spheres is taken to correspond to $S = 0$, $N = 0.25$ (due to numerical difficulties) and D is equal to the initial asymmetry of the given system. The initial injection dimensionless velocity denoted by $\left(\frac{dS(\tau=0)}{d\tau}\right)$ is given by the expression

$$\left(\frac{dS(\tau=0)}{d\tau}\right) = \frac{t_u c}{R}\left[\frac{8(1+3D)^2 \text{K.E.}}{M(1-D)^3}\right], \tag{15}$$

where c is the velocity of light. R_i, γ and $\rho\overline{\nu}$ are the radius of the fragment, the surface tension and the nucleon flux density, respectively. These fixed parameters which appeared in the present equations are taken to have the values [13]

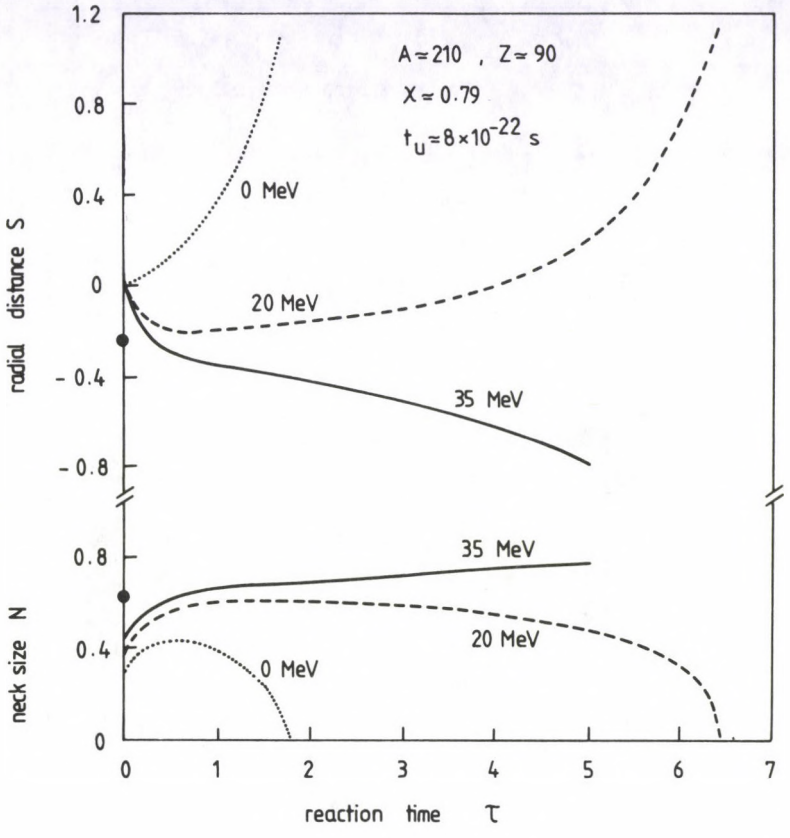

Fig. 12. The calculated trajectories of the radial distance S and the neck size N of the system $^{210}X_{90}$ as a function of the dimensionless time τ for zero asymmetry and different values of the initial kinetic energy

$$R_i = 1.224992 A_i^{1/3} \text{ fm},$$
$$\gamma = 0.951569(1 - 1.7826 I^2) \text{ MeV} \cdot \text{fm}^{-2},$$
$$I = (N - Z)/A$$

and

$$\varrho\overline{\nu} = 0.7974 \times 10^{-22} \text{ MeV} \cdot \text{s} \cdot \text{fm}^{-4}.$$

For all the systems considered presently, the target and projectile have a charge to mass ratio given by

$$\frac{Z_i}{A_i} = \frac{1}{2}\left[1 - \frac{0.4 A_i}{200 + A_i}\right], \tag{16}$$

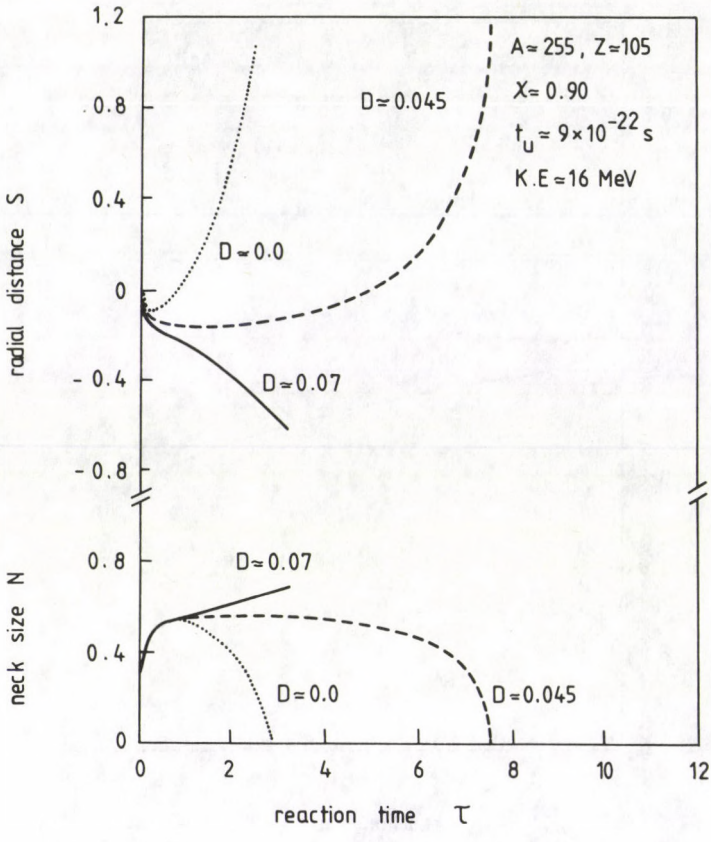

Fig. 13. The calculated trajectories of the radial distance S and the neck size N of the system $^{255}X_{105}$ as a function of the dimensionless time τ for 16 MeV initial kinetic energy and for different values of the asymmetry

where $i = 1, 2$ refers to either the target or the projectile. This ratio is satisfied for systems which lie along the valley of beta stability. The charge to mass ratio formula gives Z_i when A_i is known. The sum of the two atomic numbers gives the total number Z which is then divided between the two fragments following the ratio of their masses according to $Z_i = A_i(Z/A)$. We should like to point out that the different cases described in the present work are discussed according to the value of their fissibility parameters. A light system is considered with the case of the asymmetric collision of $A_1 = 70$ and $A_2 = 36$, for which the mass asymmetry $D \simeq 0.012$, and fissibility parameter of the total compound system $\chi \simeq 0.43$. The time evolutions of the present degrees of freedom resulting from applying the present dynamical model on this light system are given in Fig. 2. The system with zero initial injection kinetic above the Coulomb barrier goes towards a very compact shape without hesitation in a time of about $t \simeq 15\times10^{-22}$ s. The system also passes

the conditional saddle points with the parameter values $N_{s.p} \simeq 0.31$ and $S_{s.p} \simeq 0.25$ which are specified by the solid points drawn on the axes. The trajectory shown is that which corresponds to the compound system formation reaction.

For heavier asymmetric systems with $A_1 = 120$ and $A_2 = 73$ with mass asymmetry parameter $D \simeq 0.007$ and $\chi \simeq 0.73$, the situation is different and complex as shown in Figs 3–5. In Figs. 3–5, the time evolutions of the three degrees of freedom corresponding to different kinetic energies 0.6 and 10 MeV, are shown. In the case of zero injection kinetic energy, the neck grows rapidly, while the radial distance increases rapidly due to the Coulomb repulsion. The system is then stretched till the neck collapses and the reaction time becomes about 21×10^{-22} s. Since the asymmetry in this case shows no much change, the system cannot pass over the conditional saddle points which are $(0.55 - 0.06)$ and we also notice that the expected energy loss due to the deformation of the two separated fragments, and so the trajectory is classified as a deep-inelastic scattering reaction. For the case of initial injection kinetic energy with the value of 6 MeV, the system reaches its saddle point configuration with no kinetic energy remained. The system stays at this configuration until the continuous asymmetry decreasing, due to the mass drift, reaches a sufficient value that predominates the Coulomb repulsion and overcomes the nuclear attraction so that the system then starts to re-separate again.

In this case the reaction time is longer than that for the case of zero MeV and is about 56×10^{-22} s. Therefore, the results of this case with relatively long time of reaction together with the considerable amount of decrease in the asymmetry, about 0.004, lead us to classify this trajectory as a quasifission reaction. The third case in Figs 3–5 is the calculations of evolutions of our degrees of freedom for an injection kinetic energy of about 10 MeV. The kinetic energy in this case is sufficient to take the system over its saddle point configuration and the system automatically proceeds towards the compound configuration. The reaction time for this case is infinity which in practice would be equal to the compound nucleus life time. This case corresponds clearly to the compound system formation reaction.

The time evolution of our degrees of freedom has been calculated for a system with $A_1 = 200$ and $A_2 = 55$, with a mass asymmetry parameter $D \simeq 0.045$, and fissibility parameter $\chi \simeq 0.90$. The results of calculations for this system are shown in Figs 6–8 which are the same trajectories as obtained in Figs 3–5, but with higher injection kinetic energies than those in Figs 3–5, to compensate the increasing Coulomb repulsion. Increasing the fissibility parameter till reaching the value $\chi \simeq 1$, which corresponds to super heavy systems, a higher asymmetric configuration with $A_1 = 238$ and $A_2 = 48$, for which the mass asymmetry parameter $D \simeq 0.068$ and $\chi \simeq 0.98$ is considered. The time evolutions of the degrees of freedom are calculated for this system for different kinetic energies of 0.8 and 16 MeV. The results of the calculations for this super heavy system are shown in Figs 9–11. It is noticed that for super heavy systems with higher asymmetries, the different types of trajectories are obtained with energies nearly equal to those used for heavy systems with smaller asymmetries.

Now let us to consider the symmetric collision case. A symmetric collision system for which the value of the fissibility parameter is $\chi \simeq 0.79$ is studied. Cal-

culations of the evolutions of our degrees of freedom for this symmetric system are shown in Fig. 12. These results show that all types of trajectories are obtained, but with energies nearly equal to those used in Figs 6–8. This result leads us to the fact that the asymmetry effects are to decrease the required energy for proceeding the system towards spherical compound configurations. The effects of the asymmetry on a system with fissibility parameter $\chi \simeq 0.90$ are shown in Fig. 13, where the time evolutions are calculated for different values of the asymmetries of 0, 0.045 and 0.07. The injection kinetic energy given to the system for all different cases considered in Fig. 13 is the same and equal to 16 MeV. From Fig. 13 we see that the same three trajectories are obtained by changing the asymmetry and fixing the kinetic energy.

4. Discussion and conclusions

In the present work, we introduced a study for the asymmetric and symmetric cases of the dynamics of two heavy colliding nuclei with energies above the Coulomb barrier. The time evolutions of the dynamical variables considered in the present work are obtained by solving the dynamical equations of motion numerically. The effect of the initial radial kinetic energy on the fusion process has been investigated for the dynamics of different systems defined by their fissibility parameters. The compound system formation reaction is found to occur easily for light systems even with initial kinetic energy just equal to the Coulomb barrier. The compound system reaction mechanism appears in the case of light systems because of the predominance of the attractive surface tension with respect to the Coulomb repulsion. For the cases of medium and heavy systems, three types of trajectories are obtained. The obtained trajectories of the medium and heavy systems are found to depend on the energy given to the system. The different three types of trajectories are being deep-inelastic, quasi-fission or compound system formation reactions. The super heavy systems may be formed but with very large injection kinetic energies and large asymmetries. The absence of the asymmetry in the symmetric collision requires us to increase the initial kinetic energy to obtain the compound system formation.

Therefore, we can conclude from the present calculations that the effect of the asymmetry plays the same role as the injection kinetic energy on the dynamics of the fusion process.

References

1. R. Beck and D. H. E. Gross, Phys. Lett., *47B*, 143, 1973.
2. D. H. E. Gross and H. Kalinowski, Phys. Lett., *48B*, 302, 1974.
3. H. H. Deubler and K. Dietrich, Nucl. Phys., *A277*, 493, 1977.
4. J. R. Birkelund, J. R. Huizenga, J. N. De and D. Sperber, Phys. Rev. Lett., *40*, 1123, 1978.
5. W. J. Swiatecki, Phys. Scripta, *24*, 113, 1981.
6. J. P. Blocki, H. Feldmeier and W. J. Swiatecki, Nucl. Phys., *A459*, 145, 1986.
7. J. Blocki, K. Grotowski, R. Planeta and W. J. Swiatecki, Nucl. Phys., *A445*, 367, 1985.

8. W. J. Swiatecki, Nucl. Phys., *A376*, 275, 1982.
9. H. Sann, R. Bock, Y. T. Chu, A. Gobbi, A. Olmi, U. Lynen, W. Muller, S. Bjørnholm and H. Esbensen, Phys. Rev. Lett., *47*, 1248, 1981.
10. M. Blann and D. Akers, Phys. Rev., *C26*, 465, 1982.
11. S. Bjørnholm and W. J. Swiatecki, Nucl. Phys., *A391*, 471, 1982.
12. J. Randrup and W. J. Swiatecki, Nucl. Phys., *A429*, 105, 1984.
13. R. Donangelo and L. F. Canto, Nucl. Phys., *A451*, 349, 1986.
14. F. L. H. Wolfs, W. Henning, K. E. Rehm, J. P. Schiffer, Phys. Lett., *B196*, 113, 1987.
15. C. E. Aguiar, V. C. Barbose, L. F. Canto and R. Donangelo, Phys. Rev., *C38*, 541, 1988.
16. A. Osman, S. S. Abdel-Aziz and M. M. Gogary, Indian J. Theor. Phys., *37*, 1991.
17. J. Blocki, Y. Boneh, J. R. Nix, J. Randrup, M. Robel, A. J. Sierk and W. J. Swiatecki, Ann. Phys. (NY), *113*, 330, 1978.

Acta Physica Hungarica 71 (1–2), pp. 117–128 (1992)

GAUGED Q BALLS ADMITTING A $U(1) \times U(1)$ GAUGE SYMMETRY

C. WOLF

Department of Physics, North Adams College
North Adams, MA (01247) USA

(Received in revised form 28 May 1991)

A composite system of two complex scalar fields coupled to different Abelian gauge fields is studied in curved space. The mass and the conserved global charge of the configuration are expressed as functions of the scalar fields and gauge fields through an approximate solution.

1. Introduction

The term Q ball has emerged from the recognition on the part of Coleman that a theory admitting a global symmetry possesses a conserved charge or a set of conserved charges that may serve to stabilize the configuration of fields against collapse [1]. The critical criteria of the Q ball is that the mass of the configuration is less than that of the corresponding free pions of the theory. The fulfillment of this criteria would prevent the decay of the field configuration to pions. However, even if this first criteria is not met, a configuration of fields admitting a global symmetry with a stationary solution may still survive providing it is stable to other perturbations such as gravitational perturbations or any slight temporal variations of the field variables. The configuration in this latter sense sense might be stable and still be unstable over long times to decay into pions of the linearized theory. In fact, Cohen et al [2] have studied L balls which are configurations of scalar field and spinor fields inspired by the Gelmini–Roncadelli model of neutrino mass generation [3], these L balls admitting a conserved lepton number are stable except for slow decay into fermions at the surface. In the present note, we are interested in the general stationary solution of two charged scalar fields, admitting a $U(1) \times U(1)$ global symmetry also admitting a gauge symmetry and thus coupled to two gauge fields and do not require the solution to fulfil the first requirement of stability. We assume that the classical stationary solution is stable with respect to small field variations within a certain range of parameter space and calculate the mass and the conserved global charge of the composite system. In the conclusion, we will discuss two alternative methods to test for stability to small perturbations.' Actually gauged Q balls were first studied by Lee et al [4] who showed that a charged scalar field coupled to a gauge field admits a Q ball solution provided the gauge charge does not grow too large. This situation is somewhat similar to a large Z nucleus which becomes unstable due to Coulomb repulsion. Our development somewhat

resembles that of [4], only we introduce two scalar fields coupled to separate gauge fields with two different coupling constants. Since global symmetries could very well be an accidental result of an unbroken G.U.T. gauge symmetry at a high scale, we might expect our analysis to apply to any theory with two surviving $U(1)$ factors after the G.U.T. group is broken [5]. We also allow for nonstandard couplings between the scalar fields that may represent effective interactions after the fermions are integrated out of the theory. Our analysis is also in curved space and in a separate note, we have studied an $SO(2)$ Q ball in general relativity with the consequence that the Q ball was stable provided it did not grow too large [6]. From the point of view of both particle physics and cosmology the following analysis is intended to simulate gauge Higgs configurations of a non-topological nature that might somewhat resemble the soliton stars studied by Friedberg et al [7] wherein the spectrum of allowed masses has a dependence on the coupling constants and gauge charges that may well serve to classify them in an astrophysical setting with certain regularities revealing their fundamental gauge structure. If such a classification ever occurred it would also ascertain the presence of extra $U(1)$ factors in particle theory long before accelerators could ascertain their presence.

2. Gauged Q balls with two Abelian gauge symmetries

We begin our analysis by writing the Lagrangian of gravity and two charged scalar fields coupled to separate gauge fields with coupling constants given by

$$g_1 = \frac{\overline{g}_{1-}}{\hbar c}, \quad g_2 = \frac{\overline{g}_{2-}}{\hbar c},$$

as

$$L = \frac{c^4}{16\pi G} R\sqrt{-g} + L_M,$$

where

$$\begin{aligned} L_M = &\Bigg\{ D_\mu \Phi_1 (D^\mu \Phi_1)\# + D_\mu \Phi_2 (D^\mu \Phi_2)\# - \frac{A_2}{4}\left(\Phi_1\Phi_1\# - \frac{A_1}{A_2}\right)^2 \\ &- \frac{\overline{A}_2}{4}\left(\Phi_2\Phi_2\# - \frac{\overline{A}_1}{\overline{A}_2}\right)^2 + \alpha_0 \frac{\Phi_1\Phi_1\#}{4} F_{1\mu\nu}F_1^{\mu\nu} + \frac{\beta_0}{4}\Phi_2\Phi_2\# F_{2\mu\nu}F_2^{\mu\nu} \Bigg\}\sqrt{-g} \\ &+ \left(-\frac{1}{16\pi}F_{1\mu\nu}F_1^{\mu\nu} - \frac{1}{16\pi}F_{2\mu\nu}F_2^{\mu\nu}\right)\sqrt{-g}. \end{aligned} \tag{2.1}$$

Here, $A_{1\mu}, A_{2\mu}$ are the two gauge fields and $F_{1\mu\nu}, F_{2\mu\nu}$ the field tensors. Also, $\Phi_1\Phi_2$ are two scalar fields with

$$\begin{aligned} D_\mu \Phi_1 &= (\partial_\mu + ig_1 A_{1\mu})\Phi_1, \\ D_\mu \Phi_1 &= (\partial_\mu + ig_2 A_{2\mu})\Phi_2, \end{aligned}$$

representing the covariant derivatives under each $U(1)$ factor. The two potentials are specified by parameters A_1, A_2 and $\overline{A}_1, \overline{A}_2$ and the non-standard couplings specified by α_0, β_0. Note the distinction between $A_1, A_2, \overline{A}_1, \overline{A}_2$ which refer to the constants in the two Higgs-like potentials for the scalar fields and $A_{1\mu}, A_{2\mu}$ which refer to the vector gauge fields of the first and second $U(1)$ factors. As mentioned in the introduction, the non-standard coupling may arise as a result of integrating out fermions generating an effective coupling or perhaps as a result of compactification from a higher dimensional Kaluza Klein theory [8]. For a solution, we have the following form for the charged scalar fields

$$\Phi_1 = \frac{f_1(r)}{\sqrt{2}} e^{i\omega_1 t}, \Phi_2 = \frac{f_2(r)}{\sqrt{2}} e^{i\omega_2 t}.$$

Here we have imposed the condition of stationarity and spherical symmetry through $f_1(r)$ and $f_2(r)$. Actually we will demonstrate from the field equation for Φ_1, Φ_2 that the above form for the solutions are actually solutions to the field equations. The functions $f_1(r)$, $f_2(r)$ are the stationary parts and the time dependant is specified by $e^{i\omega_1 t}$, $e^{i\omega_2 t}$ which will be shown to cancel out of the field equations after substitution. The first scalar field carries one unit of gauge charge under the first $U(1)$ symmetry and the second scalar field carries one unit of gauge charge under the second $U(1)$ symmetry. Under the global $U(1) \times U(1)$ symmetry, the fields Φ_1 Φ_2 transform as

$$\delta\Phi_1 = i\alpha\Phi_1, \ \delta\Phi_1\# = -i\alpha\Phi_1\# \tag{2.2}$$

under the first global $U(1)$ and

$$\delta\Phi_2 = i\alpha\Phi_2, \ \delta\Phi_2\# = -i\alpha\Phi_2\#, \tag{2.3}$$

under the second global $U(1)$. The global symmetries will generate the global Q charges. For the gauge fields we have

$$\begin{aligned} A_{1_i} = 0, A_{1_4} = \chi_1(r), \ E_1 = F_{1_{14}} = -\chi_1'(r), \\ A_{2_i} = 0, A_{2_4} = \chi_2(r), \ E_2 = F_{2_{14}} = -\chi_2'(r), \\ i = 1, 2, 3, \end{aligned} \tag{2.4}$$

where the prime means differentiation with respect to r with the only surviving component being the fourth components for the scalar potentials. For the energy momentum tensor corresponding to the scalar-gauge field part of the Lagrangian in Eq. (2.1) we have

$$T_{\mu\nu} = \frac{2}{\sqrt{-g}} \frac{\partial L_M}{\partial g^{\mu\nu}}$$

$$
\begin{aligned}
&= D_\mu\Phi_1(D_\nu\Phi_1)^{\#} + (D_\mu\Phi_1)\#D_\mu\Phi_1 + (D_\mu\Phi_2)(D_\nu\Phi_2)\# \\
&(D_\mu\Phi_2)\#(D_\nu\Phi_2) - g_{\mu\nu}\,(D_\alpha\Phi_1(D^\alpha\Phi_1)\# + D_\alpha\Phi_2(D^\alpha\Phi_2)\#) \\
&+ g_{\mu\nu}\left[\frac{A_2}{4}\left(\Phi_1\Phi_1\# - \frac{A_1}{A_2}\right)^2 + \frac{\overline{A}_2}{4}\left(\Phi_2\Phi_2\# - \frac{\overline{A}_1}{\overline{A}_2}\right)^2\right] \\
&- \frac{\alpha_0\Phi_1\Phi_1\#}{4}(F_{1\alpha\beta}F_1^{\alpha\beta})g_{\mu\nu} + \alpha_0\Phi_1\Phi_1\#(F_{1\mu\alpha}F_{1\nu}^{\alpha}) \\
&- \frac{\beta_0\Phi_2\Phi_2\#}{4}(F_{2\alpha\beta}F_2^{\alpha\beta})g_{\mu\nu} + \beta_0\Phi_2\Phi_2\#(F_{2\mu\alpha}F_{2\nu}^{\alpha}) \\
&+ \frac{1}{16\pi}g_{\mu\nu}(F_{1\alpha\beta}F_1^{\alpha\beta} + \frac{1}{16\pi}g_{\mu\nu}(F_{2\alpha\beta}F_2^{\alpha\beta}) \\
&- \frac{1}{4\pi}F_{1\mu\alpha}F_{1\nu}^{\alpha} - \frac{1}{4\pi}F_{2\mu\alpha}F_{2\nu}^{\alpha}.
\end{aligned}
\tag{2.5}
$$

For the boundary conditions on the scalar and gauge fields, we have

$$
\begin{aligned}
\Phi_1\Phi_1\# &= \frac{A_1}{A_2}, \\
\text{giving } f_1 &= \sqrt{\frac{2A_1}{A_2}} \text{ at } r = 0, \\
\Phi_2\Phi_2\# &= \frac{\overline{A}_1}{\overline{A}_2}, \\
\text{giving } f_2 &= \sqrt{\frac{2\overline{A}_1}{\overline{A}_2}} \text{ at } r = 0.
\end{aligned}
\tag{2.6}
$$

At $r = R$ (the radius of the configuration) we choose the false vacuum, giving

$$
\begin{aligned}
&\Phi_1\Phi_1\# = 0 \text{ giving } f_1(r) = 0 \text{ at } r = R \text{ and } r > R, \\
&\Phi_2\Phi_2\# = 0 \text{ giving } f_2(r) = 0 \text{ at } r = R \text{ and } r > R.
\end{aligned}
\tag{2.7}
$$

For the gauge potentials we choose for the boundary condition

$$
\begin{aligned}
\chi_1(R) &= \frac{e_1}{R},\ \chi_1'(R) = -\frac{e_1}{R^2} \text{ at } r = R, \\
\chi_2(R) &= \frac{e_2}{R},\ \chi_2'(R) = -\frac{e_2}{R^2}.
\end{aligned}
\tag{2.8}
$$

Here e_1, e_2 are the gauge charges or electric-like charges of the two separate $U(1)$ groups and the potentials and fields are matched to the exterior potentials and fields which are Coulomb-like. If we vary the Lagrangian Eq. (2.1) with respect to the fields Φ_1, $\Phi_1^{\#}$, Φ_2, $\Phi_{2\#}$, $A_{1\mu}$, $A_{2\mu}$ we obtain

$$
\begin{aligned}
&\sqrt{-g}\left[ig_1A_{1\alpha}\partial_\beta\Phi_1^{\#}g^{\beta\alpha} + g_1^2A_{1\alpha}A_{1\beta}g^{\beta\alpha}\Phi_1^{\#}\right. \\
&\left.-\frac{\Phi_1^{\#}A_2}{2}\left(\Phi_1\Phi_1^{\#} - \frac{A_1}{A_2}\right) + \frac{\alpha_0\Phi_1^{\#}F_{1\mu\nu}F_1^{\mu\nu}}{4}\right] \\
&\qquad -\partial_\mu[\sqrt{-g}(\partial_\beta\Phi_1^{\#}g^{\mu\beta} - ig_1A_{1\beta}\Phi_1^{\#}g^{\mu\beta}] = 0,
\end{aligned}
\tag{2.9}
$$

with $i \to -i$, $\Phi_1 \leftrightarrow \Phi_1^{\#}$ to obtain the equation for $\Phi_1^{\#}$. Also for Φ_2

$$\sqrt{-g}\left[ig_2 A_{2\alpha}\partial_\beta \Phi_2^{\#} g^{\beta\alpha} + g_2^2 A_{2\alpha}A_{2\beta}g^{\beta\alpha}\Phi_2^{\#} - \frac{\Phi_2^{\#}\overline{A}_2}{2}\left(\Phi_2\Phi_2^{\#} - \frac{\overline{A}_1}{\overline{A}_2}\right) + \frac{\beta_0 \Phi_2^{\#} F_{2\mu\nu}F_2^{\mu\nu}}{4}\right] - \partial_\mu[\sqrt{-g}(\partial_\beta \Phi_2^{\#} g^{\mu\beta} - ig_2 A_{2\beta}\Phi_2^{\#} g^{\mu\beta})] = 0, \tag{2.10}$$

with $i \to -i$, $\Phi_2 \leftrightarrow \Phi_2^{\#}$ to obtain the equation for $\Phi_2^{\#}$. The field equation for $A_{1\mu}$ is

$$\frac{\partial}{\partial x^\nu}\left(\frac{1}{4\pi}\sqrt{-g}F_1^{\mu\nu}\right) - \frac{\partial}{\partial x^\nu}\left(\alpha_0 \Phi_1 \Phi_1^{\#} F_1^{\mu\nu}\sqrt{-g}\right) + g^{\beta\mu} ig_1 \Phi_1(\partial_\beta \Phi_1^{\#} - ig_1 A_{1\beta}\Phi_1^{\#})\sqrt{-g} - ig_1 \Phi_1^{\#} g^{\mu\alpha}(\partial_\alpha \Phi_1 + ig_1 A_{1\alpha}\Phi_1)\sqrt{-g} = 0 \tag{2.11}$$

and for $A_{2\mu}$ is

$$\frac{\partial}{\partial x^\nu}\left(\frac{1}{4\pi}\sqrt{-g}F_2^{\mu\nu}\right) - \frac{\partial}{\partial x^\nu}(\beta_0 \Phi_2 \Phi_2^{\#} F_2^{\mu\nu}\sqrt{-g}) + g^{\beta\mu} ig_2 \Phi_2(\partial_\beta \Phi_2^{\#} - ig_2 A_{2\beta}\Phi_2^{\#})\sqrt{-g} - ig_2 \Phi_2^{\#} g^{\mu\alpha}(\partial_\alpha \Phi_2 + ig_2 A_{2\alpha}\Phi_2)\sqrt{-g} = 0. \tag{2.12}$$

Our next task is to calculate the formal expressions for the conserved global charges, by varying Eq. (2.1) with respect to Φ_1, $\Phi_1^{\#}$ we have for the global variation of Φ_1, $\Phi_1^{\#}$ under the first global symmetry

$$\delta L = \frac{\partial L}{\partial \Phi_1}\delta\Phi_1 + \frac{\partial L}{\partial \Phi_1 \#}\delta\Phi_1^{\#} + \frac{\partial L}{\partial \Phi_{1,\mu}}\delta\Phi_{1,\mu} + \frac{\partial L}{\partial \Phi_{1,\mu}^{\#}}\delta\Phi_{1,\mu}^{\#} = 0. \tag{2.13}$$

Using the field equations for Φ_1, $\Phi_1\#$ in Eq. (2.13) gives the conserved current

$$\frac{\partial}{\partial x^\mu}\left(\frac{\partial L}{\partial \Phi_{1,\mu}}\delta\Phi_1 + \frac{\partial L}{\partial \Phi_{1,\mu}^{\#}}\delta\Phi_1 \#\right) = 0. \tag{2.14}$$

When we multiply Eq. (2.14) by $dr\, d\Theta\, d\Phi$ and integrate over the volume of the Q matter configuration (0 to R) we have upon inserting the variation from Eq. (2.2) into Eq. (2.14) at the spatial boundaries the following conserved Q charge

$$Q_1 = \int\int\int\left(\frac{\partial L}{\partial \Phi_{1,4}}\delta\Phi_1 + \frac{\partial L}{\partial \Phi_{1,4}^{\#}}\delta\Phi_1 \#\right) dr\, d\Theta\, d\Phi. \tag{2.15}$$

The time derivative of Eq. (2.15) vanishes from Eq. (2.14) and the spatial components of Eq. (2.14) vanishes upon integration over r, Θ, Φ from the form of the variation in Eq. (2.2).

Also, for the field Φ_2 and the second $U(1)$ factor we have

$$Q_2 = \int\int\int \left(\frac{\partial L}{\partial \Phi_{2,4}} \delta\Phi_2 + \frac{\partial L}{\partial \Phi^{\#}_{2,4}} \delta\Phi_2 \# \right) dr\, d\Theta\, d\Phi. \tag{2.16}$$

For the metric, we choose ($x^4 = ct$, $x^1 = r$, $x^2 = \Theta$, $x^3 = \Phi$) the spherical symmetric metric.

$$(ds)^2 = e^{\nu}(dx^4)^2 - e^{\lambda}(dr)^2 - r^2(d\Theta)^2 - r^2 \sin^2\Theta(d\Phi)^2. \tag{2.17}$$

Eq. (2.15) gives, upon using the solution

$$\Phi_1 = \frac{f_1}{\sqrt{2}} e^{i\omega t}$$

and the definition of A_{1_4} in Eq. (2.4) along with the metric in Eq. (2.17)

$$Q_1 = 4\pi \int_0^R \left(\frac{\omega_1}{c} (f_1)^2 + g_1 (f_1)^2 \chi_1 \right) e^{(\lambda - \nu/2)} r^2 dr. \tag{2.18}$$

Also, for Eq. (2.16) we have

$$Q_2 = 4\pi \int_0^R \left(\frac{\omega_2}{c} (f_2)^2 + g_2 (f_2)^2 \chi_2 \right) e^{(\lambda - \nu/2)} r^2 dr. \tag{2.19}$$

Eq. (2.18) and Eq. (2.19) can be used to solve for ω_1, ω_2 in terms of Q_1, Q_2 and the coupling constants g_1, g_2. Our next task is to obtain the equations to solve for f_1, f_2, χ_1, χ_2. Firstly, if the form of the solution for the scalar field is

$$\frac{f_1(r)}{\sqrt{2}} e^{i\omega_1 t}, \quad \frac{f_2(r)}{\sqrt{2}} e^{i\omega_2 t}, \tag{2.20}$$

we find that substitution of the solutions in Eq. (2.9), Eq. (2.10), Eq. (2.11), Eq. (2.12) along with the expressions for $A_{1\mu}$ and $A_{2\mu}$ given by Eq. (2.4) allows for the cancellation of the time dependant part since in Eq. (2.9) and Eq. (2.10) the scalar field appears in a linear fashion and in terms $(\Phi_1 \Phi_1^{\#})\Phi_1^{\#}$, $(\Phi_2 \Phi_2^{\#})\Phi_2^{\#}$, in Eq. (2.11) and Eq. (2.12) Φ_1, Φ_2 appear as $\Phi_1 \Phi_1^{\#}$, $\Phi_2 \Phi_2^{\#}$, $\Phi_1 \partial_\beta \Phi_1^{\#}$, $\Phi_2 \partial_\beta \Phi_2^{\#}$, etc. which leads to cancellation of the temporal part. We will find shortly that ω_1, ω_2 are calculated from the conserved global charges. Substitution of Eq. (2.20) along with Eq. (2.4) for

$$A_{1_4} = \chi_1, \; A_{2_4} = \chi_2$$

into Eq. (2.9), Eq. (2.10), Eq. (2.11) and Eq. (2.12) gives where we use the approximation $e^{\lambda} \simeq e^{\nu} \simeq 1$ for the interior of the Q ball configuration $(0 < r < R)$ to calculate approximate values for the scalar field and gauge fields

$$\left[\frac{f_1\omega_1^2}{c^2} + g_1^2\chi_1^2 f_1 + \frac{2g_1 f_1\chi_1\omega_1}{c} - \frac{\alpha_0}{2}f_1(\chi_{1,r})^2 - \frac{A_2 f_1}{2}\left(\frac{f_1^2}{2} - \frac{A_1}{A_2}\right)\right]r^2 + \frac{d}{dr}(r^2 f_{1,r}) = 0, \tag{2.21}$$

$$\left[\frac{f_2\omega_2^2}{c^2} + g_2^2\chi_2^2 f_2 + \frac{2g_2 f_2\chi_2\omega_2}{c} - \frac{\beta_0}{2}f_2(\chi_{2,r})^2 - \frac{\overline{A}_2 f_2}{2}\left(\frac{f_2^2}{2} - \frac{\overline{A}_1}{\overline{A}_2}\right)\right]r^2 + \frac{d}{dr}(r^2 f_{2,r}) = 0, \tag{2.22}$$

$$r^2\left(g_1^2\chi_1 f_1^2 + \frac{g_1 f_1^2\omega_1}{c}\right) - \frac{d}{dr}\left(\frac{r^2(\chi_{1,r})}{4\pi} - \frac{\alpha_0 f_1^2(\chi_{1,r})r^2}{2}\right) = 0, \tag{2.23}$$

$$r^2\left(g_2^2\chi_2 f_2^2 + \frac{g_2 f_2^2\omega_2}{c}\right) - \frac{d}{dr}\left(\frac{r^2(\chi_{2,r})}{4\pi} - \frac{\beta_0 f_2^2(\chi_{2,r})r^2}{2}\right) = 0. \tag{2.24}$$

To solve Eq. (2.21), Eq. (2.22), Eq. (2.23) and Eq. (2.24) approximately, we first write down the power series solution up to the third power

$$\begin{aligned} f_1 &= a_0 + a_1 r + a_2 r^2 + a_3 r^3, \\ f_2 &= \overline{a}_0 + \overline{a}_1 r + \overline{a}_2 r^2 + \overline{a}_3 r^3, \\ \chi_1 &= b_0 + b_1 r + b_2 r^2 + b_3 r^3, \\ \chi_2 &= \overline{b}_0 + \overline{b}_1 r + \overline{b}_2 r^2 + \overline{b}_3 r^3, \end{aligned} \tag{2.25}$$

Inserting Eq. (2.25) into Eq. (2.21), Eq. (2.22), Eq. (2.23) and Eq. (2.24) and insisting that the coefficients of r up to and including the third power in r vanish gives

$$\begin{aligned} a_1 &= 0,\ a_3 = 0,\ a_0 = \text{ to be determined}, \\ b_1 &= 0,\ b_3 = 0,\ b_0 = \text{ to be determined}, \\ a_2 &= -\frac{1}{6}\left[\frac{\omega_1^2}{c^2}a_0 + g_1^2 b_0^2 a_0 + \frac{2g_1\omega_1 a_0 b_0}{c} + \frac{A_1 a_0}{2} - \frac{A_2 a_0^3}{4}\right], \\ b_2 &= -\frac{g_1^2 b_0 a_0^2 - (a_0^2\omega_1 g_1)/c}{-(\frac{3}{2\pi}) + 3a_0^2\alpha}. \end{aligned} \tag{2.26}$$

Also

$$\begin{aligned} \overline{a}_1 &= 0,\ \overline{a}_3 = 0,\ \overline{a}_0 = \text{ to be determined}, \\ \overline{b}_1 &= 0,\ \overline{b}_3 = 0,\ \overline{b}_0 = \text{ to be determined}, \\ \overline{a}_2 &= -\frac{1}{6}\left[\frac{\omega_2^2}{c^2}\overline{a}_0 + g_2^2\overline{b}_0^2\overline{a}_0 + \frac{2g_2\omega_2\overline{a}_0\overline{b}_0}{c} + \frac{\overline{A}_1\overline{a}_0}{2} - \frac{\overline{A}_2\overline{a}_0^3}{4}\right], \\ \overline{b}_2 &= -\frac{g_2^2\overline{b}_0\overline{a}_0^2 - (\overline{a}_0^2\omega_2 g_2)/c}{-(\frac{3}{2\pi}) + 3\overline{a}_0^2\beta}. \end{aligned} \tag{2.27}$$

We now use the boundary condition in Eq. (2.6), Eq. (2.7) and Eq. (2.8) and add on the quartic term in each expansion of Eq. (2.25) and demand the solution obey the boundary conditions in Eq. (2.6), Eq. (2.7) and Eq. (2.8);

$$a_0 = \sqrt{\frac{2A_1}{A_2}},\ \sqrt{\frac{2A_1}{A_2}} + a_2R^2 + a_4R^4 = 0,$$
$$\bar{a}_0 = \sqrt{\frac{2\bar{A}_1}{\bar{A}_2}},\ \sqrt{\frac{2\bar{A}_1}{\bar{A}_2}} + \bar{a}_2R^2 + \bar{a}_4R^4 = 0. \tag{2.28}$$

This gives

$$a_4 = \frac{-\sqrt{\frac{2A_1}{A_2}} - a_2R^2}{R^4}, \tag{2.29}$$

$$\bar{a}_4 = \frac{-\sqrt{\frac{2\bar{A}_1}{\bar{A}_2}} - \bar{a}_2R^2}{R^4}, \tag{2.30}$$

where a_2, $\bar{a}_2$ are expressible in terms of a_0, $\bar{a}_0$ from Eq. (2.26) and Eq. (2.27). Also, for the potential $r = R$ we have from Eq. (2.8)

$$b_0 + b_2R^2 + b_4R^4 = \frac{e_1}{R},$$
$$2b_2R + 4b_4R^3 = -\frac{e_1}{R^2}. \tag{2.31}$$

Also,

$$\bar{b}_0 + \bar{b}_2R^2 + \bar{b}_4R^4 = \frac{e_2}{R},$$
$$2\bar{b}_2R + 4\bar{b}_4R^3 = -\frac{e_2}{R^2}. \tag{2.32}$$

Using b_2 from Eq. (2.26), and eliminating b_4 from the boundary conditions in Eq. (2.31), and solving for b_2 and then equating the two expressions for b_2 gives the following expressions for b_0

$$b_0 = \frac{\frac{5e_1}{2R^3} + \frac{(a_0^2\omega_1 g_1)/c}{-(3/2)\pi + 3a_0^2\alpha_0}}{\frac{2}{R^2} - \left(\frac{g_1^2 a_0^2}{3a_0^2\alpha_0 - (3/2)\pi}\right)}. \tag{2.33}$$

Finally, solving Eq. (2.31) for b_4 gives

$$b_4 = \frac{-e_1/R^2 - 2b_2R}{4R^3}. \tag{2.34}$$

Similarly for $\bar{b}_0$, $\bar{b}_4$ we have

$$\bar{b}_0 = \frac{\frac{5e_2}{2R^3} + \frac{(\bar{a}_0^2\omega_2 g_2/c}{-(3/2)\pi+3\bar{a}_0^2\beta_0}}{\frac{2}{R^2} - \left(\frac{g_2^2\bar{a}_0^2}{3\bar{a}_0^2\beta_0-(3/2)\pi}\right)},$$

$$b_4 = \frac{-e_2/R^2 - 2b_2R}{4R^3}. \tag{2.35}$$

We summarize by writing

$$\begin{aligned}
a_0 =& \sqrt{\frac{2A_1}{A_2}},\ a_1 = a_3 = 0,\\
a_2 =& -\frac{1}{6}\left[\frac{\omega_1^2}{c^2}a_0 + g_1^2 b_0^2 a_0 + \frac{2g_1\omega_1 a_0 b_0}{c} + \frac{A_1 a_0}{2} - \frac{A_2 a_0^3}{4}\right],\\
a_4 =& \frac{-\sqrt{\frac{2A_1}{A_2}} - a_2R^2}{R^4},\\
b_0 =& \frac{\frac{5e_1}{2R^3} + \frac{(a_0^2\omega_1 g_1)/c}{-(3/2)\pi+3a_0^2\alpha_0}}{\frac{2}{R^2} - \left(\frac{g_1^2 a_0^2}{3a_0^2\alpha_0-(3/2)\pi}\right)},\\
b_1 =& b_3 = 0,\\
b_2 =& -\frac{g_1^2 b_0 a_0^2 - (a_0^2\omega_1 g_1)/c}{-(3/2)\pi + 3a_0^2\alpha}.\\
b_4 =& \frac{-e_1/R^2 - 2b_2R}{4R^3}.
\end{aligned} \tag{2.36}$$

With similar expressions for $\bar{a}_0$, $\bar{a}_2$, $\bar{a}_4$, $\bar{b}_0$, $\bar{b}_2$, $\bar{b}_4$ with $g_1 \leftrightarrow g_2$, $A_1 \leftrightarrow \bar{A}_1$, $A_2 \leftrightarrow \bar{A}_2$, $\omega_1 \leftrightarrow \omega_2$, $\alpha_0 \leftrightarrow \beta_0$, also $\bar{a}_1 = \bar{a}_3 = 0$, $\bar{b}_1 = b_3 = 0$.

Our next task is to calculate the exterior metric and match it to the interior metric in order to calculate the mass of the Q configuration. From Eq. (2.5) we have for $r > R$

$$T_1^1 = T_4^4 = \frac{1}{8\pi}(E_1)^2 e^{-(\lambda+\nu)} + \frac{1}{8\pi}(E_2)^2 e^{-(\lambda+\nu)} + \frac{A_1^2}{4A_2} + \frac{\bar{A}_1^2}{4\bar{A}_2}. \tag{2.37}$$

For the Einstein equations upon varying Eq. (2.1) with respect to $g_{\mu\nu}$ gives

$$R_{\mu\nu} - \frac{1}{2}Rg_{\mu\nu} = \frac{-8\pi G}{c^4}T_{\mu\nu}. \tag{2.38}$$

Using the spherically symmetric metric in Eq. (2.17) and the Einstein equations in Eq. (2.38) along with the form of the energy momentum tensor in Eq. (2.37) we have $(\lambda + \nu) = 0$ for $r > R$. The $\binom{4}{4}$ component of the Einstein equation gives

$$\frac{d}{dr}(re^{-\lambda}) = 1 - \frac{8\pi G}{c^4}r^2 T_4^4. \tag{2.39}$$

Now the field equation for $F_{1\mu\nu}F_{2\mu\nu}$ for $r > R$ are

$$\frac{\partial}{\partial x^\nu}\left(\sqrt{-g}F_1^{\mu\nu}\right) = 0; \quad \frac{\partial}{\partial x^\nu}\left(\sqrt{-g}F_2^{\mu\nu}\right) = 0$$

upon varying Eq. (2.1) with respect to $A_{1\mu}$, $A_{2\mu}$; this gives, upon using the condition $\lambda + \nu = 0$

$$F_{1_{14}} = E_1(r) = \frac{e_1}{r^2}, \; F_{2_{14}} = E_2(r) = \frac{e_2}{r^2} \text{ for } r > R. \tag{2.40}$$

Here the scalar field does not contribute to the equations for $F_{1\mu\nu}$, $F_{2\mu\nu}$ for $r > R$ since $|\Phi_1| = 0$, $|\Phi_2| = 0$ for $r > R$. Inserting Eq. (2.40) into Eq. (2.37) and then inserting this value for T_4^4 into the Einstein equation in Eq. (2.39) we have upon integration

$$e^{-\lambda} = 1 - \frac{2GM}{rc^2} + \frac{Ge_1^2}{r^2c^4} + \frac{Ge_2^2}{r^2c^4} - \frac{8\pi G}{3c^4}r^2\left(\frac{A_1}{4A_2} + \frac{\overline{A}_1^2}{4\overline{A}_2}\right), \tag{2.41}$$

where we identified the integration constant with the mass of the Q configuration. We next evaluate $e^{-\lambda}$ for $r < R$ and match it to Eq. (2.41) to obtain an expression for the mass of the Q configuration, we first calculate T_4^4 for $r < R$ from Eq. (2.5) with the use of the solutions

$$\Phi_1 = \frac{f_1}{\sqrt{2}}e^{i\omega_1 t}, \; \Phi_2 = \frac{f_2}{\sqrt{2}}e^{i\omega_2 t},$$

$$\begin{aligned}
T_4^4 =& e^{-\nu}\left[\frac{\omega_1^2 f_1^2}{2c^2} + \frac{g_1^2 f_1^2 \chi_1^2}{2} + \frac{g_1\chi_1 f_1^2\omega_1}{c}\right] + \frac{e^{-\lambda}(f_{1,r})^2}{2} \\
&+ e^{-\nu}\left[\frac{\omega_2^2 f_2^2}{2c^2} + \frac{g_2^2 f_2^2 \chi_2^2}{2} + \frac{g_2\chi_2 f_2^2\omega_2}{c}\right] + \frac{e^{-\lambda}(f_{2,r})^2}{2} \\
&+ \frac{A_2}{4}\left(\frac{f_1^2}{2} - \frac{A_1}{A_2}\right) + \frac{\overline{A}_2}{4}\left(\frac{f_2^2}{2} - \frac{\overline{A}_1}{\overline{A}_2}\right)^2 \\
&+ \frac{1}{8\pi}(\chi_{1,r})^2 e^{-(\nu+\lambda)} - \frac{\alpha_0 f_1^2}{4}(\chi_{1,r})^2 e^{-(\nu+\lambda)} \\
&+ \frac{1}{8\pi}(\chi_{2,r})^2 e^{-(\nu+\lambda)} - \frac{\beta_0 f_2^2}{4}(\chi_{2,r})^2 e^{-(\nu+\lambda)}.
\end{aligned} \tag{2.42}$$

In Eq. (2.42) we next approximate

$$e^\nu \simeq e^\lambda \simeq 1$$

and using the expressions for f_1, f_2, χ_1, χ_2 from Eq. (2.25) with the quartic term added and the expressions for the coefficients from Eq. (2.36) with f_2, χ_2 being found from $g_1 \to g_2\omega_1 \to \omega_2$, $\alpha_0 \to \beta_0$ we have, from Eq. (2.39)

$$(e^{-\lambda})_R = 1 - \frac{8\pi G}{c^4 R}\int_0^R r^2 T_4^4 dr \quad \text{for} \quad r = R. \tag{2.43}$$

When Eq. (2.43) is matched to Eq. (2.41) at $r = R$, we may calculate the mass of the gauged Q configuration. To eliminate ω_1, ω_2 we may solve Eq. (2.18) and Eq. (2.19) in terms of the conserved Q charges Q_1, Q_2 and the coupling constants g_1, g_2 along with the solutions found in Eq. (2.36) containing the parameters α_0, β_0, A_1, A_2, $\overline{A}_1$, $\overline{A}_2$. This allows for the expression of the mass of the gauged Q configuration in terms of the two global charges, the electric-like charges e_1, e_2; the coupling constants g_1, g_2 and the parameters α_0, β_0, A_1, A_2, $\overline{A}_1$, $\overline{A}_2$.

3. Conclusion

It is clear from the above development that the solution obtained is approximate, both through neglecting the metric in the T_4^4 componenet of the energy momentum tensor as well as the approximate solution obtained for f_1, f_2, χ_1, χ_2 up to the fourth order of r. Nonetheless, the solution should serve as a model upon which other more complex gauge Q configurations can be constructed. As mentioned in the introduction, the stability of Q configurations is a many sided story. The stability to decay into pions was the first type of stability that occupied theorists but it also depends on the validity of the quantum field theory expanded about the minimum of the potential. This is a subject that has never been fully explored since the nonlinear nature of the field theory may change the properties of what we think to be "free pions". In view of this fact we view the solutions obtained as having meaning independent of the stability criteria based on the Q ball mass being less than the free pions of the theory. The other type of stability is that with respect to electromagnetic and gravitational perturbations, there are basically two ways of analyzing this stability, the first is to calculate the total energy of the complex scalar field within the radius R without the presence of the EM field and gravity, the vacuum energy would also have to be subtracted. When this energy is compared to that of the energy of the configuration in the presence of electromagnetism and gravity, then a criteria of stability can be found. Stability will occur when a plot of $(E_0 - E_{\mathrm{EM+G}})$ is an increasing function of R. This models the criteria originally discussed by Wright for Quasar stability [9]. The second method is to study small time dependent perturbations to the static solutions, and examine regions wherein they give non-exponential growth. This method has recently been employed by Gleiser, to study the stability of Boson stars [10]. The two methods should give the same results, although a discussion of the equivalence of the two methods of determining the stability region has not been given, at least for bosonic field configurations. It is hoped that, in an astrophysical setting, the dependence of the mass on the Q charges may serve as a probe to look for gauged Q balls when the mass of a series of similar objects may show a characteristic dependence on the Q charge as measured through the red shift or perhaps the energy of a gamma ray burst when these objects collapse through gravitational instability. In closing, we appeal to the astrophysics community to entertain the thought of looking for these characteristic signatures of Q balls in the cosmos through the red shift or gamma ray bursts.

Acknowledgement

I'd like to thank the physics departments at Harvard University and Williams College for the use of their facilities.

References

1. S. Coleman, Lecture on Q balls, M.I.T. (Nov. 21, 1984).
2. A. Cohen, S. Coleman, H. Georgi and A. Monohar, Nucl. Phys. B, *272*, 301, 1986.
3. C. B. Gelmini and M. Roncadelli, Phys. Lett. B, *99*, 411, 1981.
4. K. Lee, J. A. Stein-Schabes, R. Watkins and L. M. Widrow, Phys. Rev. D, *39*, 1665, 1989.
5. R. D. Peccei, Phenomenological Aspects of Unified Theories, Proc. of XXIII. Int. Conf. on High Energy, 16–23 July 1986, World Scientific, Singapore, 1987, 119.
6. C. Wolf, Phys. Lett. A, *117*, 443, 1986.
7. R. Friedberg, T. D. Lee and Y. Pang, Phys. Rev. D, *35*, 3640, 1987.
8. V. M. Emelyanov, Y. U. P. Nikitin, I. L. Rozental and A. V. Berkov, Phys. Rep. *143*, No. 1, 168, 1986.
9. J. P. Wright, Phys. Rev., *136*, 288, 1964.
10. M. Gleiser, Phys. Rev. D, *38*, 2376, 1988.

Acta Physica Hungarica 71 (1–2), pp. 129–139 (1992)

THE YIELD STRESS CONTRIBUTION OF DIMERS AND TRIMERS IN NaCl CRYSTALS DOPED WITH DIVALENT CATION IMPURITIES

J. SÁRKÖZI

Department of Experimental Physics, Institute of Physics
Technical University of Budapest,
1521 Budapest, Hungary

(Received in revised form 2 September 1991)

The relationship between the formation-decay processes of the simplest impurity aggregates, i.e. dimers and trimers, and the yield stress changes in sodium chloride crystals doped with divalent cation impurities has been investigated. The amount of chosen heat treatments, and the yield stress of these crystals has been determined. The measurements show that the yield stress depends on both, the kind of aggregate and the type of a quaisatomistic model of the interaction between dislocations and aggregates.

Introduction

It is a well known experimental fact that the yield stress of alkali halide crystals is strongly influenced by divalent cation impurities (Me^{2+}) [1,2]. The yield stress contribution of these impurities is related to the fact that the impurity ions form bound cation vacancy–cation impurity pairs called dipoles [3], and these dipoles strongly interact with the dislocations significantly affecting the yield stress of the crystals, if the impurity concentration is more than about 1 μmole/mole [1]. The dipoles may be associated into dipole groups (aggregates) in heavily doped, annealed crystals, and these aggregates result also in hardening the crystal.

The process of aggregation of divalent impurities in these crystals is generally investigated by the aid of dielectric loss and thermal depolarization measurements [4–8]. On the basis of such measurements, it was initially suggested that the first step of the process is the formation of trimers, i.e. aggregates consisting of three dipoles. More exact measurements and analyses show, however, that first dimers, i.e. aggregates containing two dipoles, are formed in crystals with moderate (less than about 500 μmole/mole) impurity concentrations [9–10]. This means that the aggregation process follows the scheme: dipoles → dimers → trimers → higher aggregates.

The achievements in studying the kinetics of aggregation make it possible to estimate the amount of different kinds of aggregates in the crystal in some specially chosen conditions. If we measure the yield stress of the crystal in the same conditions, we can find a relationship between the kind of aggregates and the yield stress.

The aim of this work is to estimate the contribution of dimers and trimers to the yield stress, and to give an explanation for the results by the aid of a quasiatomic model of the interaction between the dislocations and aggregates.

Experimental techniques

For all of the investigations specially grown, OH^- -free $NaCl(Me^{2+})$ crystals were used [11], in which the concentration of all unwanted divalent impurities was less than 0.2 μmole/mole. The concentration of intentionally introduced divalent impurities (Ca, Sr, Ba) varied between 1–500 μmole/mole.

In order to change the state of aggregation of the impurity, annealings at different temperatures and for different times were applied, and, in some cases, for maitaining the state achieved the samples were quenched. Then annealing and quenching of the samples were carried out in a furnace of small thermal inertia in an inert atmosphere.

In order to have a reference state of the samples, they all were first annealed at 600 °C for several hours.

For quenching the samples two different quenching rates were used. The cooling rate in "quick quenching" was 100 °C/min, while that in "slow quenching" was 0.1 °C/min. Special investigations show that even quick quenching does not cause significant stresses or plastic deformations in the samples.

The yield stress of the crystals was measured with an INSTRON testing machine at room temperature and the critical resolved shear stress (CRSS) was calculated in the usual way.

Experimental results

The CRSS contribution of the impurities (τ_c) is characterized by the difference of the CRSS of the doped crystals (τ) and that of the extra pure ones (τ_0) subjected to the same heat treatment: $\tau_c = \tau - \tau_0$ [2]. In Fig. 1 the CRSS contribution τ_c obtained in this way is shown as the function of the impurity concentration (C) for Ca, Sr and Ba impurities for three different kinds of heat treatment.

Curves 1 in Fig. 1 were measured in samples, which were first annealed at 600 °C, then quickly quenched to 80 °C and annealed at this temperature for 30 hours. The samples were finally cooled down to room temperature, and the yield stress was measured. The reason for choosing this kind of heat treatment is that, according to the kinetic analysis of the change in dielectric loss of the crystals [10], about half of the dipoles is converted into dimers at this stage of aggregation, and the formation of trimers is only at its initial stage. This means that in these samples about half of the obstacles for dislocations is in the form of dipoles and the other half is in the form of dimers.

Curves 2 in Fig. 1 correspond to samples annealed at 600 °C and quenched quickly to room temperature. Dielectric loss measurements [10] show that the impurities are practically in the form of single dipoles in such crystals, i.e. the obstacles for dislocations are mainly dipoles.

Curves 3 in Fig. 1 correspond to samples annealed at 600 °C and slowly cooled to room temperature. Dielectric loss measurements [10] show that the impurity is

mainly in the form of trimers in such crystals, and, thus, the obstacles for moving dislocations are mainly trimers.

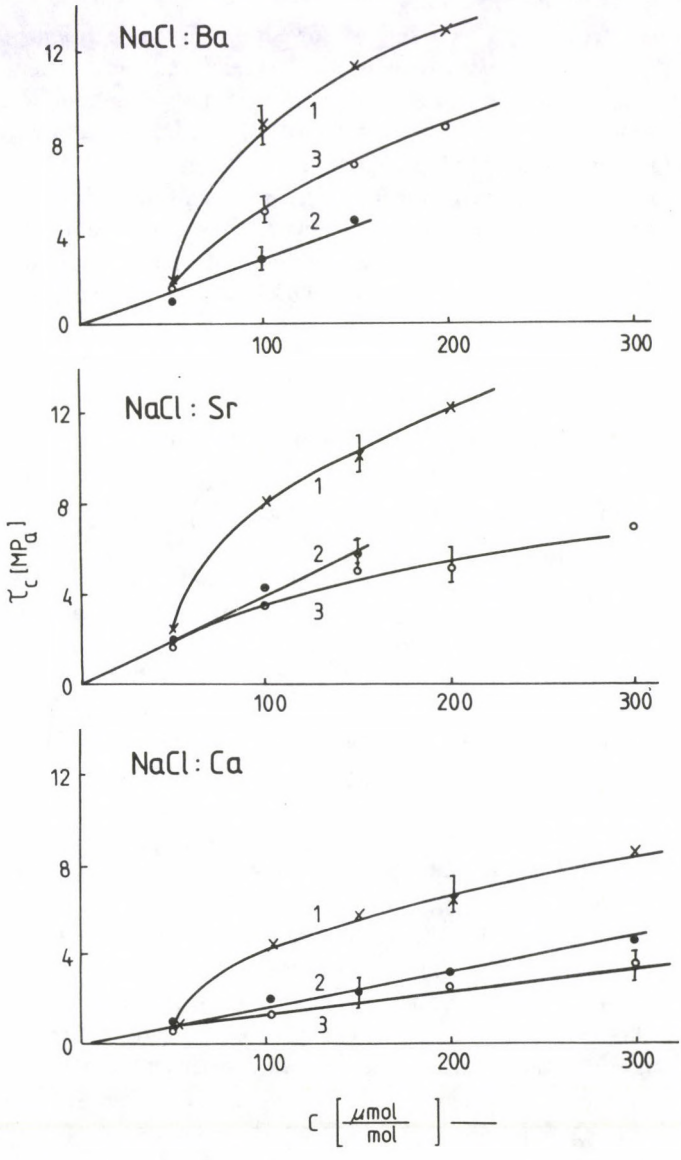

Fig. 1. The concentration (C) dependence of the CRSS contribution of impurities $(\tau_c)'$ in NaCl crystals with different divalent cation impurities (Ba, Sr, Ca) and different pretreatments (1, 2, 3). 1 — samples annealed at 80 °C for 30 hours, 2 — samples quickly quenched from 600 °C, 3 — samples slowly cooled from 600 °C

Fig. 1 shows that at small impurity concentrations ($C < 50$ ppm) curves 1 and 3 are identical with curves 2, i.e. the heat treatment does not affect the CRSS. The explanation of this fact is that practically no aggregation of dipoles takes place at such small impurity concentrations.

It can be seen from Fig. 1 that the mixture of dipoles and dimers in the crystal (curves 1) results in the highest values of yield stress, i.e. the hardening effect of dimers is the greatest among dipoles, dimers and trimers. The smallest hardening effect corresponds to trimers for Ca and Sr, and dipoles for Ba impurity.

Curves 2 in Fig. 1 show that, in agreement with earlier results [12], the yield stress contribution of dipoles is proportional to the impurity concentration: $\tau_d = K_d C$. As the theoretical estimation of coefficient K_d based on a semiatomistic model has been discussed earlier [12], we are not going to deal with the contribution of dipoles τ_d here, but we rather focus on the yield stress contribution of the other types of obstacle.

Model for the yield stress contribution of dimers and trimers

Starting from the results of Fleischer's model [13] for the hardening effect of aggregates we assume that the yield stress contribution of dimers (τ_D) and trimers (τ_T) is proportional to the square-root of the impurity concentration (C), i.e. we can write $\tau_D = K_D C^{1/2}$ for dimers, and $\tau_T = K_T C^{1/2}$ for trimers. The coefficients K_D and K_T are essentially fitting parameters in Fleischer's theory, which, in principle, could be determined by calculation of the yield stress contribution of aggregates by purely atomistic methods. But this kind of calculation is hopelessly difficult, therefore, we suggest a simpler way, which is based on finding coefficients K_D and K_T by a quasiatomistic calculation.

The model is based on a generalization of Gilman's idea [14] of calculation of the yield stress contribution of simple dipoles. Gilman assumes that this yield stress contribution originates from cutting the dipoles by sliding dislocations and it can be related directly to the energy change of the dipole during this process.

Applying this idea to the dislocation–aggregate interaction we follow the changes in the structure of the aggregate caused by the dislocation shearing it. If we assume that the CRSS contribution is equal to the cohesive shear stress of the aggregate, then this contribution can be found directly from the energy change of the aggregate caused by the rearrangement of its constituent parts.

The force exerted by the external shear stress τ_{c1} on unit length of the dislocation meeting an aggregate is $\tau_{c1} b$, while on the whole segment taking part in shearing the aggregate the force is $\tau_{c1} b(a_0/2)$. Here $a_0 = 0.563$ nm is the lattice parameter of the NaCl lattice, and $b = a_0/\sqrt{2}$ is the length of the Burgers vector. Thus the work done is $W = \tau_{c1} b^2 a_0/2 = \tau_{c1} a_0^3/4$. According to our assumption this work has to be equal to the energy change ΔU taking place during the rearrangement of the aggregate, i.e. $\Delta U = \tau_{c1} a_0^3/4$. Using this relationship τ_{c1} necessary for shearing the aggregate can be expressed in terms of the energy change of the

Table I
Defect energies according to [15]. U_d is the energy of a dipole in ground (nn) state, U'_d is the energy of an excited (nnn) dipole, U_D is the energy of a dimer, and U_T is the energy of a trimer

System	U_d (eV)	U'_d (eV)	U_D (eV)	U_T (eV)
NaCl:Ca^{2+}	−6.810	−6.730	−13.823	−21.082
NaCl:Sr^{2+}	−5.467	−5.308	−11.162	−17.128
NaCl:Ba^{2+}	−4.365	−4.145	−8.193	−13.871

aggregate as

$$\tau_{c1} = \frac{4\Delta U}{a_0^3}. \tag{1}$$

In order to find the total CRSS contribution of dimers and trimers we have to add the contributions of all the possible changes in the configuration of the aggregate caused by a sliding dislocation, taking into account the statistical weight of each change.

For the calculation outlined above the knowledge of the energies of the aggregates in their possible configurations is required. These defect energies have been determined by atomistic calculations [15], and the results for the impurities used here are given in Table I.

The analysis of the possible relative configurations of a dimer or trimer and a dislocation shearing it shows that the changes in the structure of these aggregates can be reduced to a few ground cases, which are shown in Fig. 2. Here the positions of the impurities and vacancies forming the dimer or trimer are represented by full and open circles, respectively. The initial positions of the vacancies and impurities are indicated by capital letters (A, B, C, etc.), while their final positions (if they are different from the initial ones) by primed capital letters (A', B', C', etc.). The slip plane and slip direction of the dislocation and the displacement of vacancies and impurities are shown by thin dotted lines.

The possible changes in the structure of a dimer can be reduced to two ground cases (1, 2) shown in Fig. 2a. The corresponding energy changes can be approximated as follows. In case 1 after passing the dislocation one dipole of the dimer becomes excited into nnn-state, i.e. the energy change is approximately $\Delta U_{D1} \sim U'_d - U_d$. In case 2 the dimer is, in first approximation, split into two nn-dipoles, i.e. $\Delta U_{D2} \sim 2U_d - U_D$. The analysis of the possible cases shows that the statistical weights of cases 1 and 2 are 6/8 and 2/8 respectively. Thus the average energy change can be written as

$$\Delta U_0 \sim (6\Delta U_{D1} + 2\Delta U_{D2})/8. \tag{2}$$

The energy change ΔU_T at the rearrangement of a trimer can be determined in a similar way. Here all the cases can be reduced to two ground cases (Fig. 2b).

The energy change in case 1 is approximately $\Delta U_{T1} \sim U'_D - U_d$, and in case 2 $\Delta U_{T2} \sim 0$. The weight of the two cases is the same, thus, the average change of energy can be given as

$$\Delta U_T \sim \Delta U_{T1}/2. \tag{3}$$

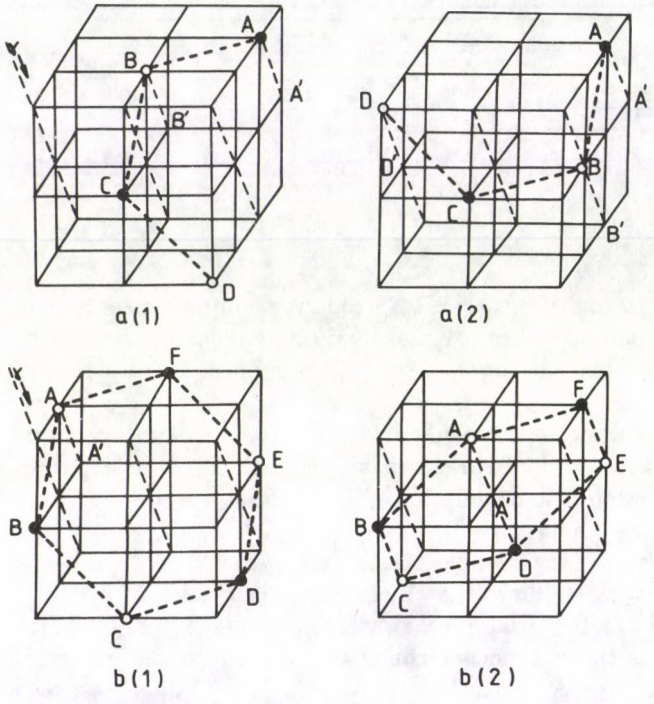

Fig. 2. The ground cases of shearing a dimer or trimer by a dislocation. Full circles denote impurity ions, open circles represent cation vacancies. The initial position of the aggregate is indicated by capital letters, its final position is denoted by primed capital letters. The slip plane and slip direction of the dislocation and the displacement of vacancies and impurities are shown by thin dotted lines. a — the two ground cases for dimer, b — the two ground cases for trimer

The assumption that aggregates can be split into independent dipoles by dislocations is supported by dielectric loss measurements carried out in deformed crystals containing aggregates [16]. These measurements show that deformation results in increasing of the number of dipoles.

In order to get the total hindering force acting on a dislocation we have to take into account that the dislocation interacts with many aggregates. These aggregates are formed from those impurities, which are located in the slip plane of the dislocation, and also in the next two planes above and under the slip plane. If the concentration of the impurity ions, which are present in form of dipoles in the crystal is C, then the concentration of the dimers corresponding to each plane is

$C/2$, thus the effective concentration of the dimers interacting with the dislocation is $C_{D\text{eff}} = 5C/2$. Similar consideration shows that the effective concentration of trimers is $C_{T\text{eff}} = 5C/3$, where C is the concentration of impurities forming trimers.

According to Gilman's argumentation [14], the critical shear stress τ_c can be expressed as

$$\tau_c = \tau_{c1}\sqrt{C_{\text{eff}}}.$$

After substituting the effective concentrations obtained above, and taking τ_{c1} from Eq. (1) we get for dimers

$$\tau_D = \frac{4\Delta U_D}{a_0^3}\sqrt{\frac{5}{2}}\sqrt{C}. \tag{4}$$

The expression for trimers can be obtained similarly

$$\tau_T = \frac{4\Delta U_T}{a_0^3}\sqrt{\frac{5}{2}}\sqrt{C}. \tag{5}$$

In (4) and (5) C is the concentration of impurities forming dimers and trimers, respectively, ΔU_D and ΔU_T can be calculated by Eqs (2) and (3) using the energies given in Table I.

Discussion of the results

The comparison of the calculated and measured τ_c — C relationships for Ca impurity is given in Fig. 3. The curves shown in the figure are calculated by using Eq. (4) and (5) for three different experimental situations discussed in the experimental part. On the basis of the experimental results it is assumed in the calculations that the concentration of the aggregates is zero for impurity concentrations less than 50 ppm in all the cases investigated.

Curve 1 corresponds to the samples annealed at 600 °C, quickly quenched to 80 °C, and annealed at this temperature for 30 hours. As has been discussed above, half of the impurity atoms are in dipoles and the other half in dimers in these samples, therefore, the CRSS contribution τ_1 can be calculated by the formulas

$$\tau_1 = \tau_d = K_d C, \qquad \text{if } C < 50 \text{ ppm},$$
$$\tau_1 = \tau_d = K_d C/2 + K_D\sqrt{C/2}, \quad \text{if } C \geq 50 \text{ ppm}.$$

The experimental results corresponding to this state of aggregation are indicated by the symbol "×".

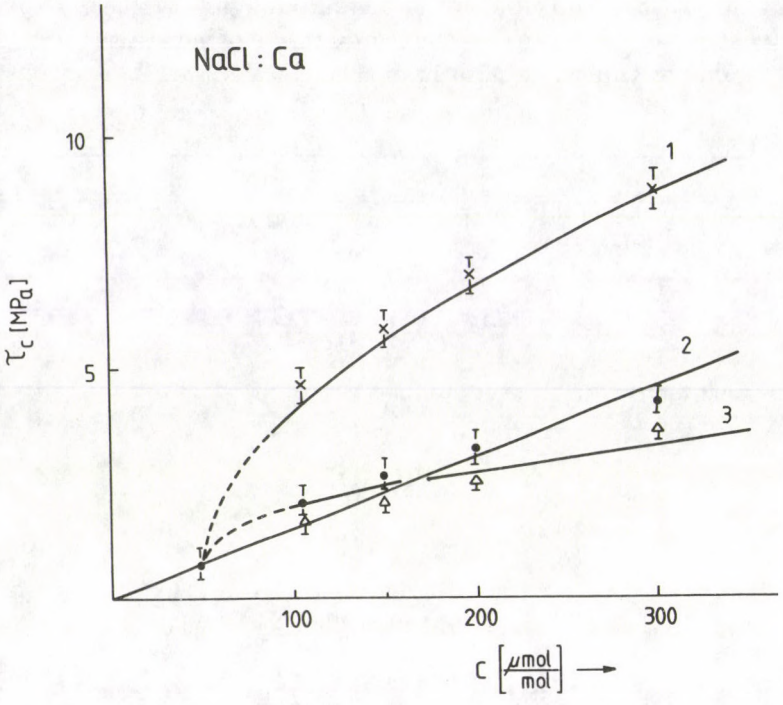

Fig. 3. The calculated (solid lines) and measured (symbols "×", "•" and "Δ") $\tau_c - C$ relationships for differently pretreated NaCl crystals doped with Ca. Curve 1 and symbol "×" correspond to samples annealed at 80 °C for 30 hours, curve 2 and symbol "•" represent samples quickly quenched from 600 °C, and curve 3 and symbol "Δ" denote samples slowly cooled from 600 °C

Curve 2 in Fig. 3 corresponds to samples annealed at 600 °C and quickly quenched to room temperature. In these samples the impurity atoms are in form of dipoles, therefore the CRSS contribution τ_2 is calculated by the expression

$$\tau_2 = \tau_d = K_d C.$$

The corresponding experimental results are represented by full circles in the figure.

Finally, curve 3 in Fig. 3 shows the calculated results for samples annealed at 600 °C, and slowly cooled to room temperature. As has been discussed, the impurity is mainly in the form of trimers in these samples for concentrations $C > 50$ ppm, thus the CRSS contribution τ_3 can be calculated as

$$\tau_3 = \tau_d = K_d C, \quad \text{if } C < 50 \text{ ppm},$$
$$\tau_3 = \tau_T = K_T \sqrt{C}, \quad \text{if } C \geq 50 \text{ ppm}.$$

The measured values are denoted by triangles in this case.

The change of CRSS with impurity concentration cannot be followed by calculation at about 50 ppm, because we do not know the relationship between the impurity concentration and the concentration of the aggregates in this range of concentration. The uncertainty caused by this fact is expressed by applying dotted lines for these parts of the curves.

Apart from the problem mentioned above, the theoretical curves fit well the measured points for all the three cases, as can be seen from Fig. 3. Similar agreement of experimental and theoretical results is obtained for Sr and Ba impurities.

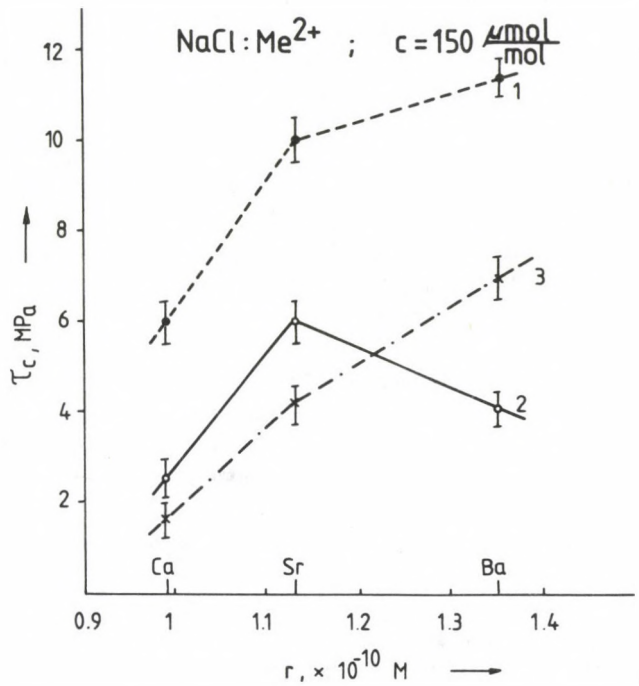

Fig. 4. The measured dependence of the CRSS contribution (τ_c) of different aggregates on the ionic radius (r) of the impurity ion. 1 — CRSS is determined mainly by dimers, 2 — CRSS contribution of dipoles, 3 — CRSS contribution of trimers. The impurity concentration is 150 μmole/mole in each case

It is interesting to compare the CRSS contributions caused by different aggregates of different impurities. In Fig. 4 the CRSS contributions of different aggregates (τ_c) at a fixed impurity concentration ($C = 150$ μmole/mole) are plotted against the ionic radius (r) of the impurity ion. Curves 1, 2 and 3 show the measured values of the CRSS contribution determined mainly by dimers, dipoles and trimers, respectively. The monotonous increase of the CRSS contribution of dimers and trimers

with the ionic radius of the impurity ion is the consequence of the similar behaviour of energy changes ΔU_D and ΔU_T, which determine the CRSS contribution. The maximum in curve 2 (dipoles) has been discussed elsewhere [12]. It is related to the fact that, among the impurities considered here, the interaction between an impurity-vacancy dipole and a dislocation is the strongest for dipoles containing Sr impurity.

Summary

The CRSS contribution of different aggregations of divalent cation impurities (Ca, Sr and Ba) in NaCl crystals was investigated. The concentration of the aggregates (dipoles, dimers and trimers) was varied by specially chosen heat treatments, which made it possible to estimate the relationship between the known total impurity concentration and the concentration of the aggregates. The CRSS of samples with different types of aggregates was measured as the function of the impurity concentration.

The experiments show that the CRSS depends on both the kind of the aggregate and the type of the impurity. The hardening effect of dimers is the greatest among dipoles, dimers and trimers for all the three impurities investigated, and the smallest hardening effect corresponds to trimers for Ca and Sr, and to the dipole for Ba impurity.

For the explanation of the experimental results a simple model is used, which is based on the assumption that the CRSS contribution originates from shearing the aggregates by sliding dislocations, and it can be related directly to the energy change of the aggregate during this process. Another basic approximation is that the smallest unit originating from the shearing process is a dipole (because of its relatively high binding energy), and that the dipoles obtained in this way have negligible interactions with each other or with the remaining part of the aggregate.

A good agreement between the calculated and measured data is found, which supports the validity of our assumptions, and shows that this simple model is suitable for the explanation of the CRSS contribution of the dimers and trimers in simple ionic crystals.

References

1. M. T. Sprackling, The Plastic Deformation of Simple Ionic Crystals, Academic Press, New York, 1976.
2. W. Skrotzki and P. Haasen, J. de Phys., *42*, C3, 119, 1981.
3. L. W. Barr and A. B. Lidiard, Defects in Ionic Crystals, Physical Chemistry — An Advanced Treatise, ed. H. Eyring, D. Henderson and W. Jost, Academic Press, New York, 1970.
4. J. S. Cook and J. S. Dryden, Aust. J. Phys., *13*, 260, 1960.
5. J. S. Cook, and J. S. Dryden, J. Phys. C. Solid State Phys. *14*, 1133, 1981.
6. S. W. S. McKeever and E. J. Lilley, J. Phys. Chem. Solids, *43*, 885, 1982.
7. J. Sárközi, A. Tóth and L. Szabó, Periodica Polytechnica, Mech. Eng., *21*, 293, 1977.
8. A. L. Guerro, S. C. Jain and P. L. Pratt, Phys. Stat. Sol. (a), *49*, 353, 1978.

9. J. S. Dryden, S. Morimoto and J. S. Cook, Phil. Mag., *12*, 379, 1965.
10. G. Berg, M. Dubiel, J. Sárközi and Cs. Kuti, Acta Phys. Hung., *51*, 319, 1981.
11. R. Voszka, I. Tarján, L. Berkes and J. Krajsovszky, Kristall und Technik, *1*, 423, 1966.
12. A. Tóth, T. Keszthelyi, P. Kálmán and J. Sárközi, Mat. Sci. Eng., *64*, 223, 1984.
13. R. L. Fleischer, Acta Metall., *10*, 838, 1962.
14. J. J. Gilman, Appl. Phys., *36*, 3156, 1965.
15. J. Corish, J. M. Quigley, P. W. M. Jacobs and C. R. A. Catlow, Phil. Mag., *A44*, 13, 1981.
16. L. V. Zuev and V. A. Rubianec, Fiz. Tverd. Tela, *23*, 8, 1981, in Russian.

Acta Physica Hungarica 71 (1–2), pp. 141–142 (1992)

BOOK REVIEWS

Interaction of Atoms and Molecules with Solid Surfaces
Edited by V. Bortolani, N. H. March and M. P. Tosi, Plenum Press, New York and London, 1990

Thre is a considerable interest, both fundamental and technological, in surface phenomena. The description of heterogeneous catalysis and other surface reactions requires a detailed understanding of atom–surface and molecule–surface interactions.

Accrding to the Preface the aim of this book is to give fairly broad coverage of atoms and molecules interacting with solid surfaces at a level suitable for graduate students and research workers in condensed matter physics, chemical physics, and material science. It is intended for experimental workers, too, interested in basic theory and concepts. This book is originated in a Spring College held at the International Centre for Theoretical Physics, Miramare, Trieste.

The Volume contains 19 Chapters, each elaborated by well-known authors.

In Chapter 1 N. H. March investigates the changes induced in a chemical bond when it is brought up from infinite separation to a finite distance from a solid surface (Physisorption, Chemisorption, Molecular or Dissociative Adsorption).

T. B. Grimley in Chapter 2 deals with gas–surface interactions. Two aspects of these interactions are equally discussed: classical and statistical thermodynamics and quantum theory.

In Chapter 3 W. Kohn treats the theory of atom–surface collisions. He starts with the rigid target model and reaches a theory where the dynamics of the target atom must be included.

In Chapter 4 F. Garcia-Moliner deals with the basic vibrational properties of surfaces.

Chapter 5 contains the treatment of the electronic structure of metal surfaces.

In Chapter 6 the basic structural and electronic properties of semiconductor surfaces are discussed.

Chapter 7 is a short review of the low energy electron diffraction.

Chapter 8 and 9 treat adsorption and chemisorption.

Chapter 10 deals with the surface vibrational spectroscopy.

Since 1982 the scanning tunneling microscopy cannot be ignored. Chapter 11 gives a short review of this rapidly developing method.

In Chapter 12 the surface-defects are discussed.

The remaining part of the book deals with fundamental surface processes (molecular scattering, photoemission, surface diffusion, heterogeneous catalysis, and growth processes).

The book gives an excellent up-to-date review of present theoretical and experimental knowledge connected with the basic surface phenomena. Therefore it can be of high value to research workers interested in this field.

E. Kapuy

ANTAL MÜLLER: *Interaction and Determination*
Publishing House of the Hungarian Academy of Sciences (Akadémiai Kiadó) Budapest, 1991

This book by Antal Müller, expert of philosophical problems in physics, is a work on natural philosophy. Its ideology relies on physics, at the same time, its applicability to physics is also the criterion of the correctness of its conception.

In the problem of determinism raised by modern physics, physical interpretation can be hardly separated from philosophical interpretation, a recognition decisive for the structure of

this book. Since the problem of determinism is closely related to the fundamental problems of philosophy, the Author's attitude to them is first expanded both ontologically and gnoseologically; since, however, a logical analysis cannot replace the analysis of reality, an analysis is given of relevant fundamental achievements of 20th-century physics which leads to a consequent theory of determination.

In the Author's approach, overall material determination is not identical with an unambiguous predetermination, accordingly, the problem of determinism raised by the statistical feature of microphysics can be properly interpreted.

His determination theory is definitely a natural philosophy; social phenomena and the conscious factor are left undiscussed. This work by Antal Müller may be of interest both to the philosopher and the physicist. The attention of readers specialising in physics is also called to the book "Quantum Mechanics: A Physical World Picture" (Akadémiai Kiadó, Budapest, 1974) by the same Author.

G. Bíró

Manuscript received by Akadémiai Kiadó:
2 October 1991
Manuscript received by TYPOTEX Ltd for TEX typesetting:
15 October 1991
Date of publication: 5 June 1992
PRINTED IN HUNGARY
Akadémiai Kiadó és Nyomda Vállalat
Budapest

NOTES TO CONTRIBUTORS

I. PAPERS will be considered for publication in Acta Physica Hungarica only if they have not previously been published or submitted for publication elsewhere. They may be written in English, French, German or Russian.

Papers should be submitted to

Prof. I. Kovács, Editor
Department of Atomic Physics, Technical University
1521 Budapest, Budafoki út 8, Hungary

Papers may be either articles with abstracts or short communications. Both should be as concise as possible, articles in general not exceeding 25 typed pages, short communications 8 typed pages.

II. MANUSCRIPTS

1. Papers should be submitted in three copies.
2. The text of papers must be of high stylistic standard, requiring minor corrections only.
3. Manuscripts should be typed in double spacing on good quality paper, with generous margins.
4. The name of the author(s) and of the institutes where the work was carried out should appear on the first page of the manuscript.
5. Particular care should be taken with mathematical expressions. The following should be clearly distinguished, e.g. by underlining in different colours: special founts (italics, script, bold type, Greek, Gothic, etc.); capital and small letters; subscripts and superscripts, e.g. x^2, x_3; small *l* and l; zero and capital O; in expressions written by hand: *e* and *l*, *n* and *u*, *v* and v, etc.

A List of Symbols on a separate sheet should be attached to each paper.

6. References should be numbered serially and listed at the end of the paper in the following form: J. Ise and W. D. Fretter, Phys. Rev., *76*, 933, 1949.

For books, please give the initials and family name of the author(s), title, name of publisher, place and year of publication, e.g.: J. C. Slater, Quantum Theory of Atomic Structures, I. McGraw-Hill Book Company, Inc., New York, 1960.

References should be given in the text in the following forms: Heisenberg [5] or [5].

7. Captions to illustrations should be listed on a separate sheet, not inserted in the text.
8. In papers submitted to Acta Physica all measures should be expressed in SI units.

III. ILLUSTRATIONS AND TABLES

1. Each paper should be accompanied by three sets of illustrations, one of which must be ready for the blockmaker. The other sets attached to the copies of the manuscript may be rough drawings in pencil or photocopies.
2. Illustrations must not be inserted in the text.
3. All illustrations should be identified in blue pencil by the author's name, abbreviated title of the paper and figure number.
4. Tables should be typed on separate pages and have captions describing their content. Clear wording of column heads is advisable. Tables should be numbered in Roman numerals (I, II, III, etc.).

IV. RETURN OF MATERIAL

Owing to high postage costs, the Editorial Office cannot undertake to return *all* material not accepted for any reason for publication. Of papers to be revised (for not being in conformity with the above Notes or other reasons) only *one* copy will be returned. Material rejected for lack of space or on account of the Referees' opinion will not be returned to authors outside Europe.

Index: 26.022

Acta Physica Hungarica

VOLUME 71 · NUMBERS 3–4, 1992

Akadémiai Kiadó, Budapest

ACTA PHYS. HUNG. APAHAQ 71 (3–4) 143-270 (1992) HU ISSN 0231–4428

ACTA PHYSICA HUNGARICA

A JOURNAL OF THE HUNGARIAN ACADEMY OF SCIENCES

EDITED BY
I. KOVÁCS

Acta Physica publishes original papers on subjects in physics. Papers are accepted in English, French, German and Russian.

Acta Physica is published in two yearly volumes (4 issues each) by

AKADÉMIAI KIADÓ
Publishing House of the Hungarian Academy of Sciences
H–1117 Budapest, Prielle Kornélia u. 19–35.

Subscription information

Orders should be addressed to

AKADÉMIAI KIADÓ
H–1519 Budapest, P.O. Box 245

Acta Physica Hungarica is abstracted/indexed in Chemical Abstracts, Mathematical Reviews, Science Abstracts, Physics Briefs, Risk Abstracts, Engineering Information, Inc. EI Page One Database

CONTENTS

Acta Physica Hungarica 71 (3-4), pp. 143-148 (1992)

THERMALLY AND DEFORMATION INDUCED FLUORESCENCE IN SODIUM IODIDE

T. R. JOSHI, A. K. NEHATE, MAHMOOD TAHER and L. H. H. PRASAD

Applied Physics Department, Faculty of Technology and Engineering
M. S. University of Baroda
Baroda 390001, India

(Received 22 April 1991)

The present paper reports the excitation and emission spectra of sodium iodide phosphor in three different physical conditions namely (i) as-received powder form, (ii) thermally treated NaI powder condition and (iii) NaI tableted condition. The fluorescence spectra have been recorded by means of Aminco-Bowman spectrophoto-fluorometer supplied by American Instrument Co. Inc. The examination of fluorescence spectra in different physical conditions of NaI phosphor reveals the fact that fluorescence spectra are found significantly influenced by pretreatments. It is presumed that the change in density of vacancy, vacancy pair and dislocation in lattice of NaI on application of pre-treatments is responsible for the observed change in fluorescence spectra of NaI in different physical conditions.

Introduction

The progress made in the field of luminescence of solids has been known for a long time. Nowadays the phenomenon of luminescence is one of the important branches of solid state physics in the present scientific world. Luminescence materials are used in a variety of applications like medicine, agriculture, radiation applications, archaeological and geological dating, etc. The luminescence from alkalihalides has been found very interesting and useful in different fields. Luminescence of alkalihalides, particularly iodides [1–3] has been studied extensively. However, the survey of literature indicates that there is no systematic study of sodium iodide (NaI). Therefore, the present paper reports the fluorescence spectra of pure NaI in different physical conditions.

Experimental

This paper discusses the effect of different physical treatments on the fluorescence spectra of sodium iodide (NaI). The specimens were prepared by the method of recrystallization from aqueous solution. They were subjected to thermal and/or mechanical pretreatments. The NaI material was examined for its luminescent behaviours in the following physical conditions:

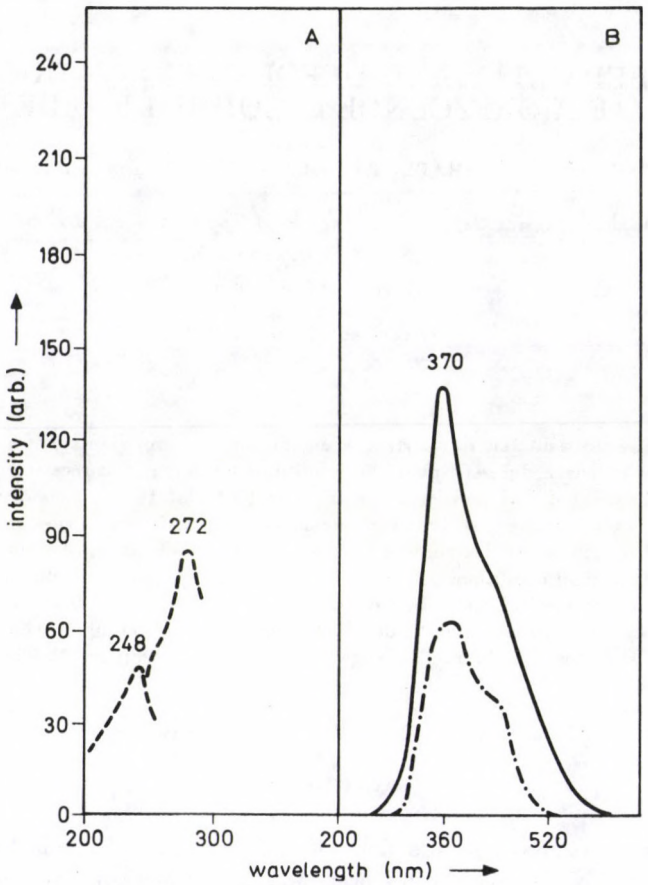

Fig. 1. Fluorescence spectra of NaI powder: in as-received condition; A – excitation spectra, B – emission spectra

(i) As-obtained NaI powder obtained from aqueous solution through recrystallization.
(ii) As-obtained NaI, annealed and rapidly cooled to room temperature from 500 °C in open air.
(iii) NaI pellet obtained from as-obtained material through plastic deformation.
(iv) NaI tablet prepared from 500 °C air-quenched powder through mechanical compression.

The emission and excitation spectra were recorded for the above mentioned specimens at room temperature under identical experimental conditions. The instrument used to study the excitation and emission spectra is Aminco-Bowmann spectrophoto-fluorometer supplied by American Instrument Co. Inc. Sodium iodide

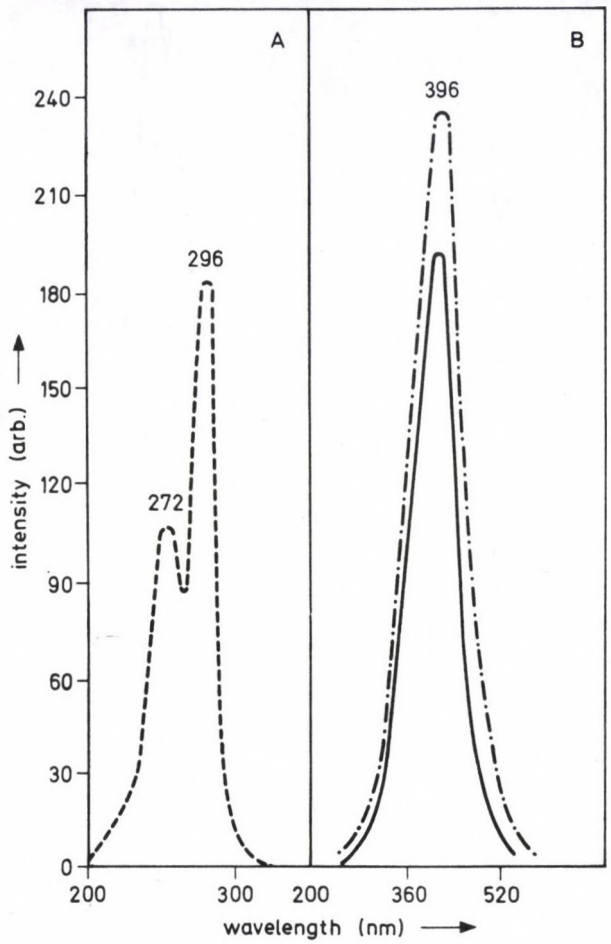

Fig. 2. Fluorescence spectra of NaI powder after annealed at 500 °C and then cooled to room temperature in air; A – excitation spectra, B – emission spectra

in powder form used in the present work was supplied by 'Loba Chemi Wien–Fischamed Austramal–Preparate' Company.

In all cases, the excitation spectrum of a given specimen was first observed and subsequently its emission spectrum stimulated by observed excitation was recorded. Each excitation and emission band is specified by the wavelength at which its peak appears.

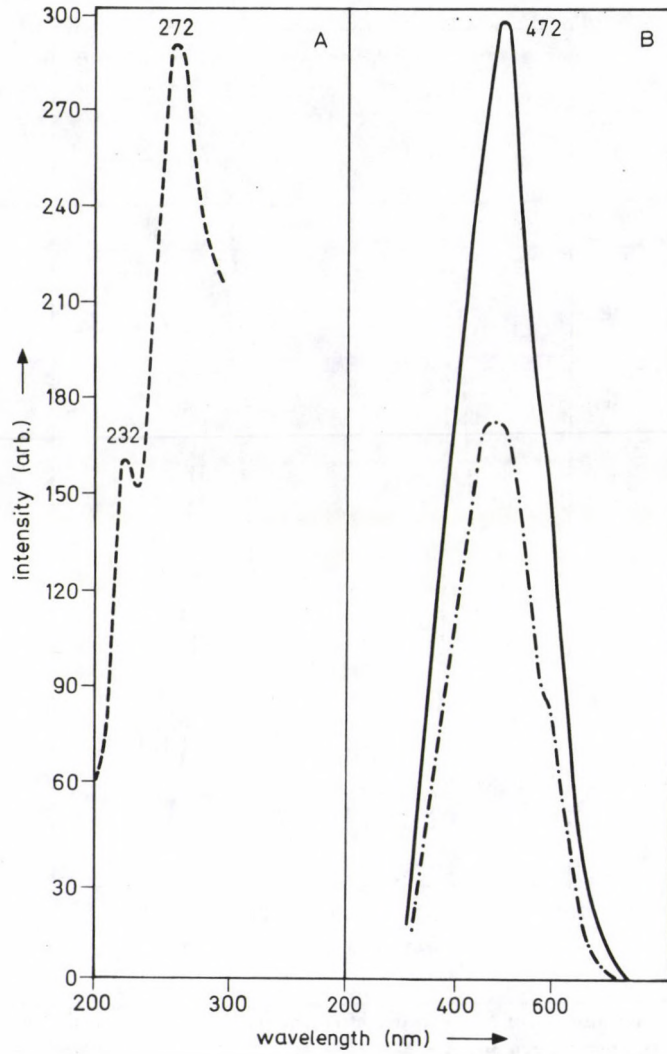

Fig. 3. Fluorescence spectra of NaI pellet, obtained from as-received NaI powder; A – excitation spectra, B – emission spectra

Results and discussion

The fluorescence characteristics exhibited by sodium iodide in different physical conditions are as follows:

(i) Untreated NaI phosphor exhibits two excitation bands at 248 and 272 nm. These excitation bands produce dominant emission around 370 nm along with a hump at 460 nm (Fig. 1).

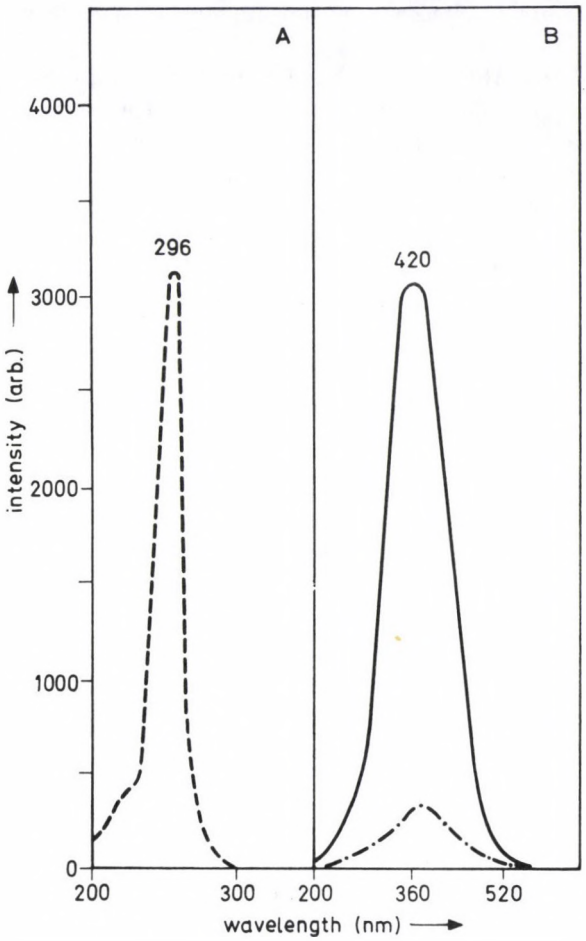

Fig. 4. Fluorescence spectra of NaI pellet obtained from the powder annealed at 500 °C, then cooled to room temperature in air, A – excitation spectra, B – emission spectra

(ii) The fluorescence spectra displayed by NaI phosphor are found sensitive to thermal treatment. The main emission, 370 nm, shifts towards the higher wavelength side, i.e. to 396 nm on execution of pre-heat-treatment. The overall intensity of the fluorescence spectrum also increases with thermal treatments. The corresponding excitation wavelengths are 272 and 296 nm (Fig. 2).

(iii) Like pre-heat-treatment, mechanical pre-treatment also enhances the overall intensity of luminescence and shifts the dominant emission band on the higher wavelength side (Figs 3 and 4).

(iv) It is very clearly found that the pellet of 500 °C air quenched NaI material exhibits optimum fluorescence output among the specimens under examination.

It is believed that the emission band exhibited by pure NaI powder may be associated with the crystallinity of the material or an inherent metallic impurity present in the phosphor. The change in fluorescence behaviours of NaI specimens on application of thermal and/or mechanical treatment may be on account of the change in density of point defect, migration of point defects, and diffusion of an inherently present impurity in NaI material. It is quite obvious that the concentration of point defect and dislocation density is high in pretreated specimens due to thermal or mechanical shock. This new situation is responsible for the high fluorescence output and other changes in fluoresecence spectra of NaI in the thermally and/or mechanically treated specimens.

References

1. R. V. Joshi, J. K. Wessly, Acta Cryst., *A–33*, 344, 1977.
2. W. R. S. Garton, The Astrophysics Journal, *165*, 23, 1971.
3. Hayashi T. Salid, Solid State Comm., *17*, 945, 1975.

Acta Physica Hungarica 71 (3-4), pp. 149–156 (1992)

OPTICAL PROPERTIES OF POLYSTYRENE-POLYCARBONATE BLEND THIN LAYERS

C. Y. Y. HANNA and A. K. ABASS

Department of Physics, College of Science, University of Basrah
Basrah, Iraq

(Received in revised form 5 July 1991)

The optical properties of polystyrene-polycarbonate blend thin layers were studied in the fundamental absorption region. The optical data were analysed and interpreted in terms of electronic transitions.

1. Introduction

The optical investigation of polymers constitutes an important tool to enhance its applications in solar energy conversion as a cover in solar collector, green house and as an optical filter. Polystyrene and bisphenol-A-polycarbonate have a wide range of industrial applications and their physical properties are listed in many articles [1]. The polymer blend field became an interesting subject to many workers. In the present work the optical properties of polystyrene, bisphenol-A-polycarbonate blends were studied in the fundamental absorption region.

2. Experimental

The commercial polystyrene (η = 91.5 gm/cm·s) and bisphenol-A-polycarbonate were purified by reprecipitation from CH_2Cl_2/petroleum ether several times. The chemical structure of commercial polystyrene and bisphenol-A-polycarbonate are given as

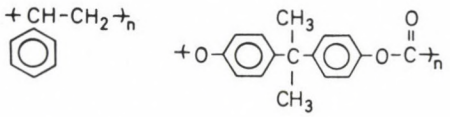

(Polystyrene) (Bisphenol-A-polycarbonate)

Thin layers of polystyrene-polycarbonate blend polymer were obtained by dissolving the desired wt % of each pure polymer in methylene chloride followed by causting the viscous solution on a clear dry glass sheet. After 24 hours the layers were collected and dried under vacuum of 0.1 mmHg overnight. At the time (Dec. 1987) when causting was carried out and due to the atmospheric conditions, it was difficult to obtain a uniform and transparent blend layer of polycarbonate

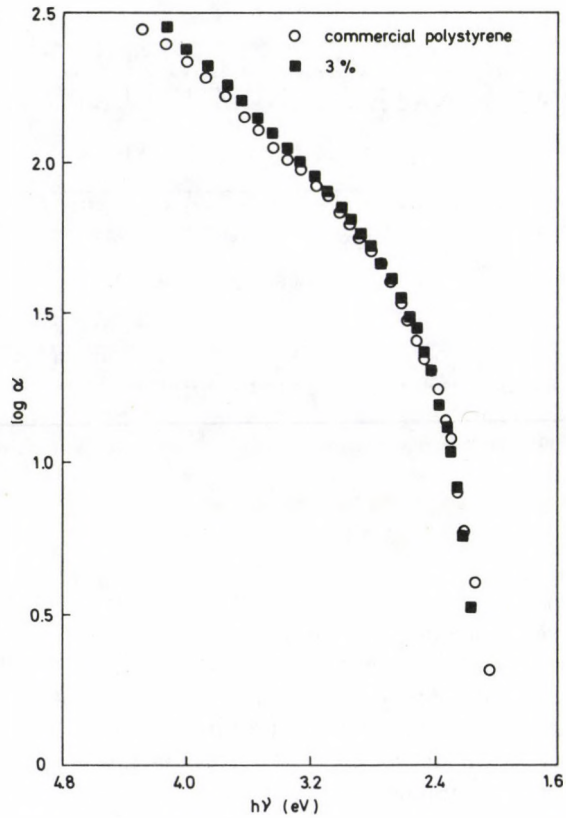

Fig. 1a

Fig. 1. Absorption coefficient versus photon energy; a – Commercial polystyrene (○) and 3 % polycarbonate in polystyrene blend (■) b – 5 % (□) and 10 % (◐) polycarbonate in polystyrene blend c – Pure polycarbonate (●) and 30 % polycarbonate in polystyrene blend (◑)

concentration greater than 30 %. The layer thickness was in the range of 0.07 to 0.15 mm.

The absorptance of the polymer layers was recorded at room temperature using Pye-Unicam SP8-100 spectrophotometer in the wavelength range 200–900 nm.

3. Results and discussion

Transmittance T through a weakly absorbing slab of reflectivity R, thickness d and absorption coefficient α in air is given by

$$T = \frac{(1-R)}{e^{\alpha d} - R^2 e^{-\alpha d}}, \tag{1}$$

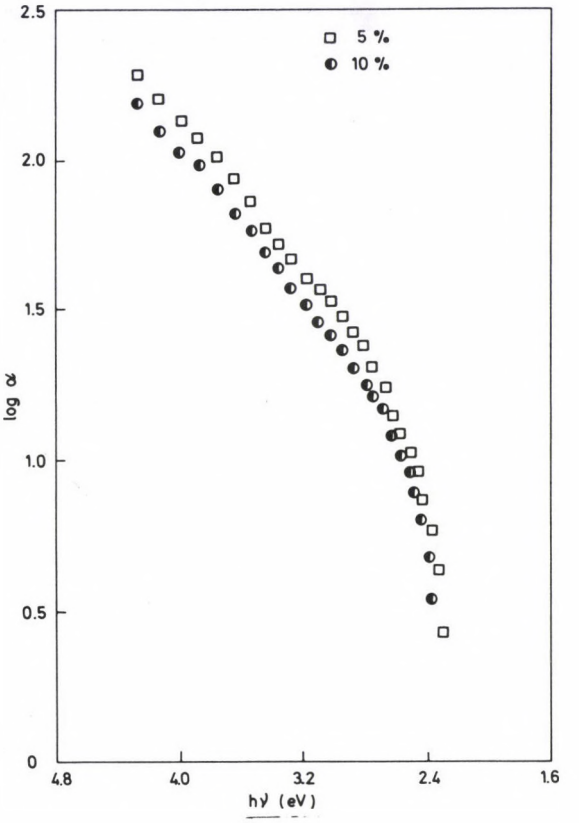

Fig. 1b

where $R = \frac{(n-1)^2}{(n+1)^2}$, n is the refractive index. In the region of band-to-band transition, the absorption is large, so that $e^{\alpha d} \gg R^2 e^{-\alpha d}$. The transmittance equation becomes

$$T = (1-R)^2 e^{-\alpha d}. \tag{2}$$

The absorption coefficient is written as

$$\alpha = \frac{2.303}{d}(A + \log(1-R)^2), \tag{3}$$

where A is the absorptance ($A = -\log T$). The reflection losses were considered to be constant. The absorption coefficient of different specimens was estimated after correcting for the reflection losses. The longwavelength tail of the absorptance spectrum (the wavelength independent part of the absorptance) extended to the short wavelength side. The correction for reflection losses was made by subtracting

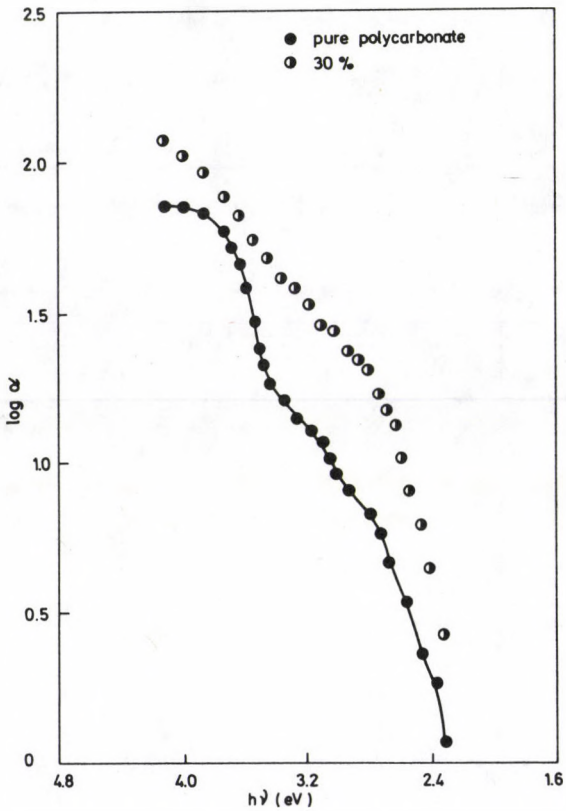

Fig. 1c

the extended straightline portion from absorptance. The method of correction of reflection losses had been employed earlier and is reasonably justified [2,3]. The absorption coefficient is calculated from the relation: $\alpha = \frac{2.303}{d} A$, after correcting for reflection losses.

The absorption coefficient spectra versus photon energy of different specimens (I. Commercial polystyrene, II. 3 %, 5 %, 10 % and 30 % polycarbonate in polystyrene blend and III. bisphenol-A-polycarbonate) are shown in Fig. 1 (a, b, c). The absorption coefficient of commercial polystyrene and polystyrene-polycarbonate blend specimens shows systematic behaviour versus photon energy. There is a hump in the absorption spectrum of bisphenol-A-polycarbonate which is related to carbonate group absorption. The specimen of 10 % polycarbonate in polystyrene blend shows lower absorption. This may be related to high uniformity in the structure.

The absorption data were analysed in terms of the theory of phonon assisted

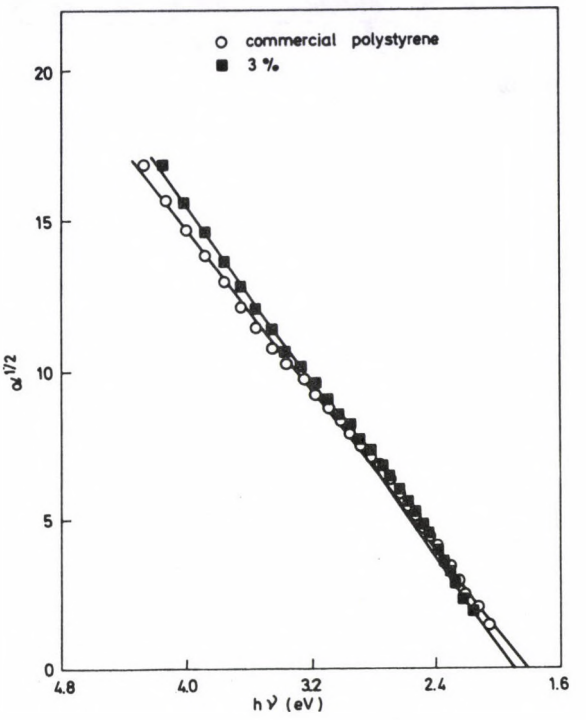

Fig. 2a

Fig. 2. Graphical analysis of absorption data; a – Commercial polystyrene (○) and 3 % polycarbonate in polystyrene blend (■) b – 5 % (□) and 10 % (◐) polycarbonate in polystyrene blend c – Pure polycarbonate (●) and 30 % polycarbonate in polystyrene blend (◑), carbonate group absorption α_c (○)

indirect electronic transitions [4]. According to this theory the absorption coefficient α depends on the photon energy $h\nu$ as

$$\alpha = \alpha_a + \alpha_e; \qquad h\nu \geq E + E_p, \tag{4}$$

$$\alpha_a = \frac{\alpha_0}{e^{E_p/KT} - 1}(h\nu - E + E_p)^{1/2}; \quad h\nu \geq E - E_p, \tag{5}$$

$$\alpha_e = \frac{\alpha_0}{1 - e^{E_p/KT}}(h\nu - E - E_p)^{1/2}; \quad h\nu \geq E + E_p, \tag{6}$$

where α_a is the absorption coefficient component involving phonon absorption, α_e is the component assisted by phonon emission, E is the indirect allowed band gap energy and E_p is the phonon energy. α_0 is a constant containing the matrix element and density-of-states effective mass of electrons and holes. Two types of indirect allowed electronic transitions were (I) the no-phonon vertical transitions describing the absorption of commercial purified polystyrene and 3 % polycarbonate in polystyrene blend, (II) phonon assisted transition processes describing the

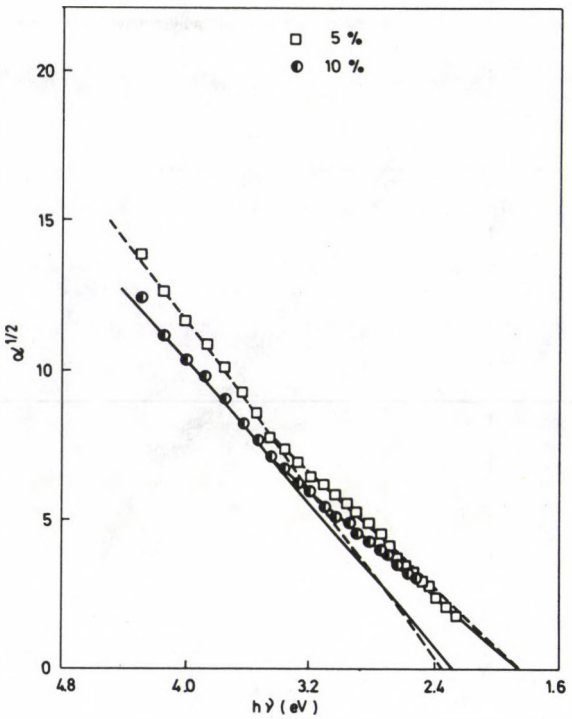

Fig. 2b

absorption of other specimens. The plots of $\alpha^{1/2}$ versus photon energy for different specimen compositions are illustrated in Fig. 2 (a, b, c). A straight line is clearly seen in the plot of commercial polystyrene and 3 % polycarbonate in polystyrene blend (Fig. 2a), indicating that the absorption is due to indirect allowed vertical transitions, i.e. no-phonon is assisting such electronic transitions. The appearance of no-phonon component in the absorption spectra is due to the disturbance of the translational symmetry of the structure. Such a reason has been mentioned in the investigations of optical absorption in $GaAs_{1-x}P_x$ [5]. The absorption data for no-phonon assisting the electronic transition processes are well described by an equation of the form

$$\alpha = \alpha_0(h\nu - E)^2.$$

The plots are resolved into two straight lines for 5 % and 10 % polycarbonate in polystyrene blend (Fig. 2b). The portion at lower energy is due to transition assisted by phonon absorption and phonon energy intercept at $E - E_p$. The other line corresponds to the phonon emission process and the phonon energy intercept at $E+E_p$. From the intercepts, the band gap estimated (Fig. 2c) shows the plot of $\alpha^{1/2}$ of bisphenol-A-polycarbonate and 30% polycarbonate in polystyrene blend. Two

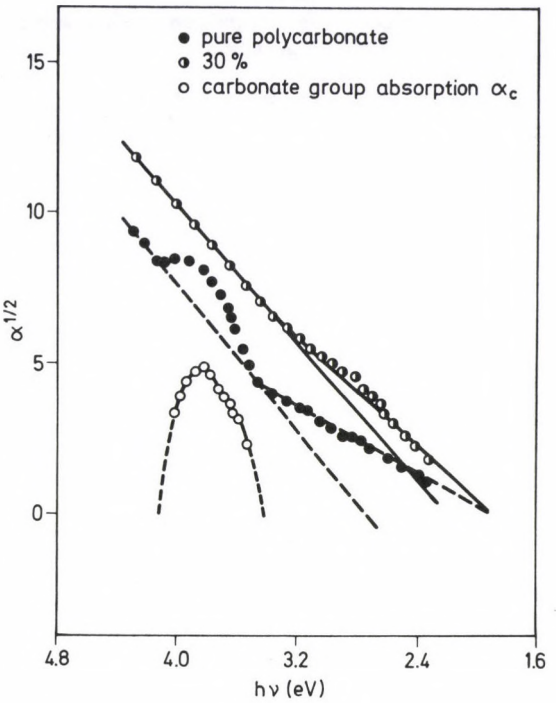

Fig. 2c

straight line portions are seen in the plot. The reason why the higher energy line of bisphenol-A-polycarbonate is not coinciding with experimental data is due to the absorption of the $-\overset{\overset{O}{\|}}{C}-$ group which takes place simultaneously with band-to-band transitions. The carbonate group absorption α_c can be estimated by subtracting the interband absorption straight line from total absorption. The absorption due to the carbonate group is weak and covers a much smaller range than transitions between the valence band and conduction band so its effect disappears in the other specimens. It is clear that the fact that some other lines are not coinciding exactly with the point may be due to extra transitions from valence band to impurity levels such as vacancies existing just below the conduction band. These transitions occur simultaneously with band-to-band transition. The indirect allowed band gaps and assisting phonons are given in Table I. The phonon energy for different specimens is too high to be considered as lattice phonon. The structure of Fig. 2b and 2c can be attributed to the internal vibrational groups of molecules or may be related to the existence of two valence bands.

Table I
Indirect allowed band gap, type of transition and assisting phonons for different layers

Specimen	Type of transition	Band gap energy (eV)	Phonon energy (eV)
Commercial polystyrene	Vertical	1.8±0.03	–
3 % polycarbonate in polystyrene blend	Vertical	1.9±0.03	–
5 % polycarbonate in polystyrene blend	Non-vertical	2.1±0.03	0.20
10 % polycarbonate in polystyrene blend	Non-vertical	2.1±0.03	0.20
30 % polycarbonate in polystyrene blend	Non-vertical	2.07±0.03	0.15
Pure polycarbonate	Non-vertical	2.3±0.03	0.4

Acknowledgement

We are grateful to Dr. S. S. Al-Kass, Department of Chemistry, College of Science, University of Basrah, for his enormous help.

References

1. J. Brandrup and E. H. Immergut (eds), Polymer Handbook, John Wiley, New York, 1975.
2. A. K. Abass, A. K. Hasen and R. H. Misho, J. Appl. Phys., *58*, 1640, 1985.
3. M. I. Cohen and R. F. Blunt, Phys. Rev., *168*, 929, 1968.
4. T. S. Moss, Optical Properties of Semiconductors, Butterworth's Scientific, London, 1959. p. 37.
5. N. Pikhtin, V. N. Razbengaev and D. A. Yaskov, Phys. stat. sol. (a), *50*, 717, 1972.

Acta Physica Hungarica 71 (3-4), pp. 157–160 (1992)

DETOUR TRANSITIONS IN INTERNAL BREMSSTRAHLUNG FROM ^{204}Tl

GÜNEŞ TANIR and BAŞAR ŞARER

Gazi University, Faculty of Arts and Sciences
06500 Ankara, Turkey

(Received 15 July 1991)

The contribution of detour transitions to the internal bremsstrahlung accompanying nuclear β-decay from ^{204}Tl was calculated. It is shown that detour transition is important for ^{204}Tl which is unique first forbidden case. The photon spectrum was calculated and compared with the experimental spectrum measured.

Introduction

The process of internal bremsstrahlung (IB) from β-decay has been studied experimentally and theoretically quite extensively [1]. There is a considerable discrepancy between the experimental and theoretical results. In general, the experimental spectrum is higher than the predicted spectrum especially at high photon energy [2,3,4]. In the theoretical calculations, inclusion of Coulomb effects reduces the disagreement but still leaves a large discrepancy [5].

Detour transitions are those in which the parent nucleus first emits the photon and goes into a virtual intermediate excited state from which it subsequently β-decays to the final state or vice-versa. Although the total intensity of radiation from the detour transitions may be small compared with that from the direct transition, the high frequency portion of the spectrum can be dominated by the detour transitions.

The β-emitter, ^{204}Tl is of the first forbidden type, an investigation of the IB of ^{204}Tl may also give an idea of the contribution to the IB from the detour transition. ^{204}Tl has a relatively low beta end-point energy (0.76 MeV) and high atomic number.

In the present work, the spectrum of detour transition was calculated and compared with the experimental IB spectrum.

The details of experimental spectrum and calculations

The effect of the detour transitions were calculated only for the ^{204}Tl that is unique first-forbidden β-decay ($\Delta J = 2$, yes).

In our calculations, we used a formalism of Ford and Martin [6]. The following expression has been given for the photon intensity per β-decay differential in photon wave number.

$$\frac{k}{\Gamma_\beta}\frac{d\Gamma_\gamma}{dk} = \frac{2\alpha}{\pi N(w_0)}(F_1(k,w_0) + \xi F_2(k,w_0) + \eta F_3(k,w_0)),$$

where

$$N(w_0) = 2\int_m^{w_0} dw(w_0 - w)^2 wp\,(p^2 + (w_0 - w)^2)(1 + \pi\alpha Z\frac{w}{p}),$$

$$p = \sqrt{w^2 - 1},$$

$$F_1(k,w_0) = \int_m^{w_0-k} dw\, q^2(1 + \pi\alpha Z\frac{w}{p})\{((w_e^2 - w^2)(w_e^2 - m^2 + q^2) + 2m^2 k w_e)$$

$$\times \log\frac{w+p}{m} - 2(w_e(w_e^2 - m^2 + q^2) + k(w_e^2 - ww_e + w^2))p\},$$

$$F_2(k,w_0) = -k\int_m^{w_0-k} dw\, q^2(1 + \pi\alpha Z\frac{w}{p})\{m^2(2w + \frac{3}{2}k)\log\frac{w+p}{m} - (2w^2 + \frac{3}{2}kw - k^2)p\}$$

$$F_3(k,w_0) = 2k^2\int_m^{w_0-k} dw\, q^2(1 + \pi\alpha Z\frac{w}{p})wp.$$

These integrals are all expressed in terms of elementary functions in [6].

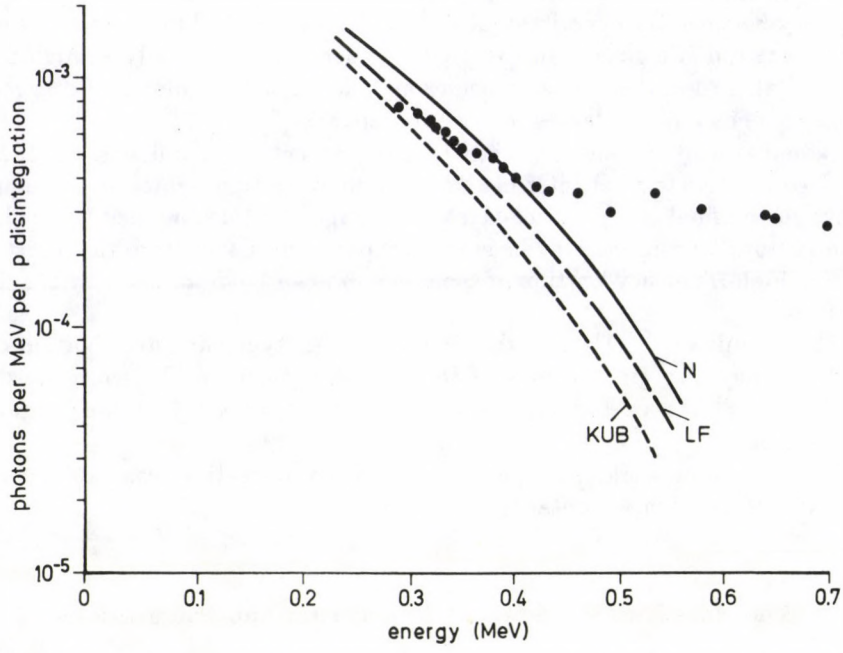

Fig. 1. ^{204}Tl internal bremsstrahlung intensity spectrum .... Experimental data; theoretical curves KUB [7],LF [8] and N [9] theories

The experimental IB spectrum from ^{204}Tl is shown in Fig. 1.

In order to obtain the true IB photon distributions, the measured pulse height spectrum has been corrected for background, energy resolution, K–X ray escape, Compton electron distribution, geometrical and γ-detection efficiency for the crystal, for backscattering from the photomultiplier window and also from the surrounding material used as shielding. Details were given in [4].

Results and discussion

We have calculated the spectrum for the decay of ^{204}Tl ($W_0 = 2.48$ m) to illustrate in magnitude of the effect of the detour transitions. In Fig. 2, the spectrum was plotted for the case where the parameters $\xi = \eta = 1$; to compare the spectrum for the direct transition alone ($\xi = \eta = 0$) was also shown. The largest effect was found near the middle of the spectrum where the detour transitions increase the intensity by about 80 %.

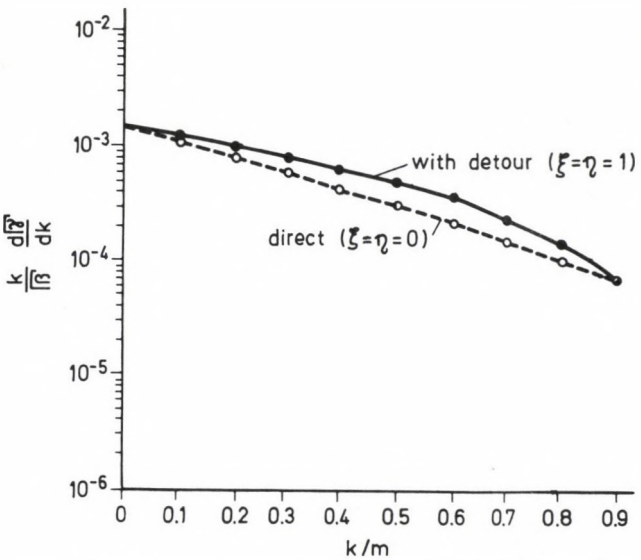

Fig. 2. **The spectrum of internal bremsstrahlung for ^{204}Tl. The photon energy is in units of electron rest energy**

It can be seen from Fig. 1 that in the high energy region of the experimental spectrum, there are disagreements with the theoretical results. In general, the observed spectrum is higher than the predicted spectrum, the discrepancy being greater the higher the photon energy. Inclusion of Coulomb effects in the theoretical

Table I
Comparison of calculated values of detour transition with the experimental values

Energy (k/m)	Calculations	Experiment
0.56	$\sim 7{\cdot}10^{-4}$	$\sim 7.8{\cdot}10^{-4}$
0.6	$\sim 5{\cdot}10^{-4}$	$\sim 7{\cdot}10^{-4}$
0.7	$\sim 4{\cdot}10^{-4}$	$\sim 5{\cdot}10^{-4}$
0.8	$\sim 2{\cdot}10^{-4}$	$\sim 4{\cdot}10^{-4}$

calculations reduces the disagreement but still leaves a large discrepancy. These might be explained partly as due to the detour transitions.

In Fig. 1, it can be seen that there is no agreement between KUB theory and any energy region of the experimental spectrum. The reason for this is that the effect of the nuclear charge on the radiation and detour transitions are neglected according to KUB theory. Because ^{204}Tl has high atomic number, the Coulomb effect is important. In the region 0.3–0.4 MeV the experimental results are in agreement with that of the LF theory. N and LF theories take into account the Coulomb effect but only this correction does not explain the discrepancy in the high energy region. Detour transitions might be considered, too. Above 0.4 MeV experimental results are higher than theoretical results. In this region, the effects of the detour transitions are dominant as it can be seen in Fig. 2. Thus the reason for disagreements between experimental and theoretical results can be explained by detour transitions.

This calculation is valid for the case of the first-forbidden transition. The calculations of the higher-order corrections are in progress.

References

1. I. S. Batkin and Yu. G. Smirnov, Sov. J. Part. Nucl., *11*, 564, 1980.
2. R. Prasad Babu, K. Narasimhamurty and V. A. Narasimhamurty, Phys. Rev., *C13*, 1267, 1976.
3. B. R. S. Babu et al, J. Phys. G: Nucl. Phys., *11*, 1213, 1985.
4. G. Tanır, B. Şarer and H. Kızıltan, Acta Phys. Hung. *71*, 45, 1992.
5. D. Gebhardt, Nucl. Phys. A, *115*, 207, 1968.
6. G. W. Ford and C. F. Martin, Nucl. Phys. A, *134*, 457, 1969.
7. J. K. Knipp and G. E. Uhlenbeck, Physica, *3*, 425, 1936.
8. R. R. Lewis and G. W. Ford, Phys. Rev., *107*, 756, 1957.
9. S. B. Nilsson, Ark. Fys., *10*, 467, 1956.

Acta Physica Hungarica 71 (3-4), pp. 161–170 (1992)

LEVEL STRUCTURE OF ^{154}Gd

S. U. EL-KAMEESY, M. S. ABDEL-WAHAB,
L. AL-HOUTY* and H. ABOU-LEILA*

Physics Department, Faculty of Science, Ain Shams University
Cairo, Egypt
**Physics Department, Faculty of Science, Qatar University*
Doha, Qatar

(Received in revised form 10 September 1991)

The decay of ^{154}Eu to ^{154}Gd has been studied using H. P. Ge and H. P. Ge-NaI(Tl) spectrometers in coincidence measurements. 141 gamma transitions have been observed. One of these transitions is found to be new and has an energy of 202.5 keV. The 165.9, 202.5, 229.8 and 484.6 keV transitions are placed correctly in the decay scheme of ^{154}Eu. The levels from this and previous work are compared with those calculated by means of the unified model.

1. Introduction

The decay of ^{154}Eu to ^{154}Gd has been studied early by Meyer [1]. Electron capture intensities to the excited states of ^{154}Sm were estimated using the log ft values of beta transitions to the corresponding states of ^{154}Gd. Hansen et al [2] and Ng et al [3] obtained the branching ratio of beta decay to the excited states of ^{154}Gd by beta ray measurements. The relative intensities of gamma rays in the decay of ^{154}Eu were measured by Yoshizawa [4]. Intensities of the 618 and 692 keV E0 transitions measured by Yamada et al [5] and the multipole mixing ratios of the 692.873 and 1005.0 keV transitions by Gupta et al [6] were used in the internal conversion and gamma ray intensity measurements by Iwata et al [7]. Angular correlation experiments were performed by Varnell et al [8] to determine the multipole mixing ratios of some transitions and several new gamma transitions were observed in ^{154}Gd. An experiment to measure the triple gamma ray directional correlation is employed to study the 723–873–123 cascade following the beta decay of ^{154}Eu by Lewis [9].

Although there is general agreement between the results of these authors, still there are some weak intensity transitions not known and/or not placed in the decay scheme of ^{154}Eu as well as doubted spin-parity assignments to some energy levels as reported by Helmer [10] in a recent publication of accumulated results. Accordingly, it was felt worthwhile to reinvestigate the gamma spectrum of ^{154}Gd following the beta decay of ^{154}Eu using a detector with better resolution (= 1.8 keV at 1.33 MeV). In addition, contributions due to gamma background spectra are highly eliminated since a complete quantitative analysis of gamma background radiations is available [11]. Another goal was to extend the comparison of the experimentally observed energy levels to those predicted by the unified model.

2. Experimental procedure

Several sources from different manufacturers have been used (ORTEC, USA, Isotope Products, Canada and French Atomic Energy Commission, France).

In the present work, successive gamma singles spectra have been investigated over a period of two years using different sources of activities ranging from 50 μC to 1 mC placed at different distances from the detector.

The gamma ray spectra over the range 80–2000 keV have been studied using an ORTEC p-type hyper pure Ge-detector. The detector active volume is 56.6 cc while its energy resolution is $\simeq$ 1.8 keV at 1.33 MeV. The obtained spectra were analysed using a NORLAND 4096 multi-channel analyzer (MCA) model 5400 with data processor, model 5430, and an IBM-XT personal computer equipped with a Nucleus 8192 MCA plug-in card.

The system was calibrated for energy and photopeak efficiency using well-known standard sources (^{22}Na, ^{60}Co, ^{133}Ba, ^{137}Cs and ^{266}Ra).

The gamma–gamma coincidence measurements were performed using a 3″×3″ NaI(Tl)-Ge fast-slow coincidence spectrometer. The time resolution of the fast coincidence pulse was about 20 ns. A triple slow coincidence pulse (time resolution 0.5 μs), was used to gate the MCA to obtain the coincidence spectra.

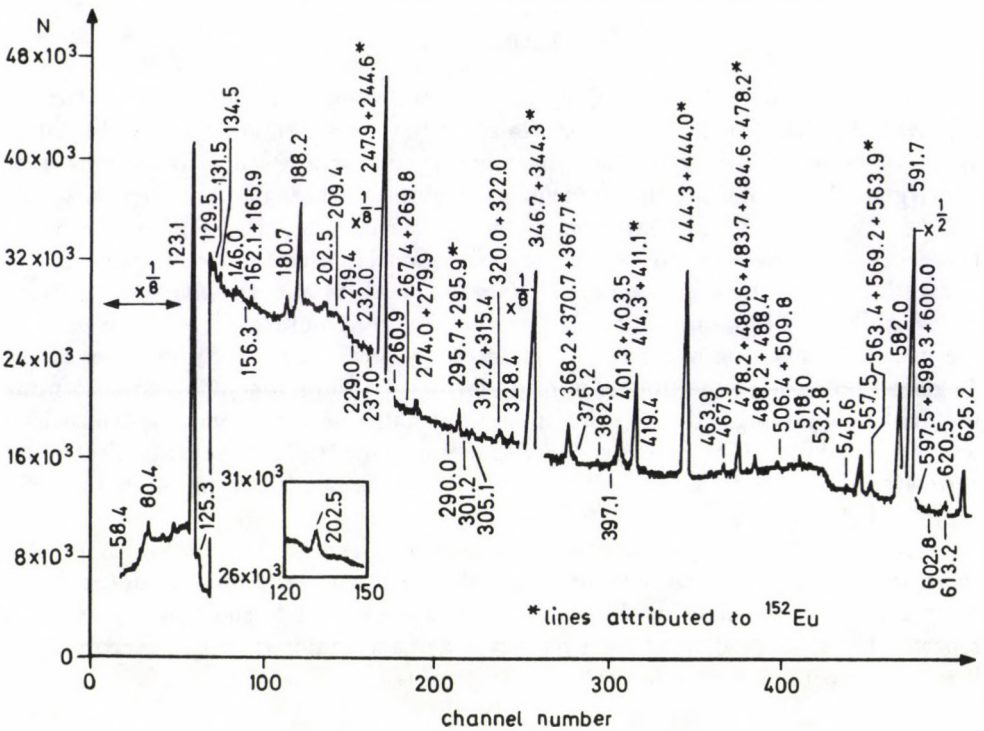

Fig. 1. A typical singles spectrum for the low energy gamma transitions of ^{154}Eu using H.P.Ge-detector where the source activity was 50 μC, source-to-detector distance was 15 cm and the measuring time was 20 h

3. Gamma-ray singles spectra

The analysis of the gamma ray spectra observed in our measurements has revealed the existence of 141 gamma transitions attributed to the decay of ^{154}Eu. Their energies and intensities, together with the previous data [7,10] are listed in Table I. The intensities were normalized to 100 for the 1247 keV gamma ray. Successive measurements were undertaken within two years to differentiate between lines of different origins. One of the gamma transitions at energy 202.5 keV is found to be new and the reduction rate of its intensity is similar to the activity decay rate of ^{154}Eu. The intensities of the 563.4, 680.0 and 801.2 keV transitions which were not known previously are estimated in the present work as shown in Table I. A typical gamma-singles spectrum of the low energy transitions is shown in Fig. 1 where the 202.5 keV gamma transition is clearly visible.

4. Gamma–gamma coincidence measurements

Gamma–gamma coincidence measurements have been performed using several window sets; only the results from three window sets are considered. These windows are: 125–185, 200–270 and 560–625 keV. There are fourteen gamma transitions not placed in the level scheme of ^{154}Gd [10]. Three of these at energies 165.9, 229.8 and 484.6 keV are placed correctly in the level scheme by means of our measurements.

To confirm the placement of the 165.9 keV transition between the 1293.3 and 1127.8 keV levels, the 131.5 keV transition depopulating the 1127.8 keV level was selected as gating transition because of two reasons worth mentioning. First, the 125–185 gate is pure from any contributions due to ^{152}Eu. Furthermore, the most intense 756.8 and 1004.7 keV transitions depopulating the 1127.8 keV level are not suitable as gating transitions because they are very close to other γ-transitions attributed to ^{152}Eu decay. The obtained spectra confirm the presence of the 165.9 keV transition as is obvious in Fig. 2.

The 229.8 and 484.6 keV transitions were proposed to populate the 1047.5 keV level. The 232.0 keV transition depopulating the 1047.5 keV level was chosen as a gating transition. Fig. 2 shows a typical coincidence spectrum gated by the energy window 200–270 keV. The analysis of the obtained spectra confirms the existence of these two transitions populating the 1047.5 keV level.

The new observed 202.5 keV transition was proposed to populate the 1415.0 keV level. The most intense lines depopulating the 1415.0 keV level are the 600.0 and 1292.0 keV transitions. The 1292.0 keV transition is close to the high intense 1299.1 keV transition attributed to ^{152}Eu decay, hence, the 600.0 keV transition was chosen as a gating transition (gate 560–625 keV). Fig. 2 shows an example of the obtained spectra which confirms the position of the 202.5 keV transition between the 1617.1 and 1415.0 keV levels.

Table I
Energy and intensity values for gamma transitions in ^{154}Gd following β^--decay of ^{154}Eu

Present work				Helmer [10]				Iwata [7]		
E_γ		I_γ		E_γ		I_γ		E_γ	I_γ	
58.40	10	0.012	10	58.4		0.0113	11	–	–	
80.40	12	0.010	6	80.4		0.008	4	–	–	
123.10	8	117.54	30	123.068	3	117.5	8	123.1	118.5	12
125.35	16	0.02	1	125.39		0.020	6	–	–	
129.52	13	0.04	1	129.5		0.039	5	–	–	
131.5	1	0.03	1	131.573	29	0.0310	11	–	–	
134.56	20	0.02	1	134.84		0.0203	11	–	–	
146.04	10	0.070	16	146.036	22	0.0733	28	–	–	
156.3	1	0.032	12	136.31	10	0.0282	11	–	–	
162.11	18	0.003	1	162.09		0.0028	14	–	–	
165.90	21	0.007	1	165.91		0.0065	14	–	–	
180.75	11	0.015	6	180.73		0.0127	28	–	–	
188.22	15	0.668	8	188.246	13	0.676	22	–	–	
202.50	16	0.08	2	–		–		–	–	
209.42	12	0.007	1	209.4	4	0.0068	23	–	–	
219.4	1	0.007	1	219.4		0.0065	25	–	–	
229.01	13	0.006	2	229.0		0.0056	22	–	–	
231.03	6	0.071	9	232.01	5	0.0677	28	–	–	
237.0	3	0.020	7	237.0		0.017	11	–	–	
247.95	17	19.9	1	247.932	15	19.87	9	248.0	19.91	13
260.92	12	0.006	1	260.9		0.0056	25	–	–	
267.41	11	0.04	1	267.44		0.0395	17	–	–	
269.82	16	0.020	6	269.8		0.0197	28	–	–	
274.0	4	0.013	5	274.0	5	0.0113	6	–	–	
279.91	21	0.009	2	279.9		0.0085	6	–	–	
290.0	3	0.011	3	290.0		0.0096	6	–	–	
295.72	12	0.007	1	295.7		0.0068	6	–	–	
301.2	2	0.035	15	301.25		0.0282	11	–	–	
305.12	13	0.05	1	305.12		0.0496	20	–	–	
312.23	18	0.042	10	312.28		0.0415	17	–	–	
315.42	15	0.015	8	314.42		0.0130	6	–	–	
320.0	1	0.003	1	320.0	1	0.0028	20	–	–	
322.02	11	0.19	1	322.01	5	0.189	8	–	–	
328.4	3	0.026	9	322.48		0.0259	14	–	–	
346.71	14	0.085	10	346.72	5	0.085	3	–	–	
368.20	11	0.010	9	368.21		0.0085	6	–	–	
370.72	8	0.015	4	370.71		0.015	4	–	–	
375.20	9	0.005	2	375.2	5	0.0051	28	–	–	
382.02	15	0.03	1	382.00	5	0.0285	11	–	–	
397.12	23	0.09	2	397.14		0.085	3	–	–	
401.36	22	0.61	8	401.30	5	0.56	3	–	–	
403.57	9	0.071	11	403.55	5	0.076	3	–	–	
414.32	8	0.015	8	414.30		0.0141	8	–	–	
419.4	1	0.015	6	419.4		0.011	6	–	–	
444.38	7	1.62	5	444.39	4	1.60	3	444.5	1.63	3
463.93	19	0.014	5	463.9		0.0121	6	–	–	

Table I (cont.)

Present work				Helmer [10]				Iwata [7]		
E_γ		I_γ		E_γ		I_γ		E_γ	I_γ	
467.90	12	0.165	9	467.92		0.161	6	–	–	
478.25	7	0.625	27	478.26	5	0.612	14	478.3	0.626	27
480.62	12	0.015	4	480.61		0.0138	6	–	–	
483.75	15	0.016	3	483.74		0.0141	8	–	–	
484.63	9	0.012	4	484.64		0.0113	6	–	–	
488.40	11	0.021	6	488.26		0.020	8	–	–	
506.4	2	0.019	4	506.4		0.017	6	–	–	
509.9	2	0.11	3	509.88		0.103	4	–	–	
518.0	1	0.135	4	518.00	5	0.132	5	–	–	
532.88	10	0.04	1	532.84		0.031	6	–	–	
545.6	1	0.05	1	545.6		0.047	6	–	–	
557.5	2	0.75	2	557.56	5	0.741	17	557.6	0.758	24
563.40	7	0.008	2	563.4		–		–	–	
569.20	7	0.03	1	569.23		0.0282	11	–	–	
582.0	1	2.62	2	582.00	5	2.60	3	582.0	2.61	3
591.70	11	14.30	18	591.76	3	14.29	6	591.7	14.35	6
597.5	1	0.020	6	597.5		0.0158	8	–	–	
598.30	9	0.015	4	598.31		0.0172	8	–	–	
600.0	1	0.017	2	600.0		0.017	11	–	–	
602.8	2	0.10	3	602.81	5	0.096	4	–	–	
613.22	16	0.281	12	613.26	5	0.267	10	–	–	
620.5	1	0.031	2	625.22	5	0.925	21	625.2	0.927	21
642.41	8	0.012	3	642.4		0.011	6	–	–	
649.4	1	0.22	2	649.44	5	0.214	8	–	–	
650.62	9	0.030	4	650.6		0.0282	11	–	–	
664.63	10	0.08	2	664.68	5	0.082	3	–	–	
668.9	2	0.035	4	668.9		0.034	4	–	–	
676.52	9	0.440	5	676.59	5	0.395	12	676.5	0.47	5
680.0	2	0.010	3	680.0		–		–	–	
692.41	7	5.183	17	692.42	4	5.182	25	692.4	5.182	25
715.76	3	0.49	1	715.76	5	0.494	15	–	–	
722.30	5	55.10	5	722.30		55.09	21	723.2	58.19	21
756.83	6	13.11	5	756.86	3	13.09	9	756.8	13.18	7
774.41	5	0.03	1	774.4		0.028	14	–	–	
790.13	4	0.032	6	790.12		0.031	8	–	–	
800.2	1	0.10	2	800.2		0.092	14	–	–	
801.21	4	0.035	7	801.2		–		–	–	
815.56	8	1.45	2	815.55	5	1.46	7	815.5	1.51	5
845.35	5	1.70	6	845.39	5	1.687	21	845.4	1.687	21
850.66	4	0.657	6	850.64	5	0.668	15	850.7	0.692	23
873.2	1	35.15	9	873.20	3	35.14	10	873.1	35.18	12
880.60	5	0.25	3	880.61	5	0.231	9	–	–	
892.73	5	1.45	3	892.73	5	1.44	4	892.8	1.497	26
898.3	1	0.006	2	898.37		0.0056	14	–	–	
904.05	5	2.46	4	904.05	5	2.47	9	904.1	2.62	3
906.15	7	0.035	5	906.1		0.0338	14	–	–	
919.25	6	0.031	7	919.24		0.0352	14	–	–	
924.5	1	0.17	2	924.49	5	0.166	7	–	–	

Table I (cont.)

Present work				Helmer [10]				Iwata [7]			
E_γ		I_γ		E_γ		I_γ		E_γ		I_γ	
981.36	5	0.02	1	981.3		0.022	6	–		–	
984.5	2	0.020	4	984.5		0.0180	34	–		–	
996.35	7	30.10	3	996.30	3	30.07	12	996.2	12	30.09	12
1004.75	9	52.1	1	1004.76	3	52.03	19	1004.7		52.04	19
1012.8	2	0.008	2	1012.8	2	0.0082	34	–		–	
1023.0	2	0.021	4	1023.0	10	0.020	8	–		–	
1033.07	9	0.034	3	1033.4		0.0338	14	–		–	
1047.43	12	0.15	3	1047.4	1	0.141	6	–		–	
1049.40	8	0.05	2	1049.4	1	0.0493	20	–		–	
1110.0	2	0.010	6	1110.0		0.008	6	–		–	
1118.52	14	0.30	3	1118.5	1	0.290	9	–		–	
1124.22	18	0.020	6	1124.2		0.0197	28	–		–	
1128.44	8	0.85	5	1128.4	1	0.85	6	1128.5		0.90	4
1136.15	7	0.022	4	1136.1		0.0211	28	–		–	
1140.92	6	0.64	3	1140.9	1	0.638	20	1140.7		0.671	14
1153.14	11	0.04	1	1153.1	5	0.039	11	–		–	
1160.6	2	0.125	12	1160.6		0.124	5	–		–	
1170.0	5	0.015	6	1170.0	5	0.012	6	–		–	
1188.63	8	0.26	5	1188.6		0.251	20	–		–	
1232.11	14	0.03	1	1232.1	5	0.026	17	–		–	
1241.65	12	0.40	3	1241.6	2	0.366	11	1241.4		0.38	5
1246.60	11	2.35	7	1246.6	2	2.33	15	1246.2		2.49	4
1274.55	10	100.00	3	1274.51	7	100.0	5	1274.4		100.00	3
1290.0	1	0.03	1	1290.0	2	0.0324	14	–		–	
1292.06	8	0.04	1	1290.0	2	0.0369	14	–		–	
1295.58	30	0.029	11	1295.5	2	0.0254	28	–		–	
1387.07	11	0.06	2	1387.0	5	0.056	6	–		–	
1400.0	3	0.00	2	1400.0		0.0084	28	–		–	
1408.44	12	0.06	2	1408.4	2	0.059	8	–		–	
1415.03	7	0.015	6	1415.0	5	0.0113	6	–		–	
1418.6	2	0.024	7	1418.6	2	0.0208	11	–		–	
1419.06	12	0.006	2	1419.0		0.0056	3	–		–	
1425.66	20	0.004	1	1425.6	6	0.0036	22	–		–	
1490.26	15	0.007	2	1490.2		0.0084	14	–		–	
1494.0	2	2.10	11	1494.08	7	2.058	16	1494.4		2.058	16
1510.0	2	0.015	4	1510.0	5	0.0141	28	–		–	
1522.1	2	0.002	1	1522.0	10	0.0017	8	–		–	
1531.44	12	0.020	7	1531.4		0.0172	11	–		–	
1537.85	15	0.15	3	1537.8		0.141	6	–		–	
1596.50	6	5.25	2	1596.45	7	5.247	26	1596.7		5.247	26
1667.33	12	0.006	2	1667.3		0.0056	8	–		–	
1673.17	21	0.004	1	1673.6		0.0039	11	–		–	
1716.9	2	0.002	1	1716.9		0.0017	10	–		–	
1773.13	23	0.0010	4	1773.0	10	0.0008	6	–		–	
1838.0	2	0.003	1	1838.0	5	0.0022	6	–		–	
1895.18	13	0.0020	6	1895.0	10	0.0017	6	–		–	

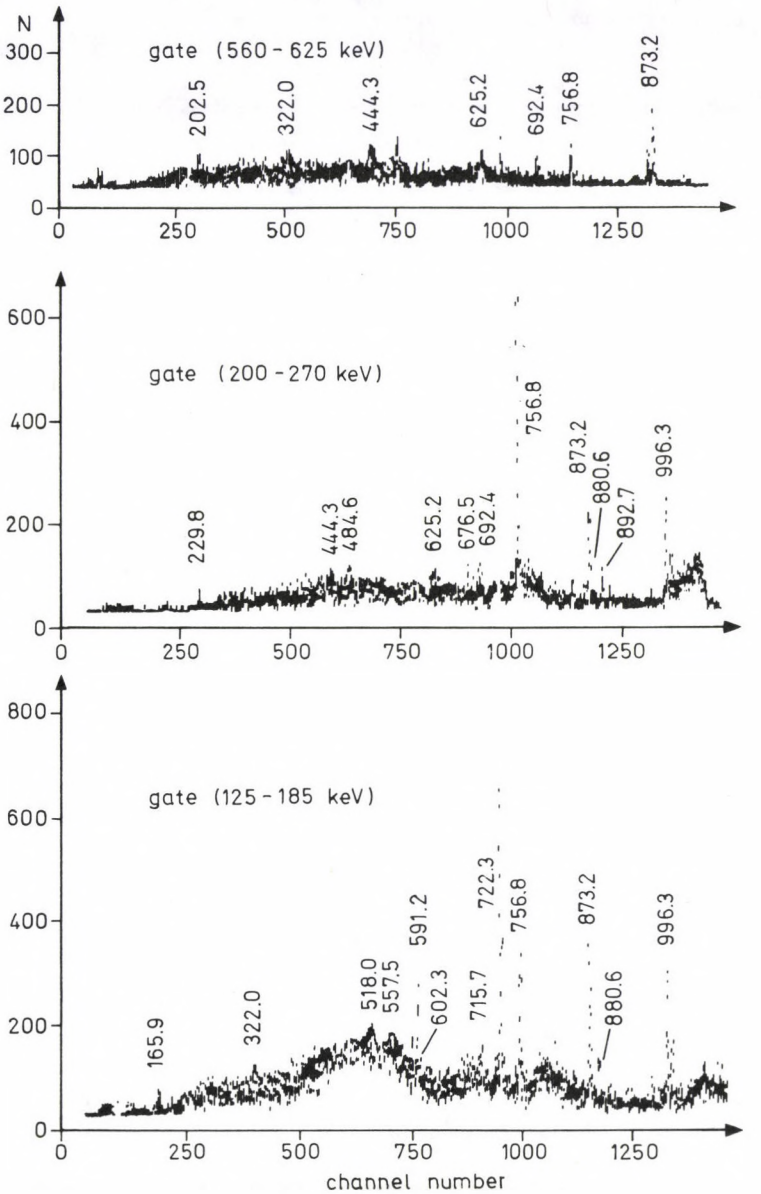

Fig. 2. Gamma–gamma coincidence spectra using NaI(Tl)-Ge detectors

The results of the present work have been used to construct a partial level scheme of ^{154}Gd as shown in Fig. 3.

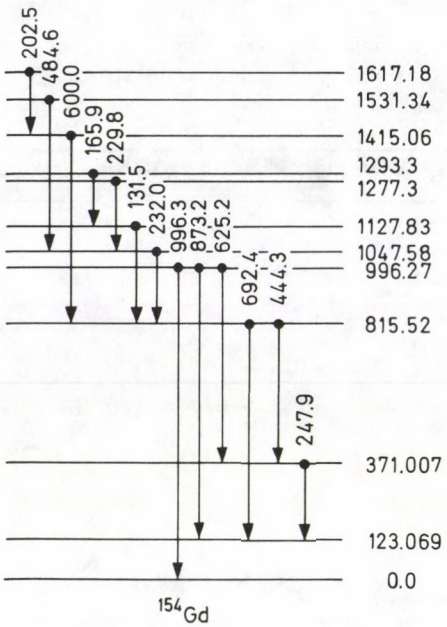

Fig. 3. Partial level scheme of ^{154}Gd

5. Analysis of the ^{154}Gd energy bands

The analysis of the spectra of strongly deformed nuclei is based on the collective model [12]. In lowest order the energy spacing in a rotational band is predicted to follow an $I(I+1)$ progression. First order corrections are attributed to Coriolis interaction, non-axial symmetry of the deformed rotor, or rotation–vibration interaction. A systematic deviation from the rotational spectrum [13] is noted. This deviation can be explained by adding correction terms to the energy representing different modes of coupling. This coupling contributes to a change in the energy given by last terms in the energy relation

$$E_{I,K} = E_k + AI(I+1) + BI^2(I+1)^2 + \ldots + (-1)^{I+k}\frac{(I+k)!}{(I-k)!}[(A_{2k} + B_{2k}I(I+1) + \ldots].$$

The energy spectra for ten bands are calculated and the set of parameters which yielded the best fit to the data by means of the foregoing energy relation are adopted for every band.

5.1. Positive parity bands

A. The $k^\pi = 0^+$ ground state, $k^\pi = 0^+$ β-vibrational, $k^\pi = 2^+\gamma$-vibrational bands

The regular spacing of energy levels of these bands indicates that they are rotational bands with fitting parameters $E_k = 58.0427$, $A = 15.14$ and $B = -0.01$ for the ground state band, $E_k = 747.7$, $A = 11.328$ and $B = -0.0045$ for the β-vibrational band, $E_k = 897.766$, $A = 19.583$, $B = -0.0615$ and $A_{2k} = -0.00295$ for the γ-vibrational band.

B. The $k^\pi = 0^+$ band

This band was proposed to consist of levels at $(0^+)1294.93$, $(2^+)1418.35$, $(4^+)1698.0$ keV. The fitting parameters are $E_k = 1294.93$, $A = 20.74$ and $B = -0.02975$. The observed level spacings indicate extreme agreement with our calculation. The calculated energy of the 6^+ member of this band is 2113.888 keV which corresponds to the 2101.0 keV level observed in (d, d') reaction and/or the 2117.1 keV level observed in $^{154}\mathrm{Sm}(\alpha, 4n\gamma)$ and $^{152}\mathrm{Sm}(\alpha, 2n\gamma)$ reactions [14].

C. The $k^\pi = 2^+$ band

The energy levels $(2^+)1531.318$, $(3^+)1660.9$, $(4^+)1790.2$ keV were proposed members of this band. The level spacing in this band can now be described by the parameters $E_k = 1531.3$, $A = 28.6$ and $B = -0.39$. The 5^+ member of this band is found to have an energy of 2038.3 keV. This may correspond to the 2040.5 keV level observed in (α, α') reaction [14].

D. The $k^\pi = 4^+$ band

This band is used on the configuration $((\pi 3/2\ [411])\ (\pi 5/2\ [413]))$ and was proposed to consist of levels at 1645.8, 1770.19, 1911.54, 2073.2 and 2253.99 keV with spin sequence 4–8. The observed level spacings indicate excellent agreement with our calculations where the fitting parameters are $E_k = 1405.855$, $A = 12.4064$, $B = -0.008728$ and $A_{2k} = 0.6 \times 10^{-8}$. The calculated energy of the 10^+ member of this band is 2665.6778 keV which may correspond to the 2668.3 keV level observed in nuclear reactions [14].

5.2 Negative parity bands

A. The $k^\pi = 0^-, 2^-, 7^-$ bands

The 0^- octupole-vibrational band was proposed to consist of levels at 1241.31, 1251.75, 1404.2, 1674.6, 2040.5 and 2482.2 keV with spin sequence 1–11. The 2^- octupole-vibrational band was proposed to consist of $(2^-)1719.565$, $(3^-)1796.45$, $(4^-)1861$ keV levels while the 7^- band consists of $(7^-)2137.49$, $(8^-)2309.47$ and $(9^-)2474.1$ keV levels. Calculations of energy levels using the foregoing formula were done for these three negative bands. All the experimental levels attributed to

each band were considered. It is noticed that this formula failed to determine the expected energy values for these bands. This may be due to the vibrational nature of these bands.

B. The $k^{\pi} = 1^{-}$ band

The $(2^{-})1347.559$, $(1^{-})1414.6$, $(4^{-})1560.09$ and $(3^{-})1617.14$ keV levels were proposed to be the members of this band. The calculated energy levels are in excellent agreement with the experimental values where the fitting parameters are $E_k = 1385.639$, $A = 6.308$, $B = 0.4811$ and $A_{2k} = 7.209$. The large value of A_{2k} is due to the strength of the Coriolis coupling.

6. Conclusion

In this work an attempt has been made making use of good resolution detectors to study the energy spectra of ^{154}Eu–β^{-} decay. A new transition is observed and placed correctly in the decay scheme. Also, the 165.9, 229.8 and 484.6 keV transitions are placed in the decay scheme by means of our $\gamma - \gamma$ coincidence measurements for the first time. Furthermore, the unified model calculations were applied to ten energy bands attributed to the ^{154}Gd level scheme. A good agreement is noticed between experimental and theoretical calculations for positive parity states giving a correct prediction for the already adopted levels and assigning the spin–parity character of some higher levels. Contrary to that, a disagreement is found between experimental and theoretical calculations for the negative parity bands (expect the $k = 1^{-}$ band) and the applied model is not suitable because of the vibrational nature of these bands.

References

1. R. A. Meyer, Phys. Rev., *170*, 1089, 1968.
2. P. G. Hansen, H. L. Nielsen and K. Wilsky, Nucl. Phys., *89*, 571, 1968.
3. L. K. Ng, K. C. Mann and T. G. Walton, Nucl. Phys., *A116*, 433, 1968.
4. Y. Yoshizawa, Y. Iwata and Y. Jinuma, Nucl. Inst. Meth., *174*, 133, 1980.
5. H. Yamada, H. Kawakami, M. Koite and K. Komura, J. Phys. Soc. Jpn., *42*, 1448, 1977.
6. J. B. Gupta, S. L. Gupta, J. H. Hamilton and A. V. Ramayya, Z. Phys., *A282*, 179, 1977.
7. Y. Iwata, M. Yasuhara, K. Maeda and Y. Yoshizawa, Nucl. Inst. Meth., *219*, 123, 1984.
8. L. Varnell, J. D. Bowman and J. Trischuk, Nucl. Phys., *A127*, 270, 1969.
9. G. C. Lewis, G. Mohammad, L. D. Wyly, E. T. Patronis and C. H. Braden, Nucl. Inst. Meth., *211*, 371, 1983.
10. R. G. Helmer, Nucl. Data Sheets, *52*, 1, 1987.
11. L. Al-Houty, H. Abou-Leila and S. El-Kameesy, Invi. Inter., *13*, 393, 1987.
12. A. Bohr and B. Mottelson, Nuclear Structure, W. A. Benjamin, New York, 1969.
13. K. Kumar and M. Baranger, Nucl. Phys., *A110*, 529, 1968.
14. C. M. Lederer and V. S. Shirley, Table of Isotopes, 1978.

Acta Physica Hungarica 71 (3-4), pp. 171–177 (1992)

14.5-MeV NEUTRON CAPTURE CROSS-SECTION MEASUREMENTS IN ^{160}Gd WITH ACTIVATION TECHNIQUE

CHR. NECHEVA, N. NENOFF, M. VLASAREV*, A. KIROV and D. KOLEV

Faculty of Physics, Sofia University
Sofia, Bulgaria
**Institute for Plant Protection*
Kostinbrod, Bulgaria

(Received in revised form 10 October 1991)

Activation cross-sections for neutron capture have been measured at an energy of 14.5 MeV for ^{160}Gd, relative to $\sigma(^{160}\mathrm{Gd}(n,2n)^{159}\mathrm{Gd}) = 1975$ mb. Gamma-ray spectra of the product nuclei were measured with a HP Ge-detector. By systematically varying the geometrical arrangement the corrections due to the influence of lower energy neutrons could be determined. The corrected activation capture cross-section at 14.5 MeV is found to be 1.0 ± 0.2 mb.

1. Introduction

The activation technique is a relatively simple method to measure fast neutron cross-sections. Applied to (n,γ) cross-sections appear to be difficult primarily due to accompanying background neutron sources. On the average, the background neutrons are of a much lower energy than the primary neutrons. Even a small contamination by background neutrons can seriously disturb the measurements, because the (n,γ) cross-section generally increases rapidly with decreasing neutron energy [1–5]. This contamination would be particularly serious for deformed nuclei, for which even a 1 % fraction of low energy neutrons can disturb the activation results considerably [6].

The neutrons with lower energy than the primary neutrons, are produced primarily by (n,n'), (n,pn) and $(n,2n)$ reactions in the sample and in the surrounding material in the target–sample assembly. This type of neutrons are called secondary neutrons and their influence was first established experimentally by Valkonen and Kantele [2]. In measurements, where we have utilized the reaction $\mathrm{T}(d,n)^4\mathrm{He}$ for the production of monoenergetic 14 MeV neutrons, the projectiles may also generate a background of low-energy primary neutrons from $\mathrm{D}(d,n)^3\mathrm{He}$ reactions. The influence of this type lower-energy neutrons would be serious when an old T-target is used for a long time by which the d-contamination could achieve a high value.

14.5–MeV neutron capture cross-sections in ^{160}Gd have been measured with activation technique by Kantele and Valkonen and have been found to be 1.0 ± 0.4 mb

[3]. The purpose of our experiment is to measure the same cross-section with another type activation technique, a Water-cooling Neutron Generator, type NA-3 (made in Hungary) and present measuring counting techniques.

The reaction $^{160}Gd(n,\gamma)^{161}Gd$ is suitable for investigation of the effects of low-energy neutrons. ^{160}Gd is a deformed nucleus and has a high capture cross-section for neutrons with low energy. The influence of low-energy background neutrons has been studied by systematically varying the target–sample arrangement.

2. Experimental arrangement and procedure

The experiment was carried out at the NA–3 Neutron Generator at the Institute for Plant Protection, Kostinbrod, Bulgaria, which produces neutrons with an energy of 14.5 MeV through the reaction $T(d,n)^4He$. We have used tritiated titanium targets (2 mg/cm^2) on a 0.4 mm thick molibdenum backing. The deuterons were accelerated to 120 keV. Beam currents around 1 μA were used. The beam spot diameter was typically 4 mm. The relative time variation of the neutron flux during the irradiation was measured and the activation results were corrected for the time variation effects.

The target is of rotating type and cooling is provided by water, which is in contact with all backing of the target. The target holder is made of stainless steel. The target head is made of aluminium. Consequently, because of existing constructive conditions, the minimal possible layer of cooling water is 1.3 mm; the Al layer between the target and samples is 2.7 mm; the minimal distance between the target and samples is 4.5 mm.

The samples of pressed Gd_2O_3 were made with a diameter of 8 mm in all cases and different thicknesses (260 mg/cm^2–670 mg/cm^2). Measurements of the activation cross-section for gadolinium were performed with various target–sample geometries. Irradiation times are generally 11 min with beam currents of typically 1 μA. The various irradiations were performed with new targets with the purpose to reduce the deuteron contamination of the targets.

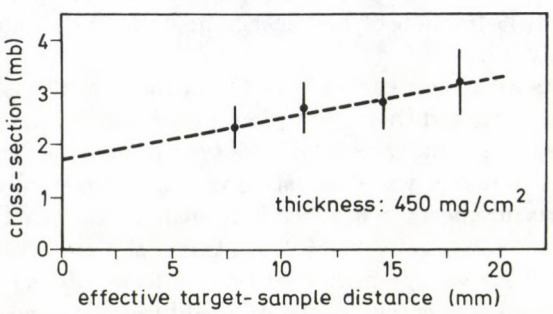

Fig. 1. Dependence of the apparent activation cross-section on the effective distance between the target and the sample. Statistical uncertainties are given

The gamma rays from the induced activity were measured by a HP Ge-detector "ORTEC" with an active volume of 166 cm^3 and a resolution of 1.9 keV for the 1332.5 keV γ-line of ^{60}Co. The strongest gamma-ray line 360.9 keV ($I_\gamma = 60.6 \pm 6.0$ %) in the decay of ^{161}Gd ($T_{1/2} = 3.7$ min) was used [8]. Like a monitor reaction we used ^{160}Gd$(n, 2n)^{159}$Gd reaction, known to have a cross-section of 1975 ± 185 mb [7]. The strongest gamma-ray line 363.3 keV ($I_\gamma = 10.8 \pm 1.0$ %) in the decay of ^{159}Gd ($T_{1/2} = 18.56$ h) we used is very close to the 360.9 keV line from the decay of ^{161}Gd, but the two lines are well resolved in the spectra. The ^{161}Gd activity measured typically 11 min, but ^{159}Gd activity measured around 1 hour. Several sets of measurements were performed and the results show good consistency.

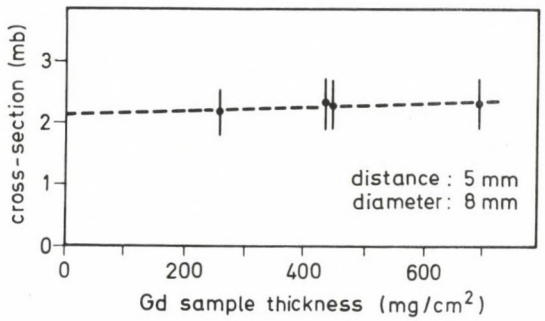

Fig. 2. Dependence of the apparent activation cross-section on the Gd-sample thickness. Statistical uncertainties are given

3. Experimental results

The results from measurements with various target–sample arrangements are shown in Figs 1–4. We have used the same representation as Valkonen and Kantele: "apparent cross-section", which means the value obtained from comparison with the known cross-section of ^{160}Gd$(n, 2n)^{159}$Gd reaction at 14.5 MeV neutron energy. The latter reaction has a cross-section which decreases rapidly with decreasing neutron energy and was used as monitor. Several sets of measurements were performed to establish the influence of primary low-energy neutrons from $d(d, n)^3$He reactions. The results show that we use a new T-target for one or two irradiations, the background of these neutrons does not influence the value of measured cross-sections. Thus, the geometrical effects observed on the apparent activation cross-section would then be caused by secondary neutrons.

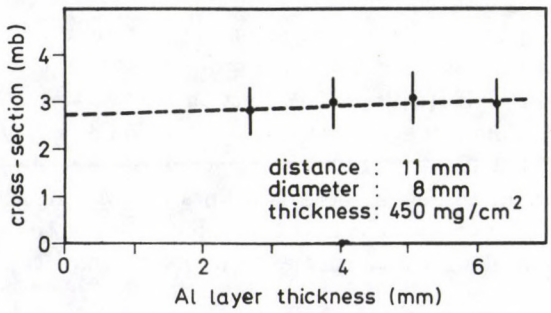

Fig. 3. **Dependence of the apparent activation cross-section on the thickness of Al layer between the target and the sample. Statistical uncertainties are given**

3.1. Dependence of apparent activation cross-section on effective target–sample distance

The influence of secondary neutrons, produced in materials surrounding the target and the sample or room-scattered neutrons can be studied through an investigation of the dependence of the total observed activation yield on effective target–sample distance. The total observed activation yield, $Y(n,\gamma)$, can roughly be described by

$$Y \sim \sigma_{14} \cdot \phi_{14} + \sigma_0 \cdot \phi_0 + \sigma_1 \cdot \phi_1, \tag{1}$$

where σ_{14} is the cross-section to be measured, σ_0 is the effective capture cross-section for room-scattered neutrons, σ_1 is the effective capture cross-section for secondary neutrons. Here ϕ_{14}, ϕ_0 and ϕ_1 are corresponding neutron fluxes.

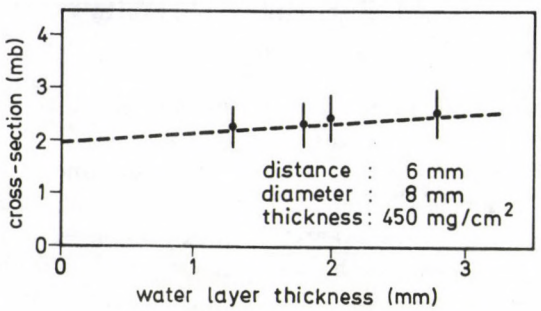

Fig. 4. **Dependence of the apparent activation cross-section on the thickness of water layer between the target and the sample. Statistical uncertainties are given**

We define an apparent cross-section for σ_{app} by

$$Y \sim \sigma_{app} \cdot \phi_{14}.$$

Thus,

$$\sigma_{app} = \sigma_{14} + \sigma_0 \cdot \frac{\phi_0}{\phi_{14}} + \sigma_1 \cdot \frac{\phi_0}{\phi_{14}}. \tag{2}$$

The distance dependence from a point source is

$$\phi_{14} \sim \frac{1}{r^2}.$$

The room-scattered neutron flux is assumed to be uniformly distributed, i.e.

$$\phi_0(r) = \text{constant}.$$

The secondary neutrons must have a distance dependence between these two extremes. Thus, we can roughly write

$$\sigma_{app} \sim \sigma_{14} + a \cdot f(r) + b \cdot f(r^2). \tag{3}$$

The influence of room-scattered neutrons and secondary neutrons from sources outside the sample itself can be determined by a measurement of the distance dependence of the apparent cross section and extrapolation to zero distance. In view of the fact that neutron source and samples are not points and have defined sizes, a change of these sizes is also a change of "effective" distance between the target and the sample [5]. The effective distance is defined by

$$\langle r \rangle = \frac{\int\int r \cdot ds_1 \cdot ds_2}{\int\int ds_1 \cdot ds_2}, \tag{4}$$

were ds_1 and ds_2 are area elements of the sample and the beam spot, respectively, and r is the distance between the two elements. Integration is carried out over the sample and beam spot areas.

The measurements were performed with samples 450 mg/cm^2 thick and 8 mm in diameter and the result are shown in Fig. 1.

3.2. Dependence on gadolinium sample size

The influence of secondary neutrons produced in the sample itself can be studied by observing the dependence of sample diameter and thickness on the apparent activation cross-section. The influence of activation sample diameter is taken into account in the target–sample effective distance (see 3.1). The effect of sample thickness was studied by varying it. The measurements were performed at a target–sample distance of 5 mm and samples with a diameter of 8 mm and various thicknesses. The experimental results are shown in Fig. 2.

3.3. Dependence on target-head thickness and cooling water

The target head is made of aluminium and there are a 2.7 mm Al layer and a 1.3 mm cooling water layer between the target and the sample. Aluminium is a material which has a small $(n, 2n)$ cross-section (< 0.17 mb [7]), but water is one of the major sources of secondary neutrons from (n, n') reactions. To study the effects of these layers the apparent activation cross-section was measured with various thicknesses of aluminium and water between the target and the sample. The measurements were performed with samples 8 mm in diameter and a thickness of 450 mg/cm^2 and constant target–sample distance. The results are shown in Figs 3 and 4.

The molibdenum target backing is another source of secondary neutrons primarily from $(n, 2n)$ reactions, but in our experiment the influence of molibdenum backing on the apparent activation cross-section is not taken into account.

3.4. Determination of the activation capture cross-section

The capture cross-section for the reaction $^{160}\mathrm{Gd}(n, \gamma)^{161}\mathrm{Gd}$ has been determined from Figs 1–4. The results indicate a linear dependence of the apparent cross-section and the lines through the experimental points have in all cases been determined by least-squares fitting. Extrapolation of the line in Fig. 1 to zero effective distance gives an apparent cross-section value corrected for both distance and diameter dependences. After that, this value was corrected for the dependences of sample, aluminium layer and cooling water thickness, respectively, taken from Figs 2–4. Thus, we obtain a corrected value of the 14.5 MeV neutron capture cross-section in ^{160}Gd of 1.0 ± 0.2 mb.

In determining the accuracy of the cross-section value, the following sources of error were taken into account:

- statistical counting error of the ^{161}Gd and ^{159}Gd activities;
- uncertainties in the least-squares fitting of the experimental results;
- uncertainties in the gamma-ray intensities in the decay of ^{161}Gd;
- uncertainties in the monitor reaction.

4. Conclusions

The 14.5–MeV neutron capture cross-section is found to be 1.0 ± 0.2 mb and this value is in good agreement with previous results obtained with activation and spectrum methods, 1.0 ± 0.4 mb and 0.9 mb, respectively [3,6]. These results indicate that the Neutron Generator with water cooling can be used for the determination of neutron activation capture cross-sections at 14–15 MeV with an accuracy of ~ 20 %. The accuracy can be even better, depending on the decay and half-life of produced nuclei, the monitor and counting technique.

A comparison with previous activation measurements indicates that in the present experiment there is an additional serious source of low-energy neutrons, namely the cooling water. For more accurate measurements, the contribution of secondary neutrons can be decreased by using a gas cooling, thin aluminium backing and smaller beam spot.

Acknowledgement

This work was financially supported by the Ministry of Culture, Science and Education under Contract No. 643.

References

1. J. Csikai, Handbook of Fast Neutron Generators, CRC Press Inc., Boca Raton, Florida, 1987, Vol. II.
2. M. Valkonen and J. Kantele, Nucl. Instr. and Meth., *103*, 549, 1972.
3. J. Kantele and M. Valkonen, Phys. Lett., *39 B*, 625, 1972.
4. K. Ponnert, G. Magnusson and I. Bergqvist, Physica Scripta, *10*, 35, 1974.
5. G. Magnusson and I. Bergqvist, Nucl. Technology, *34*, 114, 1977.
6. D. Drake, I. Bergqvist and D. K. Mc. Daniels, Phys. Lett., *36 B*, 557, 1971.
7. Handbook of Spectroscopy, Vol. III. CRC Press, Inc. Boca Raton, Florida, 1981.
8. Atomic Data and Nuclear Data Tables, Vol. 29, 2, 1983.

Acta Physica Hungarica 71 (3-4), pp. 179–191 (1992)

A STUDY OF CRYSTAL PROPERTIES OF RARE GAS SOLIDS IN THE SELF-CONSISTENT PHONON THEORY

C. MALINOWSKA-ADAMSKA, I. MACIEJEWSKA and J. TOMASZEWSKI

Institute of Physics, Technical University of Lódź
Lódź, Poland

(Received 18 October 1991)

Thermodynamic and dynamic properties of strongly anharmonic rare gas solids by the help of the self-consistent phonon theory are investigated. The system of equations describing the dynamics and thermodynamics of the crystal lattice is solved for the Singh and Neb potential energy curve. Results obtained for the static lattice energy Φ_0, binding energy D, free F and free Gibbs energies G, heat capacity C_V, C_p, isothermal bulk modulus B, coefficients of anisotropy A, δ have been compared with available experimental data as well as with those calculated for various potential energy functions in the previous papers by the help of the quasi-harmonic approximation and the lowest order of the self-consistent phonon theory of Werthamer.

1. Introduction. Potential energy functions for rare gas solids

Rare gas solids (RGS) are prototype molecular crystals. They crystallize in simple close-packed arrangements to be expected for atoms with spherical symmetry [1]. The lattice atoms interact with weak forces, principally van der Waals–London attractions [2].

The existence of the van der Waals–London attractions necessitates the consideration of an additional repulsive energy to stabilize the crystal lattice of spherical atoms. This repulsive interaction is short-range and overlap dependent in nature [3].

Earlier results of theoretical calculations of the short-range repulsion and the long-range attractive portion for a variety of pairwise interactions of atoms in the RGS have been reviewed in the articles by Pollack [4] and Horton [5] and in the books of Hirschfelder and co-workers [3], Goodisman [6] and Klein and Venables [7].

Next, the potential energy curves appropriate for the rare gas atoms have been analyzed in [8]. Relative merits of these curves have been tested by calculating the values of the vibrational energy eigenvalue differences and comparing them with the experimental values. Reliable estimates of the function parameters have been collected and compared with those obtained from molecular beam experiments.

Interatomic potential functions proposed for the solids have been collected in [9]. The parameters of these functions were determined by the help of the Corner method [10] using experimental data for the energy of sublimation of the crystal

at 0 K, the distance between nearest neighbours in the crystal lattice and the Debye characteristic temperature. The comparison of the numerical values of the parameters for the Rydberg and Varshni potential models allowed to state that for the RGS the three-parametrical function by Rydberg and the first Varshni's function gave nearly the results calculated for the Morse and for the Buckingham exp–six potential. Since, Meisel and Cox [11] have found from the analysis of the equation of state measurements that the Buckingham exp-six potential was the most appropriate for solid Ne and Ar in the paper [12] we used the Morse, Rydberg and Varshni potential functions for the description of the dynamic and thermodynamic properties of the RGS.

It should be noted that [9] the various shapes of the potential functions have been considered in terms of parameters determined in the nearest-neighbours approximation. In order to assure the accuracy of our calculations we used in [12] the parameters of the potential energy functions determined in higher approximation with respect to the number of shells n of nearest neighbours having influence on the pair interaction [13,14].

More recently, Singh and Neb [15] proposed a new potential energy curve appropriate for the RGS. This two-parameter model of interatomic interactions consists of the attractive van der Waals force modified by the three-body interactions arising from the variable induced dipoles and the repulsive Born–Mayer interaction. The results presented in [15] showed that the above potential model successfully explained many properties such as the harmonic and anharmonic elastic constants $C_{\alpha\beta}$, Debye temperature Θ_D, Grüneisen parameter γ, cohesive energy at $T = 0$ K. The purpose of this paper is to investigate the applicability of the Singh and Neb potential model to the description of the temperature and pressure dependence of the dynamic and thermodynamic functions of the RGS at low and high temperature by the help of the self-consistent phonon theory [16].

2. Temperature-dependent properties of the RGS described in previous literature

The principal theoretical results concerning the lattice properties of ideal inert-gas crystals have been presented and discussed in [4, 5 to 17–29]. The free energy, molar heats C_p, C_V, volume thermal expansion coefficient β, second-order elastic constant $c_{\alpha\beta}$ of solid Ar, Kr and Xe obtained in harmonic and quasi-harmonic approximations by the help of the Mie–Lennard–Jones (M–L–J) Morse (M) and Buckingham (B) potentials, have been collected in [4, 5]. The results given in [4,5] as well as the calculations of the temperature dependence of $c_{\alpha\beta}$ [17] and C_p, β [18] for Ar, Kr and Xe in the case of the (12,6) M–L–J potential showed that the quasi-harmonic approximation was unreliable for $T \geq \frac{1}{3}T_m$ — the melting temperature.

Using the quasi-harmonic approximation and the pair potential function of Barker and Pompe [29] together with the Axilrod–Teller triple-dipole interaction [30], in the papers [19–21] Θ_D, β, $c_{\alpha\beta}$ and the bulk modulus B for Kr at low

temperatures (0–12 K) were calculated. The agreement between theoretical and experimental data for $c_{\alpha\beta}$ was not good [20].

An improved description of the second-order elastic constants [22, 23] and selected thermodynamic properties (C_p, C_V, β) [24–26], compared to the quasi-harmonic approximation, has been obtained in the lowest order self-consistent phonon theory (ISC) [31]. As the potential energy of the solid Ar the M–L–J potential was taken. The ISC theory is known to be adequate up to about 3/4 of the melting temperature, so that up to this temperature the above calculations were performed.

C_p, C_V, β and B of Ar and Kr have been calculated using the ISC theory in [28]. The potential energy functions of the solids were assumed in the forms derived by Barker–Bobetic–Pompe (B–B–P) [29] and Barker–Fischer–Watts (B–F–W) [32]. For these potentials C_V and B differ by only 1 % over the whole temperature ($0 - 3/4\,T_m$). The B–F–W expansivity ($\sim$ 5 % lower than one for the B–B–P potential) was in excellent agreement with experiment over a large temperature range.

The Monte-Carlo method with B–B–P and M–L–J potentials was used to calculate the elastic constants of Ar, Kr and Xe in paper [27]. The results for Ar (80 K) and Kr (85 and 115 K) have been obtained for the B–B–P pair potential. For Ar (80 K) and Xe (156 K) the calculations were carried out for the (12,6) M–L–J potential. The results obtained agreed well with the previous work of Klein and et al [26].

Contributions of the various terms to the anharmonic free energy of the RGS in terms of the M–L–J potentials have be computed by Leech and Reisland [25]. The anharmonic effect was represented by using the vibrational elongation that is defined by the average increase of the effective interatomic distances.

From the above considerations it follows that the Mie–Lennard–Jones potential [4, 5 to 17, 18, 22–27] and the Bobetic–Barker–Pompe function [19–21, 27] were mainly used for descriptions of the second-order elastic constants, molar heat, volume thermal expansion coefficient of the RGS by the help of the quasi-harmonic approximation and the lowest order improved self-consistent phonon theory of Werthamer. The quasi-harmonic and ISC approximations become unreliable $T \geq \frac{1}{3}T_m$ and $T \geq \frac{3}{4}T_m$, respectively, so that up to those temperatures the above calculations were performed.

In none of the cited papers has the pressure dependence of the thermodynamic functions been investigated. The temperature dependence of the free energy was obtained in [25] by the help of the quasi-harmonic method only.

For this reason, in this paper the dynamic and thermodynamic properties of strongly anharmonic RGS are described by the help of the self-consistent phonon theory developed by Plakida and Siklós [16, 33, 34], which allows to take into account all the higher order anharmonic terms in a self-consistent manner in the lower order perturbation theory [35].

3. Basic self-consistent equations for the dynamic and thermodynamic functions of cubic crystals

As was shown in [16] the renormalized potential energy function $\Phi(l,T)$ for a cubic crystal can be written in the form:

$$\Phi(l,T) = \sum_{k=0}^{\infty} \frac{1}{k!} \cdot \left(\frac{1}{2} \cdot \overline{u^2}(l,T)\right) \cdot U^{2k}(l), \tag{1}$$

where $U(l)$ is the interatomic pair potential, $\overline{u^2}(l,T)$ is the mean square relative displacement of neighbouring atoms at a distance l.

In the low ($\Theta \ll \omega_L$) and high ($\Theta \gg \omega_L$) temperature limits we get the following equations for $\overline{u^2}$ [16]:

$$\overline{u^2}(l,T) = \lambda \cdot \left(\omega_L/B_1 + C \cdot \Theta/\beta_1^3\right), \quad \Theta \ll \omega_L, \tag{2}$$

$$\overline{u^2}(l,T) = \sigma \cdot \lambda \cdot \Theta \cdot \left(A + \beta_1^2/24\right), \quad \Theta \gg \omega_L. \tag{3}$$

The symbols used in Eqs (2) and (3) have the following meaning:

$$\Theta = k_B \cdot T, \quad \lambda = 1/z \cdot f(l,T), \quad f(l,T) = \frac{\partial^2 \Phi(l,T)}{\partial l^2} = \Phi''(l,T),$$

$$\omega_L^2 = 8 \cdot \hbar^2 \cdot f(l,T)/m, \quad B_1 = 0.49 \cdot \left[1 - 7.446 \cdot 10^{-3} \cdot \gamma(l,T)\right],$$

$$\gamma(l,T) = \omega_L \cdot \beta(l,T)/\Theta, \quad \beta(l,T) = \Theta \cdot g^2(l,T)/f^3(l,T),$$

$$g(l,T) = \Phi'''(l,T), \quad C = 0.518 \cdot \pi^2 \cdot \left[1 + 0.102 \cdot \gamma(l,T)\right],$$

$$\beta_1 = \omega_L/\Theta, \qquad A = \left[1 - 0.11 \cdot \beta(l,T)\right]^{-1}.$$

k_B, z, $\hbar$ and m are the Boltzmann constant, the number of nearest neighbours, the Planck constant divided by 2π and the mass of atom, respectively.

The thermodynamical properties of the cubic lattice consisting of N identical atoms are determined by the internal energy $1/N \cdot E$, free energy $1/N \cdot F$ and thermodynamical potential $1/N \cdot G$ which can be written in the following form [36]:

$$\frac{1}{N} \cdot E = \frac{1}{2} \cdot z \cdot \left[\Phi(l,T) + \frac{1}{2} \cdot \overline{u^2}(l,T) \cdot f(l,T)\right] + F_3(\Theta), \tag{4}$$

$$\frac{1}{N} \cdot F = F_0 + \frac{1}{N} \cdot E - \overline{u^2}(l,T) \cdot f(l,T) - 4 \cdot F_3(\Theta), \tag{5}$$

$$\frac{1}{N} \cdot G = \frac{1}{N} \cdot F + 3 \cdot P \cdot v, \tag{6}$$

Table I
Singh and Neb potential constants for the pairwise atomic interaction in the rare gas solids

Solids	Parameters			
	C 10^{-79} [J·m^6]	b 10^{-19} [J]	p nm	$f(r_0)$ 10^{-3}
Ar	12.474	497.459	3.056	1.71
Kr	33.317	652.080	3.347	3.03
Xe	76.938	736.875	3.706	5.82

where the effective cubic anharmonic contributions to the free energy $F_3(\Theta)$ are given in the low and high temperature limits, respectively, by [36]:

$$F_3(\Theta) = 1.02 \cdot \gamma(l,T) \cdot (B_1' \cdot \omega_L + C_1 \cdot \Theta \cdot \beta_1^{-3}), \quad (\Theta \ll \omega_L), \tag{7}$$

$$F_3(\Theta) = -A_1 \cdot \Theta \cdot \beta(l,T), \quad (\Theta \gg \omega_L), \tag{8}$$

with the numerical coefficients:

$$A_1 \simeq 5.6 \cdot 10^{-2}, \quad B_1' \simeq 1.887 \cdot 10^{-3}, \quad C_1 \simeq 6.475 \cdot 10^{-3}.$$

By applying the method developed by Plakida and Siklós [16] we get an analytical expression for the anharmonic isothermal elastic constants $c_{\alpha\beta}(T)$ in the form [37]:

$$c_{\alpha\beta}(T) = c_{\alpha\beta}^0 \cdot r_e \cdot \alpha^2(l,T) \cdot [1 - 2 \cdot \beta(l,T) \cdot S_{\mathbf{k},j}]/l, \tag{9}$$

where $c_{\alpha\beta}^0$ are the harmonic elastic constants, r_e is the average distance between neighbouring atoms at external pressure $P = 0$, $\alpha^2(l,T) = f(l,T)/f$. The function $S_{\mathbf{k},j}$ is defined by the appropriate choice of the type of the mode j and the direction $\mathbf{k} = \mathbf{q}/|q|$ of the vector yielding the corresponding elastic constants c_{11}, c_{44} and $(c_{11} - c_{12})$ [37].

If the isothermal elastic constants are known then the isothermal bulk modulus

$$B = (c_{11} + 2 \cdot c_{12})/3 \tag{10}$$

and the coefficients of anisotropy

$$A = 2 \cdot c_{44}/(c_{11} - c_{12}), \tag{11}$$

$$\delta = (c_{44} - c_{12})/c_{12} \tag{12}$$

can be calculated.

Eqs (1)–(12) were solved explicitly for the shape of $U(l)$ (Eq. (1)) as follows [15]:

$$U(l) = 12 \cdot b \cdot \exp(-l/p) - \frac{C_1 \cdot (1 + 12 \cdot f(l))}{l^6} + \frac{9}{8} \cdot R \cdot \Theta_D/N, \tag{13}$$

Table II

The binding energy of lattice atoms D, static lattice energy Φ_0, free energy F and free Gibbs energy G of rare gas solids at 0 K using the Singh and Neb (S–N) self-consistent potential. Experimental (Ex) [15, 38, 39] and the best theoretical data obtained in terms of the Mie–Lennard–Jones (M–L–J) [5, 40], Morse (M) [12] as well as Barker–Fisher–Watts (B–F–W) [28] potentials are collected for comparison. $P = 10^5$ Pa

Solids	Potential	-D 10^{-22} [$\frac{J}{atom}$]	$-\Phi_0$	$-F$ [$\frac{kJ}{mol}$]	$-G$
Ar	S–N	12.535	7.547	12.772	12.771
	M	19.632	7.336	16.594	16.586
	M–L–J	14.095	8.489		
	B–F–W	12.850	7.740		
	Ex	12.753	7.712		
Kr	S–N	18.602	11.204	24.573	24.572
	M	24.668	10.814	18.692	18.683
	M–L–J	19.506	11.749		
	B–F–W	18.539	11.166		
	Ex	17.463	11.162		
Xe	S–N	23.698	14.273	36.619	36.617
	M	33.896	14.626	23.292	23.285
	M–L–J	27.489	16.557		
	Ex	24.672	16.035		

Table III

Comparison of the values for the isothermal bulk modulus B and coefficients of anisotropy A and δ at 0 K obtained in terms of the Singh and Neb self-consistent potential with experimental [15, 41–44] and other theoretical data [15, 22, 40] of RGS. The meaning of symbols is as in Table II

Solids	Potential	Method of calculation	B 10^9 [Pa]	A	δ
Ar	S–N	RSCPA	2.473	3.109	−0.139
	M		2.470	2.621	−0.039
	M–L–J	Q–H*	2.617	2.620	0.038
		ICS*	2.636	2.584	0.332
	Ex		3.020	2.432	−0.054
Kr	S–N	RSCPA	3.660	3.360	−0.068
	M		3.069	2.744	−0.019
	M–L–J	Q–H	3.206	2.639	0.019
		ICS	3.242	2.627	0.328
	Ex		3.607	2.330	−0.056
Xe	S–N	RSCPA	3.660	3.360	−0.068
	M		3.561	2.640	−0.019
	M–L–J	QH	3.643	2.663	0.020
		ICS	3.647	2.641	0.328
	Ex		3.636	2.407	−0.056

*Q–H: the quasi-harmonic approximation;
ISC: the lowest order self-consistent phonon theory

Table IV

The effect of temperature and pressure on anharmonic force constants $f(l,T)$ and $g(l,T)$ of RGS in the RSCPA for the Singh and Neb (S–N) potential. Theoretical data for the Morse self-consistent potential are shown for comparison

Solids	T	$f(l,T)$ [N/m]		$-g(l,T)\ 10^{10}$ [Pa]	
	[K]	S–N	M***	S–N	M***
Ar	0*	0.8969	0.7720	4.9973	4.3508
	0**	0.9861	0.7931	5.2770	4.3518
	80*	0.8467	0.7566	4.7629	4.1511
	80**	0.9120	0.7679	5.0210	4.1678
	83.6*	0.8402	0.7503	4.7325	4.0918
	83.6**	0.9047	0.7651	4.9848	4.0938
Kr	0*	1.3188	1.1481	6.9930	5.8772
	0**	1.3892	1.1486	7.2487	5.8793
	80*	1.2507	1.1264	6.6860	5.6458
	80**	1.3157	1.1230	6.9222	5.6483
	115*	1.1920	1.1112	6.4209	5.5568
	115**	1.2523	1.1159	6.6408	5.5631
Xe	0*	1.3452	1.1393	6.9362	6.3263
	0**	1.4150	1.1397	7.1687	6.3289
	80*	1.2928	1.1261	6.6932	6.1858
	80**	1.3582	1.1294	6.9111	6.1881
	156*	1.2013	1.1116	6.2733	6.1277
	156**	1.2593	1.1148	6.4670	6.1309

*$P = 0$ Pa; **$P = 10$ MPa; *** Values obtained on the basis of analytical results given in [46] with the help of Morse potential parameters reported in [12].

where the last term is the zero-point energy with R and Θ_D as gas constant and Debye temperature at 0 K, respectively,

$$C_1 = 14.4539 \cdot C,$$

$$f(l) = f_0 \cdot \exp(-1/p),$$

C is the dipole–dipole van der Waals coefficient, $f(l)$ is the three-body force parameter.

4. Numerical results

Using the values of potential parameters for the Singh and Neb function given in Table I we have computed, at first, the properties of RGS at $T = 0$ K: the binding

Table V

The effect of temperature on free energy F and free Gibbs energy G of RGS in the RSCPA. The meaning of symbols is as in Table IV

Solids	T	$-F$ [kJ/mol]		$-G$ [kJ/mol]	
	[K]	S–N	M***	S–N	M***
Ar	0*	12.772	16.594	12.772	16.586
	0**	12.861	16.597	12.628	16.589
	80*	11.983	10.964	11.984	10.964
	80**	12.085	10.965	11.847	10.930
	83.6*	11.935	9.694	11.932	9.687
	83.6**	12.038	10.506	11.797	10.199
Kr	0*	24.573	18.692	24.573	18.683
	0**	24.686	18.696	24.411	18.687
	80*	23.545	14.083	23.545	14.083
	80**	23.664	14.084	23.383	14.992
	115*	22.952	12.844	22.952	12.074
	115**	23.085	15.892	22.798	14.835
Xe	0*	36.619	23.292	36.619	23.285
	0**	35.443	16.575	33.899	16.458
	80*	35.269	16.574	34.164	16.574
	80**	35.443	16.575	33.899	16.458
	156*	33.494	13.116	31.259	13.104
	156**	33.691	14.341	30.900	14.330

energy of lattice atoms D, the static lattice potential energy Φ_0, the free energy F and the free Gibbs energy G (Table II). The results are compared with experimental [15, 38, 39] and the best theoretical data obtained in terms of the Mie–Lennard–Jones (M–L–J) [5, 40], Morse (M) [12] as well as Barker–Fisher–Watts (B–F–W) [28] potentials.

The values calculated in RSCPA of the isothermal bulk modulus B and the coefficients of anisotropy A and δ are given in Table III together with the observed [15, 41–44] and other theoretical results [15, 22, 40]. The coefficients A and δ express the deviation from the Cauchy relation for the isothermal elastic constants [20].

It is evident from Tables II and III that the agreement between the experimental and our theoretical results for the static lattice energy and isothermal bulk modulus at 0 K is reasonably good. For this reason, as a next reliable test of validity of self-consistent equations (1)–(12) we will explore the temperature and pressure dependence of various dynamical and thermodynamical functions, i.e.: the anharmonic force constants $f(l,T)$ and $g(l,T)$ (Table IV), free energy F, free Gibbs energy G (Table V) as well as the molar heat at constant pressure C_p (Table VI). Our results for C_p as a function of P, are compared with those obtained on the basis of the Fomin formula in the quasi-harmonic approximation [45].

The experimental measurements of the heat capacity at constant volume C_V

at high temperature limit are compared in Table VII with theoretical data calculated in RSCPA for the S–N and M [46] potentials as well as with those computed for the M–L–J and Bobetic–Barker (B–B) potentials by the help of the Monte-Carlo (M–C) method [27].

The results presented in Table VII show that the agreement of experimental data for C_V with those calculated in terms of the Singh and Neb function is a little better than the corresponding agreement for the Morse potential at the high temperature limit. Reasonably good agreement between the experimental [47, 51] and our theoretical results is also evident from Table VIII in which we show the comparison of the values reported in the literature for C_V [12, 25] with values calculated in the RSCPA over a wider temperature region.

From Table VIII we see that our results for the heat capacity show the same temperature behaviour as has been found experimentally. The values of C_V corrected by means of the anharmonicity of lattice vibrations are higher than those obtained in the lowest order self-consistent phonon theory by Leech and Reisland [25] which confirm the thesis on the significance of contributions of anharmonicity to the thermal phenomena.

To show the importance of the anharmonic contribution to the heat capacity at constant volume, $\Delta C_V = -T \cdot \left(\frac{\partial^2 F_a}{\partial T^2}\right)$, we present in Table IX the comparison of data on the basis of the Feldman and Horton approximation [52] for the Mie–Lennard–Jones potential with values calculated in RSCPA for the Singh and Neb and Morse [12] models. From this Table we see that the anharmonic effects are not negligible in calculations concerning the thermal phenomena in the high temperature region.

5. Conclusions

The self-consistent phonon theory (SCPT) of anharmonic crystals has been used so far for the investigation of physical properties of the face-centred (fcc) and body-centred (bcc) lattices [33–37, 46]. However, all these calculations are not relative to the rare gas solids (RGS).

The SCPT of anharmonic crystals was used in [12] for the investigation of physical properties of the RGS. This paper presents a continuation of our investigation of the dynamic and thermodynamic properties of RGS. The calculations performed in the reduced second-order self-consistent phonon approximation, concern two cases with respect to the initial potential curves:

1) Singh and Neb potential in which the accuracy of thermodynamic properties of RGS in the anharmonic approximation is the best in comparison with other kinds of potential curves still considered.
2) Morse potential widely used by Plakida and Siklós (e.g. [16]) as a model potential for the description of thermodynamic properties of the fcc structure for the reduced parameters T^* and P^*.

The system of self-consistency equations describing the thermodynamical and mechanical properties of the RGS is solved for the parameters of potential energy

Table VI

The effect of pressure on molar heat at constant pressure C_P obtained in terms of the Singh and Neb (S–N) as well as Morse (M) self-consistent potentials in the RSCPA. Theoretical data calculated on the basis of the Fomin formula in the quasi-harmonic approximation (Q–H) [45] are given for comparison

Solids	P	C_P [J/mol·K]		
			RSCPA	
T [K]	[MPa]	Q–H	S–N	M
Ar	0	21.30	22.71	22.731
80	0.1	23.207	22.72	23.611
	10	26.482	23.76	25.659
Kr	0	22.90	23.67	21.668
115	0.1	25,79	23.75	24.972
	10	27.568	24.46	25.882
Xe	0	21.80	21.92	23.991
156	0.1	24.332	22.0	24.681
	10	28.991	22.73	26.355

Table VII

Comparison of the values for the molar capacity at constant volume C_V at high temperature limit obtained in terms of the Singh and Neb (S–N) as well as Morse (M) self-consistent potentials with experimental (Ex) [27] and theoretical data calculated for the Mie–Lennard–Jones (M–L–J) and Bobetic–Barker (B–B) potentials by the help of the Monte–Carlo (M–C) method [27]

Solids	T [K]	C_V [J/mol·K]				
		Ex	M–C		RSCPA	
Ar	80	22.7 ± 0.5	B–B	21.8 ± 0.7	S–N	22.670
			M–L–J	22.5	M	22.731
Kr	115	22.9	B–B	21.6 ± 0.7	S–N	23.540
					M	24.668
Xe	156	21.2 ± 1.4	M–L–J	22.8	S–N	21.900
					M	23.991

functions determined in higher approximation with respect to the number of nearest neighbours having influence on the pair interaction in the lattice [14].

Detailed numerical results for the binding energy of lattice atoms, static energy (Table II), isothermal bulk modulus (Table III), heat capacity at constant volume C_V (Tables VII and VIII) have been compared with available experimental data as well as with those calculated in previous papers by the help of the quasi-harmonic and improved self-consistent phonon approximations.

Table VIII

Comparison of the values for the molar heat at constant volume C_V obtained in terms of the Singh and Neb (S–N) self-consistent potential with experimental (Ex) [47–51] and other theoretical data [12, 25] of RGS. The meaning of symbols is as in Table II

Solids	T	C_V [J/mol·K]			
	[K]	Ex	S–N	M [12]	M–L–J [25]
Ar	10	3.296	3.136	4.146	3.591
	40	19.954	19.081	20.270	19.229
	60	23.322	24.241	22.275	20.775
	70	25.718	23.468	22.673	20.950
Kr	10	5.907	7.772	4.506	
	40	21.594	22.920	21.525	21.150
	80	23.070	24.451	23.583	23.372
	100	23.180	24.377	24.616	22.172
Xe	10		7.787	3.566	
	40	22.734	22.573	22.862	21.997
	80	23.446	25.352	23.844	23.095
	100	23.111	24.475	23.883	23.020
	140	21.897	22.652	23.864	22.571

Table IX

Cubic anharmonic contributions to the heat capacity at constant volume ΔC_V of the RGS using the Singh and Neb (S–N) and Morse (M) [12] self-consistent potentials and Feldman–Horton approximation [52] in the case of Mie–Lennard–Jones (M–L–J) nearest neighbour force model

Solids	T	C_V [J/mol·K]		
	[K]	S–N	M	M–L–J
Ar	10	0.2160	0.2274	0.4438
	40	1.0520	1.1074	1.7756
	60	1.7911	1.8854	2.6634
	70	2.1645	2.2785	3.1073
Kr	10	0.1574	0.1657	0.2843
	40	0.8619	0.9027	1.1372
	80	1.9304	2.0320	2.2744
	100	2.5471	2.6812	2.8430
Xe	10	0.1034	0.1089	0.1920
	40	0.5697	0.5869	0.7681
	80	1.2795	1.5360	
	100	1.5725	1.6553	1.9200
	140	1.1800	1.2412	2.6881

Acknowledgement

The authors are grateful to Professor Dr. T. Siklós for reading the manuscript.

References

1. E. R. Dobbs and G. O. Jones, Rep. Progr. Phys., *20*, 516, 1957.
2. C. Kittel, Introduction to Solid State Physics, PWN, Warsaw, 1974, p. 98 (in Polish).
3. J. O. Hirschfelder, Ch. F. Curtiss, R. B. Bird, Molecular Theory of Gases and Liquids, J. Wiley and Sons, New York–London, 1954.
4. G. L. Pollack, Rev. Mod. Phys., *36*, 748, 1964.
5. G. K. Horton, Am. J. Phys., *36*, 748, 1964.
6. J. Goodisman, Diatomic Interaction Potential Theory, Vol. 1. Academic Press, New York, 1976.
7. M. L. Klein, J. A Venables ed., Rare Gas Solids, Vol. 1, Academic Press, New York, 1976.
8. C. Malinowska-Adamska, Acta Universitatis Szegediensis, ser. Phys. et Chem., *25*, 9, 1979.
9. C. Malinowska-Adamska, Acta Phys. Hung., *42*, 295, 1977.
10. J. Corner, Trans. Faraday Soc., *44*, 914, 1948.
11. L. V. Meisel, J. C. Cox, Phys. Rev., *B11*, 1762, 1975.
12. C. Malinowska-Adamska, Acta Phys. Hung., *59*, 257, 1986.
13. E. A. Guggenheim and M. L. Mc. Glashan, Proc. Roy. Soc. (London), *A255*, 456, 1960.
14. C. Malinowska-Adamska, Acta Phys. Hung., *45*, 221, 1978.
15. R. K. Singh and D. K. Neb, Phys. Stat. Sol., *(b)112*, 735, 1982.
16. N. M. Plakida and T. Siklós, Acta Phys. Hung., *45*, 37, 1978.
17. J. L. Feldman, M. L. Klein and G. K. Horton, Phys. Rev., *184*, 968, 1969.
18. M. L. Klein, G. K. Horton and J. L. Feldman, Phys. Rev., *184*, 968, 1969.
19. M. V. Bobetic and J. A. Barker, Phys. Rev., *B2*, 4169, 1970.
20. J. A. Barker, M. L. Klein and M. V. Bobetic, Phys. Rev., *B2*, 4176, 1970.
21. M. V. Bobetic, J. A. Barker and M. L. Klein, Phys. Rev., *B5*, 3185, 1972.
22. M. L. Klein, G. K. Horton and V. V. Goldman, Phys. Rev., *B2*, 4995, 1970; *B4*, 567, 1971.
23. M. L. Klein and W. G. Hoover, Phys. Rev., *B4*, 537, 1971.
24. V. V. Goldman, G. K. Horton and M. L. Klein, Phys. Rev. Lett., *21*, 1524, 1968.
25. J. W. Leech and J. A. Reissland, J. Phys., *C3*, 975, 987, 1970.
26. M. L. Klein and W. G. Hoover, Phys. Rev., *B4*, 539, 1971.
27. M. L. Klein and R. D. Murphy, Phys. Rev., *B6*, 2433, 1972.
28. M. L. Klein, T. R. Koehler and R. L. Gray, Phys. Rev., *B7*, 1571, 1973.
29. J. A. Barker and A. Pompe, Aust. J. Chem., *21*, 1683, 1968.
30. B. M. Axilrod, J. Chem. Phys., *17*, 1343, 1949; *19*, 713, 1951.
31. N. R. Werthamer, Phys. Rev., *B1*, 572, 1970.
32. J. A. Barker, R. A. Fisher and R. O. Watts, Mol. Phys., *21*, 657, 1971.
33. N. M. Plakida and T. Siklós, Phys. Stat. Sol., *33*, 103, 113, 1969; *39*, 171, 1970.
34. N. M. Plakida, The Method of Green Function in the Theory of Anharmonic Crystals, in: Statistical Physics and Quantum Field Theory, ed. N. N. Bogoliubov, Nauka, Moscow, 1973, (in Russian), pp. 205–240.
35. T. Siklós, Acta Phys. Hung., *30*, 181, 1971.
36. a) T. Siklós and V. L. Aksienov, Acta Phys. Hung., *31*, 335, 345, 1972; b) Phys. Stat. Sol., *50*, 171, 1972.
37. N. M. Plakida, V. L. Aksienov, Fiz. Tverd. Tela, *15*, 2573, 1973; Phys. Stat. Sol., *(b)62*, 261, 1974.
38. M. L. Klein, Chem. Phys. Letters, *18*, 203, 1973.
39. G. E. R. Schulze, Metallphysik, Wydawnictwo Naukowe, Warsaw, 1982, p. 281 (in Polish).
40. T. H. K. Barron and M. L. Klein, Proc. Phys. Soc. (London), *85*, 523, 533, 1965.
41. J. Skalyo, Jr, V. L. Minkiewicz, G. Shirane and W. B. Daniels, Phys. Rev., *B6*, 4766, 1972.
42. Y. Fujii, N. A. Lurie, R. Pynn, G. Shirane and W. B. Daniels, Phys. Rev., *B10*, 3647, 1974.
43. J. Skalyo, Jr, Y. Endoh and G. Shirane, Phys. Rev., *B9*, 1797, 1974.
44. N. A. Lurie, G. Shirane and J. Skalyo, Jr, Phys. Rev., *B9*, 2661, 5300, 1974.
45. N. W. Fomin, Fiz. Tverd. Tela, *23*, 533, 1981.

46. C. Malinowska-Adamska, M. Owsiejczyk and L. Wojtczak, Phys. Stat. Sol., *(b)115*, 335, 1983.
47. P. Flubacher, A. J. Leadbetter and J. A. Morrison, Proc. Phys. Soc. (London), *78*, 1449, 1961.
48. R. H. Beaumont, H. Chihara and J. A. Morrison, Proc. Phys. Soc. (London), *78*, 1462, 1961.
49. D. L. Losee and R. O. Simmons, Phys. Rev., *172*, 994, 1968.
50. V. G. Manzhelli, V. G. Gavrilko and V. I. Kuchnev, Phys. Stat. Sol., *34*, K55, 1968.
51. V. G. Manzhelli, V. G. Gavrilko and E. I. Voitovich, Fiz. Tverd. Tela, *9*, 1483, 1969.
52. J. L. Feldman and G. K. Horton, Proc. Phys. Soc. (London), *92*, 227, 1967.

Acta Physica Hungarica 71 (3-4), pp. 193-200 (1992)

THE EFFECTS OF TORSION FOR FIELDS OF AXIAL SYMMETRY

SERVILIA OANCEA

Department of Physics, Polytechnical Institute
Iaşi, Romania

(Received 5 November 1991)

This article presents several particular aspects in relation to torsion. We have also studied the gravitational field of axial symmetry with torsion as well as the electromagnetic field and we have suggested a generalization of Maxwell's equations.

The theory of the gravitational field in spaces with torsion (that use a more general affine space, the Riemann–Cartan space) separates the affine characteristics from the metric ones, so that torsion should be linked to certain characteristics that are not described in the Theory of General Relativity.

The theory of gravitation for such spaces is developed under the form of Theory U_4 by Hehl [1], Aldersley [2] and Davis [3]. In [4] Hayashi sets forth a new theory of the gravitational field using a Weitzenböck space, with torsion and without a curvature. Müller–Hoissen and Nitsch [5] starting from a Lagrangean depending on torsion, study the field equations for the homogeneous and isotropic space. The development of Dirac's theory also finds its place within spaces with torsion, as it presented by Andretsch [6].

While in the Theory of General Relativity matter appears as an energy-momentum carrier, a phenomenological description of matter possessing but energy-momentum is not sufficient to describe its characteristics. A series of articles connects torsion with the structure of the bodies that produce the gravitational field and a most important question is that concerning the physical aspects and the microscopic origin of torsion (for example, the spin of the particles that produce the gravitational field [7]).

At the same time, if torsion is a real quantity, there should exist experiments that spotlight it. In [8] the models of such experiments are given, but as the assessed results are extremely reduced, they cannot, for the time being, be spotlighted owing to technical reasons.

Thus, at present, it is only the theoretical models that can show phenomena where torsion can play an important part [9], [10].

Since the above mentioned articles consider that the theories of gravitation developed on spaces with torsion are of interest because they cover a wider field of the properties of the gravitational field than the standard ones, we too have studied some aspects linked with exact solutions on spaces with torsion.

The present paper contains several applications of the equations of the gravitational field of the Theory U_4. One gets accurate solutions and, at the same time,

one can draw a comparison with the results that are obtained when torsion gets anulled. In order to study the compatibility of the gravitational and the electromagnetic field we suggested a generalization of Maxwell's equations for spaces with torsion.

Our applications refer to fields of axial symmetry. We considered this symmetry since it has also been studied much in the theories without torsion in order to find exact solutions.

Thus, the first Section of our paper presents the equations of the gravitational field with torsion for a particular metric of axial symmetry, using the Newman-Penrose formalism for spaces with torsion. In the second Section of this paper these equations are solved for the case of the electromagnetic field, taking only a non-null component of the electromagnetic field tensor.

The third Section deals with the generalization of Maxwell's equations in the presence of torsion. Then, the system of Einstein–Maxwell's generalized equations is solved for the metric of axial symmetry under consideration; the metric and torsion are established.

In the fourth Section the equations of the gravitational field created by a fluid without pressure are solved.

I. Let the gravitational field of axial symmetry given by the metric be:

$$ds^2 = -e^{-2u}(d\varrho^2 + dz^2 + \varrho^2 d\varphi^2) + e^{2u}dt^2, \tag{I.1}$$

with variables $x^1 = \varrho$, $x^2 = z$, $x^3 = \varphi$, $x^4 = t$ that constitute a particular case of the axial symmetry given in [11].

In what follows we shall consider the case when both functions that define the metric and the torsion depend only on the variable ϱ.

Using the Newman–Penrose formalism written for spaces with torsion [12] (to determine the components of the Ricci tensor) and the equations of the gravitational field of Theory U_4 [13], for metric (I.1), the equations of the gravitational field can be written as:

$$\begin{aligned}
e^{2u}\left[(u')^2e^{2u} - 2f^2\right] &= -\kappa T^{11},\\
e^{2u}\left[-(u')^2e^{2u} + 2f^2\right] &= -\kappa T^{22},\\
\frac{e^{2u}}{\varrho^2}\left[-(u')^2e^{2u} + 2f^2\right] &= -\kappa T^{33},\\
e^{-2u}\left[-2u''e^{2u} + (u')^2e^{2u} - \frac{2u'e^{2u}}{\varrho} + 6f^2\right] &= -\kappa T^{44}.
\end{aligned} \tag{I.2}$$

Here f is the tetrad component of contorsion, T^{ik} stand for the contravariant components of the energy-momentum tensor and "$'$" represents the derivative with respect to variable ϱ [14].

II. We consider the gravitational field of axial symmetry of a body such that the only non-null component of the tensor of the electromagnetic field be $F_{14} = iF$.

This choice simplifies the system (I.2) and is compatible with it. Under these conditions system (I.2) is reduced to the following equations:

$$(u')^2 e^{2u} - 2f^2 = \frac{\kappa}{8\pi} F^2, \tag{II.1}$$

$$-2u'' e^{2u} - \frac{2u' e^{2u}}{\varrho} + (u')^2 e^{2u} + 6f^2 = -\frac{\kappa}{8\pi} F^2.$$

If, besides these, for the function that defines the electromagnetic field one chooses $F = a/\varrho$, where a is a constant, then, system (II.1) becomes:

$$-2u'' - \frac{2u'}{\varrho} + 4(u')^2 - \frac{\alpha e^{-2u}}{\varrho^2} = 0, \tag{II.2}$$

with $\alpha = \frac{2\kappa a^2}{8\pi}$.

Noting $y = e^{-2u}$ and with a change of variable $t = \ln\varrho$, Eq. (II.2) becomes:

$$\ddot{y} - \alpha y^2 = 0, \tag{II.3}$$

where "$\cdot$" represents the t derivative.

Integrating Eq. (II.3) we get:

$$3\dot{y}^2 - 2\alpha y^3 = C, \tag{II.4}$$

C being an integration constant.

From (II.4) there follows:

$$t = \sqrt{3} \int \frac{dy}{\sqrt{C + 2\alpha y^3}}. \tag{II.5}$$

Substituting $y = (\frac{1}{x} - 1)^{1/3}$ and inserting for simplicity $2\alpha/C = 1$, the integral (II.5) is reduced to the form of Euler type integrals.

Therefore, for the case of the gravitational field considered above, the general solution is difficult to explain. The fact that this solution is not explicit, does not reduce the generality of the question of the compatibility of the gravitational and electric field in spaces with torsion.

From (II.1) one can see that torsion depends both explicitly on the electric field, through the function F and implicitly, through the function that defines the metric. One can say that, for this case, torsion is compatible with the electromagnetic field.

In order to spotlight the effects of torsion, let us consider for the instances above that torsion is annulled.

From the first equation of system (II.1), with $F = a/\varrho$ it follows:

$$(u')^2 e^{2u} = \frac{\gamma}{\varrho^2}, \tag{II.6}$$

with $\gamma = \kappa a^2/8\pi$ and for the second equation of the same system:

$$-2u'' + 2(u')^2 - \frac{2u'}{\varrho} = 0, \tag{II.7}$$

whose solution is function

$$u = -\ln(C_1 + C_2 \ln \varrho), \tag{II.8}$$

C_1, C_2 being likewise constants of integration.

Therefore, the annulling of torsion within the system of equations that describes the gravitational field (II.1) implies the passing from an elliptical solution, given implicitly, to a simple logarithmical solution given by (II.8). The modification of the function that defines the metric can lead to the modification of the properties of the gravitational field it defines.

III. Within Einstein's General Theory of Relativity, Maxwell's equations regarding the electromagnetic field allow for finding exact solutions for the electromagnetic field in the presence of gravitation. The fact that this theory considers a symmetrical connection has, as aftermath, the fact that Maxwell's first set of equations has the same form as in the Special Theory of Relativity., and the second set of equations is modified. For a Riemann–Cartan space with torsion there arises the very asymmetry of the connection which brings about the modifications of Maxwell's first set of equations as well.

Starting from this observation, we have studied the equations of the electromagnetic field in a space with curvature and torsion, within axial symmetry.

Treating the electromagnetic field within the framework of the theories developed for spaces with torsion requires the redefining of the tensor of the electromagnetic field and the generalization of Maxwell's equations.

Thus, we define the electromagnetic field tensor, in the presence of torsion, in a manner that is different from other authors, under the form [15]:

$$\tilde{F}_{ik} = \overset{*}{\nabla}_i A_k - \overset{*}{\nabla}_k A_i, \tag{III.1}$$

where A_i is the quadripotential of the electromagnetic field and $\overset{*}{\nabla}_= \nabla_i + K^{\alpha}_{\alpha i}$, $K^{\alpha}_{\alpha i}$ is the contorsion vector.

We have chosen this definition of the electromagnetic field since, within the framework of theory U_4 on which we founded our researches, derivative $\overset{*}{\nabla}$ is used to express the conservation laws.

Using the same covariant derivative and keeping the significance of the physical quantities from the standard theory, we suggest the following form for Maxwell's equations:

$$\begin{aligned} \overset{*}{\nabla}_p \tilde{F}_{ik} + \overset{*}{\nabla}_i \tilde{F}_{kp} + \overset{*}{\nabla}_k \tilde{F}_{pi} &= 0, \\ \overset{*}{\nabla}_k \tilde{F}^{ik} &= j^i. \end{aligned} \tag{III.2}$$

Here j^i is the fourcurrent that is conserved, therefore:

$$\overset{*}{\nabla}_i j^i = 0. \tag{III.3}$$

If $\overset{*}{\nabla}_i j^i \neq 0$, there arise serious difficulties in the case of describing the non-static gravitational field.

We also impose the condition:

$$\overset{*}{\nabla}_l g_{ik} = 0. \tag{III.4}$$

If $\overset{*}{\nabla}_l g_{ik} \neq 0$, the raising and lowering of indices are no longer unique.

For metric (I.1) for the case of choosing only one non-null component of the electromagnetic field fourpotential A_4, Einstein–Maxwell's generalized equations in the presence of torsion are:

$$\begin{aligned}
e^{2u}\left[(u')^2 e^{2u} - 2f^2\right] &= -\frac{\kappa e^{2u}}{8\pi}\left[(A_4')^2 + 8f^2 e^{-2u} A_4^2\right], \\
e^{-2u}\left[-2u'' e^{2u} - \frac{2u' e^{2u}}{\varrho} + (u')^2 e^{2u} + 6f^2\right] &= \frac{\kappa e^{2u}}{8\pi}\left[(A_4')^2 + 8f^2 e^{-2u} A_4^2\right], \\
f + f'\varrho - 3u'\varrho f &= 0, \\
e^{2u} A_4'' + 8f^2 A_4 &= -j_4.
\end{aligned} \tag{III.5}$$

For system (III.5) one finds for contorsion:

$$f = C\frac{e^{3u}}{\varrho} \tag{III.6}$$

and for the metric a particular solution:

$$u = -\frac{1}{2}\ln(c_1 \pm c_2 \ln \varrho), \tag{III.7}$$

where C, C_1, C_2 are integrating constants.

With solution (III.7), metric (I.1) can be identified with the metric of a cylinder with a mass and charge on condition $\frac{L}{2} \gg \varrho \gg r_0$ where L is the length and r_0 the radius of the cylinder. The identification of the constants is in this instance:

$$c_1 \pm c_2 \ln \varrho \equiv 1 + 4\frac{G}{c^2}\sigma \ln\left(\frac{2\varrho}{L}\right),$$

where σ is the linear density of mass.

Using (III.6) and (III.7) from system (III.5) one can find the fourpotential of the electromagnetic field and then, the fourcurrent, j_4.

In case torsion is annulled, for Maxwell's equations in the presence of torsion we get the equations known from the General Theory of Relativity.

From the first equations of system (III.5) in the case of vanishing torsion, we get an equation of the form (II.7) with a solution (II.8). For the four potential of the electromagnetic field we get

$$A_4 = -\frac{i}{C_1 + C_2 \ln \varrho}, \tag{III.8}$$

and for the fourcurrent:

$$j_4 = \frac{iC_3}{\varrho^2 (C_1 + C_2 \ln \varrho)^5}. \tag{III.9}$$

One can notice that, although when torsion is different from zero, the solutions to equations (II.2) and (III.5) are different, in case of zero torsion both of them are of the same form (II.8). Even if the properties of the electromagnetic field that result from the two equations are different, when torsion is absent, the metric is of the same form.

If, in the case when torsion is annulled, for the case when only component F_{14} is non-null, one gets the solution:

$$e^{-2u} = (c_1 + c_2 \ln \varrho)^2$$

for the case of generalizing Maxwell's equations in the presence of torsion, with the same non-null component of electromagnetic field tensor, one gets for the metric:

$$e^{-2u} = c_1 + c_2 \ln \varrho.$$

We reckon that the generalization of Maxwell's equations in spaces with curvature and torsion, alongside with the field equations of Theory U_4, describes the physical field under consideration.

We shall also note something else. Torsion is linked to the metric by relation (III.6). As e^{3u} cannot vanish, it means that the annulling of torsion implies annulling the integrating constant C.

If in the expression of torsion we replace solution (II.8) we find that we cannot get the constant C annulled with the help of constants C_1, C_2, which means that our solution does not satisfy "the principle of correspondence" that is solution (II.8) does not imply the annulling of torsion, the way torsion annulling leads to (II.8). We reckon this could be explained by both the particular choice of integrating constants and by the fact that, generally speaking, this lack of reciprocity reflects the physical and geometric aspects that we have not taken into consideration above.

IV. We consider the gravitational field of axial symmetry produced by a fluid without pressure, for which the energy-momentum tensor is of the form

$$T^{ij} = \mu u^i u^j. \tag{IV.1}$$

Here u_i represents the fourspeed that we prefer to be of the following form:

$$u^i = f(l^i + n^i), \tag{IV.2}$$

where l^i and n^i are the contravariant components of the tetrad for metric (I.1).

This choice shows that the fourspeed is only capable of producing the torsion of the space that should be compatible with the gravitational field described by the system of equations (I.2).

The system of equations (I.2) becomes for this fluid:

$$(u')^2 e^{2u} = 2f^2, \tag{IV.3}$$

$$e^{-2u}\left[-2w'' e^{2u} - \frac{2u' e^{2u}}{\varrho} + (u')^2 e^{2u} + 6f^2\right] = -2\kappa\mu f^2 e^{-2u}.$$

System (IV.3) is reduced to equation:

$$-2u'' - \frac{2u'}{\varrho} + (4+\beta)(u')^2 = 0, \tag{IV.4}$$

with $\beta = \kappa\mu$.

The solution to the equation is of the form:

$$u = -\ln(c_i' + c_2' \ln \varrho), \tag{IV.5}$$

where c_i' and c_2' are constants.

Since for metric (I.1) the spatial components of the fourspeed are null, (IV.5) represents the gravitational field of a fluid (dust) without motion.

For the fluid without pressure, the vanishing of torsion is meaningless because the situation described corresponds to those properties of the fluid that are due exclusively to torsion.

Acknowledgement

The author thanks Prof. N. Ionescu-Pallas for many helpful discussions.

References

1. F. W. Hehl, GRG, *4*, 333, 1973.
2. S. J. Aldersley, GRG, *8*, 397, 1977.
3. W. R. Davis, W. K. Atkins, W. M. Baker, Il Nuovo Cimento, *44B*, 23, 1978.
4. Kenji Hayashi, Phys. Rev. D, *19*, 3524, 1979.
5. F. Müller-Hoissen, J. Nitsch, GRG, *17*, 747, 1985.
6. J. Andretsch, Phys. Rev. D, *24*, 1470, 1981.

7. F. W. Hehl, GRG, *6*, 123, 1975.
8. W. R. Stoeger, GRG, *17*, 981, 1985.
9. Yu. N. Obukhov, V. N. Ponomariev, V. V. Zhytnikov, GRG, *21*, 1107, 1989.
10. B. P. Dolan, Physics Letters, *159B*, 279, 1986.
11. D. Kramer, H. Stephani, E. Herlt, M. Mac Callum, Exact Solutions of Einstein's Field Equations, Cambridge University Press, Cambridge, London, 1980.
12. S. Jogia, J. B. Griffiths, GRG, *12*, 587, 1980.
13. J. B. Griffiths, GRG, *13*, 227, 1981.
14. S. Oancea, Gh. Maftei, Gh. Zet, Anal. st. Univ. Iaşi (in print).
15. S. Oancea, Rev. Roum. Phys. (in print).

Acta Physica Hungarica 71 (3-4), pp. 201-209 (1992)

THE EFFECT OF TEMPERATURE AND PRESSURE ON THE THERMODYNAMIC PROPERTIES OF RARE GAS SOLIDS IN ANHARMONIC APPROXIMATION

C. MALINOWSKA-ADAMSKA and J. TOMASZEWSKI

Institute of Physics, Technical University of Lódź
Lódź, Poland

(Received 14 January 1992)

On the basis of the reduced second order self-consistent phonon approximation the temperature and pressure dependence of the thermodynamic functions of rare gas solids are computed and compared with experimental and other theoretical data in the high temperature region. The instability parameters are calculated also. The system of self-consistent equations is solved for the generalized form of the Lennard-Jones (n, m) interatomic potential.

1. Introduction

In a previous paper [1] we have used the Plakida and Siklós self-consistent method [2] for investigating the dynamic and thermodynamic properties of highly anharmonic rare gas solids (RGS) in terms of the Morse, Rydberg and Varshni potential models. In this paper the effect of temperature and pressure on the thermal properties of the RGS is investigated with the generalized form of the Lennard-Jones (n, m) potential [3] as a model of nearest-neighbour (NN) central force interaction by the reduced second-order self-consistent phonon approximation (RSCPA) [2].

The Lennard-Jones (n, m) potential has been previously tested and used by Klein et al [4] in evaluating the temperature dependence of the molar heat and thermal expansion coefficient of certain RGS. Also, Massa et al [5] used this model of NN interaction for the investigation of volume dependence of the elastic constants, phonon frequencies and related thermodynamic properties of solid argon by the help of pseudo-harmonic approximation. However, this approximation becomes unreliable at high temperatures [5, 6]. It is worth pointing out that the parameters inherent in the (n, m) potential were determined in [5] with the aid of experimental elastic constant values and the melting curve. In this paper the parameters of the Lennard-Jones potential have been determined in the highest approximation with respect to the number of shells of NN using experimental values for the energy of sublimation, the compressibility and the distance between NN in the crystal lattice by help of the method described in [3, 7]. This approach is expected to be more useful than those previously used in [5].

2. Thermal properties of the anharmonic crystals in the RSCPA

Let us take the generalized form of the Lennard–Jones (n, m) potential as a model potential

$$U(l) = D_0 \cdot \left[\frac{m}{n-m} \cdot \left(\frac{r_0}{l}\right)^n - \frac{n}{n-m} \cdot \left(\frac{r_0}{l}\right)^m\right], \quad n > m, \tag{1}$$

where r_0 is the equilibrium distance between the neighbouring atoms in the harmonic approximation, $U'(r_0) = 0$, and D_0 is the depth of the potential, $U(r_0) = -D_0$.

Applying the method developed by Plakida and Siklós [2] we get the following expression for the self-consistent potential:

$$\tilde{\Phi}(l) = C \cdot \sum_{k=0}^{\infty} (C_n^k - C_m^k) \cdot B^k, \tag{2}$$

where

$$C = n \cdot m \cdot D_0/n - m, \quad C_n^k = A_n^k \cdot \left(\frac{r_0}{l}\right)^n, \quad C_m^k = A_m^k \cdot \left(\frac{r_0}{l}\right),$$

$$A_n^k = \begin{cases} \frac{1}{n}, & k = 0 \\ \frac{1}{k!} \cdot (n+1) \cdot (n+2) \cdot \ldots \cdot (n+2k-1), & k = 1, 2, \ldots \end{cases}$$

$$A_m^k = \begin{cases} \frac{1}{m}, & k = 0 \\ \frac{1}{k!} \cdot (m+1) \cdot (m+2) \cdot \ldots \cdot (m+2k-1), & k = 1, 2, \ldots \end{cases}$$

$$B = y^k \cdot \left(\frac{r_0}{1}\right)^{2k}, \qquad y = \frac{\overline{u^2(l)}}{2 \cdot r_0^2}.$$

$\overline{u^2(l)}$ is the mean square relative displacement of neighbouring atoms at a distance l [2].

Then the thermal properties of the cubic lattice consisting of N identical atoms can be written as follows:

a) The equation of state is

$$p = \frac{z \cdot C}{6 \cdot v} \cdot \sum_{k=0}^{\infty} \left[(n+2k) \cdot C_n^k - (m+2k) \cdot C_m^k\right] \cdot B^k, \tag{3}$$

z and v are the number of nearest neighbours and the specific volume, respectively.

b) The internal energy E, the free energy F and the molar heat at constant volume C_v are respectively:

$$E = \frac{1}{2} \cdot z \cdot N \cdot \left[\tilde{\Phi}(l) + \frac{1}{2} \cdot f(l, T) \cdot \overline{u^2(l)}\right] + 5 \cdot N \cdot \tilde{F}_3(T), \tag{4}$$

$$F = F_0 + E - f(l, T) \cdot \overline{u^2(l)} \cdot N - 4 \cdot N \cdot \tilde{F}_3(T), \tag{5}$$

$$C_v = \left(\frac{\partial E}{\partial T}\right)_v. \tag{6}$$

The symbols used in (4)–(6) have the following meaning:

$$
\begin{aligned}
f(l,T) =& f \cdot (1 + \alpha \cdot y + \delta \cdot p_1), \\
f =& n \cdot m \cdot D_0 / r_0^2, \quad \alpha = \tau^2 - t, \\
\tau =& n + m + 3, \quad t = n^2 + m^2 + 6 \cdot (n + m) + n \cdot m + 11, \\
\delta =& 4 \cdot \tau / n \cdot m, \quad p_1 = 3 \cdot p \cdot v \cdot r_0 / 2 \cdot z \cdot D_0 \cdot l_0, \\
l_0 =& r_0 \cdot (1 + \tau \cdot y).
\end{aligned}
$$

F_0 and $\tilde{F}_3(T)$ are the free energy in the harmonic approximation [8] and the effective cubic anharmonic contribution to the temperature dependent part of F [9], respectively.

The system of self-consistency equations which describe the effect of pressure on the thermodynamic properties of cubic crystals near the lattice instability point T_s was solved analytically in terms of the Lennard–Jones (n, m) potential function in [10]. We shall not collect here analytical equations derived there but applying them to the lattice of RGS we will explore the pressure dependence of various functions i.e.: the instability temperature T_s, relative displacements of atoms $\sqrt{\langle w_s^2 \rangle}/l_s$, free energy F_s and the free Gibbs energy G_s.

3. Numerical results

Using the values of model parameters reported in Table I, we have computed at first the temperature and pressure dependence of various thermodynamical functions, i.e.: the binding energy of lattice atoms D, Grüneisen parameter γ, internal energy E, free energy F, thermodynamical potential G, relative displacement of atoms $\sqrt{\langle u^2 \rangle}/l$ and molar heat at constant volume C_v.

The calculated in RSCPA values of D and γ are given in Table II together with the experimental data [11–13].

In Table III the temperature variations of the thermodynamical functions as well as the relative displacement of atoms for some values of the external pressure are presented. From this Table we can see the thermal expansion of the crystals and the decrease of the internal energy E when the temperature increases. So, for larger T values of the self-consistency potential (2) sufficiently differs from the harmonic interaction potential (1), i.e. the behaviour of the crystals in RSCPA differs sufficiently from the calculated in harmonic approximation.

The detailed numerical results of the molar heat at constant volume C_v for considered potential at various temperatures are given in Table IV together with the observed data (Ex) [15, 16] as well as those computed for the Morse (M) self-consistent potential [1] and the Lennard–Jones (12,6) nearest neighbour force model [17] using the Feldman–Horton approximation [18]. The experimental values of C_v for Ar and Kr were obtained from the equation: $C_v = C_p - \beta_1^2 \cdot T / \kappa \cdot \varrho$ using experimental data for all quantities on the right hand side of the equation. (C_p is the molar heat at constant pressure, β_1 is the volume coefficient of thermal

Table I
Lennard–Jones (n, m) potential constants for the pairwise atomic interaction in rare gas solids

Solids	Parameters			
	n	m	r_0 [nm]	D_0 10^{-21} [J]
Ar	14.7	7.0	0.375	1.5812
Kr	14.42	6.88	0.399	2.3795
Xe	13.83	6.52	0.434	3.3648

Table II
The effect of pressure on the binding energy of lattice atoms D and Grüneisen parameter γ of rare gas solids at 0 K using the Lennard–Jones (n, m) self-consistent potential. Experimental data (Ex) [12–14] are collected for comparison. p in units of $1.01325 \cdot 10^5$ Pa

Solids	p	$-D \cdot 10^{-21}$ [J/atom]		γ^{**}	
		n, m	Ex [12]	n, m	Ex [13,14]
Ar	0	11.170	12.7527	4.4715	2.80
	10	11.173		4.4713	(3.10)*
	100	11.200		4.4682	
	1000	11.427		4.4395	
Kr	0	17.293	17.4629	4.2080	2.75
	10	17.296		4.2078	(2.80)
	100	17.324		4.2060	
	1000	17.547		4.1881	
Xe	0	25.559	24.6723	3.9760	2.75
	10	25.563		3.9759	(2.87)
	100	25.601		3.9744	
	1000	25.907		3.9598	

*Values in parentheses correspond to experimental results given in [14]
**Theoretical values obtained on the basis of analytical formula given in [15]

expansion, κ is the isothermal compressibility, ϱ is the density.) The calculations of C_v for Xe were impossible because of incomplete experimental data set. From Table IV we see that our results for the heat capacity show the same temperature behaviour as has been found experimentally. The values of C_v obtained in terms of the (n, m) potential are somewhat lower than those calculated for the Morse model. It follows from this that the values of thermodynamic functions of crystals strongly depend on the depth of the potential well D_0. The value of D_0 is always lower in the Lennard–Jones (n, m) potential than in the Morse potential [1].

As a next reliable test of validity of the self-consistent phonon theory and the generalized form of the Lennard–Jones (n, m) model of interatomic interactions in the lattice of RGS we will explore the pressure dependence of thermodynamical

Table III
Temperature and pressure variations of the internal energy E, free energy F, free Gibbs energy G and the relative displacement of atoms $\sqrt{\langle u^2 \rangle}/l$ of rare gas solids in the RSCPA for the Lennard–Jones (n, m) potential

Solids	T [K]	$-E$ [kJ/mol]	$-F$ [kJ/mol]	$-G$ [kJ/mol]	$\sqrt{\langle u^2 \rangle}/l$
Ar	40*	4.3484	5.5590	5.5590	0.0529
	40**	4.3824	5.5635	4.8088	0.0517
	60*	3.3010	6.1447	6.1447	0.0746
	60**	3.4972	6.1946	5.3624	0.0703
	70*	2.0428	5.9651	5.9651	0.0988
	70**	2.4606	6.3697	5.4039	0.0893
Kr	80*	5.8623	10.3374	10.3374	0.0645
	80**	5.9828	10.3592	9.4038	0.0625
	100*	3.6805	10.8659	10.8695	0.0924
	100**	4.4710	11.2658	10.1824	0.0817
	110*	2.8667	10.8504	10.8504	0.1027
	110**	3.1103	11.2099	9.9325	0.0989
Xe	120*	7.8513	16.5432	16.5432	0.0719
	120**	8.0880	16.5918	15.3245	0.0692
	140*	5.0677	17.0473	17.0473	0.0976
	140**	6.3445	17.7185	16.3041	0.0852
	160*	3.6355	17.4646	17.4646	0.1094
	160**	3.9779	17.8807	16.1150	0.1069

*$p = 0$ Pa
**$p = 101.325$ MPa

functions near the lattice instability point T_s. Numerical results for T_s are listed in Table V together with ones obtained in terms of the Lennard–Jones (12,6) and Morse renormalized potentials. The values of melting temperature T_m [19, 20] are shown in this Table because the melting point, which is determined by the balance of free energy between solid and liquid, must be a little lower than the temperature of lattice instability [21]. For qualitative comparison we have also collected in Table V theoretical data for T_m of Ar obtained by Kumari et al [22]. From Table V we see that the instability temperature increases as the crystal volume is compressed and this qualitative tendency obtained is consistent with the observed melting data [19] as well as theoretical ones [22, 23].

Pressure variations of the relative displacement of atoms $\sqrt{\langle u_s^2 \rangle}/l_s$, free energy F_s and the free Gibbs energy G_s of RGS at $T = T_s$ in the RSCPA for the Lennard–Jones (n, m) potential are shown in Table VI. Theoretical results obtained in terms of the Morse renormalized potential are collected in this Table for comparison. Table VI shows that the mean distances between the atoms l_s are much larger than the mean square displacements $\sqrt{\langle u_s^2 \rangle}$ up to the instability point. Therefore the

Table IV

Comparison of the values for the molar heat at constant volume obtained in terms of the Lennard–Jones (n, m) self-consistent potential with experimental [16, 17] and theoretical data computed for the Morse (M) [1] and Lennard–Jones (12,6) potentials [18] of rare gas solids

Solids	T	C_v [J/mol·K]			
	[K]	Ex	(n, m)	(12,6) [18]	(M) [1]
Ar	5	0.369	0.383		0.482
	10	03.296	3.066	3.591	04.146
	20	12.222	14.550	12.046	8.595
	40	19.954	20.410	19.229	20.270
	60	23.322	21.570	20.775	22.275
	70	25.718	21.320	20.950	22.673
Kr	5	0.854	0.695		0.986
	10	5.198	5.918		4.506
	20	15.661	19.320	15.612	16.482
	40	21.923	21.980	21.149	21.525
	60	23.376	22.070	22.222	23.108
	80	25.587	23.640	22.371	23.583
	100	27.775	23.050	22.172	24.616
Xe	5		1.133		1.614
	10		9.068		3.565
	20		20.680	17.084	17.958
	40		22.810	21.997	22.862
	60		22.860	22.945	23.649
	80		22.540	23.095	23.844
	100		22.310	23.020	23.883
	120		21.630	22.795	23.896
	140		21.130	22.571	23.864

long-range correlations due to the attractive part of the potential play an essential role and the instability point corresponds to the transition from the crystal state to the uniform density state [24]. This transition is accompanied by singularities in the specific heat [24, 25].

4. Conclusions

The self-consistent phonon theory of anharmonic crystals [2] has been used last time for the investigation of physical properties of metallic crystals [10, 26] in terms of the generalized form of the Lennard–Jones (n, m) central force interactions [3]. This generalized potential has four adjustable parameters m, n, D_0 and r_0 compared with the Lennard–Jones (12,6) potential, which has only two. Then, making use of additional physical property data to determine these parameters a more sensitive description can be obtained for crystals.

Applying the method formulated in [2] in this paper we investigate the pres-

Table V

Pressure variations of the instability temperature T_s of RGS in the self-consistent phonon theory for the Lennard–Jones (n, m) and (12,6) as well as Morse (M) potentials. Experimental values (Ex) of the melting temperature T_m [20, 21] and, in parentheses, theoretical ones obtained by Kumari et al [23] are given for comparison. p in units of 10^5 Pa

Solids	p	T_s [K]			T_m [K]
		(n, m)	(12,6)	(M)	(Ex)
Ar	0	83.756	79.354	86.887	—
	0.689	83.809	79.680	86.930	83.810 (83.810)
	101.325	86.961	85.339	92.240	—
	923.40	109.428	95.632	125.853	105.281 (103.725)
	1210.25	114.271	106.809	147.279	11.433 (109.730)
	2462.06	143.991	135.584	170.784	136.269 (134.932)
Kr	0	115.736	102.420	109.620	
	0.73	115.804	102.368	109.664	115.78
	101.325	125.390	112.756	115.771	
Xe	0	161.180	147.310	164.822	
	0.81	161.284	147.359	164.886	161.37
	101.325	174.435	153.650	172.889	

Table VI

Pressure variations of the relative displacement of atoms $\sqrt{\langle u_s^2 \rangle}/l_s$, free energy F_s and the free Gibbs energy G_s of RGS at $T = T_s$ in the RSCPA for the Lennard–Jones (n, m) potential. Other theoretical data obtained in terms of the Morse (M) renormalized potential are shown for comparison. p in units of 10^5 Pa

Solids	p	$\sqrt{\langle u_s^2 \rangle}/l_s$		$-F_s$ [kJ/mol]		$-G_s$ [kJ/mol]	
		n, m	M	n, m	M	n, m	M
Ar	0	0.1045	0.1190	6.5250	6.735	6.5250	6.735
	0.689	0.1047	0.1191	6.5292	6.736	6.5116	6.732
	101.325	0.1059	0.1233	6.9667	6.737	5.8231	6.730
Kr	0	0.1062	0.1280	10.9535	10.267	10.9535	10.267
	0.63	0.1063	0.1289	10.9542	10.269	10.9419	10.265
	101.325	0.1087	0.1294	11.5504	10.271	10.1209	10.262
Xe	0	0.1105	0.1207	17.4287	17.254	17.4287	17.254
	0.81	0.1111	0.1208	17.4292	17.258	17.3653	17.253
	101.325	0.1120	0.1234	18.4891	17.261	16.6004	17.250

sure and temperature dependence of the thermodynamic functions of rare gas solids (RGS) in terms of the above interatomic potential. It should be noted that the parameters of the (n, m) renormalized potential listed in Table I have been determined in the highest approximation with respect to the number of nearest-neighbour shells having influence on the pair interaction by the help of the method described in [3]. Numerical results of thermodynamical quantities, which account for the (n, m) self-consistent potential, are in reasonable agreement with the measured data (Tables II, IV and V). At the same time these results represent the appreciable improvement over those which account for the (12,6) renormalized potential. The values of thermodynamical functions obtained by the help of (n, m) potential are somewhat lower than those calculated for the Morse model. From this it follows that the values of the above mentioned quantities strongly depend on the depth of the potential well D_0. The value of D_0 is always lower in the Lennard–Jones (n, m) potential than in the Morse potential curve [1].

Detailed analysis of the results collected in Tables II–VI shows that the Lennard–Jones (n, m) and Morse renormalized potentials are quite good representations for the initial pair interaction in RGS. Let us recall here that the Lennard–Jones (12,6) potential was widely used [27] and regarded as a satisfactory quantitative representation of real potential in RGS. However, the arbitrariness of the (12,6) potential was pointed out by Guggenheim and McGlashan [28] and found to lead to an incorrect value (by a factor of about 2) for the coefficient of r^{-6} in the long-range region, and to a value for the depth of the potential well which is very likely incorrect by as much as about 20 % in the case of argon. This reduces the effectiveness of the Lennard–Jones (12,6) potential as a description of the interatomic potential for rare gas solids. One way to improve the agreement between the potential model and the experimental data is to use the generalized form of the interatomic potential — the Lennard–Jones (n, m) potential. The results obtained with its application are reported in Section 3.

Acknowledgement

The authors are grateful to Professor Dr. T. Siklós for reading the manuscript.

References

1. C. Malinowska-Adamska, Acta Phys. Hung., *59*, 257, 1986.
2. N. M. Plakida and T. Siklós, Acta Phys. Hung., *45*, 37, 1978.
3. Shu Zhen and G. J. Davies, Phys. Stat. Sol., *(a) 78*, 595, 1983.
4. M. L. Klein, G. K. Horton and J. L. Feldman, Phys. Rev., *184*, 968, 1969.
5. N. E. Massa, S. S. Mitra and J. F. Vetelino, Phys. Stat. Sol., *(b) 94*, 387, 1979.
6. H. R. Glyde and M. L. Klein, CRC Crit. Rev. Solid State Phys. Mater. Sci., *2*, 181, 1971.
7. C. Malinowska-Adamska, Acta Phys. Hung., *45*, 221, 1978.
8. A. Maradudin, P. A. Flinn and R. A Coldwell-Horsfall, Ann. Phys., *15*, 337, 1961.
9. T. Siklós and V. L. Aksienov, Phys. Stat. Sol., *50*, 171, 1972.
10. C. Malinowska-Adamska, Phys. Stat. Sol., *(b) 151*, 53, 1989.

11. G. E. R. Schulze, Metallphysik, Wydawnictwo Naukowe, Warsaw, 1982, p. 281 (in Polish).
12. J. A. Reissland, Physics of Phonons, Izd. Mir, Moscow 1975 (in Russian).
13. G. K. Horton and J. W. Leech, Proc. Phys. Soc., *82*, 816, 1963.
14. R. K. Singh and D. Neb, Phys. Stat. Sol., *(b) 112*, 735, 1982.
15. P. Flubacher, A. J. Leadbetter and J. A. Morrison, Proc. Phys. Soc., *78*, 1449, 1961.
16. R. H. Beaumont, H. Chicara and J. A. Morrison, Proc. Phys. Soc., *78*, 1462, 1961.
17. J. W. Leech and J. A. Reissland, J. Phys., *C3*, 975, 987, 1970.
18. J. L. Feldman and G. K. Horton, Proc. Phys. Soc. (London), *92*, 227, 1967.
19. W. H. Hardy, R. K. Crawford and W. B. Daniels, J. Chem. Phys., *54*, 1005, 1971.
20. G. L. Pollack, Rev. Mod. Phys., *36*, 93, 1968.
21. Y. Ida, Phys. Rev., *187*, 951, 1968; *B1*, 2488, 1970; *B7*, 5416, 1973.
22. M. Kumari, K. Kumari and N. Dass, Phys. Stat. Sol., *(a) 99*, K23, 1987.
23. A. Michels and C. Prins, Physica (Utrecht), *28*, 101, 1962.
24. N. M. Plakida and T. Siklós, Phys. Stat. Sol., *39*, 171, 1970.
25. N. M. Plakida, Fiz. Tverd. Tela, *11*, 700, 1969.
26. C. Malinowska-Adamska, Acta Phys. Hung., *69*,71, 1991.
27. M. L. Klein, J. A Venables, ed., Rare Gas Solids, Vol. 1, Academic Press, New York, 1976.
28. E. A. Guggenheim and M. L. McGlashan, Proc. Roy. Soc., *A255*, 456, 1960.

Acta Physica Hungarica 71 (3-4), pp. 211–218 (1992)

ELECTRON DENSITY OF METALLIC SURFACES BY VARIATION METHOD

A. ISKANDER

Institute of Physics, Technical University of Budapest
1521 Budapest, Hungary

(Received in revised form 24 January 1992)

In this paper variational calculation is performed for simple jellium metal surface electron density using the density functional theory. A trial function of the local electron density is proposed. The free parameters are obtained by minimization of the total energy functional. The effect of the high density gradient expansions of the kinetic emergy is studied (i.e. Kirzhnits energy). The results obtained are similar to those of Lang and Kohn, which use a more exact method.

1. Introduction

Hohenberg, Kohn and Sham (HKS) have shown that the total energy of an inhomogeneous electron gas can be expressed as a unique functional of the local electron density and that this functional attains its minimum at the real electronic density [1, 2]. Making use of that, the surface energy was calculated in our previous work [3]. Here, a modified formula of the local electron density is suggested and the effect of the second gradient expansion of kinetic energy is studied. That was omitted in the work mentioned. Our results approximate the results of Lang [6] well; for example, the maximum difference between our calculation of local electron density and that of Lang's result is $0.056 \cdot n_+$ at $r_s = 6.0$, where n_+ is the bulk density and r_s is the Wigner–Seitz radius which characterizes the bulk electron density.

The jellium model of metal surface is used; the energy is the Hartree and the unit of length is the Fermi wavelength.

2. Statement of the problem

Using the (HKS) method some important physical quantities were calculated; for example, the surface energy, chemical potential and the work function [4, 5]. On the other hand, using (HKS) formalism, Lang and Kohn have calculated the local electron density by solving a Schrödinger-like equation with the self-consistent field method [6]. The electron densities resulting from these calculations have been reported in numerical Tables for the integer values of Wigner–Seitz radius from 2 to 6. On the other hand, there are no experimental data on the local electron density

which would provide a direct validity test of these numerical Tables. The local electron density obtained by Lang and Kohn is considered as its exact calculation, owing to the fact that the kinetic energy is exact and only the exchange-correlation energy was taken in an approximate formula.

In the present model, the metal is assumed to be in the positive region of x and the zero point is on the surface of the metal. The analytical formula of the suggested electron density is

$$n(x) = n_+ \left\{ \frac{1}{2}[1 + \mathrm{th}(p(x-\varphi))] + \theta(x-\varphi) \cdot k \cdot \left[\frac{\sin(q(x-\varphi))}{[q(x-\varphi)]^{\alpha}} - \frac{\cos(q(x-\varphi))}{[q(x-\varphi)]^{\gamma}} \right] \right\}. \tag{1}$$

This formula is a generalization of the one employed by Szeifert [7] and that of our previous work [3]. Here $\theta(x-\varphi)$ is the step function and p, q, k, φ, α, γ are variational parameters. The formula must satisfy the following physical conditions:

a) charge balance, which means that

$$\int_{-\infty}^{\infty} [\theta(x) - n(x)]\, dx = 0, \tag{1a}$$

where $\theta(x)$ is the step function.

b) continuity of $n(x)$; i.e., the second term of Eq. (1) has to be zero when $x = \varphi$ which results in

$$\gamma = \alpha - 1. \tag{1b}$$

Since the application of the physical conditions has reduced the six parameters to four we choose p, q, k and α as free variational parameters.

The energy functional, $E[n]$, is given in the following form:

$$E[n] = E_k[n] + E_{es}[n] + E_{xc}^{\mathrm{LDA}}[n], \tag{2}$$

where $E_{es}[n]$ is the electrostatic energy, $E_{xc}^{\mathrm{LDA}}[n]$ is the exchange-correlation energy in local density approximation and $E_k[n]$ is the kinetic energy contribution, which consists of Thomas–Fermi energy plus the first and second order gradient expansion terms for the kinetic energy. The first gradient term was derived by Weizsäcker [8] and the second one by Kirzhnits [9]. The components of the total energy are given below.

The kinetic energy may be expressed in this component equation by

$$E_k[n] = E_k^{\mathrm{TF}}[n] + E_k^{\mathrm{WK}}[n] + E_k^{\mathrm{Kr}}, \tag{3}$$

where E_k^{TF} is the Thomas–Fermi energy, $E_k^{\mathrm{WK}}[n]$ is the Weizsäcker energy and $E_k^{\mathrm{Kr}}[n]$ is the Kirzhnits energy. Their analytical expressions have the following form:

$$E_k^{\mathrm{TF}}[n] = \frac{1.105}{r_s^2} \int_{-\infty}^{\infty} n(x)^{5/3} dx, \tag{3a}$$

$$E_k^{\mathrm{WK}}[n] = \frac{0.0013}{r_s^2} \int_{-\infty}^{\infty} \frac{1}{n(x)} \left(\frac{dn(x)}{dx}\right)^2 dx, \tag{3b}$$

$$E_k^{\mathrm{Kr}}[n] = \frac{0.584659 \cdot 10^{-5}}{r_s^2} \int_{-\infty}^{\infty} \left[\left(\frac{1}{n(x)}\right)^{5/3} \cdot \left(\frac{d^2 n(x)}{d^2 x}\right)^2 - \frac{9}{8} \left(\frac{1}{n(x)}\right)^{8/3} \cdot \left(\frac{d^2 n(x)}{d^2 x}\right) \cdot \left(\frac{dn(x)}{dx}\right)^2 + \frac{1}{3} \left(\frac{1}{n(x)}\right)^{11/3} \cdot \left(\frac{dn(x)}{dx}\right)^4 \right] dx. \tag{3c}$$

The electrostatic energy is given by

$$E_{es}[n] = \frac{1}{2} \int_{-\infty}^{\infty} [n(x) - n_+(x)] v_{es}(x) dx, \tag{4}$$

where $n_+(x)$ is the positive background charge density described by a step function and $v_{es}(x)$ is the electrostatic potential produced by the electric dipole layer $(n(x) - n_+(x))$ on the surface.

$E_{xc}^{\mathrm{LDA}}[n]$ is expressed by the Wigner interpolation formula [10], [11] (in local density approximation),

$$E_{xc}^{\mathrm{LDA}}[n] = -\frac{0.458}{r_s} \int_{-\infty}^{\infty} n(x)^{4/3} \cdot dx - \int_{-\infty}^{\infty} \frac{0.44 \cdot n(x)^{4/3}}{r_s + 7.8 \cdot n(x)^{1/3}} dx. \tag{5}$$

3. Results

In the present paper, model calculation for Eq. (1) as a trial function of local electron density has been performed. At first the calculation was performed by introducing the first gradient expansion only (Weizsäcker approximation Eq. (3b)) and, secondly, by introducing the second gradient expansion (Kirzhnits energy, Eq. (3c)) in the kinetic energy. The inclusion of Kirzhnits energy in the energy functional is the inherent difference between this and our previous work [3]. The calculations were performed at $r_s = 2, 3, 4, 5, 6$ (the range of metallic density).

Table I gives the values of the chosen free parameters of Eq. (1), introducing only Eq. (3a) and Eq. (3b) in the kinetic energy term. The last column in this Table represents the defined minimum value of total energy. Table II is the same as Table I with the only difference that Eq. (3c) has been taken into account during the calculation. As we see in Tables I and II the minimum value of the total energy at $r_s = 2.0$ is very high and it has a positive value. At the other values of r_s the minimal values of the total energy are smaller and they have a negative value. This

Table I
Calculated parameters of electron density with Kirzhnits energy omitted

r_s	p	q	k	α	φ	$E[n]$
2.0	5.205331	7.895049	0.069164	2.719804	0.007003	$0.18886302 \cdot 10^{-2}$
3.0	7.720699	6.930177	0.038432	2.591169	0.004543	$-0.36767144 \cdot 10^{-1}$
4.0	10.375072	8.953466	0.085654	2.400219	0.008242	$-0.24193683 \cdot 10^{-1}$
5.0	12.943867	10.423628	0.170325	2.388006	0.014134	$-0.15306272 \cdot 10^{-1}$
6.0	15.462465	12.558343	0.285127	2.337805	0.019953	$-0.100788668 \cdot 10^{-1}$

Table II
Calculated parameters of electron density with Kirzhnits energy included

r_s	p	q	k	α	φ	$E[n]$
2.0	4.902696	6.282076	0.061510	2.321621	0.008651	$0.19874771 \cdot 10^{-2}$
3.0	6.223999	329366	0.111859	2.233857	0.013921	$-0.36720419 \cdot 10^{-1}$
4.0	7.320741	9.047756	0.176699	2.16406	0.018397	$-0.24166628 \cdot 10^{-1}$
5.0	8.137526	10.356304	0.268837	2.141908	0.024695	$-0.15289046 \cdot 10^{-1}$
6.0	8.755995	11.470215	0.368613	2.039834	0.031837	$-0.10066852 \cdot 10^{-1}$

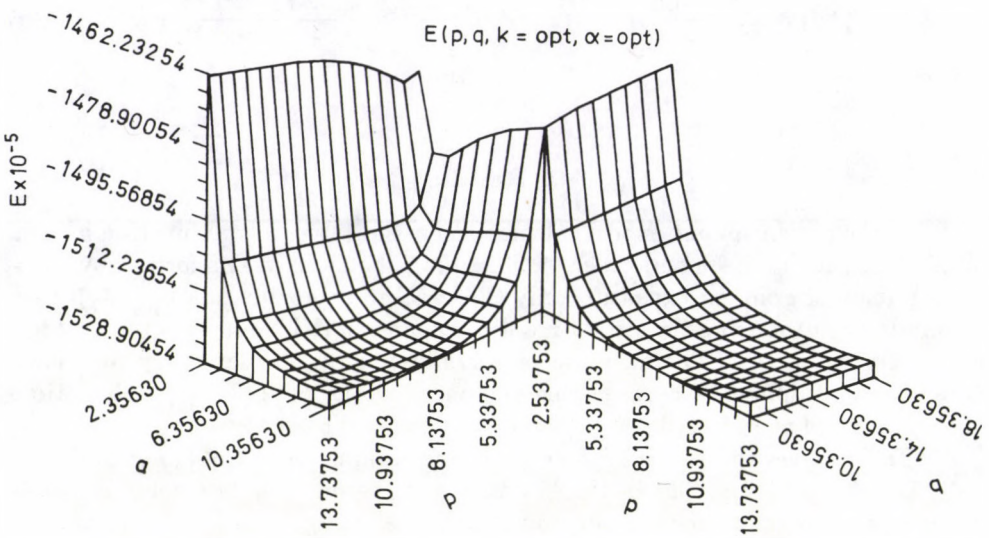

Fig. 1. The extremal nature of the energy functional at the optimum value of α and K, while p and q have been selected at 17 different values around the minimum at $r_s = 5.0$

result is also encountered in the calculation of Lang [6]. The reason for this result is that the used jellium model does not represent the very high density metals well. This basic shortcoming of the jellium model has been corrected by Lang [6] by going over to a model in which the positive ions are more realistically treated.

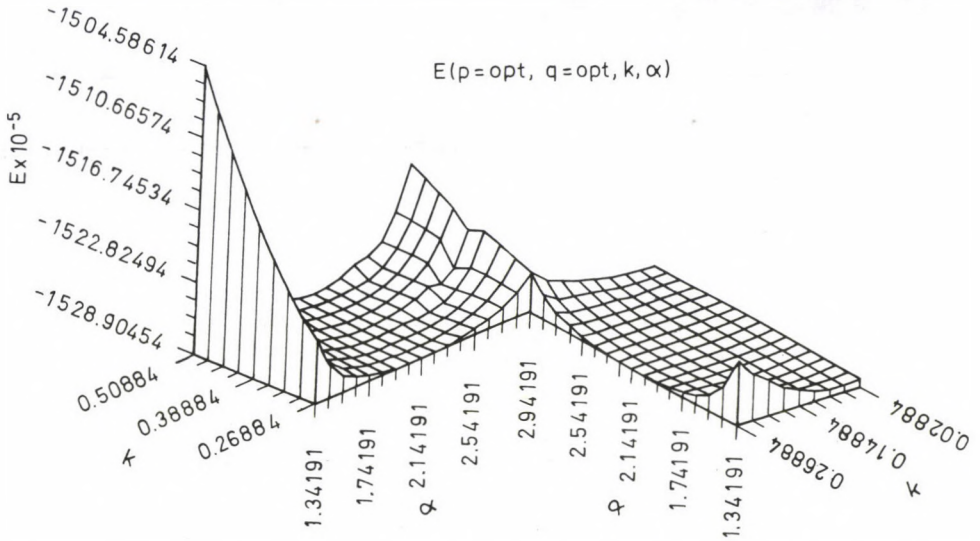

Fig. 2. The extremal nature of the energy functional at the optimum value of p and k, while α and k have been selected at 17 different values around the minimum at $r_s = 5.0$

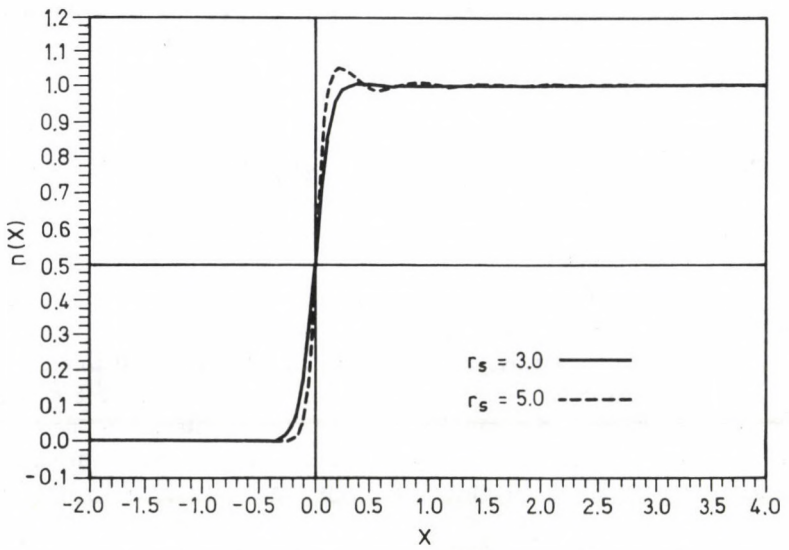

Fig. 3. The calculated electron density by omitting Kirzhnits energy at $r_s = 3.0$ (solid line) and $r_s = 5.0$ (dashed line)

Figure 1 gives good information on the extremal nature of the energy functional, Eq. (2), by the aid of 3-D computer graphics drawn at the optimum values of k and α while p and q have been selected at 17 different values around the minimum at $r_s = 5.0$. Figure 2 presents the same information at the optimum values of p and q, while k and α are the variables.

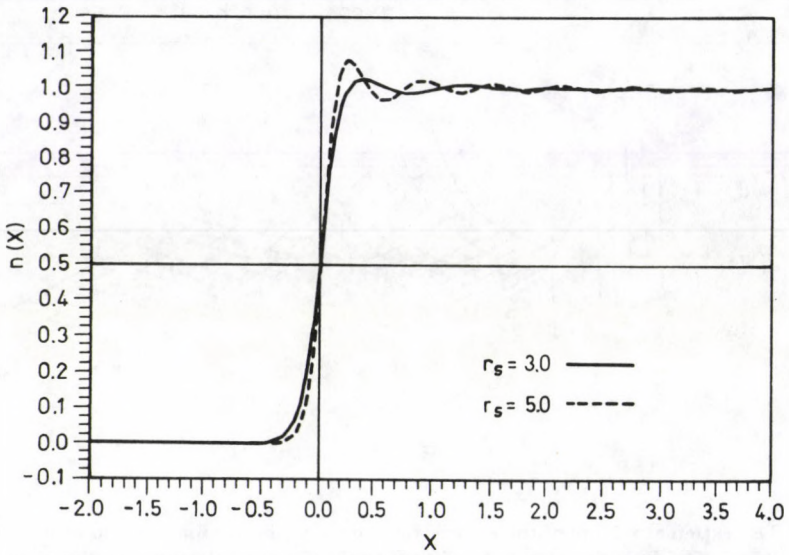

Fig. 4. The calculated electron density by introducing all the suggested terms of kinetic energy at $r_s = 3.0$ (solid line) and at $r_s = 5.0$ (dashed line)

Figure 3 shows the local electron density obtained by Eq. (1) for $r_s = 3.0$ and $r_s = 5.0$, using Eq. (3a) and Eq. (3b) in the kinetic energy. Figure 4 is the same as the previous Figure, but all the suggested terms of kinetic energy are included in the energy functional $E[n]$.

In Fig. 5 the differences between our calculations of local electron density and that of Lang [6] at $r_s = 5.0$ can be seen, where the solid line represents these differences if the Kirzhnits energy [9] is omitted and the dotted line demonstrates those if that term of kinetic energy has been taken into account. In Fig. 5, as we see, the differences between our calculations an Lang's calculation of electron density when all the suggested terms of energy were included are small compared with the same differences when the Kirzhnits energy is omitted, especially at the metallic surface.

The calculations were performed by an efficient computer program by minimizing the energy functional. The convergence is rapid for every low electronic density ($r_s > 4.0$) and slow for high electronic density ($r_s < 4.0$).

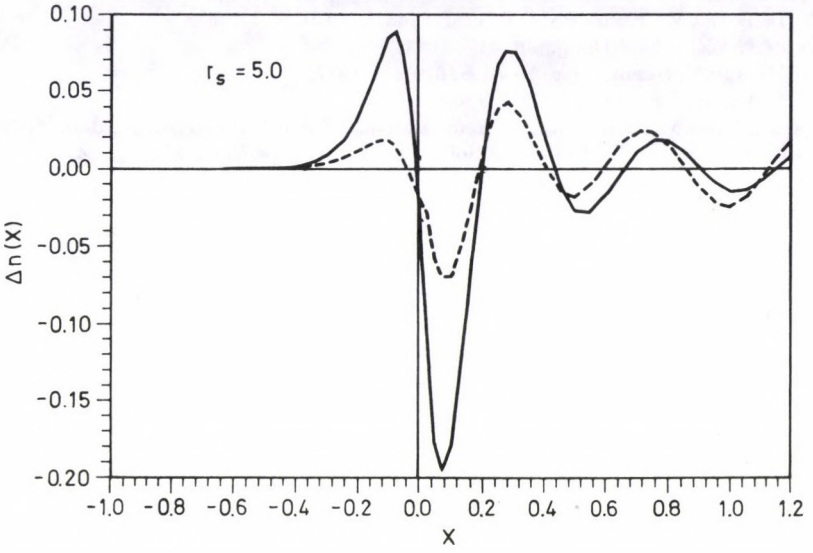

Fig. 5. The differences between our calculation of local electron density and that of Lang when Kirzhnits energy is omitted (solid line) and without omitting this term of kinetic energy (dashed line) at $r_s = 5.0$

4. Conclusions

The function of local electron density suggested in the present paper gives good results for the model used. This paper also shows the importance of introducing the gradient expansions of the kinetic energy during solving similar problems such as this one.

Acknowledgements

I wish to thank Prof. Z. Füzessy for giving me the possibility to complete my work after the end of my scholarship and for his valuable comments. I am very grateful to Dr. L. Orosz for his useful advice and his help during my work.

References

1. P. Hohenberg and W. Kohn, Phys. Rev., *136*, B864, 1964.
2. W. Kohn and L. J. Sham, Phys. Rev., *140*, A1133, 1965.
3. A. Iskander and L. Orosz, Acta Phys. Hung., *65*, 391, 1989.
4. J. R. Smith, Phys. Rev., *181*, 522, 1969.

5. W. Schmickler and D. Henderson, Phys. Rev., *B30*, 3081, 1984.
6. N. D. Lang and W. Kohn, Phys. Rev., *B1*, 4555, 1970.
7. Z. Szeifert, Acta Phys. Hung., *56*, 419, 1981.
8. C. G. Ma and V. Sahni, Phys. Rev., *B16*, 4249, 1977.
9. D. A. Kirzhnits, Sov. Phys. JETP, *5*, 64, 1957.
10. S. Rames, Wave Mechanics of Electrons in Metals, North-Holland, Amsterdam, 1961, p. 177.
11. D. Pines, Elementary Excitations in Solids, Benjamin, New York, 1963, p. 94.

Acta Physica Hungarica 71 (3-4), pp. 219–223 (1992)

ANALYTIC FORMULA FOR THE ELECTRON DENSITY OF METAL SURFACES

A. ISKANDER

Institute of Physics, Technical University of Budapest
1521 Budapest, Hungary

(Received in revised form 24 January 1992)

In this paper an analytical expression for electron density will be suggested. One of the fitting methods is applied to the self-consistent calculation of Lang through the use of this analytical expression. The density for all metals can be calculated very easily, while the electron density has been calculated by Lang only for the integer values of r_s (Wigner–Seitz radius) in range (2–6). The results have been compared with a similar work of Szeifert. The calculated results approximate the exact solution of Lang well at all the values of r_s.

1. Introduction

Making use of the self-consistent calculation of electron density [1, 3], Szeifert has derived an analytic formula for electron density which approximates the self-consistent results of Lang [1, 3]. Inthe present paper a modified formula of electronic density has been worked out. The method which estimates the values of the parameters differs from Szeifert's method. The results obtained approximate the self-consistent calculation better than those of Szeifert.

The jellium model of metal surface is used. The unit of the electron density is positive bulk density and the unit of length is the Fermi wavelength.

2. The model

Much attention has been paid to the electron density calculation at the metallic surfaces in the last three decades. Using the self-consistent method, Lang [1] has calculated numerically the electron density for the interger values of a parameter which characterizes the electron density in metallic range (from 2 to 6). This parameter has been called Wigner–Seitz radius, r_s. The values of this parameter have been given in Table I of [2] for 41 metals. Using these numerical Tables in the case of other problems which depend on electron density, for example work function, chemical potential, surface energy and so on, causes some difficulties.

The form of the suggested analytic formula for electron density is:

$$n(x) = n_+ \left\{ \frac{1}{2}[1 + \mathrm{th}(p(x-\varphi))] + \theta(x-\varphi) \cdot k \cdot \left[\frac{\sin(q(x-\varphi))}{[q(x-\varphi)]^\alpha} - \frac{\cos(q(x-\varphi))}{[q(x-\varphi)]^\gamma} \right] \right\}, \tag{1}$$

Table I
Values of the parameters in the analytic formula of electron density

r_s	p	q	k	α	φ
2.0	4.4653171	8.1720701	0.2224990	2.5199734	0.0225499
3.0	5.2937105	10.1527914	0.3156489	2.2835416	0.0279401
4.0	5.8812459	10.6206928	0.4070619	2.2671306	0.0344539
5.0	6.4114674	11.2140308	0.4715537	2.2018746	0.0389946
6.0	7.0035399	11.4913645	0.5166687	2.1761765	0.0420772

where $\theta(x-\varphi)$ is a step function and p, q, k, φ, α and γ are the parameters. This formula must satisfy the following physical conditions:

a) Neutrality of the charges, which means that

$$\int_{-\infty}^{\infty} [\theta(x) - n(x)]\, dx = 0, \tag{1a}$$

where $\theta(x)$ is the step function.

b) Continuity of $n(x)$ (i.e. the second term of Eq. (1) has to be zero when $x = \varphi$). This leads to

$$\gamma = \alpha - 1. \tag{1b}$$

Since the application of the physical conditions has reduced the six parameters to four, we choose p, q, k and α as the free parameters. As it can be seen, Eq. (1) is easy to transform to Szeifert's formula by putting $\alpha = 2.0$ and using Eq. (1b).

The theory that was used to determine the values of the chosen parameters was to make the sum of the squares of the differences between self-consistent calculation and our calculation a minimum [5] for the non-linear forms, starting with a trial set of these parameters. In other words, we have to look for the values of parameters for which the following equation has a minimum:

$$\Omega(p, q, k, \alpha) = \sum_{i=1}^{n} \left(n(x) - n^{\mathrm{L}}(x)\right)^2, \tag{2}$$

where $n(x)$ is the suggested formula of electron density and $n^{\mathrm{L}}(x)$ are given as numerical values by Lang. Szeifert [2] has used another method to fit Lang's calculation.

3. Results

Making use of the method developed here, values of the chosen parameters were calculated with the aid of a computer program at $r_s = 2, 3, 4, 5$ and 6. Table I shows the resulting values of these parameters.

As we can see in Table I the values of every parameter in this range of r_s can be fitted to an analytic equation as a function of r_s, having the form

$$a[r_s] = c_1 \cdot r_s^{c2} + c_3, \tag{3}$$

where "a" is a parameter and c_1, c_2 and c_3 are the fitting parameters. Using the theory of fitting mentioned above, one finds

$$\begin{aligned} p &= 2.4149 \cdot r_s^{0.4988} + 1.0701, \\ q &= -11.4343 \cdot r_s^{-1.5136} + 13.0275, \\ k &= 1.1246 \cdot r_s^{0.1916} - 1.0644, \\ \alpha &= 1.6678 \cdot r_s^{-2.2097} + 2.1567, \\ \varphi &= 0.0292 \cdot r_s^{0.3862} - 0.0159. \end{aligned} \tag{4}$$

Using this family of equations, the electron density for all the values of r_s may be calculated. It can be considered as the most important result of the suggested technique.

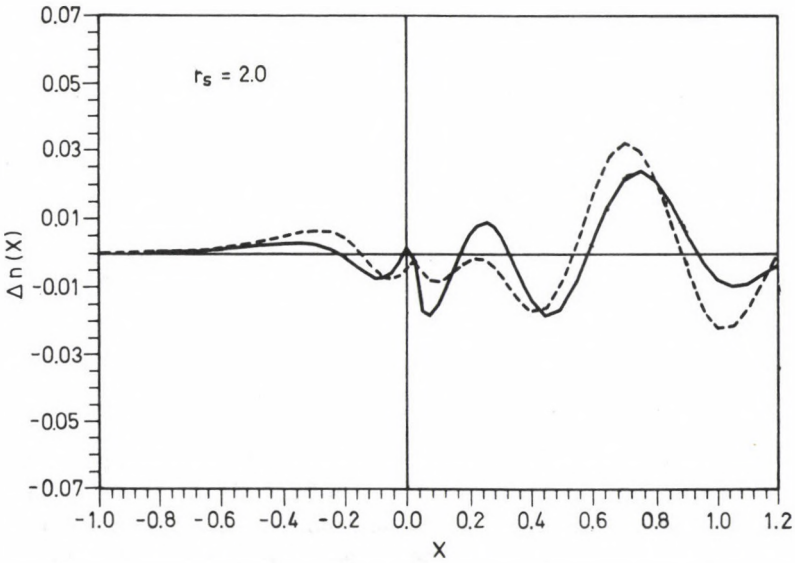

Fig. 1. The differences between our calculation of electron density and that of Lang (solid line) and between Szeifert's calculation and that of Lang (dashed line) at $r_s = 2.0$

Figure 1 shows the difference between our fitted calculations of electron density and that of Lang (solid line). Also shown is the difference between Szeifert's

calculation and that of Lang (dotted line) at $r_s = 2.0$. Figure 2 also shows these differences at $r_s = 6.0$.

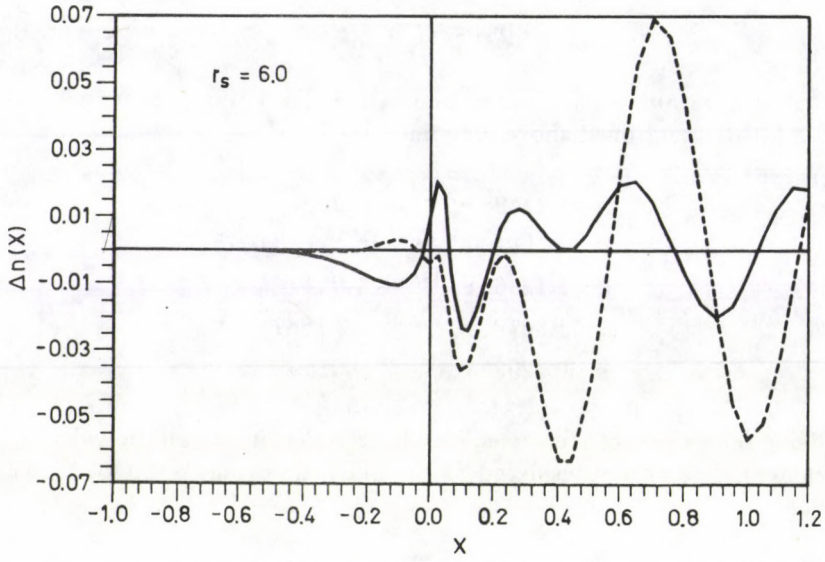

Fig. 2. The same as Fig. 1 at $r_s = 6.0$

It can be concluded from Fig. 1 and Fig. 2 that our results approximate Lang's calculation better than Szeifert's results. For example, the maximum error in Szeifert's calculation is $0.069n_+$, while in our case it is $0.023n_+$ at $r_s = 6.0$. Another important difference between the two calculations is that the errors in Szeifert's calculation increase rapidly as r_s increases, (the maximum error at $r_s = 2.0$ is $0.032n_+$ and at $r_s = 6.0$ it is $0.0693n_+$), while the errors' increase is very low in the method suggested above (the maximum error at $r_s = 2.0$ is $0.0238n_+$ and at $r_s = 6.0$ it is $0.024n_+$).

4. Conclusion

This simple analytical formula for electron density with four parameters gives good results for the self-consistent calculation of Lang. On the other hand, by using this formula the electron density for all the simple metals may be calculated. We need only to know the value of r_s for the metal, then simple substitution in Eq. (4) and Eq. (1) gives the electronic density of the metal surface.

Acknowledgements

I wish to thank Prof. Z. Füzessy for giving me the possibility to complete my work after the end of my scholarship and for his valuable comments. I am very grateful to Dr. L. Orosz for his useful advice and his help during my work.

References

1. N. D. Lang and W. Kohn, Phys. Rev., *B1*, 4555, 1970.
2. Z. Szeifert, Acta Phys. Hung. *56*, 419, 1981.
3. N. D. Lang, Solid State Comm., *7*, 1047, 1969.
4. Z. Szeifert, Thesis (unpublished).
5. S. Jazmati, Methods in Applied Mathematics, Alleppo University, 1981, p. 371.

Acta Physica Hungarica 71 (3-4), pp. 225-231 (1992)

DILATATION ET FUSION D'UN ARRANGEMENT LINEAIRE D'ATOMES

Y. THOMAS

Institut de Recherches Scientifiques et Techniques
49045 Angers Cedex, France

(Reçu 6 février 1992)

Le potentiel de Mie–Grüneisen appliqué à un arrangement linéaire montre l'instabilité du réseau au-delà d'un certain écartement limite entre les atomes. La fusion résulte de vibrations d'amplitude excédant une valeur critique qui est évaluée à environ 12 % de la distance interatomique d'équilibre.

Introduction

La transition de l'état solide à l'état liquide est assez mal connue. On constate que les solides ayant une grande température de Debye Θ_D prèsentent des points de fusion T_f élevés dépendant de la distance interatomique r donc de la solidité des forces de liaison (proportionnelle à Θ_D^2) dans le réseau [1]. Il est généralement admis que la fusion résulte d'un apport d'énergie provoquant une cassure de la structure pour une distance interatomique maximale [2]. Explicitons ce phénomène pour une chaîne linéaire à l'aide du modèle de Mie–Lennard–Jones qui rend compte de la variation du volume par élévation de température.

L'énergie potentielle d'interaction d'une paire d'atomes distantes entre elles de r est $W(r) = -a/r^m + b/r^n$ où m et n sont des entiers ($n > m$) et a et b des constantes (courbe la). Cette fonction permet aux atomes d'osciller autour de leur position d'équilibre et doit rendre compte de l'instabilité du réseau à hautes températures. Les coordonnées du minimum d'équilibre: $r_0 = (a^m/b^n)^{1/(n-m)}$ et l'énergie de dissociation W_0 permettent d'écrire:

$$W(r) = \frac{W_0}{n-m}\left[-n\left(\frac{r_0}{r}\right)^m + m\left(\frac{r_0}{r}\right)^n\right].$$

$W(r) = 0$ pour $r_1 = r_0(\frac{m}{n})^{1/(n-m)}$. Son asymétrie donne un point d'inflexion pour $r_i = r_0(\frac{n+1}{m+1})^{1/(n-m)}$. La force $F(r)$ entre les atomes est donnée par la dérivée $W'(r)$, c'est la superposition des composantes attrative et répulsive (courbe 1b). La dérivée seconde, nulle pour $r = r_i$, est analogue à la constante de rappel d'un oscillateur harmonique.

Energie potentielle d'une chaine linéaire à 0 K

Considérons un arrangement linéaire de p atomes, espacés irrégulièrement de r_{ij} entre eux:

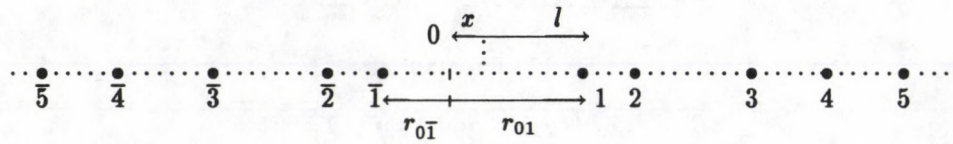

La longueur totale est $L = pl$ si l est la valeur moyenne de r_{ij}. L'énergie potentielle totale d'interaction des p atomes est:

$$W = \frac{W_0}{n-m} \sum_k \left\{ \sum_j \left[-n \left(\frac{r_0}{r_{jk}} \right)^m + m \left(\frac{r_0}{r_{jk}} \right)^n \right] \right\} \text{ où } r_{jk} = r_{0j} - r_{0k} \text{ et } j \neq k.$$

Si parmi les valeurs de $k \in [0, \pm\, p/2]$, on considère, par exemple, l'atome central ($k = 0$), son énergie potentielle d'interaction due à la présence de tous les autres est:

$$W(r_{0j}) = \frac{W_0}{n-m} \sum_{j \neq 0} \left[-n \left(\frac{r_0}{r_{0j}} \right)^m + m \left(\frac{r_0}{r_{0j}} \right)^n \right]$$

où les termes très prépondérants sont seulement dus aux interactions avec les plus proches voisins ($j = \pm 1$):

$$W(r_{0j}) \simeq \frac{W_0}{n-m} \left\{ -n \left[\left(\frac{r_0}{r_{01}} \right)^m + \left(\frac{r_0}{r_{0\bar{1}}} \right)^m \right] + m \left[\left(\frac{r_0}{r_{01}} \right)^n + \frac{r_0}{r_{0\bar{1}}}^n \right] \right\}.$$

Si x est la distance de l'atome central au point milieu entre ses deux plus proches voisins séparés en moyenne par $2l$: $r_{01} = l + x$ et $r_{0\bar{1}} = l - x$. L'énergie devient une fonction symétrique de x par le paramètre l:

$$W(x) = \frac{W_0}{n-m} \left\{ -n r_0^m \left[\frac{1}{(l+x)^m} + \frac{1}{(l-x)^m} \right] + m r_0^n \left[\frac{1}{(l+x)^n} + \frac{1}{(l-x)^n} \right] \right\}. \quad (1)$$

Etudions cette énergie d'interaction $W(x)$ pour diverses valeurs de l selon la théorie quasi harmonique:

$$W(x) = \frac{W_0}{n-m} \left\{ -n r_0^m \left[l^{-m} \left(1 + \frac{x}{l} \right)^{-m} + l^{-m} \left(1 - \frac{x}{l} \right)^{-m} \right] \right.$$
$$\left. + m r_0^n \left[l^{-n} \left(1 + \frac{x}{l} \right)^{-n} + l^{-n} \left(1 - \frac{x}{l} \right)^{-n} \right] \right\}$$

où par des développements limités de $(1 \pm \frac{x}{l})^{-n(et-m)}$ au 4è ordre ($x < l$):

$$W(x) \simeq \frac{W_0}{n-m}\left\{-nr_0^m l^{-m}\left[2+m(m+1)\frac{x^2}{l^2}+m(m+1)(m+2)(m+3)\frac{x^4}{12l^4}\right]\right.$$
$$\left.+mr_0^n l^{-n}\left[2+n(n+1)\frac{x^2}{l^2}+n(n+1)(n+2)(n+3)\frac{x^4}{12l^4}\right]\right\}.$$

Sa dérivée:

$$W'(x) = \frac{W_0 nm}{n-m}\left(\frac{x}{l}\right)\left\{2\left[-r_0^m l^{-(m+1)}(m+1)+r_0^n l^{-(n+1)}(n+1)\right]\right.$$
$$\left.+\frac{x^2}{3l^2}\left[-r_0^m l^{-(m+1)}(m+1)(m+2)(m+3)+r_0^n l^{-(n+1)}(n+1)(n+2)(n+3)\right]\right\}$$

s'annule pour $x = 0$ et pour:

$$x^2 = 6\left[\frac{(\frac{r_0}{l})^m(m+1)-(\frac{r_0}{l})^n(n+1)}{-\frac{r_0^m}{l^{(m+2)}}(m+1)(m+2)(m+3)+\frac{r_0^n}{l^{(n+2)}}(n+1)(n+2)(n+3)}\right],$$

on pose

$$x_0 = \pm\left(\frac{6N}{D}\right)^{1/2}.$$

$N = 0$ et change de signe pour $l = r_0\left(\frac{n+1}{m+1}\right)^{1/(n-m)} = r_i$, $N < 0$ pour $l < r_i$ et $N > 0$ pour $l > r_i$ ($D = 0$ et change de signe pour une valeur supérieure à r_i). En conséquence, $W(x)$ peut être représenté (courbes 2a à f): $l < r_i : x_0^2 < 0$, $W(x)$ est minimal pour $x = 0$. Chaque atome de l'arrangement linéaire reste dans une position moyenne entre ses plus proches voisins comme un oscillateur harmonique. $l_1 = r_0$ distance minimale d'équilibre (a), $l_2 > r_0$ (b). Les droites $x = l$ sont toujours asymptotes. $l = r_i : x_0^2 = 0$, $x = 0$ est racine double, $l_3 = r_i(c)$. $l > r_i : x_0^2 > 0$, l'énergie $W(x)$ présente deux minimums situés à r_0 des atomes voisins (pour $x = 0$ on a $W(x)$ maximale). La valeur absolue de x_0 croît avec celle de $l(d, e, f)$.

Dès que $l > r_i$, l'atome central occupe une position stable dans l'un des deux minimums. Cette situation est caractéristique de l'état liquide. La chaîne se dilate régulièrement depuis pr_0 jusqu'à pr_i puis elle devient instable, c'est la fusion, il y a fracture en l'absence d'agitation thermique (courbe 1c).

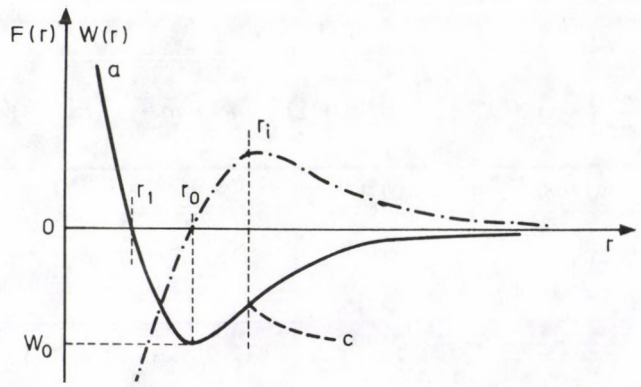

Courbe 1. a) _____ Énergie potentielle $W(r)$, b) – · – · – force $F(r) = \text{grad } W(r)$, c) – – – – fracture de la chaîne par tension

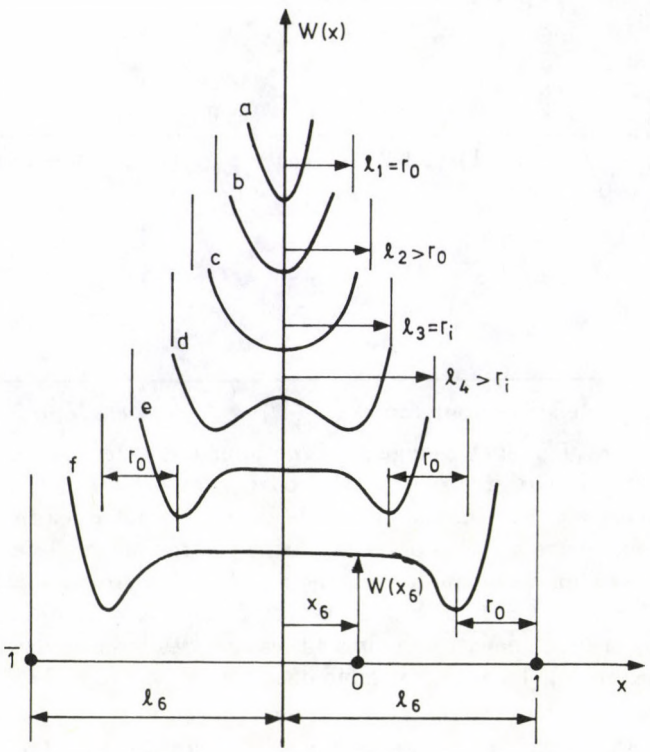

Courbe 2. L'énergie $W(x)$ pour diverses valeurs de l (avec deux minimums si $l > r_i$)

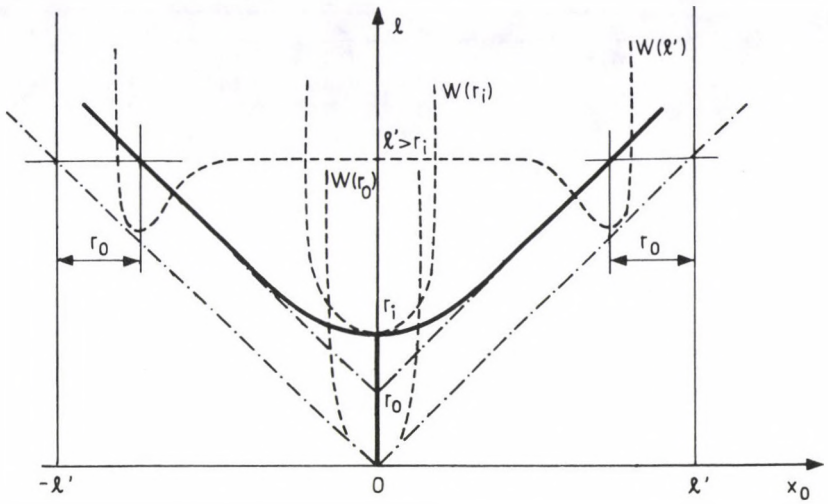

Courbe 3. Représentation de l en fonction de x_0

Représentons l en fonction de x_0 (courbe 3):

- Si $l < r_i$, toutes les courbes $W(x)$ out leur minimum pour $x_0 = 0$ sur un segment vertical. L'ordonnée du minimum est égale à l'abscisse des asymptotes des courbes 2.
- Si $l = r_i$, le point $x_0 = 0$ et $l = r_i$ correspond à la racine double.
- Enfin si $l > r_i$, on a deux minimums d'écartement croissant sur une hyperbole rectangulaire.

Vibrations atomiques à T K

En conséquence, à T K, lorsque l'amplitude moyenne des vibrations atomiques atteint et excède la valeur maximale $\overline{e}_M = r_i - r_0$, les atomes vibrent loin de leur position d'équilibre et le réseau est instable. Des ondes longitudinales de longueur d'onde kl (k entier), avec des points d'instabilité à $kl/2$, se propagent le long de la chaîne. Si on pose $r_i = r_0(1+\alpha)$, on a $\alpha = \frac{\overline{e}_M}{r_0} = \frac{r_i - r_0}{r_0}$, la dilatation maximale avant la fusion. Avec

$$A = \left(\frac{n+1}{m+1}\right)^{1/n-m} = \left(\frac{x}{y}\right)^{1/x-y},$$

$$\ln A = \frac{1}{y-x}\ln\frac{y}{x} = \frac{2}{y-x}\ln\left[1 - \frac{\sqrt{x}-\sqrt{y}}{\sqrt{x}}\right]$$

Tableau I
Valeurs de $\alpha = \frac{r_i - r_0}{r_0}$

m:	2	3	4	5	6
n : 6	0,18	0,16	0,16	0,15	0,14
7	0,16	0,15	0,15	0,14	0,13
8	0,15	0,14	0,14	0,13	0,12
9	0,14	0,13	0,13	0,12	0,11
10	0,13	0,12	0,12	0,11	0,11
11	0,12	0,11	0,11	0,11	0,10
12	0,11	0,11	0,11	0,10	0,10

où $0 < \frac{\sqrt{x}-\sqrt{y}}{\sqrt{x}} < 1$ car $n < m$. En développant:

$$\ln A = \frac{2}{(\sqrt{x}+\sqrt{y})\sqrt{x}} + \frac{\sqrt{x}-\sqrt{y}}{(\sqrt{x}+\sqrt{y})x} + \cdots \geq \frac{2}{x+\sqrt{xy}}$$

d'où l'approximation:

$$\ln A \simeq \frac{2}{x+y} = \ln\left(1+\frac{2}{m+n+2}\right) \text{ soit } r_i \simeq r_0 \frac{m+n+4}{m+n+2} \text{ et } \alpha = \frac{2}{m+n+2}.$$

Pour les valeurs de m et n généralement admises, la fraction de r_0 au delà de laquelle il y a perte de la stabilité reste relativement constante (tableau I).

Pour la plupart des solides, près du point de fusion, l'amplitude moyenne maximale des vibrations des atomes est comprise entre 10 et 15 % de la distance interatomique d'équilibre. Des estimations voisines ont été avancées par divers auteurs [3]. Ceci est en accord avec les résultats trouvés par des méthodes différentes [4] et avec ceux de Lindemann [1]: $\overline{e^2} = 4,364 \cdot 10^{-14} \frac{T}{T_f} L l^2$ cm^2 donnant l'équation réduite $\frac{\overline{e^2}}{e_M^2} = \frac{T}{T_f}$ et $\alpha = \frac{\overline{e_M}}{r_0} \simeq 0,11$. Nous savons aussi [5] que: $\overline{e^2} \simeq \frac{3r_0^2}{8\pi^2\gamma\Lambda}(0,06)$ d'où $\alpha \simeq 0,12$. L'amplitude des vibrations devient une fonction linéaire (comme les autres propriétés thermiques) de la température réduite $\frac{T}{T_f}$ pour chaque type de structure.

L'énergie potentielle de l'atome central, déplacé de x de sa position moyenne d'équilibre par agitation thermique, est d'après l'équation (1) si $x \ll l$:

$$W(x) \simeq \frac{2W_0}{n-m}\left[\frac{-nr_0^m}{l^m} + \frac{mr_0^n}{l^n}\right] + \frac{W_0 mn}{nm}\left[-\frac{(m+1)r_0^m}{l^m} + \frac{(n+1)r_0^n}{l^n}\right]\frac{x^2}{l^2}.$$

Le premier terme est l'énergie nécessaire pour atteindre la position d'équilibre. Le second est l'énergie nécessaire à la vibration d'amplitude x. La force $F(x)$, rappelant vers sa position d'équilibre l'atome central de l'arrangement vibrant comme un oscillateur harmonique, est:

$$F(x) = \frac{dW(x)}{dx} = \frac{2W_0 mn}{n-m}\left[-\frac{(m+1)r_0^m}{l^m} + \frac{(n+1)r_0^n}{l^n}\right]\frac{x}{l^2} = -K_0 x$$

où K_0 est la constante de rappel sous l'action des plus proches voisins si $l \simeq r_0$.

References

1. F. A. Lindemann, Phys. Z., *11*, 609, 1910.
2. J. D. Dheer, B. Sharan, Proc. Phys. Soc., *91*, 225, 1967.
3. P. Debye, Verh. Dtsh. Phys. Ges., *15*, 678, 738, 8517, 1913.
   I. Waller, Z. Physik, *17*, 398, 1923.
   Kathleen Londsale, Z. Kristallographie, *112*, 188, 1959.
4. J. K. Roberts, Heat and Thermodynamics, London, Blackie, 1951;
   Ja. M. van Liempt, Rec. Trav. Chim., *51*, 114, 1932.
5. Y. Thomas et G. Goureaux, C.R. Acad. Sc. Paris, *268*, 1518, 1969.

Acta Physica Hungarica 71 (3-4), pp. 233-238 (1992)

DYNAMICS OF A BINARY METALLIC GLASS $Cu_{57}Zr_{43}$

P. C. AGARWAL, K. A. AZEZ* and C. M. KACHHAVA

Department of Physics, University of Rajasthan
Jaipur-302004, India
**Physics Department, Jordan University of Science and Technology*
Irbid, Jordan

(Received in revised form 3 March 1992)

Computations of the frequencies of the longitudinal and transverse phonon modes in a binary metallic glass ($Cu_{57}Zr_{43}$) based on a simple model approach have been presented. The model assumes a central force effective between nearest neighbours, and a volume dependent force. Both types of excitations of phonons are computed for the self-consistent screening and are compared to those computed by Kobayashi and Takeuchi using recursion method.

1. Introduction

Metallic glasses are such solids whose electronic properties are normally associated to metals but their atomic arrangements are not spatially periodic. Amorphous and non-crystalline are equivalent terms used to describe the atomic scale structure of such materials. In recent years the experimental studies [1] of metallic glasses have demonstrated their special characteristics which made the researches on the subject more interesting and meaningful. Metallic glasses have notable applications [1, 2] in memory devices used in computers, in remote sensing devices and in high critical magnetic field materials as superconductors.

The understanding of the vibrational dynamics is a prerequisite to any understanding of thermodynamic and transport properties of solids. In our present work we would like to study one of the dynamical properties — dispersion relation. There are two main theoretical approaches to derive phonon frequencies of metallic glasses: one is to choose a suitable interatomic pseudopotential as was done by Saxena et al [3, 4] for $Ca_{70}Mg_{30}$ and $Mg_{70}Zn_{30}$ glasses, respectively. In this approach the quasicrystalline approximation developed by Takeno and Goda [5] was used. A second way of calculating phonon frequencies consists in the evaluation of force constants β, δ and k_e as was done by Bhatia and Singh [6] for $Ca_{70}Mg_{30}$ and by Agarwal and Kachhava [7] for $Mg_{70}Zn_{30}$ glass using a simple model given by Bhatia [8]. In the present work we would like to follow Bhatia and Singh in adopting a simple model which assumes a central force, effective between the nearest neighbours and a volume dependent force due to conduction electrons. The model is applied for the calculation of dispersion curves of a binary glass, i.e. $Cu_{57}Zr_{43}$, for the first time both for longitudinal and transverse phonons. The results computed in the present calculation are compared to those by Kobayashi and Takeuchi [9] using a recursion method.

2. Theory

The longitudinal and transverse phonon frequencies are respectively given by [6]

$$\omega_L^2 = \frac{2N}{\varrho a^2}[\beta I_0 + \delta I_2] + \frac{k_e^2 K_{TF}^2 q^2 [G(qr_s)]^2}{\varrho[q^2 + K_{TF}^2 \epsilon(q)]} \tag{1}$$

and

$$\omega_T^2 = \frac{2N}{\varrho a^2}\left[(\beta + \frac{1}{2}\delta)I_0 - \frac{1}{2}\delta I_2\right], \tag{2}$$

where N is the coordination number, a is the nearest neighbour distance, $\varrho = n_i M$ is the mean atomic density in which n_i is the ion density and

$$M = 0.57 \times \text{ atomic mass of Cu} + 0.43 \times \text{ atomic mass of Zr} \tag{3}$$

is the mean atomic mass. β, δ and k_e are force constants. β and δ are defined in terms of derivatives of interatomic potential $W(r)$, as

$$\beta = \frac{\varrho a^2}{2M}\left[\frac{1}{r}\frac{dW(r)}{dr}\right]_{r=a}, \tag{4}$$

$$\delta = \frac{\varrho a^3}{2M}\left[\frac{d}{dr}\left[\frac{1}{r}\frac{dW(r)}{dr}\right]\right]_{r=a}. \tag{5}$$

The conduction electron screening to interatomic potential is represented by the Thomas–Fermi screening length defined in terms of charge e and mass m of electrons as

$$K_{TF}^2 = \left(\frac{4me^2}{\hbar^2}\right)\left(\frac{3n_e}{\pi}\right)^{1/3}. \tag{6}$$

Then the relevant force constant k_e due to the conduction electrons on the basis of the Thomas–Fermi model can be derived [6] as

$$k_e = \frac{4\pi n_e n_i z e^2}{K_{TF}^2}, \tag{7}$$

where n_e is the number density so that $n_e = n_i z$ and z is the mean valence of the glassy system. In Eq. (1), $\epsilon(q)$ is the self-consistent dielectric screening function [10]

$$\epsilon(q) = \frac{1}{2}\left[1 + \frac{k_F}{q}\left[1 - \frac{q^2}{4k_F^2}\right]\ln\left|\frac{q + 2k_F}{q - 2k_F}\right|\right], \tag{8}$$

where $k_F = (3\pi^2 n_e)^{1/3}$ is the Fermi wave number.

To incorporate the correlation effects in $\epsilon(q)$, Eq. (8) is modified to the form

$$\epsilon(q) = \frac{1}{2}\left[1 + \frac{k_F}{q}\left[1 - \frac{q^2}{4k_F^2}\right]\ln\left|\frac{q + 2k_F}{q - 2k_F}\right|\right][1 - f(q)], \tag{9}$$

where $f(q)$ is given by the Hubbard function [11]

$$f(q) = \frac{1}{2}q^2/(q^2 + k_F^2 + \frac{1}{2}K_{TF}^2). \tag{10}$$

The cancellation effects of kinetic and potential energies inside the core of ions making the effective potential weak in core gives a shape factor, $[G(qr_s)]^2$, to be multiplied with the electronic term in Eq. (1), and is therefore of the form [12]

$$[G(qr_s)]^2 = \left[\frac{3[\sin(qr_s) - (qr_s)\cos(qr_s)]}{(qr_s)^3}\right]^2, \tag{11}$$

where $r_s = \left[\frac{3}{(4\pi n_i)}\right]^{1/3}$, is the radius of the Wigner–Seitz sphere.

In Eqs (1) and (2)

$$I_n = \int_0^{\pi} \sin\Theta \cos^n\Theta \left[\sin^2\left(\frac{1}{2}qa\cos\Theta\right)\right] d\Theta, \tag{12}$$

so that with $x \equiv qa$, I_0 and I_2 are, respectively,

$$I_0(x) = 1 - \frac{\sin x}{x}, \tag{13}$$

$$I_2(x) = \frac{1}{3} - \sin x\left[\frac{1}{x} - \frac{2}{x^3}\right] - \frac{2\cos x}{x^2}. \tag{14}$$

For the limiting case $q \to 0$, i.e. $x \to 0$; $I_0 \approx x^2/6$ and $I_2 \approx x^2/10$; on substituting these in Eqs (1) and (2), we have longitudinal and transverse sound velocities, respectively, as $V_L(0) = \omega_L/q$ and $V_T(0) = \omega_T/q$ in low momentum region ($q \to 0$) as

$$\varrho V_L^2(0) = N\left(\frac{1}{3}\beta + \frac{1}{5}\delta\right) + k_e, \tag{15}$$

$$\varrho V_T^2(0) = N\left(\frac{1}{3}\beta + \frac{1}{15}\delta\right). \tag{16}$$

3. Calculations, results and discussion

The values of $V_L(0)$, $V_T(0)$ and ϱ are taken from Kobayashi et al [9], n_i is calculated from the relation $\varrho = n_i M$, whereas k_e is calculated using Eq. (7) with $z = 2.29$ and is found to be 9.106×10^{10} Nm^{-2}. Finally we take $N = 12$, so that the relation $n_i a^3 = \sqrt{2}$ corresponding to fcc lattice gives $a = 3.13 \times 10^{-10}$ m.

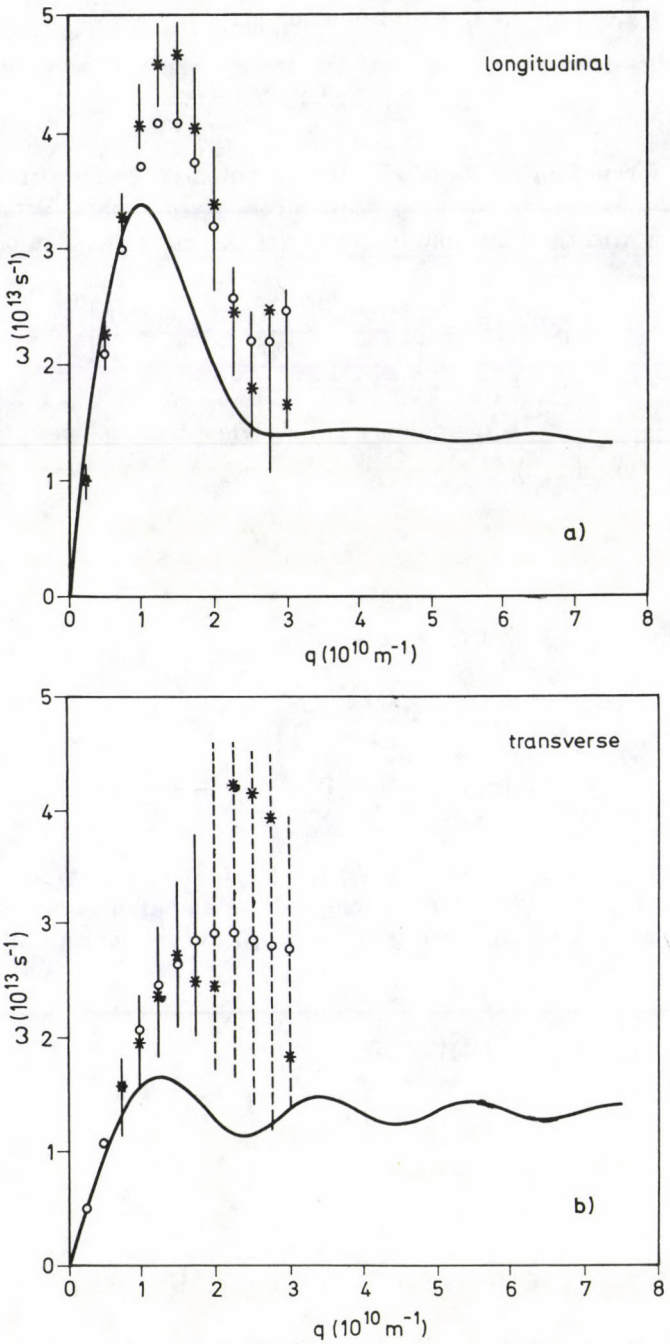

Fig. 1. Dispersion curves for $Cu_{57}Zr_{43}$ glass; a – ω_L (—) on the basis of Eq. (1); b – ω_T (—) on the basis of Eq. (2). Vertical bars denote 90 % width of peak; open circles denote the positions of the first moment; crosses denote the peak positions (ref. [9])

Table I
Parameters used in calculations of phonon dispersion in $Cu_{57}Zr_{43}$ metallic glass

β (10^{10} Nm^{-2})	δ (10^{10} Nm^{-2})	k_e (10^{10} Nm^{-2})	k_F (10^{10} m^{-1})	r_s (10^{-10} m)	K_{TF}^2 (10^{20} m^{-2})
0.891	−1.408	9.106	1.460	1.732	3.514

By substituting the values of ϱ, $V_L(0)$, $V_T(0)$ and k_e in Eqs (15) and (16), β and δ are found. Table I contains the relevant parameters used for obtaining dispersion curves on the basis of Eqs (1) and (2).

Figures 1a and b give dispersion curves for longitudinal and transverse phonons, respectively. The first maximum of the $\omega_L - q$ curve is found at $q = 1.0 \times 10^{10}$ m^{-1}. The first peak of the $\omega_T - q$ curve is obtained at higher q-values than the first peak of the $\omega_L - q$ curve. As expected, both longitudinal and transverse phonons show strictly linear dispersion curves at low momentum transfers.

4. Conclusion

Although the model approach used in the calculations is basically defined for pure metals yet it has been found to a good approximation for metallic glass as well. The basic difference between the two systems is that metal has a long-range order, while the glass has a short-range as is obvious from Eqs (1) and (2), which implies the coordination number. This approach involves the structure relevant to the conditions in which the glasses are formed. This model provides knowledge of how results might depend on the starting structure from which the glass is made.

Since the experimental data for phonon dispersion of the system are not available, the results might be used for correlating other properties of the metallic glass. The results presented are compared with those given by Kobayashi et al [9] and are found to be in good qualitative agreement at low q as shown in Fig 1a and b. The deviations at higher momentum transfers might point to the fact that the coupling of β and δ to sound velocities provides a rather coarse evaluation of these parameters. A more realistic calculation would certainly require the knowledge of a detailed form for the interatomic potentials in the metallic glass. Such efforts are made in our research group, and the results are expected to be obtained in the near future.

Acknowledgements

We are thankful to Prof. R. N. Singh (Bhagalpur University, Bihar) for his valuable suggestions. One of us (P. C. Agarwal) acknowledges with pleasure the senior research fellowship (NET) offered to him by CSIR, New Delhi.

References

1. A. Hernando, M. Vázquez and J. M. Barandiarán, J. Phys. E: Sci. Instrum., *21*, 1129, 1988.
2. T. R. Anantharaman, Metallic Glasses: Production, Properties and Applications, Trans Tech Publications, Switzerland, 1984.
3. N. S. Saxena, Meeta Rani, Arun Pratap, Prabhu Ram and M. P. Saksena, Phys. Rev., *B38*, 8093, 1988.
4. N. S. Saxena, Deepika Bhandari, Arun Pratap and M. P. Saksena, J. Phys.: Condens. Matter, *2*, 9475, 1990.
5. S. Takeno and M. Goda, Prog. Theor. Phys., *45*, 331, 1971.
6. A. B. Bhatia and R. N. Singh, Phys. Rev., *B31*, 4751, 1985.
7. P. C. Agarwal and C. M. Kachhava, Physica *B*, (accepted).
8. A. B. Bhatia, Phys. Rev., *97*, 363, 1955.
9. S. Kobayashi and S. Takeuchi, J. Phys., *C13*, L969, 1980.
10. J. Lindhard, Kgl. Danske Videnskab. Selskab., Mat. Fys. Medd., *28*, 8, 1954.
11. J. Hubbard, Proc. R. Soc. London, Ser. *A243*, 336, 1958.
12. L. J. Sham and J. M. Ziman, Solid State Physics, ed. F. Seitz and D. Turnbull, Academic Press, New York, *15*, 259, 1963.

Acta Physica Hungarica 71 (3-4), pp. 239-267 (1992)

SURVEY ARTICLE

STRUCTURE OF ODD–ODD Sb NUCLEI

T. FÉNYES, ZS. DOMBRÁDI, Z. GÁCSI and J. GULYÁS

Institute of Nuclear Research of the Hungarian Academy of Sciences (ATOMKI)
4001 Debrecen, Hungary

(Received 3 March 1992)

The structure of ^{112,114,116,118}Sb nuclei was studied with complex γ and electron spectroscopic methods via $(p,n\gamma)$ and also $(\alpha,n\gamma)$ reactions (in the case of ^{116}Sb, ^{118}Sb) at 5.5–9.2 MeV proton and 14.5–16.0 MeV α-particle energies. New level schemes have been deduced. The energy splitting of the proton–neutron multiplet states of ^{116,118,120,122,124}Sb was calculated on the basis of the "parabolic rule". Many $p-n$ multiplet states have been identified and conclusions have been drawn on the applicability of the parabolic rule as a simple guideline for experimental investigations.

Detailed description of the energy spectra and electromagnetic properties of ^{116,118,120,122,124}Sb nuclei is given on the basis of the *i*nteracting *b*oson-*f*ermion-*f*ermion/odd-odd truncated *q*uadrupole phonon *m*odel (IBFFM/OTQM). The calculations give account both of the "regular" and "irregular" behaviour of the energy splitting of the $p-n$ multiplets, as well as of the electromagnetic moments, γ-branching and γ-mixing ratios. Conclusions have been drawn on the role of different interactions in the multiplet energy splitting.

The IBFFM interpretation of the high-spin intruder bands and the spectroscopic factors of the neutron transfer reactions are also shortly discussed for Sb nuclei.

1. Introduction. Experimental methods and results

The 103-cm isochronous cyclotron of Hungary was put into operation in 1985–86. In the first nuclear spectroscopic program, based on this accelerator, we have systematically studied the structure of odd–odd $^{104-116}$In and $^{112-124}$Sb nuclei (Fig. 1).

The method of experimental work was in-beam spectroscopy, more exactly: study of $(p,n\gamma)$ and $(\alpha,n\gamma)$ reactions with complex γ- and e^--spectroscopic methods. The targets were prepared form isotopically enriched Ag, Cd, In and Sn isotopes.

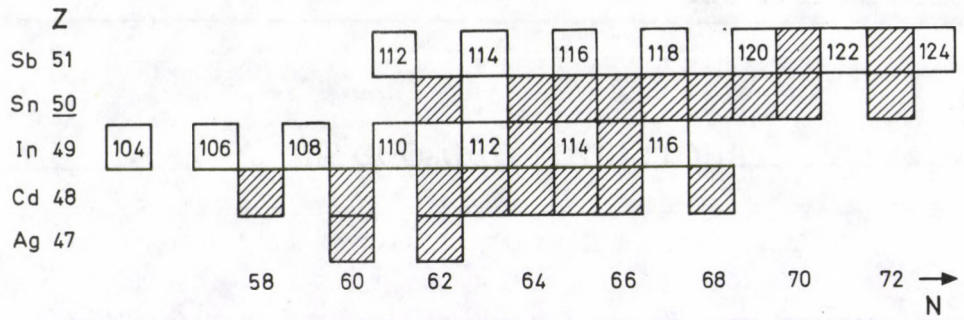

Fig. 1. **Part of the chart of nuclides. Z: atomic number, N: neutron number, shaded areas show stable isotopes. Nuclei, investigated in this program, are marked with mass numbers**

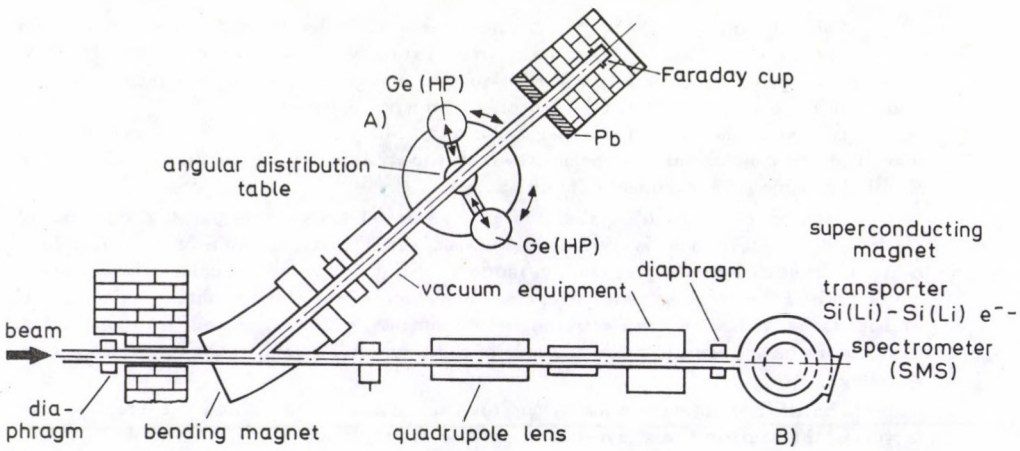

Fig. 2. **Layout of the γ- (A) and electron-spectroscopic (B) beam channels of the Debrecen 103-cm isochronous cyclotron**

The nuclear spectroscopic channels of the Debrecen cyclotron are shown in Fig. 2. On the $\gamma(-e^-)$-spectroscopic channel (A) a turning "angular distribution" table was installed for supporting various semiconductor detectors. Replaceable reaction chambers and high resolution Ge (HP and LEPS) γ spectrometers provided possibility for single γ-spectrum, γ-ray angular distribution, $\gamma\gamma$- (and other) coincidence, as well as lifetime measurements. For conversion electron studies a miniorange Si(Li) spectrometer [1] was used in a special chamber.

On the electron spectroscopic channel (B in Fig. 2) a superconducting magnet transporter Si(Li)–Si(Li) spectrometer (SMS) was installed, which was operated mainly in swept current lens spectrometer (SMLS) mode. This spectrometer, developed in ATOMKI, provides unique possibility for in-beam electron spectroscopic studies (high transmission, good energy resolution, low background, etc.). A detailed description of the spectrometer is given in [2], the schematic drawing of SMLS is shown in Fig. 3.

In order to obtain "complete" spectroscopic information on odd–odd indium and antimony nuclei, γ-ray (E_γ, I_γ), $\gamma\gamma$-coincidence and internal conversion electron spectra, as well as γ-ray angular distributions, lifetimes of excited levels (by means of Doppler-shift and delayed coincidence methods) and relative reaction cross sections $[\sigma_{\mathrm{rel}}(E_{\mathrm{LEV}})]$ were measured at different bombarding particle energies. Level schemes, level energies (E_{LEV}), spins, parities, γ-branching and γ-mixing ratios have been deduced.

Great attention was paid to the reliability and consistency of the obtained data. For example the level spins have been determined with three different methods: a) from Hauser–Feshbach analysis of the (p, n) reaction cross sections, b) from internal conversion coefficients of transitions and c) from γ-ray angular distributions.

As a result of experimental work more than 1200 (among them $\sim$ 700 new) γ-rays have been identified, $\sim$ 350 (among them $\sim$ 320 new) α_k internal conversion coefficients have been determined, and about 460 (among them $\sim$ 250 new) levels have been deduced for ^{112,114,116,118}Sb and ^{106,108,110,112,114}In nuclei.

The theoretical interpretation of the experimental results was performed on the basis of "parabolic rule" and interacting boson–fermion–fermion model calculations.

The experimental and theoretical results have been published in the following papers: ^{116}In [3], ^{114}In [4, 5], ^{112}In [6], ^{110}In [7, 8], ^{108}In [9], ^{106}In [10], ^{104}In [11], ^{120}Sb [12], ^{118}Sb [13, 14], ^{116}Sb [15, 16], ^{114}Sb [17] and ^{112}Sb [18]. The results obtained on odd–odd In nuclei are summarized in [19]. In this paper we overview the results of the antimony program.

2. Proton–neutron multiplet states and the parabolic rule

In zeroth order approximation the level energies of odd–odd nuclei can be obtained by addition of energies of the odd proton and odd neutron states. In higher order approximation the proton–neutron residual interaction must be taken into account, too. If we consider the residual interaction as a consequence of quadrupole and dipole (spin-vibrational) phonon exchange between proton and neutron through the nuclear core, a "parabolic rule" can be deduced from the cluster vibration model (Paar [20]). In the present work the applicability of the parabolic rule is studied in the case of ^{116,118,120,122,124}Sb nuclei.

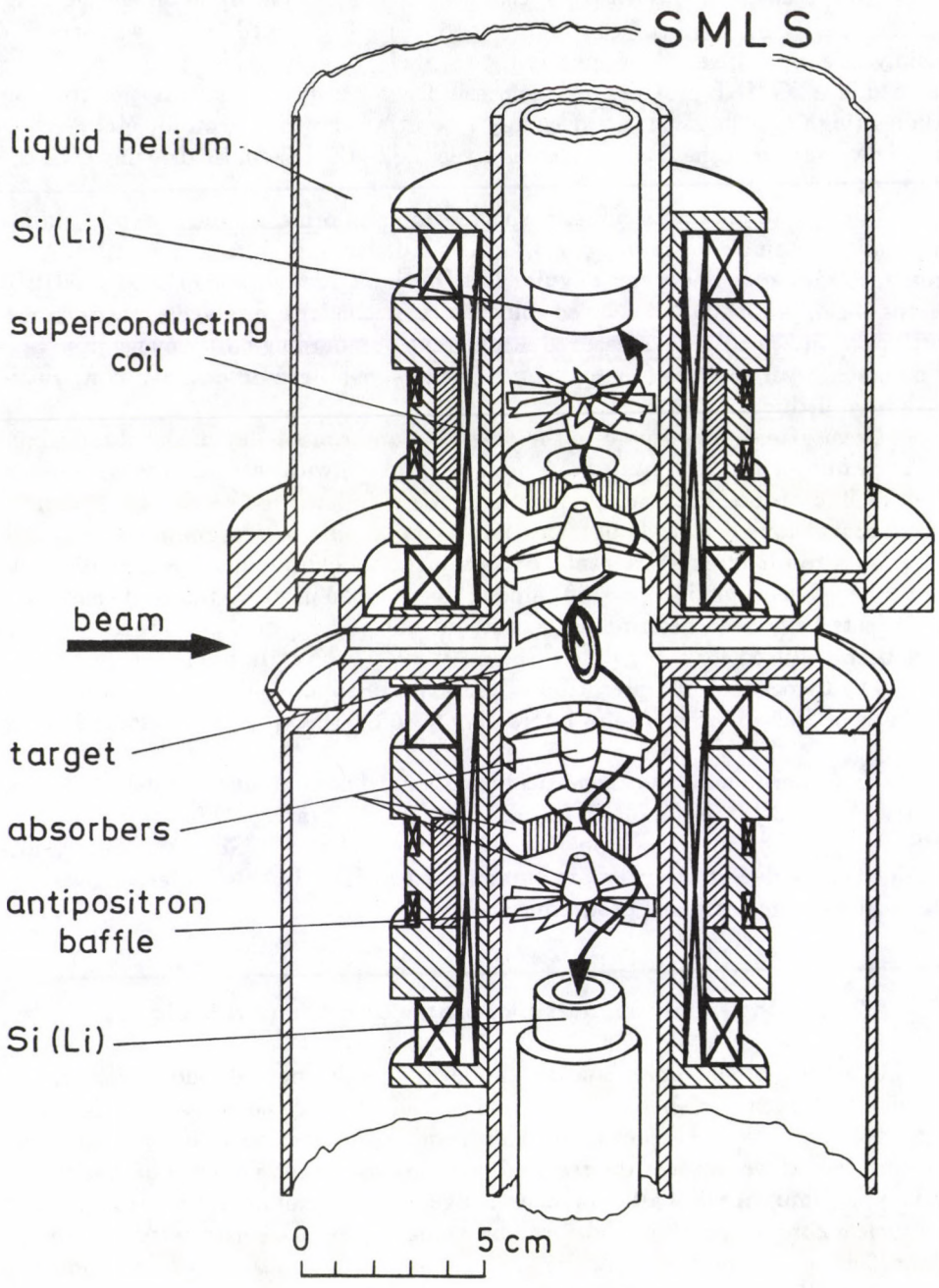

Fig. 3. Schematic drawing of the superconducting magnetic lens electron spectrometer (SMLS), developed in ATOMKI [2]

2.1. Basic formulas

The energy levels of the proton–proton multiplet states can be described in leading order approximation by the following formulas [20], assuming quadrupole–quadrupole and spin–spin residual interactions

$$E(I) = E_{j_p} + E_{j_n} + \Delta E_2 + \Delta E_1, \tag{1}$$

where $E(I)$ is the energy of the level, E_{j_p} and E_{j_n} denote the proton and quasineutron energies, respectively,

$$\Delta E_2 = -\alpha_2 \mathcal{V} \cdot \left\{ \frac{[I(I+1) - j_p(j_p+1) - j_n(j_n+1)]^2 + I(I+1) - j_p(j_p+1) - j_n(j_n+1)}{2j_p(2j_p+2)2j_n(2j_n+2)} - \frac{1}{12} \right\}, \tag{2}$$

$$\Delta E_1 = -\alpha_1 \xi \frac{I(I+1) - j_p(j_p+1) - j_n(j_n+1)}{(2j_p+2)(2j_n+2)}. \tag{3}$$

Here $I = |j_p - j_n|, \ldots j_p + j_n$, where j is the total angular momentum of the quasiparticle, ΔE_2 and ΔE_1 describe the energy splitting of the proton–neutron multiplet as a consequence of the quadrupole and dipole interactions between proton and quasineutron through the nuclear core. α_2 and α_1 are the quadrupole and dipole interaction strengths, respectively. The definitions of $\mathcal{V}$ and ξ coefficients are given in [20].

The dependence of the coupling strengths on the occupation probability of levels may be described by the following approximate formulas

$$\alpha_2(j_p, j_n) = \alpha_2^{(0)} |(U_{j_p}^2 - V_{j_p}^2)(U_{j_n}^2 - V_{j_n}^2)|, \tag{4}$$

$$\alpha_1(j_p, j_n) = \alpha_1^{(0)}, \tag{5}$$

where V_j^2 is the occupation probability of level j and $U_j^2 = 1 - V_j^2$.

2.2. Parameters

The (quasi)particle energies can be taken from the experimental data of the neighbouring single–odd nuclei. Nevertheless, in practice, a separate energy normalization was necessary at each $p - n$ multiplet on the basis of one (or more) reliably identified state(s) of the odd–odd nucleus. Thus, the parabolic rule is effective mainly for the description of the relative energy splitting of the different members of the same $p - n$ multiplet.

The $\alpha_1^{(0)}$, $\alpha_2^{(0)}$ and V^2 parameters used in the calculations are summarized in Table I.

Table I
Parameters of the parabolic rule calculations

Isotope	$\alpha_1^{(0)}$ MeV	$\alpha_2^{(0)}$, MeV		V^2			
		fitted to exp. data	from natural parametrization	$\nu d5/2$	$\nu g7/2$	$\nu d3/2$	$\nu h11/2$
^{116}Sb	0.13	5.4	^{114}Sn : 4.1 ^{116}Sn : 3.8 ^{120}Te : 19.7	0.88	0.72	0.20	0.21
^{118}Sb	0.13	4.4	^{116}Sn : 3.8 ^{118}Sn : 4.2 ^{120}Te : 19.7	0.88	0.85	0.30	0.23
^{120}Sb	0.12	6	^{118}Sn : 4.2 ^{120}Sn : 4.1 ^{120}Te : 19.7			0.33	0.23
^{122}Sb	0.12	6	^{120}Sn : 4.1 ^{122}Sn : 4.7 ^{122}Te : 22.7			0.33	0.41
^{124}Sb	0.12						

Explanation of the symbols see in the text (Section 2.2)

The $\alpha_1^{(0)}$ values were calculated from the expression $\alpha_1^{(0)} = \alpha_1 \approx 15/A$ MeV, where A is the mass number.

$\alpha_2^{(0)}$ may be estimated from the data of the neighbouring even–even nuclei, on the basis of the formula $\alpha_2^{(0)} = 382\beta_2^2/\hbar\omega_2$ MeV (natural parametrization), where $\hbar\omega_2$ is the energy of the first 2^+ state $[E(2_1^+)]$ in MeV and β_2 is the quadrupole deformation parameter. The $E(2_1^+)$ and β_2 data were taken from [21]. In practice, the phenomenological $\alpha_2^{(0)}$ values, obtained from fitting the parabola to experimental data, gave better results.

The proton (above the $Z = 50$ core in $_{51}$Sb) has been considered as a particle, the neutrons as quasiparticles. The occupation probabilities of the quasiparticle states were taken from the systematics of the experimental data (from about 30 publications, citations in [6]).

2.3. Results

The experimental and theoretical level schemes of ^{116,118,120,122}Sb are shown in Figs 4–7, respectively.

In columns a) the low-lying levels of the neighbouring single–odd nuclei are given, as well as the main components of the wave functions of the states. The configurations were deduced mainly from one-nucleon transfer reactions.

Columns b) and c) show the results of the parabolic rule calculations.

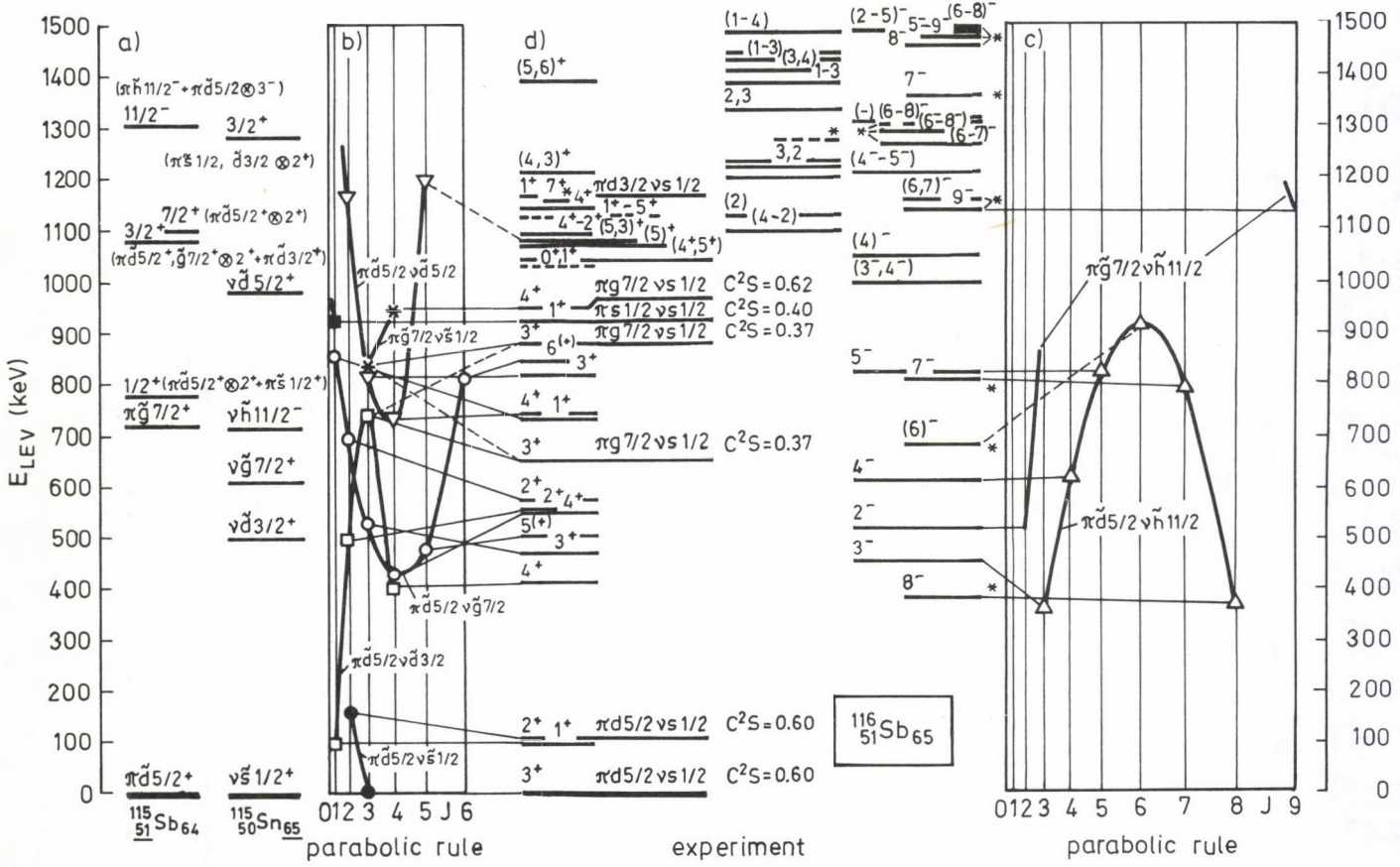

Fig. 4. Level scheme and $p - n$ multiplet states of ^{116}Sb. a) Experimental level energies (E_{LEV}) and main configurations of the low-lying states of ^{115}Sb and ^{115}Sn. b) and c) Results of the parabolic rule calculations, separately for positive and negative parity levels. The abscissa is scaled according to $J(J+1)$, where J is the spin of the state. d) Experimental results on ^{116}Sb [15]

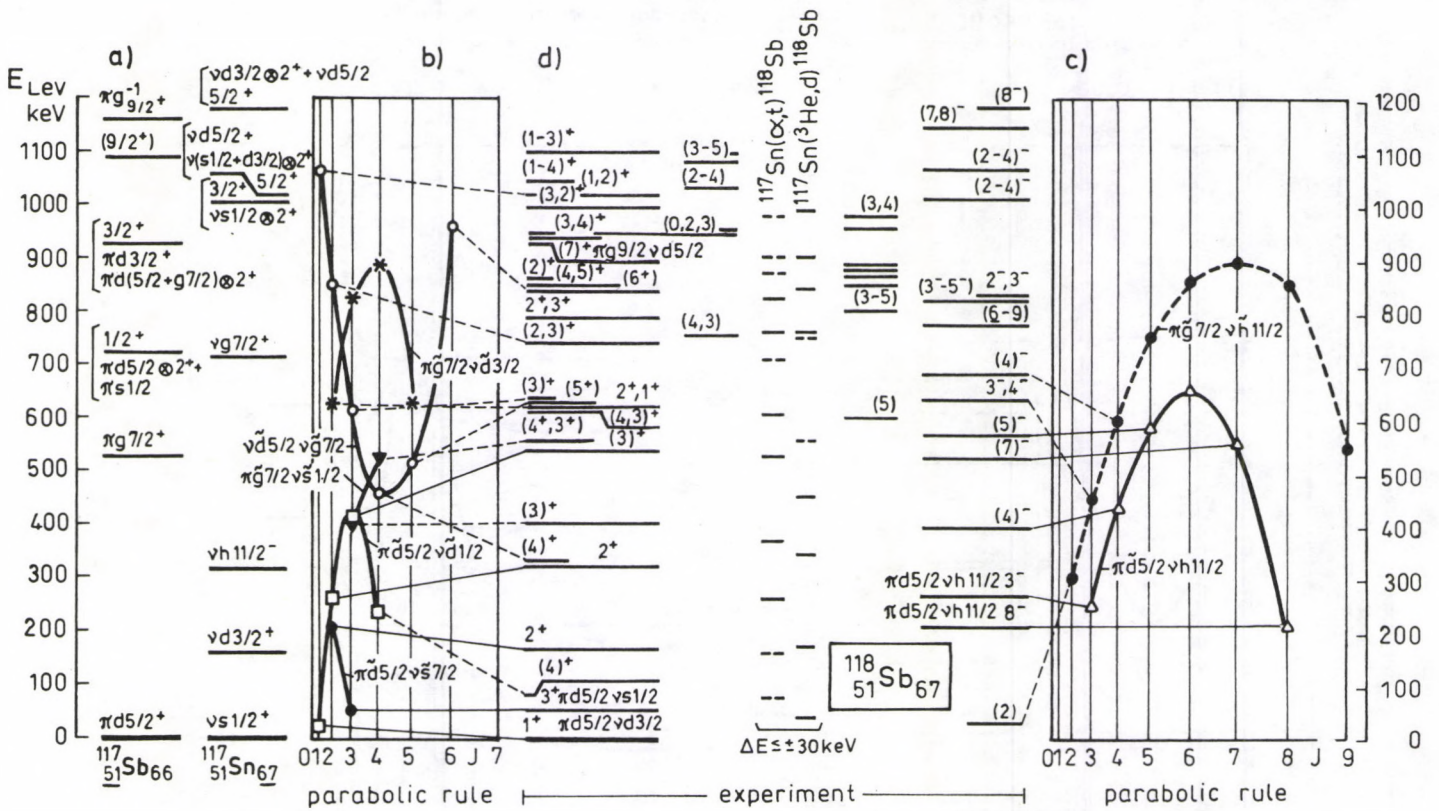

Fig. 5. Level scheme and $p-n$ multiplet states of ^{118}Sb [13]. Further explanations see under Fig. 4 and in text

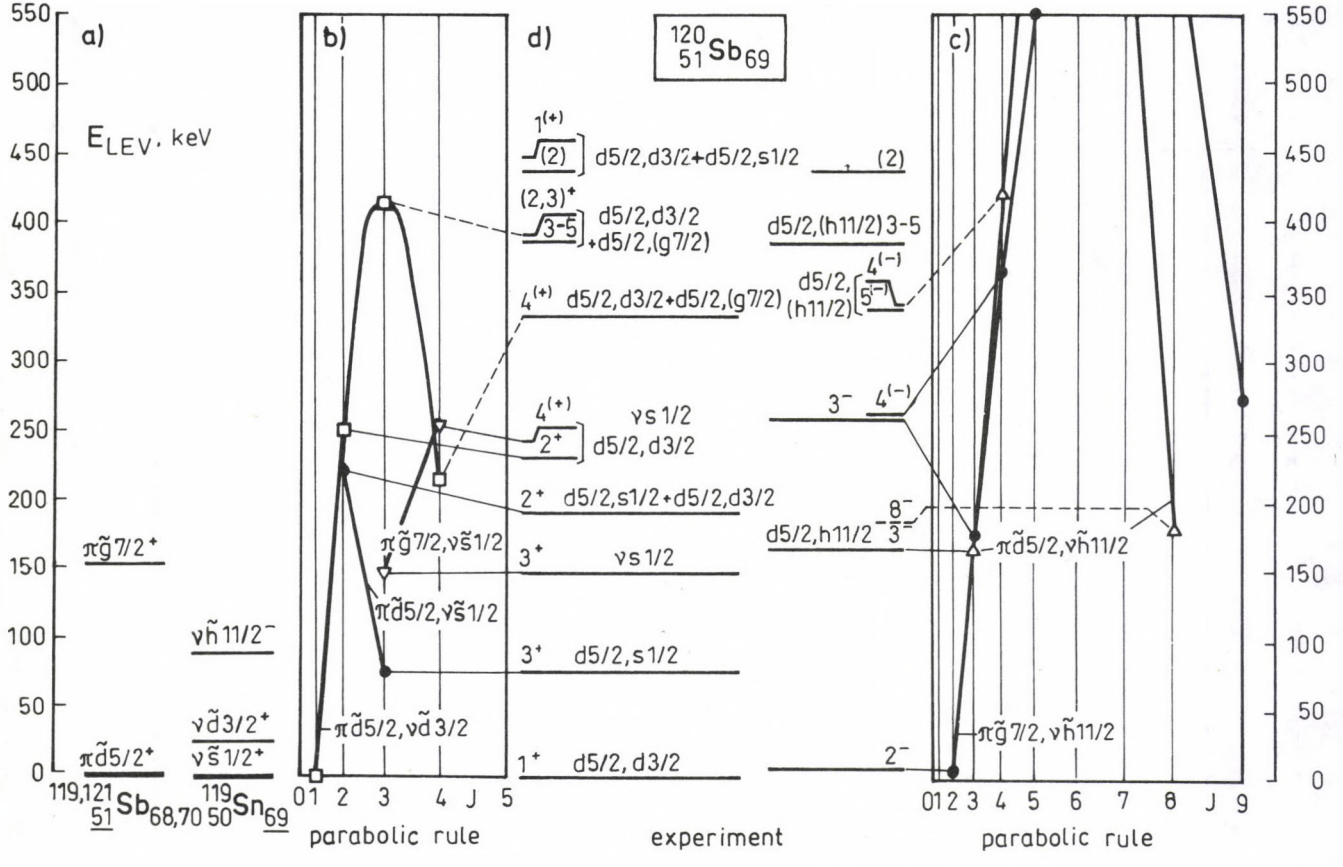

Fig. 6. Level scheme and $p-n$ multiplet states of ^{120}Sb. The experimental data, relating to ^{120}Sb, were taken from [22, 23]. Further explanations see under Fig. 4 and in text

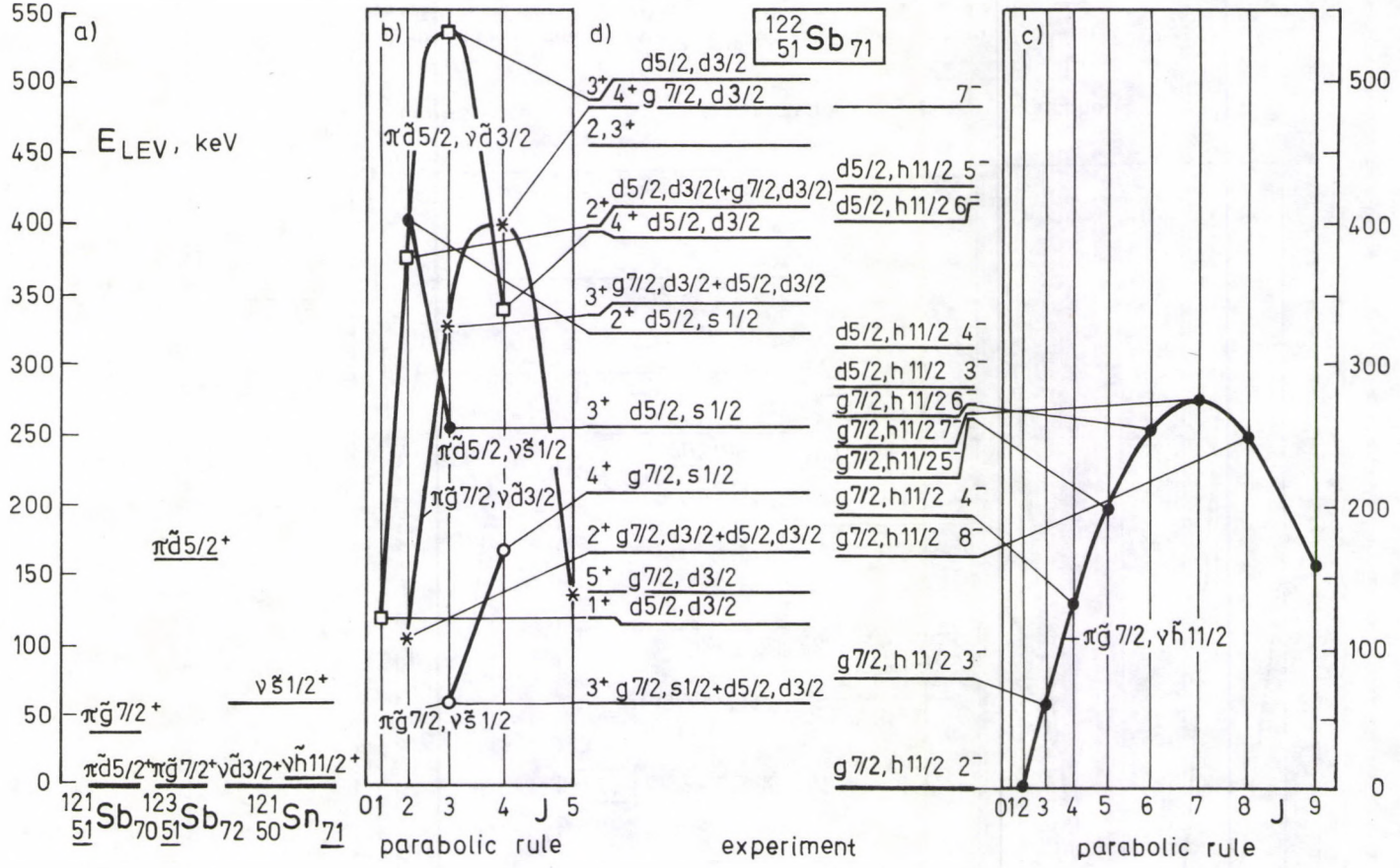

Fig. 7. **Level scheme and $p-n$ multiplet states of ^{122}Sb. The ^{122}Sb experimental data were taken from [23–25]. Further explanations see under Fig. 4 and in text**

In columns d) the experimental level schemes are given as well as the main components of the wave functions obtained from all available experimental results (spectroscopic factors of one-nucleon transfer reactions, magnetic dipole and electric quadrupole moments, log ft values of β-decay, etc.).

The members of proton–neutron multiplets have been identified on the basis of experimental level energies, spins, parities, electromagnetic moments, l_p, l_n values of one-nucleon transfer reactions and electromagnetic decay properties of levels (multipolarities of transitions and reduced γ-branching ratios). It is known that between neighbouring $J \rightarrow J \pm 1$ states of the same $p-n$ multiplet one can expect strong M1 transitions.

In the case of the $\pi g7/2 \nu \tilde{s}1/2$ and $\pi d5/2 \nu \tilde{s}1/2$ doublets of ^{124}Sb the "parabolic rule" gives data, which are very similar to IBFFM results (see later in Fig. 14). Both theoretical results are in good agreement with experimental data. At the same time the experimental energy splitting of the $\pi g7/2 \nu \tilde{d}3/2$, $\pi d5/2 \nu \tilde{h}11/2$ and $\pi g7/2 \nu \tilde{h}11/2$ multiplets clearly deviates from the simple parabolic shape.

2.4. Conclusions

About 70 $p-n$ multiplet states have been identified in ^{116,118,120,122,124}Sb*. In all cases the calculations correctly reproduced the type of parabola (i.e. open up or down). The minimum energy members of the multiplets were also correctly reproduced almost in all cases (in 22 cases from the 24 total). Even in the remaining two cases the predicted minimum energy member of the $p-n$ multiplet was close to the experimental one.

Using $\alpha_1^{(0)} \approx 15/A$ and $4.4 \lesssim \alpha_2^{(0)} \lesssim 6$ interaction strengths for all multiplets, the energy splitting of about 70 multiplet states could be described within ~ 70 keV rms deviation. The $\alpha_2^{(0)}$ parameters, obtained by fitting to measured data, were not far from the "natural parametrization" values (Table I).

All these results, obtained on odd–odd $^{116-124}$Sb nuclei, show that the parabolic rule can be applied as a simple guideline for the experimental investigations. At the same time the energy splitting of some multiplets clearly deviates from the parabolic shape, e.g. the $\pi g7/2 \nu d3/2$ multiplet in ^{124}Sb and $\pi d5/2 \nu h11/2$, $\pi g7/2 \nu h11/2$ multiplets in ^{122,124}Sb (see later in Fig. 15). In these cases the $V^2(\nu d3/2)$ and $V^2(\nu h11/2)$ occupation probabilities are close to 0.5, and the effective α_2 values, which determine the strength of the parabolic splitting, are small [formula (4)]. If the effect of dynamical particle–core interaction is weak, other (for example exchange) interactions may play an important role in the energy splitting (see later in Section 3.3).

We remark that $\alpha_1^{(0)}/\alpha_2^{(0)}$ was less than 0.03 for the identified $p-n$ multiplets of ^{116,118,120,122,124}Sb. This indicates that the influence of dipole interaction, compared with the quadrupole one, is weak.

*This number does not include the $\pi g7/2 \nu \tilde{d}3/2$ multiplet of ^{124}Sb and the $\pi d5/2 \nu \tilde{h}11/2$ and $\pi g7/2 \nu \tilde{h}11/2$ multiplets of ^{122,124}Sb.

3. IBFFM/OTQM calculations

In order to get deeper insight into the structure of the low-energy states of odd-odd Sb isotopes, we have calculated the energies and electromagnetic properties of the states on the basis of the interacting boson–fermion–fermion/truncated quadrupole phonon model for odd–odd nuclei (IBFFM/OTQM) [27].

3.1. Hamiltonian

The Hamiltonian of the IBFFM is [27]

$$H_{\mathrm{IBFFM}} = H_{\mathrm{IBFM}}(p) + H_{\mathrm{IBFM}}(n) - H_{\mathrm{IBM}} + H_{pn},$$

where $H_{\mathrm{IBFM}}(p)$ and $H_{\mathrm{IBFM}}(n)$ denote the IBFM Hamiltonians for the neighbouring odd–even nuclei with an odd proton and odd neutron, respectively [28]. H_{IBM} denotes IBM Hamiltonian [29] for the even–even core nucleus.

Depending on whether we use the Schwinger or the Holstein–Primakoff representation of the SU(6) boson Hamiltonian, we can distinguish between the interacting boson–fermion–fermion and odd–odd truncated quadrupole phonon models. The two representations are equivalent on phenomenological level.

The H_{pn} Hamiltonian of the residual proton–neutron interaction has the following form:

$$H_{pn} = V_0 \delta(\mathbf{r}_p - \mathbf{r}_n)(1 + \alpha \sigma_p \cdot \sigma_n) + V_{\sigma\sigma}[\sigma_p \cdot \sigma_n]_0,$$

where V_0 and α are the parameters of the Wigner and Bartlett forces, δ is the Dirac symbol, $\mathbf{r}_p$ and $\mathbf{r}_n$ are the position vectors of the proton and neutron, respectively, σ's are the Pauli spin matrices and $V_{\sigma\sigma}$ is the parameter of the spin–spin interaction.

The IBFFM/OTQM Hamiltonian was diagonalized in the proton–neutron–boson basis: $|(j_p, j_n)I_{pn}, NR;\ J >$, where j_p and j_n stand for the proton and neutron angular moments coupled to I_{pn}, N is the number of bosons, R is their total angular momentum, and J is the spin of the state.

The computer codes IBM/TQM, IBFM/PTQM and IBFFM/OTQM were written by Brant, Paar and Vretenar [30] and adopted for the Debrecen computers by Zs. Dombrádi.

3.2. Parametrization

The parameters used in the calculations are summarized in Table II and Fig. 8.

The d-boson energies of the cores were taken as the energies of the 2_1^+ states of the neighbouring even–even tin isotopes. Since we treated only the low-lying states of nearly spherical nuclei, the maximum number of the d-bosons was restricted to 2. It is known that the restriction of the boson number in the presence of SU(5)

Table II
Parameters of the IBFFM calculation

Parameters		^{116}Sb Set 1	^{116}Sb Set 2	^{118}Sb	^{120}Sb	^{122}Sb	^{124}Sb
d-boson (quadrupole phonon) energies, MeV	$\hbar\omega_2$	1.3		1.29	1.23	1.14	1.13
Single-proton energies, MeV	$\epsilon(\pi d5/2)$	0	0	0	0.01	0.2	0.25
	$\epsilon(\pi g7/2)$	0.85	0.68	0.33	0	0	0
	$\epsilon(\pi s1/2)$	2.65	1.62	1.5	1.2	1.6	2.0
	$\epsilon(\pi d3/2)$	2.0	1.45	1.2	1.2	1.5	1.8
	$\epsilon(\pi h11/2)$			1.38	1.4	1.5	1.6
Quasineutron energies, MeV	$E(\nu d5/2)$	0.80	0.60	1.2	1.4	1.6	1.8
	$E(\nu g7/2)$	0.45	0.25	0.50	0.8	1.1	1.4
	$E(\nu s1/2)$	0	0	0.0	0	0	0.07
	$E(\nu d3/2)$	0.47	0.71	0.44	0.33	0.21	0
	$E(\nu h11/2)$			0.51	0.38	0.21	0.08
Strength parameters of nucleon-core interaction, MeV	Dynamical Γ_0^p	1.0	0.53	0.65	0.65	0.65	0.65
	Exchange: Λ_0^p	0	0	0	0	0	0
	Monopole: A_0^p			0.08	0.1	0.1	0.1
	Γ_0^n	0.7	1.414	0.6	0.6	0.6	0.6
	Λ_0^n	2.3	1.3	1.3	1.3	1.3	1.3
	A_0^n			0.1	0.1	0.1	0.1
Parameters of effective $p-n$ interaction	MeV.fm^3 V_0	214	3.60	396	500	500	500
	α	0.25	0.2	0.25	0.15	0.15	0.15
	MeV.fm $V_{\sigma\sigma}$	0.11		0.09	0.06	0.06	0.06
	b	2.253	2.253	2.260	2.296	2.296	2.296
Eff. charges, e	e^p	1.5		1.5	1.5	1.5	1.5
	e^n	0.5		0.5	0.5	0.5	0.5
	e^{vibr}	1.8	2.0	1.7	1.6	1.6	1.6
Eff. gyromagnetic ratios	g_s^p	$0.65g_s^p$(free)		$0.65g_s^p$(free)	$0.6g_s^p$(free)	$0.6g_s^p$(free)	$0.6g_s^p$(free)
	g_l^p	1		1	1	1	1
	g_s^n	$0.5g_s^n$(free)		$0.6g_s^n$(free)	$0.5g_s^n$(free)	$0.5g_s^n$(free)	$0.5g_s^n$(free)
	g_l^n	0		0	0	0	0
	$g_p = Z/A$	0.4397		0.432	0.425	0.418	0.411

symmetry can be accounted for by renormalization of parameters. According to our calculations even the two-boson components were weak in the wave functions. The boson–boson interaction was omitted.

The model space consisted of the $d5/2$, $g7/2$, $s1/2$, $d3/2$ and $h11/2$ states both for protons and neutrons (with the exception of ^{116}Sb, where we have calculated only positive parity level spectrum and omitted the $\nu h11/2$ orbit). The single proton was considered as a particle and the neutrons as quasiparticles. The occupation probabilities for the neutrons were taken from the systematics of experimental data (for citations see [6]).

The proton and quasineutron energies, as well as the strength parameters of

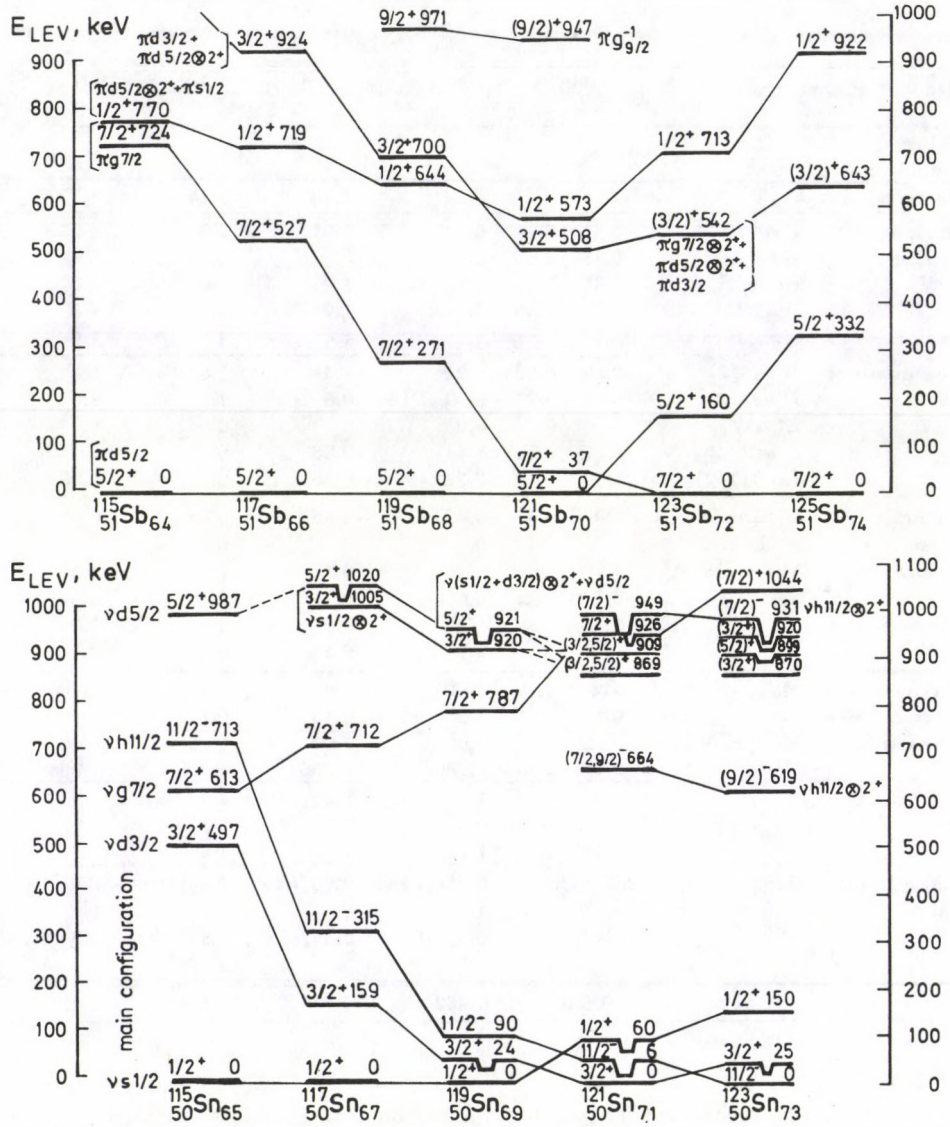

Fig. 8. Proton particle (ε) and quasineutron (E) energies, as well as the neutron occupation probabilities (V^2) for different odd–odd Sb nuclei. The adopted values for IBFFM/OTQM calculations

nucleon–core interaction were fitted to level energies (Fig. 9) and electromagnetic moments [31] of the neighbouring odd–A Sb and Sn nuclei by IBFM calculations.

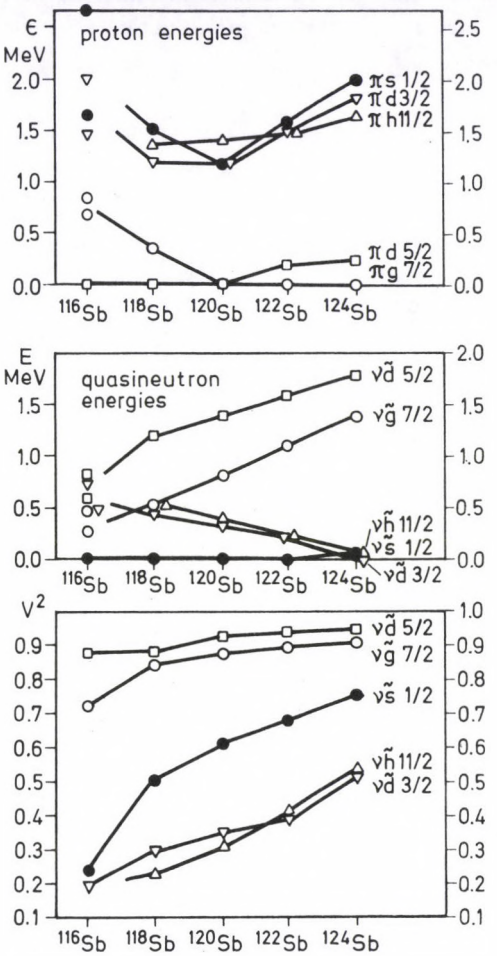

Fig. 9. Level energy systematics of single-odd $^{115-125}$Sb and $^{115-123}$Sn nuclei. Data were taken from corresponding Nucl. Data Sheets and original papers

Finally, these parameters were slightly adjusted to the level energies and electromagnetic moments of ^{116}Sb, ^{118}Sb, ^{120}Sb, ^{122}Sb and ^{124}Sb, respectively, with a restriction of smooth variation from one isotope to the next. The adopted proton and quasineutron energies, as well as the occupation probabilities for neutrons are shown in Fig. 8.

The short range proton–neutron effective interaction strengths, V_0 and α were estimated from the corresponding data of the double closed shell nuclei [19b, 32]. The radial matrix elements of the effective interaction were calculated using har-

monic oscillator wave function with oscillator parameters "b", given in Table II.

The effective charges and gyromagnetic ratios were close to the commonly used, standard values.

3.3 Results and discussion

The IBFFM *energy spectra* of ^{116,118,120,122}Sb and ^{124}Sb are compared with experimental data in Figs 10–14, respectively. Although the energy splitting of different $p-n$ multiplets shows great variety, and in some multiplets shape change of the splitting can be observed as we proceed from one isotope to the next, reasonable agreement has been obtained between experiment and theory.

The IBFFM *wave functions* of the states are complex, nevertheless the low-lying levels are dominated usually with one proton–neutron component. For example in the case of ^{120}Sb the 1_1^+, 2_2^+, 3_3^+ and 4_2^+ states are dominated by components with $\pi d5/2\nu\tilde{d}3/2$ (quasi)particles, the 3_1^+, 2_1^+ states with $\pi 5/2\nu\tilde{s}1/2$, the 3_2^+, 4_1^+ states with $\pi g7/2\nu\tilde{s}1/2$ (quasi)particles, etc. (Table III), in accordance with the approximate classification of the parabolic rule. Similar results on wave functions have been obtained for ^{116,118,122,124}Sb nuclei, too.

The *systematics of the energy splitting* of the ^{116,118,120,122,124}Sb $p-n$ multiplets and the corresponding IBFFM results are presented in Fig. 15.

The splitting of the $\pi d5/2\nu\tilde{d}3/2$ multiplets shows a regular, open-down parabolic shape in ^{116,118,120,122}Sb nuclei, in agreement with IBFFM calculations. This parabolic shape is characteristic for the (quasi)particle-core dynamical interaction. Strong effect of the dynamical interactions can be expected in odd–odd Sb nuclei, when the V^2 occupation probability of the neutron subshell is far from 0.5.

The splitting of the $\pi d5/2\nu\tilde{s}1/2$ and $\pi g7/2\nu\tilde{s}1/2$ doublets is quite regular in ^{116,118,120,122,124}Sb, and the experimental and IBFFM data agree well. Although the $\tilde{s}1/2$ quasineutron is particle-like in ^{116}Sb and hole-like in $^{118-124}$Sb (Fig. 8), the character of energy splitting does not change. This is because the splitting of the doublets is determined by the spin dependent part of the effective interaction, which does not depend on occupation probability [formula (5)].

The energy splitting of the $\pi g7/2\nu\tilde{d}3/2$, $\pi d5/2\nu\tilde{h}11/2$ and $\pi g7/2\nu\tilde{h}11/2$ multiplets shows an open-down, nearly parabolic shape in the lighter nuclei, while in ^{124}Sb the parabolas are strongly deformed. Clearly they are "preparing" for inversion, because the $V^2(\nu\tilde{d}3/2)$ and $V^2(\nu\tilde{h}11/2)$ occupation probabilities are close to 0.5. As Fig. 15 shows, the IBFFM calculations could give a reasonable description of the energy splitting of these multiplets. The exchange interaction (the account of the Pauli principle in the (quasi)particle–core interaction) has a strong effect around $V^2 \approx 0.5$, and plays an important role in the interpretation of the "irregular" (non-parabolic) energy splitting.

The $\pi d5/2\nu g7/2$ multiplet was observed only in ^{116}Sb and ^{118}Sb. The energy splitting shows (slightly distorted) open-up parabolic shape, in agreement with the IBFFM calculations.

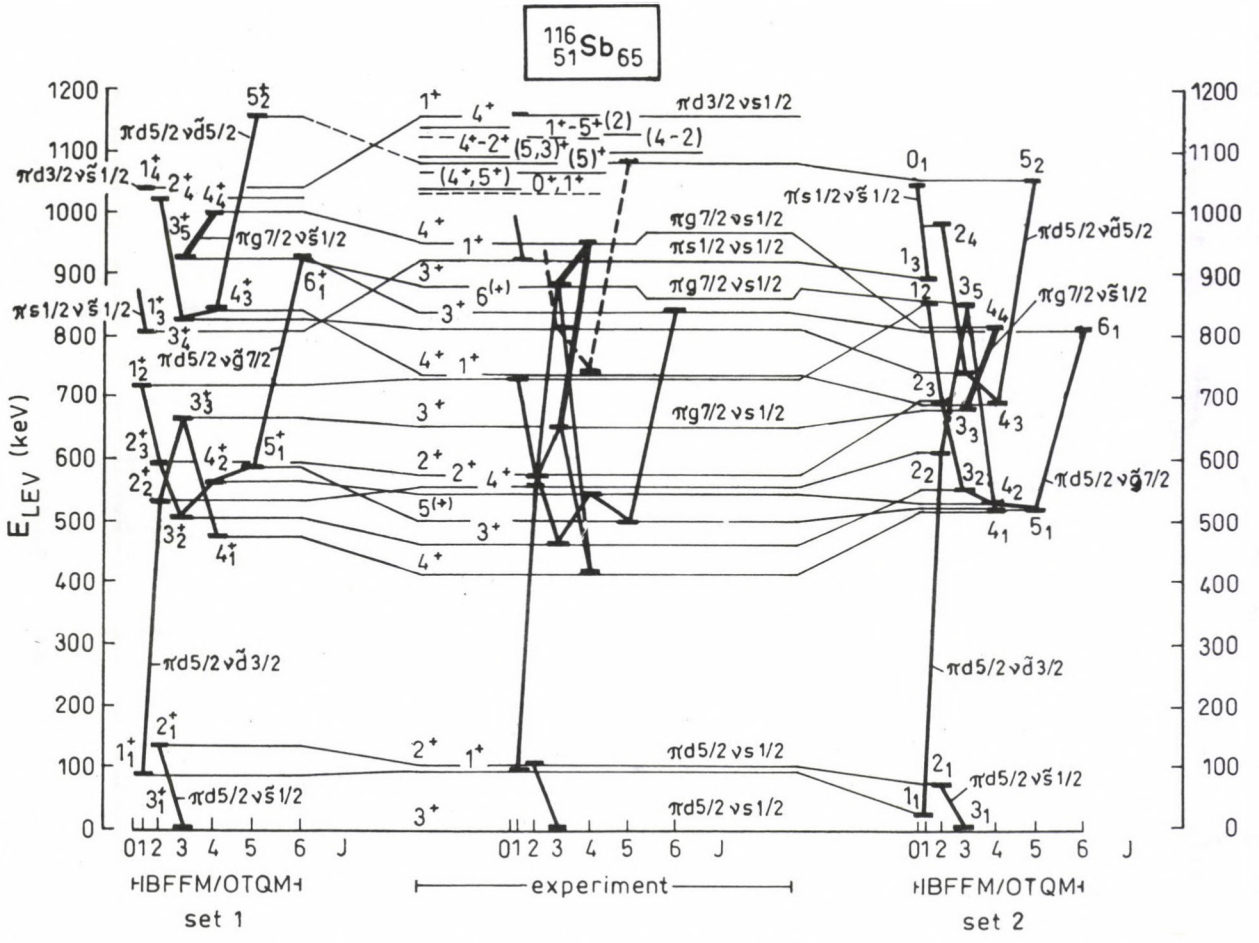

Fig. 10. Level scheme of the low-lying positive parity states of ^{116}Sb [16]. Levels belonging to the same multiplet are connected. The abscissa is scaled according to $J(J+1)$, where J is the spin of the state

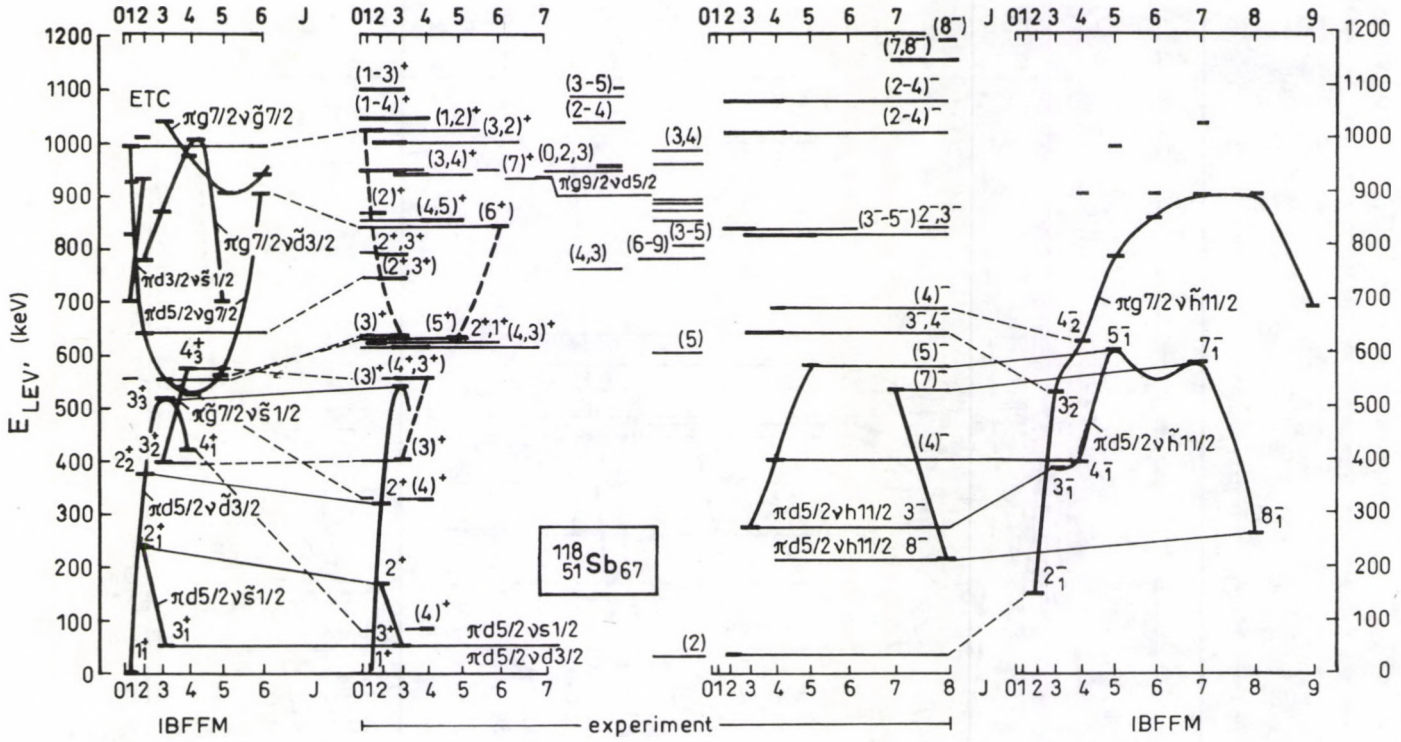

Fig. 11. Level scheme of the low-lying states of ^{118}Sb [14]. Further explanations see under Fig. 10

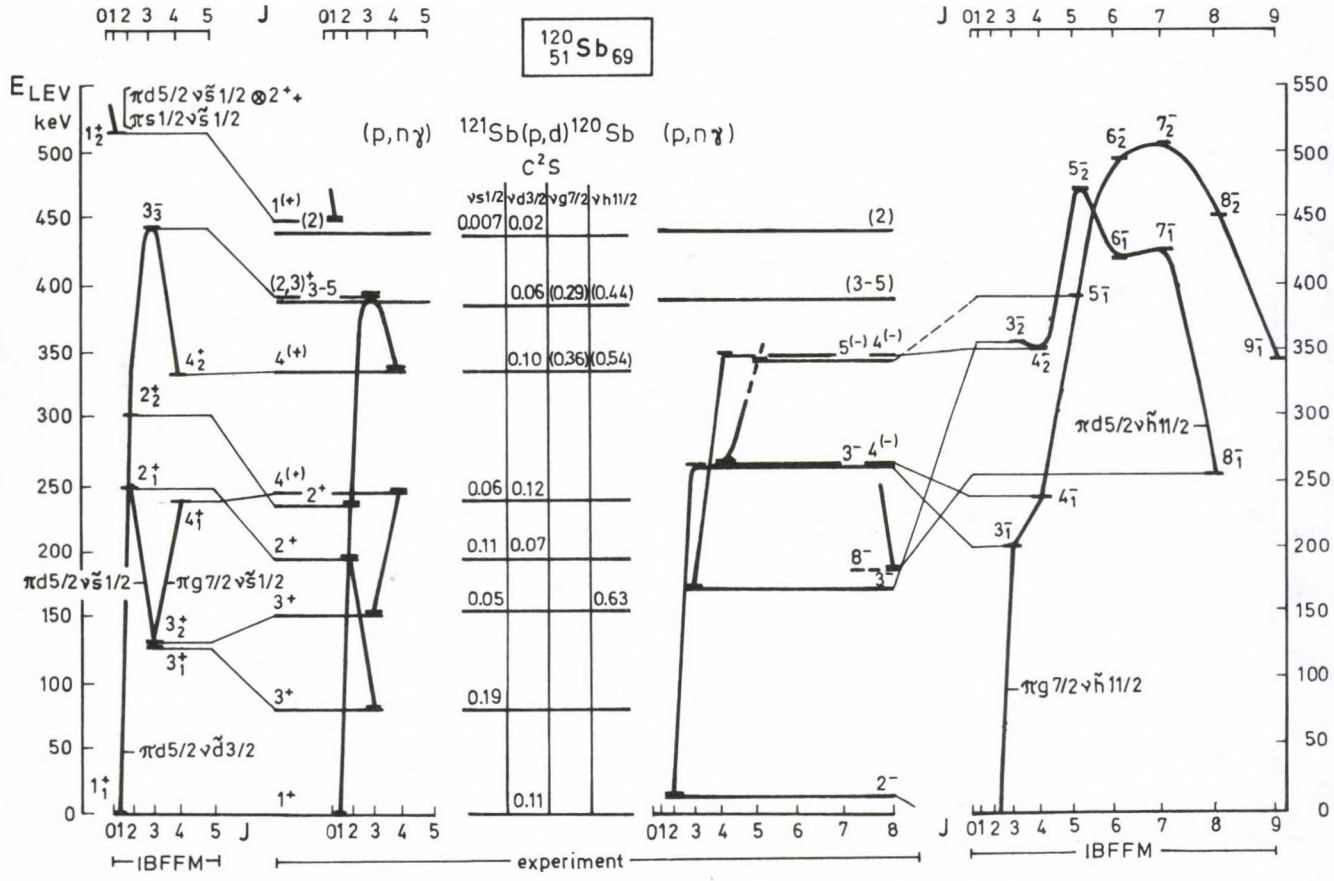

Fig. 12. The low-lying levels of ^{120}Sb [12]. The experimental data were taken from [22, 23]

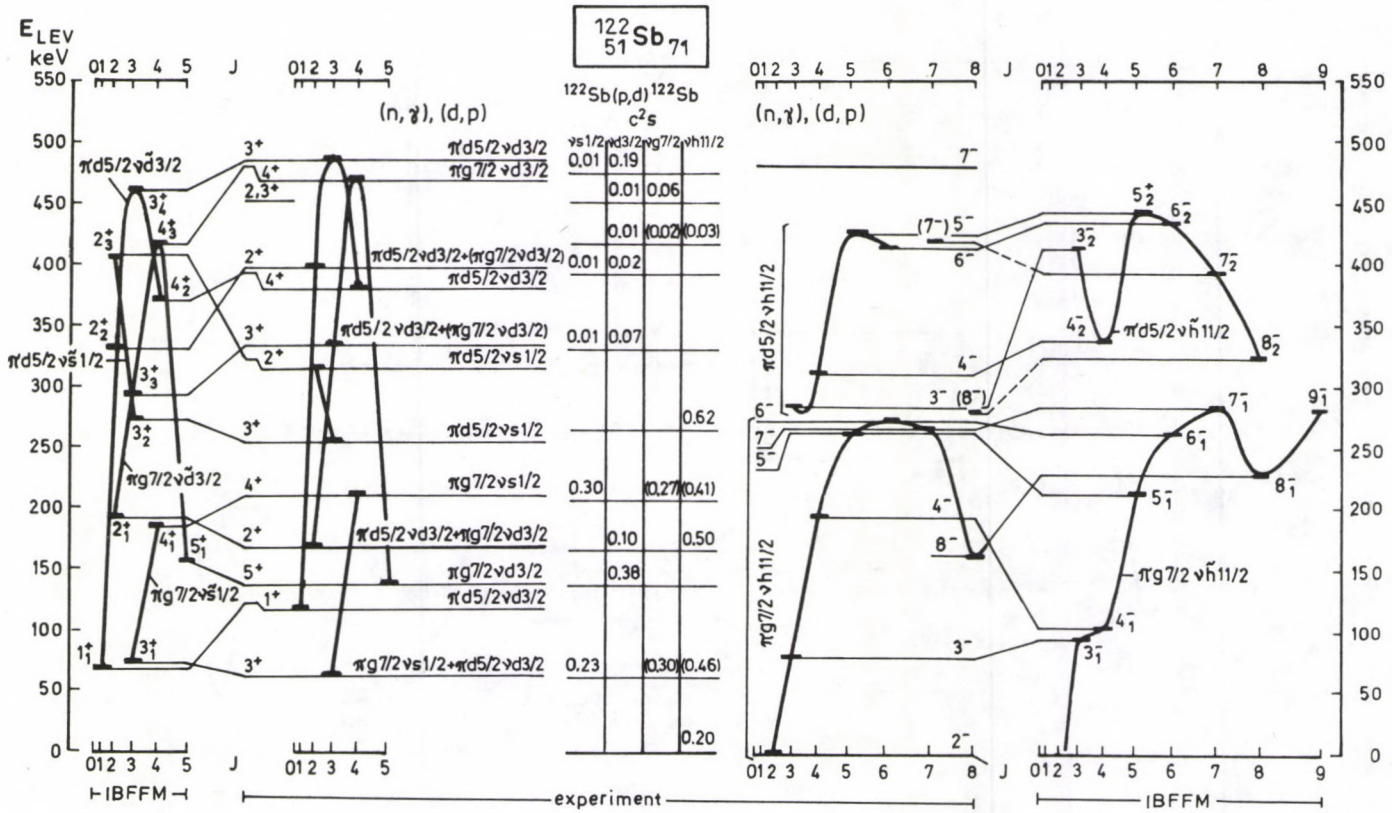

Fig. 13. The low-lying levels of ^{122}Sb. The experimental data were taken from [23–25]

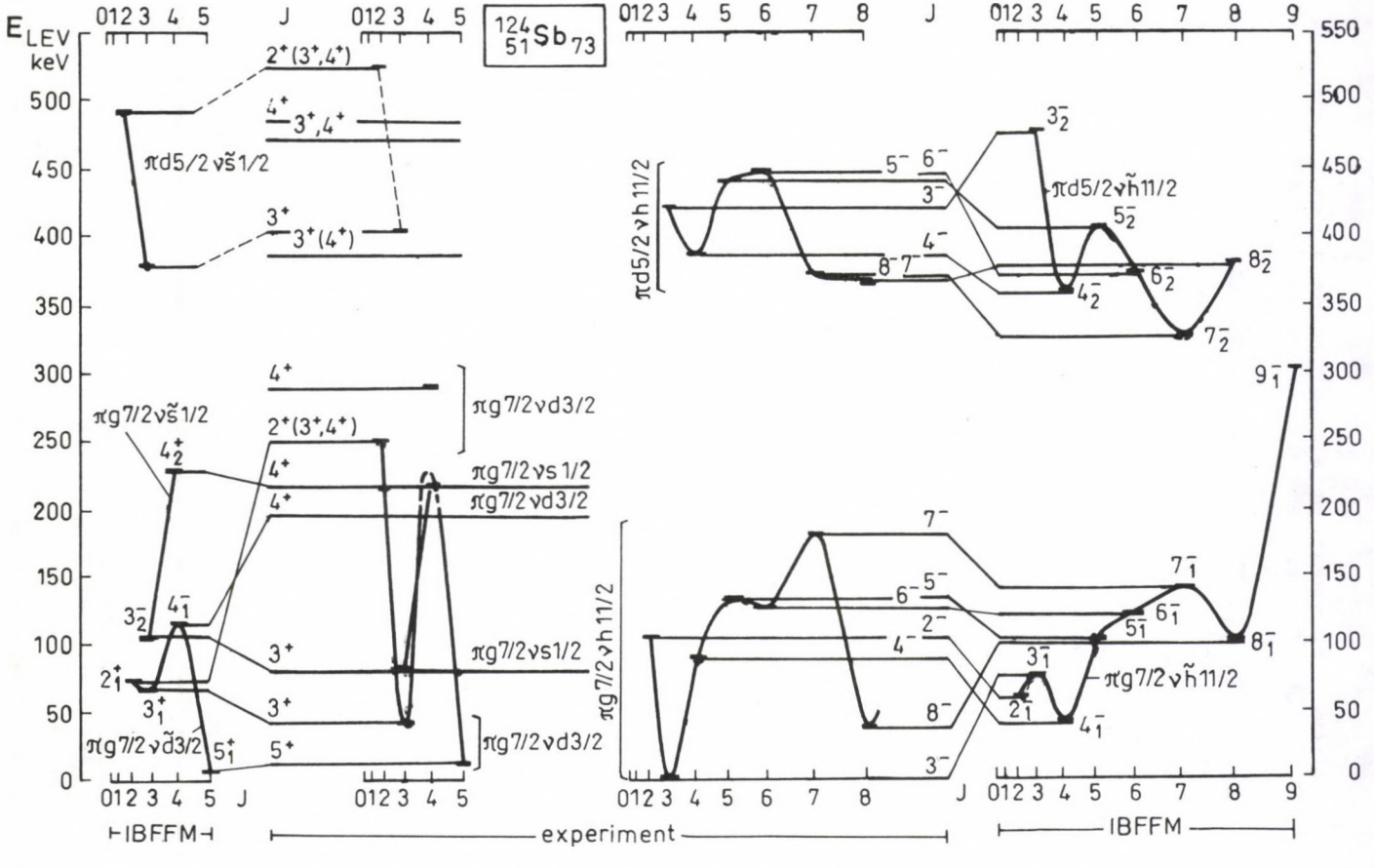

Fig. 14. The low-lying levels of ^{124}Sb. The experimental data were taken from [33]

Table III
Wave functions of some low-lying states of ^{120}Sb. For the given J^π states the $|(j_p, j_n)I; NR>$ wave function components and the corresponding amplitudes are given. Only amplitudes larger than 10 % weight are shown

J^π	$\|(j_p, j_n)I; NR>$	Amplitude	J^π	$\|(j_p, j_n)I; NR>$	Amplitude
1_1^+	(5/2, 3/2)1;00	-0.857	2_1^-	(7/2, 11/2)2;00	-0.867
1_2^+	(5/2, 1/2)3;12	0.619	3_1^-	(7/2, 11/2)3;00	-0.767
	(1/2, 1/2)1;00	0.587		(7/2, 11/2)2;12	-0.344
2_1^+	(5/2, 1/2)2;00	0.678		(7/2, 11/2)5;12	0.318
	(5/2, 3/2)2;00	-0.453	3_2^-	(5/2, 11/2)3;00	-0.774
2_2^+	(5/2, 3/2)2;00	0.590		(5/2, 11/2)4;12	0.363
	(5/2, 1/2)2;00	0.469	4_1^-	(7/2, 11/2)4;00	-0.717
	(7/2, 3/2)2;00	0.326		(5/2, 11/2)4;00	-0.368
3_1^+	(5/2, 1/2)3;00	-0.816		(7/2, 11/2)6;12	0.327
	(5/2, 1/2)3;12	0.328	4_2^-	(5/2, 11/2)4;00	-0.619
3_2^+	(7/2, 1/2)3;00	0.810		(7/2, 11/2)2;12	-0.453
	(7/2, 1/2)3;12	-0.327		(5/2, 11/2)6;12	0.325
	(5/2, 1/2)3;00	0.311	5_1^-	(7/2, 11/2)5;00	0.800
3_3^+	(5/2, 3/2)3;00	-0.690		(7/2, 11/2)7;12	-0.347
	(7/2, 3/2)3;00	-0.459		(7/2, 11/2)3;12	-0.343
4_1^+	(7/2, 1/2)4;00	-0.859	5_2^-	(5/2, 11/2)5;00	-0.759
	(7/2, 1/2)4;12	0.370		(5/2, 11/2)7;12	0.352
4_2^+	(5/2, 3/2)4;00	-0.830	8_1^-	(5/2, 11/2)8;00	0.833
	(5/2, 3/2)4;12	0.415		(5/2, 11/2)8;12	-0.376

We note that the 1_1^+ ground states of ^{118}Sb and ^{120}Sb belong to the $\pi d5/2\nu\tilde{d}3/2$ multiplet, although the $\nu\tilde{d}3/2$ states in ^{117}Sn and ^{119}Sn have higher energy than the $\nu\tilde{s}1/2$ ones (Fig. 9). This effect is caused probably by the stronger interaction between the πd and $\nu\tilde{d}$ states, owing to the stronger overlap of the wave functions.

The *electromagnetic moments* and the corresponding IBFFM results are summarized in Table IV. The signs of moments of odd–odd Sb nuclei were properly reproduced almost in all cases. The experimental and theoretical magnetic dipole moments agree usually within 10 %. The electric quadrupole moments of the positive parity states are reproduced within 17 %, while the moments of the negative parity states of ^{122}Sb and ^{124}Sb are somewhat low. (Here we remark that the electric quadrupole moments of the $\tilde{h}11/2$ neutron states have negative sign in ^{117}Sn, ^{121}Sn and positive in ^{123,125}Sn [31]. This corresponds to the fact that in the lighter odd Sn nuclei the $\tilde{h}11/2$ quasiparticle has a particle-like [$V^2(\nu\tilde{h}11/2) < 0.5$], while in the heavier ones hole-like [$V^2(\nu\tilde{h}11/2) > 0.5$] character. The 2_1^- ^{122}Sb and 3_1^- ^{124}Sb $\pi g7/2\nu\tilde{h}11/2$ ground states have small quadrupole moments, very sensitively depending on the actual value of the $V^2(\nu\tilde{h}11/2) \approx 0.5$ parameter.)

According to the IBFFM calculations the contribution of the collective M1 operator to the magnetic moments is small, while the collective components are dominant in the quadrupole moments.

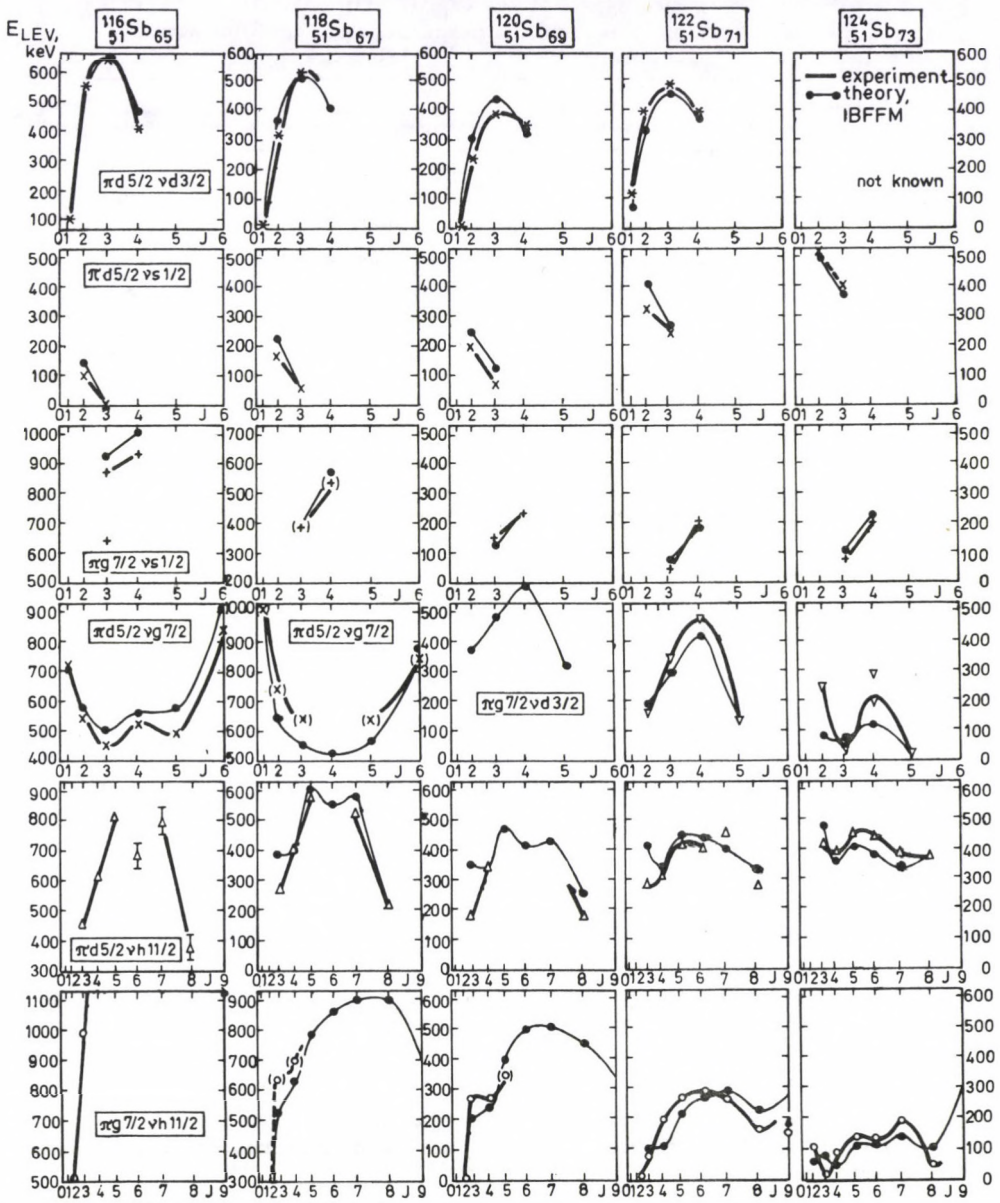

Fig. 15. Systematics of energy splitting of different $p - n$ multiplets in ^{116,118,120,122,124}Sb. The abscissa is scaled according to $J(J+1)$, where J is the spin of the state

Table IV
Magnetic dipole (μ in μ_N) and electric quadrupole (Q in eb) moments of some $^{116,\ 118,\ 120,\ 122,\ 124}$Sb states

Nucleus	J^π, main configuration	μ		Q	
		Exp*	IBFFM	Exp*	IBFFM
^{116}Sb	3_1^+ (ground) $\pi d5/2\nu\tilde{s}1/2$	$\pm 2.715(9)$	+2.79(set 1) +2.88(set 2)		
	1_1^+ (94 keV) $\pi d5/2\nu\tilde{d}3/2$	+2.47(9)	+2.30(set 1) +2.18(set 2)		
^{119}Sb	1_1^+ (ground) $\pi d5/2\nu\tilde{d}3/2$	$\pm 2.47(7)$	+2.31		−0.14
	3_1^+ (51 keV) $\pi d5/2\nu\tilde{s}1/2$	$+2.63(5)^h$	+2.58	$\pm 0.57(14)^{st}$	−0.57
	8_1^- (212 keV) $\pi d5/2\nu\tilde{h}11/2$	$\pm 2.32(4)$	+2.54		−0.92
	3_1^- (270 keV) $\pi d5/2\nu\tilde{h}11/2$	−3.76(9)	−3.43	$\pm 0.25(5)^{st}$	−0.26
^{120}Sb	1_1^+ (ground) $\pi d5/2\nu\tilde{d}3/2$	$\pm 2.34(22)$	+2.32		−0.11
	3_1^+ (78 keV) $\pi d5/2\nu\tilde{s}1/2$	$+2.584(6)^h$	+2.64	$\pm 0.41(4)^{st}$	−0.46
	8_1^- ($T_{1/2}$ = 5.76 d) $\pi d5/2\nu\tilde{h}11/2$	$\pm 2.34(1)$	+2.51		−0.55
^{122}Sb	2_1^- (ground) $\pi g7/2\nu\tilde{h}11/2$	−1.905(20)	−2.37	$+0.86(17)^{st}$	−0.12
	3_1^+ (61 keV) $\pi g7/2\nu\tilde{s}1/2$	$+2.983(12)^h$	+3.09	$\pm 0.41(4)^{st}$	−0.48
	5_1^+ (137 keV) $\pi g7/2\nu\tilde{d}3/2$	+3.05(10)	+3.03		−0.64
^{124}Sb	3_1^- (ground) $\pi g7/2\nu\tilde{h}11/2$	$\pm 1.20(2)$	−1.23	$+1.87(38)^{st}$	+0.35
	3^+ (41 keV)	+2.970(33)			
	3_1^+ $\pi g7/2\nu\tilde{d}3/2$		+2.32		−0.32
	3_2^+ $\pi g7/2\nu\tilde{s}1/2$		+2.91		−0.46
	6_1^- (125 keV) $\pi g7/2\nu\tilde{h}11/2$	+0.384(12)	+0.352		+0.15

*The experimental data were taken from Raghavan's compilation [31]. "h": does not include Knight-shift correction, "st": Sternheimer or other polarization correction included

As we have mentioned before, the wave functions of the odd–odd Sb states are usually very complex. There are states, which contain more than 200 components. At the same time the γ-transition probabilities depend critically even on weak components of the wave function. As an example the E2/M1 γ-*mixing* (δ) *and* γ-

Table V
Transitions within some low-lying ^{120}Sb states

Experiment									IBFFM calc.	
E_i keV	J_i^π	E_f keV	J_f^π	E_γ keV	Multi-polarity	δ Ref. [26]	I_γ Ref. [26]	I_γ Ref. [22]	$\lvert\delta\rvert$	I_γ
149	3_2^+	78	3_1^+	71	(M1+E2)	0.12 ± 0.12	100	100	0.02	100
193	2_1^+	78	3_1^+	114	(M1+E2)	0.0 ± 0.04	100	100	0.01	100
		0	1_1^+	193	M1+E2	0.09 ± 0.21	32(2)	46	0.06	76
233	2_2^+	149	3_2^+	84			4(2)	1.7	0.03	1
		78	3_1^+	155		-0.16 ± 0.16	33(2)	27	0.01	35
		0	1_1^+	233		0.07 ± 0.12	100	100	0.06	100
244	$4_1^{(+)}$	149	3_2^+	95		0 ± 0.11	89(14)	69	0.01	133
		78	3_1^+	166		0 ± 0.18	100	100	0.02	100
334	$4_2^{(+)}$	244	$4_1^{(+)}$	90				10	0.01	28
		149	3_2^+	185		-0.05 ± 0.12	100	100	0.02	100
390	$2, 3_3^+$	244	$4_1^{(+)}$	146			19(7)	21	0.01	5
		233	2_2^+	157			19(7)	7	0.03	90
		193	2_2^+	189			100	100	0.05	100

branching ratios of ^{120}Sb transitions are given in Table V. The IBFFM calculations reasonably reproduced the experimental data. The experimental γ-branching ratios agree with the calculated ones within a factor of ≈ 5. The results obtained on ^{116}Sb and ^{118}Sb are described in [14] and [16], respectively.

Effect of dynamical and exchange core–particle interactions on the energy splitting of p–n multiplets. The IBFFM calculations gave reasonable description of the "regular" and "irregular" energy splitting of different Sb $p-n$ multiplets. In "regular" cases (where V_ν^2 is close to 0 or 1) the IBFFM energies can be approximated with the parabolic rule. The correspondence between IBFFM and its quasiparticle approximation remains valid as long as only dynamical interaction influences the splitting of the multiplets. The exchange interaction may cause deviation from the above picture, which is most significant when the neutron occupation probability is around 0.5. Although the exchange interaction works only for the d-boson states, the proton dynamical interaction admixes also d-boson components to the wave function of the proton–neutron multiplets, and makes effective the exchange interaction for multiplet-like states, too. In this way the proton–boson dynamical and the neutron quasiparticle–boson exchange interactions together produce the additional splitting of the multiplets. The combined effect of the proton dynamical and neutron exchange interactions is shown in Fig. 16 for the $\pi g7/2\nu\tilde{h}11/2$ multiplet. The $\Gamma_0^p = 0$ case corresponds to the quasiparticle picture. It is seen, how the core–particle interactions kink the ends of the multiplet. The possible shape of the multiplet depends on the neutron occupation probability, since it determines the

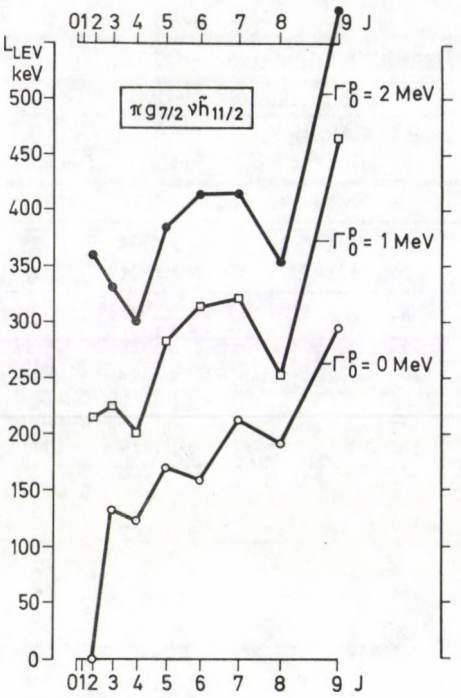

Fig. 16. The energy splitting of the $\pi g7/2\nu\tilde{h}11/2$ multiplet as a function of the proton–core dynamical interaction strength (Γ_0^p). J is the spin of the state. All other parameters were kept constant (case of ^{124}Sb, in Table II). The curves are shifted relative to each other

weight of the exchange and dynamical interactions.

Comparison with other theoretical results. The present IBFFM calculations gave the first comprehensive theoretical description of the structure of ^{118}Sb and ^{120}Sb nuclei. In the case of ^{116,122,124}Sb the former theoretical works [24, 33–36] were based on particle–quasiparticle models. Our IBFFM calculations show that the explicit treatment of collective effects is important.

The $\pi g7/2\nu\tilde{h}11/2$ multiplet is longer than the other ones, so it is more sensitive to the details of interactions. Most of the members of this multiplet have been found experimentally. In Fig. 17 we compared the energy splitting of the ^{122}Sb $\pi g7/2\nu\tilde{h}11/2$ multiplet with different theoretical results.

In the calculations of Gunsteren and Rabenstein [35] a proton was coupled to a number projected neutron quasiparticle assuming $Z = N = 50$ core. They have used renormalized Schiffer interaction. Alexeev et al [24, 33] have calculated the energy splitting of different two-quasiparticle multiplets. The residual interaction contained short-range Wigner, singlet and (in the case of ^{124}Sb) also tensor forces.

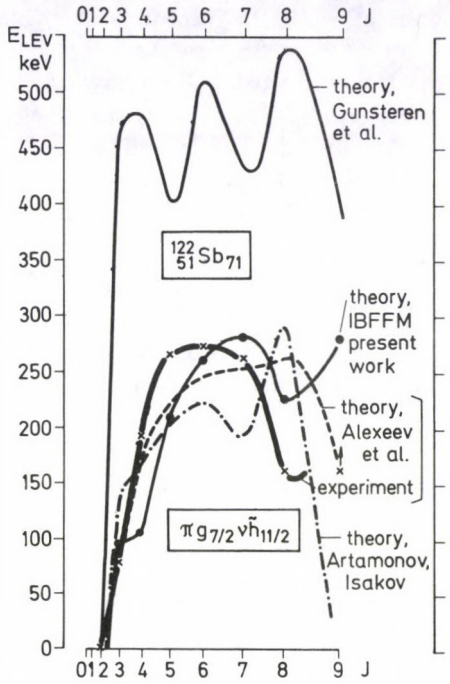

Fig. 17. Comparison of the experimental energy splitting of the ^{122}Sb $\pi g7/2\nu\tilde{h}11/2$ multiplet with different theoretical results. The abscissa shows $J(J+1)$, where J is the spin of the state

In the model of Artamanov and Isakov [36] the odd–odd nucleus is considered as a system of neutron and proton quasiparticles.

As Fig. 17 shows, the renormalized Schiffer interaction causes a very strong staggering compared with experimental data (calculations of Gunsteren and Rabenstein [35]). The other theoretical curves indicate smoother $J(J+1)$ dependence and they are closer to the observed values.

It is known from the works of Shroy et al [37], Van Nes et al [38], Duffait et al [39] and Vajda et al [40] that in the odd–A and odd–odd ^{114,116,118,120}Sb nuclei there are *high-spin bands* which show very regular behaviour. We have observed the lowest members of these bands in ^{116}Sb and ^{118}Sb from $(\alpha, n\gamma)$ reactions. The bandheads in odd-A Sb isotopes are the $g_{9/2}^{-1}$ intruder states, which have prolate deformation [41, 42].

In the framework of the IBF/PTQ and IBFF/OTQ models we have calculated the level spectra of these bands in ^{117}Sb and ^{118}Sb [14]. The calculations showed that the experimental data could be interpreted only in the case, if we supposed $h_3 \neq 0$ (in OTQM parametrization) for intruder states; it is the presence of γ-

deformation. These results indicate shape co-existence in Sb nuclei: the majority of low-lying states have spherical, while the intruder states (bands) deformed shapes.

The low-lying levels of ^{120,122,124}Sb were studied also through (d,p), (d,t) and (p,d) neutron transfer reactions. In work [43] we have calculated the *spectroscopic factors* for the low-lying states of ^{120,122,124}Sb within the framework of the interacting boson–fermion–fermion model. The calculated and measured spectroscopic factors agree in most cases within a factor of two.

Acknowledgements

We are indebted to all co-authors of Refs. [1–19, 43] for fruitful collaboration. The financial support of the Hungarian National Scientific Foundation (OTKA) is gratefully acknowledged.

References

1. J. Gulyás, A. Domonyi, T. Kibédi, A. Krasznahorkay, T. Fényes and Zs. Schram, Prib. Tech. Ekszp., No 3, 53, 1984.
2. Z. Árvay, T. Fényes, K. Füle, T. Kibédi, S. László, Z. Máté, Gy. Mórik, D. Novák and F. Tárkányi, Nucl. Instrum. Meth., *178*, 85, 1980; T. Kibédi, Z. Gácsi, A. Krasznahorkay and S. Nagy, Inst. of Nuclear Research, ATOMKI Ann. Rep. 1986, Debrecen, p. 55; T. Kibédi, Z. Gácsi and A. Krasznahorkay, ATOMKI Ann. Rep. Debrecen, p. 100.
3. T. Fényes and Zs. Dombrádi, Acta Phys. Hung., *65*, 295, 1989.
4. J. Timár, T. Fényes, T. Kibédi, A. Passoja, M. Luontama, W. Trzaska and V. Paar, Nucl. Phys., *A455*, 477, 1986.
5. Zs. Dombrádi and T. Fényes, Inst. of Nucl. Research, ATOMKI Ann. Rep. 1988, p. 22.
6. T. Kibédi, Zs. Dombrádi, T. Fényes, A. Krasznahorkay, J. Timár, Z. Gácsi, A. Passoja, V. Paar and D. Vretenar, Phys. Rev., *C37*, 2391, 1988.
7. A. Krasznahorkay, T. Fényes, J. Timár, T. Kibédi, A. Passoja, R. Julin and J. Kumpulainen, Nucl. Phys., *A473*, 471, 1987.
8. A. Krasznahorkay, Zs. Dombrádi, J. Timár, Z. Gácsi, T. Kibédi, A. Passoja, R. Julin, J. Kumpulainen, S. Brant and V. Paar, Nucl. Phys., *A503*, 113, 1989.
9. A. Krasznahorkay, Zs. Dombrádi, J. Timár, T. Fényes, J. Gulyás, J. Kumpulainen and E. Verho, Nucl. Phys., *A499*, 453, 1989.
10. J. Gulyás, Zs. Dombrádi, T. Fényes, J. Timár, A. Passoja, J. Kumpulainen and R. Julin, Nucl. Phys., *A506*, 196, 1990.
11. Zs. Dombrádi, S. Brant and V. Paar, Phys. Rev., *C44*, 1701, 1991.
12. T. Fényes and Zs. Dombrádi, Phys. Lett., *B275*, 7, 1992.
13. J. Gulyás, T. Fényes, M. Fayez F. M. Hassan and Zs. Dombrádi, Inst. of Nucl. Res. of Hung. Acad. Sci., Debrecen, ATOMKI Preprint 4–1992, P, 1992. In print in Phys. Rev. *C46*, 1992.
14. J. Gulyás, T. Fényes, M. Fayez F. M. Hassan, J. Kumpulainen and R. Julin, Inst. of Nucl. Res. of Hung. Acad. Sci., Debrecen, ATOMKI Preprint 5–1992, P, 1992. In print in Phys. Rev. *C46*, 1992.
15. Z. Gácsi, T. Fényes and Zs. Dombrádi, Phys. Rev., *C44*, 626, 1991.
16. Z. Gácsi, Zs. Dombrádi, T. Fényes, S. Brant and V. Paar, Phys. Rev., *C44*, 642, 1991.
17. Z. Gácsi, Inst. of Nucl. Res. of Hung. Acad. Sci., Debrecen, ATOMKI Ann. Rep. 1991, p. 19.
18. J. Gulyás, J. Kumpulainen and R. Julin, Inst. of Nucl. Res. of Hung. Acad. Sci., Debrecen, ATOMKI Ann. Rep. 1991, p. 18.

19. T. Fényes, Zs. Dombrádi, A. Krasznahorkay, J. Gulyás, J. Timár, T. Kibédi and V. Paar, Fizika, *22*, 273, 1990; Zs. Dombrádi, S. Brant and V. Paar, Mod. Phys. Lett., *A7*, 271, 1992.
20. V. Paar, Nucl. Phys., *A331*, 16, 1979.
21. P. H. Stelson and L. Grodzins, Nucl. Data, *A1*, 21, 1965.
22. R. A. Emigh, C. A. Fields, M. L. Gartner, L. E. Samuelson and P. A. Smith, Z. Phys., *A308*, 173, 1982.
23. R. A. Emigh, C. A. Fields, M. L. Gartner, L. E. Samuelson and P. A. Smith, Z. Phys., *A308*, 165, 1982.
24. V. L. Alexeev, B. A. Emelianov, A. I. Egorov, L. P. Kabina, D. M. Kaminker, Yu. L. Khazov, I. A. Kondurov, E. K. Leushkin, Yu. E. Loginov, V. V. Martynov, V. L. Rumiantsev, S. L. Sakharov, P. A. Sushkov, H. G. Börner, W. F. Davidson, J. A. Pinston and K. Schreckenbach, Nucl. Phys., *A297*, 373, 1978.
25. K. Kitao, M. Kambe, Z. Matsumoto and T. Seo, Nucl. Data Sheets, *49*, 315, 1986.
26. M. Adachi, T. Matsuzaki and H. Taketani, Nucl. Phys., *A314*, 80, 1979.
27. V. Paar, in: In-Beam Nuclear Spectroscopy, ed. Zs. Dombrádi and T. Fényes, Akadémiai Kiadó, Budapest, 1984, vol. 2, p. 675.
28. F. Iachello and O. Scholten, Phys. Rev. Lett., *43*, 679, 1979; V. Paar, S. Brant, L. F. Canto, G. Leander and M. Vouk, Nucl. Phys., *A378*, 41, 1982.
29. D. Janssen, R. V. Jolos and F. Dönau, Nucl. Phys., *A224*, 93, 1974; A. Arima and F. Iachello, Phys. Rev. Lett., *35*, 1069, 1975.
30. S. Brant, V. Paar and D. Vretenar, Computer codes IBM/TQM, IBFM/PTQM, IBFFM/OTQM, Inst. für Kernphysik, KFA Jülich, 1985 (unpublished).
31. P. Raghavan, At. Data Nucl. Data Tables, *42*, 189, 1989.
32. Zs. Dombrádi, S. Brant and V. Paar, Proc. Int. Conf. on Capture γ-ray Spectroscopy, Pacific Grove, CA 1990, ed. R. W. Hoff, Am. Inst. of Phys. 238, New York, 1990, p. 150.
33. V. L. Alexeev, I. A. Kondurov, Yu. E. Loginov, V. V. Martynov, S. L. Sakharov, P. A. Sushkov, H. G. Börner, W. F. Davidson, J. A. Pinston and K. Schreckenbach, Nucl. Phys., *A345*, 93, 1980.
34. W. F. Van Gunsteren, K. Allaart and E. Boeker, Nucl. Phys., *A266*, 365, 1976.
35. W. F. Van Gunsteren and D. Rabenstein, Z. Phys., *A282*, 55, 1977.
36. S. S. Artamonov and V. I. Isakov, Izv. AN SSSR, ser. fiz., *43*, 2071, 1979.
37. R. E. Shroy, A. K. Gaigalas, G. Schatz and D. B. Fossan, Phys. Rev., *C19*, 1324, 1979.
38. P. Van Nes, W. H. A. Hesselink, W. H. Dickhoff, J. J. Van Ruyven, M. J. A. De Voigt and H. Verheul, Nucl. Phys., *A379*, 35, 1982.
39. R. Duffait, J. Van Maldeghem, A. Charvet, J. Sau, K. Heyde, A. Emsallem, M. Meyer, R. Béraud, J. Tréherne and J. Genevey, Z. Phys., *A307*, 259, 1982.
40. S. Vajda, W. F. Piel, Jr., M. A. Quader, W. A. Watson III, F. C. Yang and D. B. Fossan, Phys. Rev., *C27*, 2995, 1983.
41. K. Heyde, P. Van Isacker, M. Waroquier, J. L. Wood and R. A. Meyer, Phys. Reports (Rev. Sect. of Phys. Lett.), *102*, 293, 1983.
42. J. Van Maldeghem, J. Sau and K. Heyde, Phys. Lett., *116B*, 387, 1982.
43. Zs. Dombrádi, S. Brant and V. Paar, Inst. of Nucl. Res. of Hung. Acad. Sci., Debrecen, ATOMKI Ann. Rep. 1992, p. 29.

Acta Physica Hungarica 71 (3-4), pp. 269-270 (1992)

BOOK REVIEW

MARCELL WELLNER: *Elements of Physics*, 693 pp. Plenum Press, New York and London, 1991. ISBN 03-306-433540-0

This textbook has been written for a two or three semester introductory course for students in engineering or science who need reasonable familiarity with physics as a whole. Although a calculus course, concurrent with the presentation of the material of the book, is supposed, no previous knowledge of calculus is necessary, because the early concepts are explained in the book as needed, although not in a mathematically rigorous manner.

The book is clearly and carefully written and well illustrated with figures and tables. The latter are very well arranged to demonstrate the scale and order of magnitude of the physical quantity. To promote the successful study of the book, every chapter is supplemented by the following three parts: "Condensed checklist", "True or false" and "Problems". The condensed checklists contain the definitions of the most important concepts and the list of the formulas of the chapters. In the other two supplementations an abundant collection of questions and problems is given.

The book includes 28 chapters which contain the basic laws of classical physics (mechanics, electrodynamics, thermodynamics and the kinetic theory of gases), the elements of special relativity and three short chapters on atomic physics.

The first nine chapters give a relatively detailed and good treatment of the basic laws of mechanics although the description of fluids is shorter than it is usual in books of similar type. (There is no mention of viscosity and surface tension.) The structure of the text itself and its presentation of topics are done much in the usual manner and the explanations are generally clear and helpful for the students. However, for the explanation of weightlessness the author uses questionable and mistakable terminology, and the interpretation of the centrifugal force is simply wrong. (According to the author ... "while rounding a curve, a car subjects a passenger to a net centripetal force, but the passenger exerts a centrifugal force on the car.")

The next three chapters, covering thermodynamics and the kinetic theory of gases are built up also in a traditional way; the concept of temperature is based on gas thermometer, heat is introduced by calorimetry, and the entropy is defined through the discussion of the Carnot cycle. It may cause difficulty in understanding of these chapters that besides the SI units, the Fahrenheit temperature scale, the calorie and the British thermal unit are also used.

The next two chapters deal with vibrations and waves. The latter one includes the discussion of the properties of the sound waves and the Doppler effect. The presentation of waves is somewhat poorer than that of the previous chapters. There is no mention of interference, diffraction and polarization. As a minor point, though, it is difficult to see what purpose is served by stating the wave equation with partial derivatives.

The seven chapters on electromagnetism deal with the description of the electromagnetic field in a vacuum, and a clear way is given from the Coulomb's law to the integral form of the Maxwell equations. A questionable point of this section is the revival of the old concept of magnetic poles at the introductory part of magnetism. It is difficult to decide whether the didactic advantages of using electrostatic analogy is worth enough confusing the basic ideas of magnetic field. In spite of this the presentation is quite clear and really gets to the core of the theory from the basic laws. An especially well written part of the book is the elementary explanation of the energy and momentum of the electromagnetic waves.

The chapters on optics, on the one hand, are too long, on the other hand, they are slightly incomplete. The derivation of the lens and mirror equation is missing from the book. At the same time the geometrical optics is beginning with a relatively long and superficial wave optical introduction. The Snell's law and the laws of reflection are based on ideas which are similar to that of the Huygens–Fresnel principle although the clear description of the latter one cannot be found in the book.

The chapter on relativity, even for an elementary introduction to the subject, is by necessity very incomplete. It is oriented only toward some frequently used practical results, namely, the well-known mass–energy relation and the Doppler effect for light. The results of this chapter might have been put into an Appendix.

The last three chapters on atomic and nuclear physics constitute a section similar to that with which most introductory physics texts usually conclude. The presentation is clear and easy to read.

In summary, Wellner's text is a very well written presentation of the most important laws of physics for an introductory course. It is on a par with most of the presently available books addressing the same audience. The good collection of examples and problems of the book is also worth serious consideration.

E. Sas

Manuscript received by Akadémiai Kiadó:
18 March 1992
Manuscript received by TYPOTEX Ltd for TEX typesetting:
17 April 1992
Date of publication:28 October 1992
PRINTED IN HUNGARY
Akadémiai Kiadó és Nyomda Vállalat
Budapest

CONTENTS

Vol. 71

CONDENSED MATTER

NOTES TO CONTRIBUTORS

I. PAPERS will be considered for publication in Acta Physica Hungarica only if they have not previously been published or submitted for publication elsewhere. They may be written in English, French, German or Russian.

Papers should be submitted to

Prof. I. Kovács, Editor
Department of Atomic Physics, Technical University
1521 Budapest, Budafoki út 8, Hungary

Papers may be either articles with abstracts or short communications. Both should be as concise as possible, articles in general not exceeding 25 typed pages, short communications 8 typed pages.

II. MANUSCRIPTS

1. Papers should be submitted in three copies.
2. The text of papers must be of high stylistic standard, requiring minor corrections only.
3. Manuscripts should be typed in double spacing on good quality paper, with generous margins.
4. The name of the author(s) and of the institutes where the work was carried out should appear on the first page of the manuscript.
5. Particular care should be taken with mathematical expressions. The following should be clearly distinguished, e.g. by underlining in different colours: special founts (italics, script, bold type, Greek, Gothic, etc.); capital and small letters; subscripts and superscripts, e.g. x^2, x_3; small *l* and l; zero and capital O; in expressions written by hand: *e* and *l*, *n* and *u*, *v* and v, etc.

A List of Symbols on a separate sheet should be attached to each paper.

6. References should be numbered serially and listed at the end of the paper in the following form: J. Ise and W. D. Fretter, Phys. Rev., *76*, 933, 1949.

For books, please give the initials and family name of the author(s), title, name of publisher, place and year of publication, e.g.: J. C. Slater, Quantum Theory of Atomic Structures, I. McGraw-Hill Book Company, Inc., New York, 1960.

References should be given in the text in the following forms: Heisenberg [5] or [5].

7. Captions to illustrations should be listed on a separate sheet, not inserted in the text.
8. In papers submitted to Acta Physica all measures should be expressed in SI units.

III. ILLUSTRATIONS AND TABLES

1. Each paper should be accompanied by three sets of illustrations, one of which must be ready for the blockmaker. The other sets attached to the copies of the manuscript may be rough drawings in pencil or photocopies.
2. Illustrations must not be inserted in the text.
3. All illustrations should be identified in blue pencil by the author's name, abbreviated title of the paper and figure number.
4. Tables should be typed on separate pages and have captions describing their content. Clear wording of column heads is advisable. Tables should be numbered in Roman numerals (I, II, III, etc.).

IV. RETURN OF MATERIAL

Owing to high postage costs, the Editorial Office cannot undertake to return *all* material not accepted for any reason for publication. Of papers to be revised (for not being in conformity with the above Notes or other reasons) only *one* copy will be returned. Material rejected for lack of space or on account of the Referees' opinion will not be returned to authors outside Europe.

Index: 26.022